Aus CharitéCentrum 6 für Diagnostische und lnterventionelle Radiologie und Nuklearmedizin
Klinik für Radiologie mit dem Bereich Kinderradiologie
Direktor: Prof. Dr. med. Bernd Hamm

Habilitationsschrift

Translationale Neuromolekulare Bildgebung

zur Erlangung der Lehrbefähigung
für das Fach Radiologie
vorgelegt dem Fakultätsrat der Medizinischen Fakultät
Charité Universitätsmedizin Berlin

von

Dr. med. Johannes Lohmeier

Eingereicht: 11/2023
Dekan: Prof. Dr. Joachim Spranger

Inhaltsverzeichnis

Glossar

ADC	„Apparent diffusion coefficient“
	(Deutsch: Angenommener Diffusionskoeffizient)
AUC	„Area Under the Curve“
	(Deutsch: Fläche unter der Kurve)
BHS	Blut-Hirn-Schranke
FA	„Fractional Anisotropy“
	(Deutsch: Fraktionale Anisotropie)
Gd	Gadolinium
MD	„Mean Diffusivity“
	(Deutsch: Mittlere Diffusivität)
MKT	„Mean Kurtosis Tensor“
	(Deutsch: Mittlerer Kurtosis Tensor)
MRT	Magnet-Resonanz-Tomographie
MS	Multiple Sklerose
PET	Positronen-Emissions-Tomographie
ROC	„Receiver Operating Characteristic“
	(Deutsch: Grenzwertoptimierungskurve)
SNR	„Signal-to-Noise Ratio“ (SNR)
	(Deutsch: Signal-Rausch-Verhältnis)
SUV	“Standardized Uptake Value“
	(Deutsch: Standardisierter Aufnahmewert)
TBR	„Target-to-Background Ratio“
	(Deutsch: Zielregion-zu-Gehirn Aufnahmeverhältnis)
WHO	„World Health Organization“
	(Deutsch: Weltgesundheitsorganisation)
ZNS	Zentrales Nervensystem

1. Einleitung und Fragestellung

1.1. Hybride Bildgebung - PET/MRT

Die Magnet-Resonanz-Tomographie (MRT) hat sich in der radiologischen Diagnostik aufgrund eines exzellenten Weichgewebekontrasts sowie hoher räumlicher und zeitlicher Auflösung in vielen Fragestellungen als Bildgebungsstandard durchgesetzt. Bei der MRT erfolgt eine systematische und schichtweise Abtastung von Gewebestrukturen mittels hochfrequenter (nicht-ionisierender) elektromagnetischer Felder, die biophysikalische Eigenschaften erfassen können. Dabei basiert das Verfahren auf dem Prinzip der Kernspinresonanz. Durch das externe Magnetfeld werden Protonen im Gewebe ausgerichtet und durch spezielle Hochfrequenzpulse zu einer Ausrichtungsänderung angeregt. Nach der Anregung geben die Protonen während der sog. Relaxation (Längs- und Querrelaxation) die Energie in Form von elektromagnetischen Signalen ab, die von Spulen detektiert werden. Diese Rohdaten werden gespeichert und anschließend mit Hilfe von Rekonstruktionsalgorithmen unter Nutzung der Fourier-Transformation in Schnittbilder umgewandelt. Durch Anpassung der Sequenzparameter können verschiedene Bildkontraste, wie T1-, T2- und PD (Protonendichte)-gewichtete Bilder, erzeugt werden. Nach intravenöser (i.v.) Applikation von paramagnetischen Kontrastmitteln kann durch deren magnetisches Moment eine messbare lokale Veränderungen der Relaxationszeiten induziert werden, sodass bestimmte Strukturen und Regionen kontrastverstärkt zur Darstellung kommen. In der klinischen Versorgung werden sowohl unspezifische (z.B. Gadobutrol oder Gadotersäure) als auch spezifische (z.B. Gadoxetatsäure) Kontrastmittel eingesetzt. Nachteile der MRT-Bildgebung sind zumeist langwierige Bildakquisitionen sowie eine geringe Spezifität. In den letzten Jahren wurden auf Grundlage der Kernspinresonanz zahlreiche neue Techniken entwickelt, die eine Charakterisierung verschiedener biologischer Aspekte ermöglichen, wie die Diffusion von Wasserprotonen oder die Perfusion von Gewebe.

Die Positronen-Emissions-Tomographie (PET)-Bildgebung ist ein nuklearmedizinisches Verfahren, bei dem Positronen emittierende kurzlebige Radiopharmaka nach i.v. Applikation gemessen werden. Das radioaktive Isotop unterliegt einem Prozess des positiven Beta-Zerfalls, bei dem ein Positron freigesetzt wird. Dieses Positron verliert dann sukzessiv seine kinetische Energie. Sobald ein Positron auf ein Elektron trifft (gewöhnlich weniger als

1 Millimeter von der Ursprungsposition entfernt), resultiert eine gegenseitige Annihilation. Die hierbei entstehende sekundäre Vernichtungsstrahlung wird in Form von zwei entgegengesetzt gerichteten Photonen, den sogenannten Gamma-Quanten, freigesetzt. Diese Gamma-Quanten werden von Detektoren erfasst, wodurch räumliche Informationen über die Verteilung der radioaktiven Substanz im Körper gewonnen werden können. Dabei wird jedes detektierte Strahlenpaar, das innerhalb eines vorgegebenen Zeitfensters an zwei gegenüberliegenden Szintillatoren ankommt, als koinzident betrachtet. Mittels spezieller Rekonstruktionsalgorithmen können hieraus Bilddatensätze über die Verteilung der radiomarkierten Sonden, die beispielsweise als synthetische Analoga fungieren und/oder Zielstrukturen spezifisch binden, erzeugt werden. Zu den Nachteilen der PET-Bildgebung zählt die Strahlenexposition, die besondere Vorsichtsmaßnahmen und Überwachung erfordert, sowie die im Vergleich zu MRT- und Computer-Tomografie (CT)-Schnittbildgebung niedrigere räumliche Auflösung. Hinzu kommen logistische Herausforderungen, insbesondere im Hinblick auf die kurze Halbwertszeit der verwendeten Radionuklide.

In den letzten Jahrzehnten hat sich herausgestellt, dass sowohl die PET als auch die MRT, wenn sie unabhängig voneinander betrachtet werden, in ihrer diagnostischen Leistungsfähigkeit deutlich begrenzt sind. Die modernsten Entwicklungen in der Hybrid-Bildgebungstechnologie haben die simultane PET/MRT-Bildgebung zu einem wichtigen Werkzeug in der klinischen Routine gemacht [1]. Diese vereint den informativen Wert beider Modalitäten mit zusätzlichen Vorteilen in Hinblick auf hohe räumliche und zeitliche Konkordanz sowie verbesserte technische PET-Korrekturverfahren. Durch eine Kombination von strukturellen, metabolischen und molekularen Informationen kann die diagnostische Genauigkeit erheblich verbessert werden. Neben infrastrukturellen Vorzügen, kann zudem die Untersuchungszeit durch simultane Bildgebung verkürzt werden. Angesichts der steigenden Verfügbarkeit von hybriden PET/MRT-Systemen und Empfehlungen für einen kombinierten Einsatz von PET und MRT in der onkologischen Bildgebung [2] besteht ein hoher Bedarf an neuartigen neurobildgebenden Methoden, die multimodale Bildgebungsdaten integrieren und damit eine molekulare Charakterisierung von Krankheitsprozessen ermöglichen. Zudem können durch die komplementäre Auswertung bislang unbeantwortete Fragen zur Pathophysiologie diverser Krankheiten adressiert werden. Die Integration von PET und MRT bietet eine klinisch relevante und technologisch fortschrittliche Kombination bildgebender Verfahren, die eine multidisziplinäre Perspektive auf die diagnostische Bildgebung eröffnet.

1.2. Quantitative molekulare Bildgebung

Bildgebende Verfahren haben die moderne Medizin grundlegend geprägt [3, 4]. Die technologischen Fortschritte der letzten Jahrzehnte haben zur Entstehung eines neuen interdisziplinären Forschungsgebiets an der Schnittstelle zwischen Bildgebungsverfahren und Molekularbiologie geführt [5], das sich speziell der Detektion von molekularen Signaturen biologischer Prozesse und Krankheiten mittels Bildgebung widmet. Mit dem Paradigmenwechsel zur Präzisionsmedizin und individualisierten Behandlungsstrategien ist die molekulare Bildgebung zu einer der wichtigsten Säule der modernen Medizin geworden und eröffnet neue Anwendungsmöglichkeiten, beispielsweise in der Krebsforschung und -behandlung [6, 7].

Im Kontrast zur strukturellen Bildgebung nutzen molekulare Bildgebungsansätze markierte Sonden, die es ermöglichen, bestimmte Moleküle unter Nutzung von Fluoreszenzproteinen, Radionukliden, paramagnetischer Substanzen oder Nanopartikeln sichtbar zu machen, sowie nicht-markierte Bildgebungsverfahren (wie z.B. die Magnet-Resonanz-Spektroskopie oder „Chemical Exchange Saturation Transfer“), die endogene Zielstrukturen messen, wie eisenhaltiges Hämoglobin oder Metaboliten [8]. Die Entwicklung von diagnostischen Sonden ist ein zeit- und ressourcenintensiver Prozess und ähnelt in vielerlei Hinsicht der Entwicklung neuer therapeutischer Arzneistoffe. Dabei hat sich insbesondere die klinische Translation dieser technologischen Bildgebungsinnovationen als herausfordernd erwiesen. Molekulare Sonden durchlaufen einen komplexen Prozess, von der präklinischen Entwicklung und Validierung, bis hin zu klinischen Studien und langwierigen Zulassungsverfahren – sofern sie eine Reihe von günstigen Eigenschaften in Bezug auf Spezifität/Sensitivität/Selektivität, Biokompatibilität, Stabilität und Toxizität, Pharmakokinetik und -dynamik bis hin zu ökonomischen Aspekten, wie Kosteneffizienz und Skalierbarkeit, aufweisen. Nicht-markierte molekulare Bildgebungsverfahren sehen sich mit anderen Herausforderungen konfrontiert, wie etwa der Entwicklung von Pulssequenzen, biophysikalischer Modelle und Datenverarbeitungsschritte, gefolgt von (prä-)klinischen Pilotstudien bis hin zu multizentrischen Studien.

Quantitative Bildgebung. Mit der klinischen Translation von molekularen Bildgebungsverfahren wird die bildgestützte Charakterisierung von Krankheitsprozessen auf molekularer und zellulärer Ebene möglich. In der klinischen Praxis ist die visuelle und

qualitative Interpretation von Bildgebungsverfahren etabliert. Diese Herangehensweise an die Bildinterpretation bietet häufig den Vorteil einer zügigen, wenn auch subjektiven und vom jeweiligen Kenntnisstand abhängigen Beurteilung. Im Gegensatz dazu reduziert die Messung standardisierter und reproduzierbarer Kenngrößen die Einflussnahme subjektiver Faktoren und schafft günstigere Rahmenbedingungen für die Normierung von Bildinterpretation oder die Definition diagnostischer Grenzwerte als Hilfsmittel in der klinischen Behandlung. Weiterhin eröffnen standardisierte (semi-)quantitative Metriken neue Möglichkeiten für die Charakterisierung von Krankheitsbildern und stellen eine objektivere Entscheidungsgrundlage dar. Allerdings erfordert die quantitative Auswertung sowohl gewisse Erfahrung und Fachwissen als auch entsprechende zeitliche und technische Ressourcen. Die Interoperabilität zwischen unterschiedlichen Geräten und klinischen Kontexten setzt eine rigorose Methodenstandardisierung voraus, die in der klinischen Praxis oft nur schwer umsetzbar ist. Zudem birgt die isolierte oder unerfahrene Betrachtung quantitativer Daten das Risiko für Fehlinterpretationen, insbesondere wenn der klinische Kontext nicht berücksichtigt wird. Daher ergänzen sich qualitative und quantitative Methoden in der medizinischen Bildgebung. Bei komplexen klinischen und wissenschaftlichen Fragestellungen nehmen quantitative Methoden einen immer größeren Stellenwert ein. Zu den wichtigsten limitierenden Faktoren für eine reliable qualitative und quantitative Auswertung gehören u.a. der Partialvolumeneffekt (insbesondere bei niedriger räumlicher Auflösung), Bewegungsartefakte und ein ungünstiges Signal-Rausch-Verhältnis (SNR).

Mittels parametrischer PET kann eine (semi-)quantitative Bewertung der spezifischen Aktivitätskonzentration im Zielgewebe bzw. der jeweiligen Zielstruktur vorgenommen werden. Der am häufigsten verwendete semi-quantitative Indikator in der klinischen PET-Diagnostik wird als „Standardized Uptake Value“ (SUV) bezeichnet. Im Bereich der MRT-Bildgebung stellen T1-, T2- und Protonendichte (PD)-Mapping-Verfahren einen wertvollen Fortschritt dar und ermöglichen eine präzisere Gewebecharakterisierung. Quantitative Diffusionsbildgebung ermöglicht indirekt Einblicke in die Gewebemikrostruktur durch Messung der Diffusion von Wasserprotonen. „Quantitative susceptibility mapping“ (QSM) kartiert magnetische Eigenschaften der Gewebe und hat sich bei der Beurteilung von Eisenablagerungen oder Kalzifikationen als nützlich erwiesen. Schließlich spielen Perfusionsbildgebungsverfahren, wie die „Dynamic susceptibility contrast“ (DSC) und „Dynamic contrast-enhanced (DCE)“ MRT, eine wichtige Rolle bei der Bewertung der Durchblutung oder Gefäßpermeabilität.

Bildgestützte Biomarker. Biomarker sind allgemein definiert als messbare Merkmale, die als Indikator für normale biologische Prozesse sowie Krankheitsmechanismen dienen und Antworten auf bestimmte Behandlungen oder Expositionen liefern [9]. Bildgestützte Biomarker sind Instrumente für die Überprüfung wissenschaftlicher Fragestellungen oder klinische Hilfsmittel zur Entscheidungsfindung. In medizinischen Kontexten werden Biomarker für diverse Zwecke eingesetzt, beispielsweise für die Krankheitserkennung, Prognose, Therapieplanung und -kontrolle. Bildgestützte Biomarker können sowohl quantitative als auch qualitative Merkmale aufweisen. Quantitative Bewertungen werden in der Patientenversorgung zunehmend relevant (z.B. in der Myokarditis-Diagnostik), aber auch qualitative Graduierungen, wie Tumor-Stadien (TNM-Klassifikation), haben sich klinisch etabliert. Verschiedene Organisationen haben Konsensrichtlinien für die Datenerfassung, die Bildverarbeitung, die Validierungsprozesse im Rahmen der Entwicklung sowie die letztendliche Implementierung von Bildgebungsbiomarkern herausgegeben und unterstreichen so die Bedeutung einer rigorosen Validierungs- und Qualifizierungsstrategie [10–12].

Gemäß Conor et. al. (2017) [12] sollen Biomarker in einem zweistufigen Prozess zunächst als robuste Forschungsinstrumente qualifiziert werden, bevor sie als Werkzeuge für die klinische Entscheidungshilfe legitimiert werden können. Die technische, biologische und klinische Validierung sowie die Bewertung der Kosten-Effizienz sind hierbei wesentliche translationale Hürden [12]. Die Translation von neuen Biomarkern in die klinische Anwendung ist häufig ein komplexer Prozess, der mit zahlreichen Herausforderungen und Fallstricken verbunden ist [13]. Hierzu zählt beispielsweise eine unzureichende Vorauswahl von Biomarkern vor Studienbeginn in „omics“-Studien (z.B. Radiomics). Häufig fehlt es zudem an geeigneten Strategien für eine technische, biologische und klinische Validierung der Biomarker sowie an standardisierten und reproduzierbaren Analysemethoden für multizentrische klinische Studien.

1.3. Molekulare Bildgebung bei entzündlichen Erkrankungen des ZNS

Die Neuroinflammation ist eine spezifische Antwort des angeborenen und erworbenen Immunsystems, die durch schädigende Einflüsse auf das Zentralnervensystems (ZNS) ausgelöst wird (z.B. infektiös, traumatisch, autoimmun-entzündlich) [14]. In solchen Fällen wird eine Entzündungsreaktion aktiviert, um den auslösenden Faktor zu isolieren und zu neutralisieren. Dieser Prozess ist komplex und kann sowohl protektive als auch destruktive Auswirkungen auf das ZNS haben. Neuroinflammatorische Prozesse spielen eine zentrale Rolle in einer Vielzahl von neurologischen Erkrankungen, wie Enzephalitiden, Vaskulitiden, Infektionen oder Autoimmunerkrankungen, die bei längerfristigem Fortbestehen in Neurodegeneration münden können [14]. Eine frühzeitige Diagnose und rascher Behandlungsbeginn sind prognostisch häufig entscheidend bei der Prävention von kognitiven und physischen Einschränkungen bzw. Behinderungen.

Obwohl die konventionelle MRT sich als Bildgebungsverfahren der Wahl für entzündliche ZNS-Erkrankungen, wie Multiple Sklerose (MS), etabliert hat, ist ihre Sensitivität und Spezifität bei der Interpretation bestimmter Krankheitsprozesse begrenzt [15]. Während in der klinischen Routine und Forschung häufig indirekte Manifestationen verschiedener pathophysiologischer Abläufe (z.B. Hirnatrophie bei Neurodegeneration) bewertet werden, kann die molekulare Bildgebung zelluläre und metabolische Prozesse direkt darstellen [16]. Mittels bildgestützter quantitativer Biomarker besteht die Möglichkeit, Schlüsselprozesse der Pathophysiologie nicht-invasiv zu quantifizieren, wie beispielsweise De-/Remyelinisierung oder neuroaxonale Schädigung. Molekulare Marker können verschiedene Aspekte der inflammatorischen und neurodegenerativen Kaskade charakterisieren, wie die Aktivierung von Mikroglia mittels Translokator-Protein (TSPO) PET [17]. TSPO ist ein vorrangig mitochondrial lokalisiertes Protein, das u.a. in Zellen des Immunsystems, einschließlich ortsständiger Makrophagen, exprimiert wird und als Marker für die Aktivierung von Mikroglia bei diversen neuroinflammatorischen und -degenerativen Erkrankungen verwendet wird. So bietet die TSPO-PET eine vielversprechende Möglichkeit, die Pathogenese und den Verlauf der MS [18] zu verstehen und prognostizieren. Ein wesentlicher Nachteil der bisher entwickelten TSPO-Radiotracer ist jedoch die variierende Bindungsaffinität in Abhängigkeit von Polymorphismen, weswegen häufig eine genetische Testung vorgeschaltet wird. Zudem wird TSPO auch von anderen Zellpopulationen, wie Astrozyten oder Endothelzellen, exprimiert [19], was dessen Spezifität als Marker für mikrogliale Aktivierung einschränkt.

Ein weiterer häufig verwendeter Radiotracer bei der Beurteilung von Neuroinflammation und Neurodegeneration ist ^{18}F-Fluordeoxyglukose (^{18}F-FDG), der eine Beurteilung des Glukosemetabolismus ermöglicht. Analog zur Glukose wird ^{18}F-FDG durch Glukosetransporter in die Zelle transportiert und durch die Hexokinase zu 2-[^{18}F]Fluor-2-desoxy-D-glucose-6-phosphat phosphoryliert. Da dieses Zwischenprodukt nicht weiter metabolisiert werden kann und bis zur Dephosphorylierung in der Zelle verbleibt, spiegelt dessen zelluläre Anhäufung die Glukoseaufnahme wider [20]. So zeigt sich bei aktiven Entzündungsprozessen häufig eine gesteigerte Glukoseaufnahme, wohingegen bei neurodegenerativen Erkrankungen, wie der Alzheimer-Krankheit, oft eine regional reduzierte Aufnahme zu beobachten ist [18]. Eine verringerte Glukoseaufnahme in der grauen Substanz, die mit Fatigue und kognitiven Einschränkungen in Zusammenhang steht, wird auch bei MS beschrieben [21]. Allerdings ist ^{18}F-FDG nicht spezifisch für neuroinflammatorische und/oder -degenerative Prozesse und der Glukosestoffwechsel wird bekanntermaßen von diversen Faktoren beeinflusst.

Auch molekulare MRT-Anwendungen wurden in den letzten Jahren entwickelt und bieten zwar eine günstigere räumliche Auflösung (z.B. durch den Einsatz von neuen 3D-Sequenzen und/oder Ultrahochfeld-Bildgebung) bei jedoch geringerer Sensitivität. Im Kontext der Neuroinflammation wurden so z.B. ein Myeloperoxidase-aktivierbarer paramagnetischer Sensor [22, 23] oder molekulare Sonden zur Darstellung von „intercellular adhesion molecule-1“ (ICAM-1) [24] oder „vascular cell adhesion molecule 1“ (VCAM-1) [25] entwickelt.

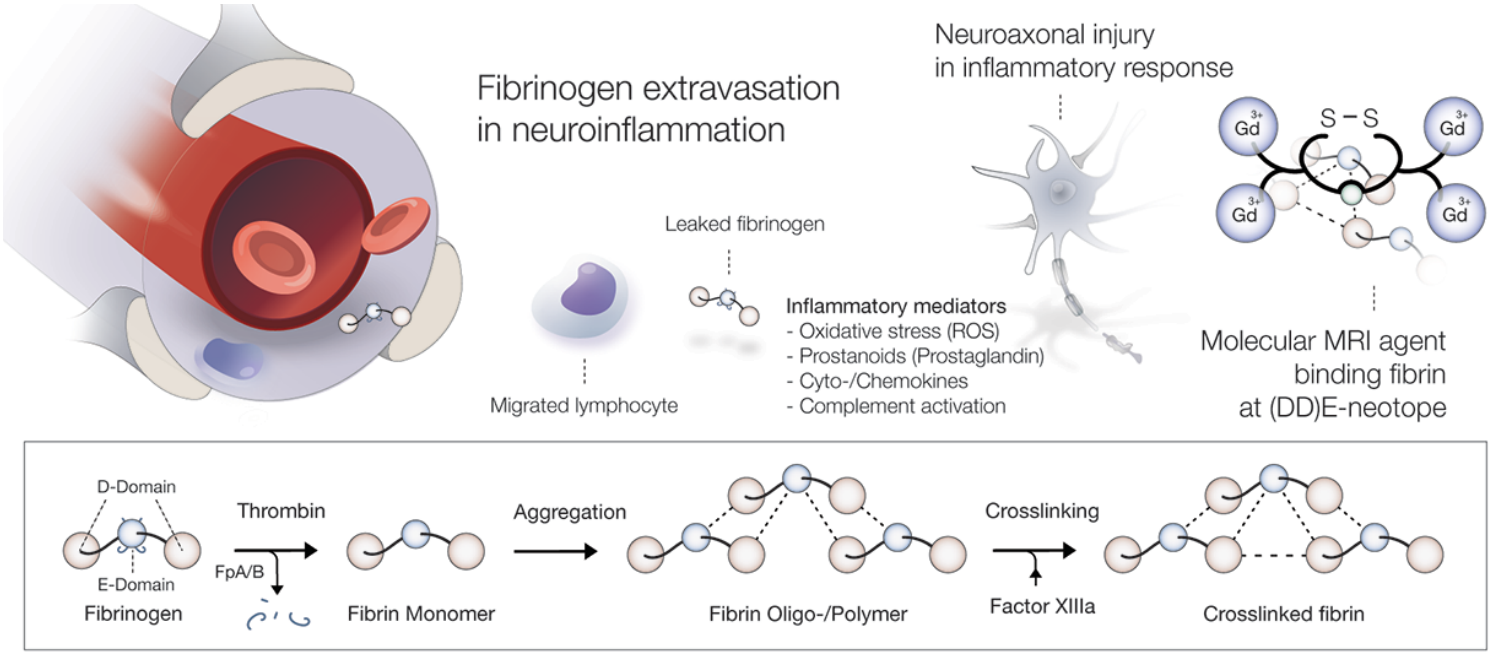

Abbildung 1. Fibrin-Ablagerungen bei entzündlichen Erkrankungen des ZNS. Akute ZSN-Erkrankungen gehen charakteristischerweise mit einer bereits früh im Krankheitsgeschehen auftretenden Dysfunktion der Blut-Hirn-Schranke (BHS) einher. Eine erhöhte BHS-Permeabilität führt zu einer Extravasation von Plasmabestandteilen, wie beispielsweise Fibrinogen, oder exogenen kleinmolekularen Kontrastmitteln, die in den interstitiellen oder perivaskulären Raum übertreten. Dies geht charakteristischerweise auch mit der Konversion von Fibrinogen zu Fibrin einher (s. untere Teilabbildung), sodass parenchymale Fibrin-Plaques gebildet werden. Jenseits seiner traditionellen Rolle im Gerinnungsprozess induziert Fibrin eine immun-entzündliche Reaktion über (CD11b-CD18-)Integrin-Rezeptoren, u.a. mit oxidativer Stressreaktion sowie einer Aktivierung von Mikroglia und peripheren Immunzellen. Bei neuroinflammatorischen Erkrankungen, wie beispielsweise der MS, unterhält dies den Entzündungsprozess und kann langfristig zur Neurodegeneration beitragen. EP2104-R, ein Peptid-konjugiertes Gadolinium-basiertes (Gd^{3+}) Kontrastmittel, kann mit hoher Affinität Fibrin binden, was mittels MRT-Bildgebung visualisiert und als bildgestützter Biomarker für Neuroinflammation und BHS-Störung quantifiziert werden kann. ROS, reaktive Sauerstoffspezies; FpA/B, Fibrinopeptid A/B; *(adaptierte Originalabbildung des Autors; entnommen aus Originalarbeit 1)*.

1.4. Metabolische Bildgebung in der Neuroonkologie

Die Neuroonkologie als interdisziplinäres und rasch expandierendes Fachgebiet ist an der Schnittstelle zwischen den bildgebenden Fachgebieten, den Disziplinen der Neuropathologie, Neurologie, Neurochirurgie, und Strahlentherapie, sowie den Gebieten der Rehabilitation und Palliativpflege. Dieses Gebiet befasst sich mit der Diagnostik, Therapie und Nachsorge von PatientInnen mit Tumoren des ZNS. Weltweit stellen diese Neoplasien eine signifikante Quelle von Morbidität und Mortalität dar, wobei gegenwärtig etwa 5 von 100.000 Menschen pro Jahr betroffen sind [26]. Maligne Tumoren stellen in den USA weniger als ein Drittel aller diagnostizierten Tumoren des zentralen und peripheren Nervensystems dar, sind jedoch für den Großteil der verzeichneten Todesfälle verantwortlich [27]. Ionisierende Strahlung wird als anerkannter Umweltrisikofaktor für Hirntumoren betrachtet, wobei der Zusammenhang bei PatientInnen mit Meningeomen und Gliomen im jüngeren Alter stärker ausgeprägt erscheint [27]. Strahlenexponierte Kinder und Jugendliche, bei denen eine therapeutische Hirnbestrahlung oder mehrere diagnostische CTs durchgeführt wurden, zeigen ein überdurchschnittlich hohes Risiko für die Entwicklung primärer Hirntumoren [27–29]. Weitere potenzielle Risikofaktoren sind derzeit noch Gegenstand der Forschung. Obwohl bei manchen Hirntumoren eine erbliche Komponente (z.B. bei genetischen Syndromen, wie der Neurofibromatose (Typ 1 und 2), tuberösen Sklerose oder von Hippel-Lindau) vorliegt [30], betrifft dies nur eine Minderheit. Tumoren des ZNS stellen insgesamt eine heterogene Gruppe dar, wobei sich die Neoplasien bei Kindern und Heranwachsenden deutlich zu den Manifestationen der Erwachsenen unterscheiden [31]. Während benigne Neoplasien im ZNS häufiger beim weiblichen Geschlecht beobachtet werden, zeigen sich maligne Hirntumoren prädominant bei männlichen Individuen [31]. Da Erfolgsaussichten, Therapieansprechen und Toxizität stark variieren, wird eine multimodale Therapie auf Basis der individuellen Patientenmerkmale und der Tumorcharakteristik durchgeführt.

In der Gruppe der malignen Hirntumoren sind Gliome die häufigste histologische Manifestation. Insbesondere höhergradige Gliome, wie das Glioblastom, sind durch eine rasche Proliferation und ein invasives Wachstumsverhalten gekennzeichnet, was den Therapieerfolg erheblich einschränkt [32]. Während Glioblastome oft eine 5-Jahres-Überlebensrate von unter 10% aufweisen, kann diese bei niedriggradigen Gliomen mehr als 90% betragen [31]. Dabei erweist sich eine Erkrankung in jüngeren Jahren in Hinblick auf die Überlebensrate bei den meisten Tumorarten als vorteilhaft [31].

Der häufigste maligne Hirntumor in der Gruppe der Gliome ist das Glioblastom. Eine wirksame Therapie gestaltet sich oft als ein multidisziplinäres Unterfangen, das neurochirurgische Interventionen, Strahlentherapie und Chemotherapie miteinschließt [32, 33]. Die frühzeitige Erkennung eines Rezidivs ist häufig von entscheidender Bedeutung für die Prognose. Im Falle eines Glioblastom-Rezidivs wird die mittlere Gesamtüberlebenszeit auf 24 bis 44 Wochen geschätzt [32].

Mit den Fortschritten in der Krebsgenomik wurden eine Vielzahl klinisch relevanter Mutationen bei primären Hirntumoren entdeckt. Mittlerweile spielen molekulare Marker eine zentrale Rolle in der Klassifikation, Prognose und Behandlung (z.B. zielgerichtete Therapien oder Planung des Resektionsausmaßes) von Hirntumoren [34]. Sie ermöglichen eine differenzierte Betrachtung der Tumorbiologie, die weit über die konventionelle histopathologische und/oder konventionell-radiologische Beurteilung hinausgeht. Hierdurch ist auch ein Bedarf an neuen nicht-invasiven Biomarkern zur Integration dieser genetischen Informationen in die klinische Patientenversorgung entstanden.

In der klinischen Routine wird bei Tumorerkrankungen in der Regel die bildgebende Diagnostik mittels kontrastmittelgestützter MRT und/oder CT angewandt. Darüber hinaus ermöglichen fortgeschrittene MRT-Methoden und die PET-Bildgebung eine detaillierte Charakterisierung diverser biologischer Merkmale von Tumoren, wie dem Tumorstoffwechsel [35]. Trotz dieser fortschrittlichen Bildgebungstechnologien gibt es jedoch weiterhin klinische Herausforderungen, wie z.B. bei der Klassifizierung, Risikostratifizierung, OP- und Bestrahlungsplanung und Überwachung von Hirntumoren sowie der Nutzung der aus der Genomik gewonnenen Informationen zur Entwicklung nicht-invasiver bildgestützter Biomarker.

So ermöglicht beispielsweise die Magnetresonanz-Spektroskopie (MRS) die Detektion von 2-Hydroxyglutarat, was zur bildgestützten Klassifizierung des IDH-Genotyps genutzt werden kann [36]. Angelehnt an die Kernspinresonanz-Spektroskopie (NMR-Spektroskopie) wurde die MRS als eine nicht-invasive MRT-Technik zur Messung von Stoffwechselprodukten entwickelt. Sie ist aufgrund ihrer hohen Sensitivität und Verfügbarkeit ein wichtiges klinisches und wissenschaftliches Instrument. Mit der MRS können metabolische Veränderungen in Tumorgewebe direkt gemessen werden. Ein wesentlicher Nachteil der MRS ist jedoch ihre begrenzte räumliche Auflösung, die insbesondere bei der Definition der Messregion in oftmals heterogenen Läsionen Schwierigkeiten bereiten kann. Darüber hinaus kann es für eine angemessene SNR notwendig sein, eine erhebliche Anzahl von Mittellungen durchzuführen, was wiederum die Messzeit erheblich verlängern kann.

In nuklearmedizinischen Untersuchungen können unter Anwendung diverser PET-Radiotracer verschiedene metabolische Eigenschaften von Hirntumoren, wie Glukoseverbrauch, Aminosäuretransport, Immunantwort, Hypoxie oder Angiogenese, erfasst werden [37]. In Hinblick auf die Untersuchung von Gliomen sind insbesondere radiomarkierte Aminosäure-Analoga klinisch etabliert. O-(2-[^{18}F]Fluorethyl)-L-Tyrosin (^{18}F-FET) ist eine nicht-natürliche Aminosäure, die für die Darstellung des Tumormetabolismus eingesetzt wird. Dabei spiegelt die Aufnahme von ^{18}F-FET primär die zelluläre Aminosäuretransportrate wider, die über Aminosäuretransporter des L-Typs (LAT) vermittelt wird [38]. Da der radioaktiv markierte Tracer weder in Proteine eingebaut noch innerhalb der Zelle metabolisiert wird, findet eine Anreicherung u.a. im Tumorgewebe mit erhöhtem zellulären Bedarf an Aminosäuren statt [39]. Im Gegensatz zu den seit längerem in der Neuroonkologie eingesetzten Tracern, wie ^{18}F-FDG, wird ^{18}F-FET etwas geringer in aktiven Entzündungsprozessen angereichert [40, 41] und erzeugt geringere Hintergrundsignale. Mittlerweile sind ^{18}F-FET PET Untersuchungen klinisch etabliert und werden beispielsweise bei der Diagnose von primären Gehirntumoren, der Planung von Behandlungen oder der posttherapeutischen Kontrolle eingesetzt [42].

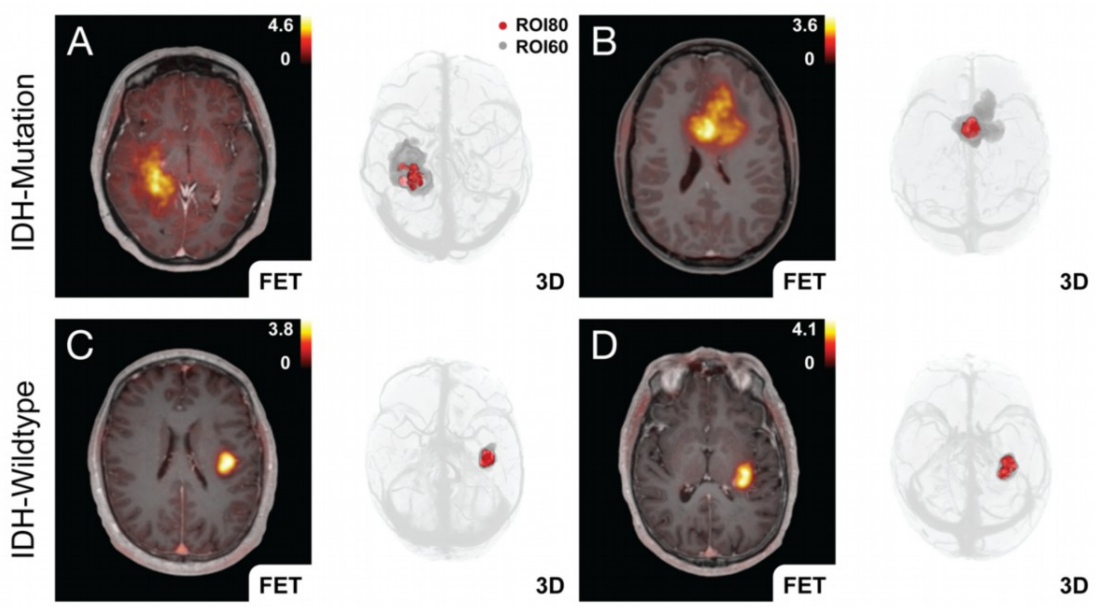

Abbildung 2. Erfassung der metabolischen Heterogenität zur Unterscheidung des IDH-Genotyps in Gliomen. Repräsentative Fallbeispiele eines (**A**) IDH-mutierten Astrozytoms (ZNS WHO Grad 3) und eines (**B**) IDH-mutierten Oligodendroglioms (ZNS WHO Grad 2) veranschaulicht anhand eines ^{18}F-FET PET/MPRAGE-Fusionsbild und 3D-Modellierung. Im Gegensatz dazu weisen IDH-Wildtyp Tumoren (**C** und **D**) eine geringere metabolische Heterogenität auf, wie es anhand von Glioblastomen IDH-Wildtyp (ZNS WHO Grad 4) gezeigt wird. Mittels automatisiert definierter „Region-of-Interests" (ROIs) kann diese Heterogenität drei-dimensional erfasst und als Biomarker quantifiziert werden. (*adaptierte Originalabbildung des Autors; entnommen aus Originalarbeit 3*)

1.5. Fragestellung und Zielsetzung

Die Bildgebung spielt eine zentrale Rolle in der nicht-invasiven Beurteilung von Neuroinflammation und Hirntumoren. Die Charakterisierung dieser Krankheitsprozesse mittels quantitativer Bildgebungsverfahren ist von entscheidender Bedeutung für die Präzisionsmedizin. Sie bieten eine ergänzende Perspektive zur konventionellen Bildgebung und eröffnen neue Wege für die Forschung und klinische Versorgung durch „virtuelle Biopsien“. Durch die Integration von bildgestützten Biomarkern in die medizinische Versorgung werden individualisierte Behandlungskonzepte ermöglicht und klinische Abläufe nachhaltig verbessert. Hierzu zählen die Früherkennung von Krankheiten, die Therapiekontrolle, die prognostische Einschätzung und die molekulare Stratifizierung durch das Erfassen bestimmter molekularer Signaturen.

Die Zielsetzung dieser Arbeiten war daher die Entwicklung und Validierung bildgestützter molekularer Biomarker für die nicht-invasive Beurteilung von malignen und neuroinflammatorischen Prozessen. Dabei stützen sich die Forschungsarbeiten auf die innovative MRT- und PET-Bildgebung, um die molekularen Eigenschaften von Hirntumoren und entzündliche Prozesse im ZNS zu bestimmen.

2. Eigene Arbeiten

2.1. Molekulare Fibrin-spezifische MRT in der Neuroinflammation (Originalarbeit 1)

Lohmeier J, Silva RV, Tietze A et al. (2022) Fibrin-targeting molecular MRI in inflammatory CNS disorders.
European Journal of Nuclear Medicine and Molecular Imaging.
DOI: 10.1007/s00259-022-05807-8

Eine der ersten pathophysiologischen Manifestationen von Neuroinflammation ist die Beeinträchtigung der BHS. Hierbei können Plasmaproteine, wie Fibrinogen, in den perivaskulären Raum und das Hirnparenchym übertreten. Da dies meist mit einer Aktivierung der Komplementkaskade vergesellschaftet ist, kommt es zu einer Umwandlung von löslichem Fibrinogen in das Fibrin-Monomer, welches sich als unlösliches Fibringeflecht um die betroffenen Gefäße absetzt. Neben seiner allgemein bekannten Funktion in der Gerinnungskaskade spielt Fibrin eine aktive Rolle in neuroinflammatorischen Prozessen [43, 44]. Dies trägt signifikant zur Pathophysiologie verschiedener neurologischer Erkrankungen bei, wie beispielsweise bei der Alzheimer-Krankheit [45] und MS [46].
MS ist eine weit verbreitete neurologische Erkrankung, die durch eine immunvermittelte Entzündung und Degeneration des ZNS gekennzeichnet ist. Im Spektrum der neuroinflammatorischen Erkrankungen hat sich die MRT dank eines exzellenten Gewebekontrasts und einer hohen räumlichen Auflösung als Bildgebungsstandard durchgesetzt. Jedoch sind die bildgebenden Befunde und das tatsächliche Ausmaß der kognitiven und physischen Beeinträchtigung oftmals diskrepant, was eine erhebliche Limitation darstellt [47, 48]. Darüber hinaus weisen traditionelle bildgebende Verfahren in der Detektion von demyelinisierenden und kortikalen Läsionen sowohl in Bezug auf ihre Sensitivität als auch auf ihre Spezifität erhebliche Einschränkungen auf [49]. Darin begründet sich das starke klinische Interesse an neuartigen bildbasierten Biomarkern, die dazu beitragen können, diese diagnostische Lücke zu schließen und neue Wege für personalisierte und prognostische Therapieansätze zu ebnen.

Daher widmete sich die vorliegende experimentelle Studie der Evaluation der molekularen

MRT bei neuroinflammatorischen Erkrankungen mittels EP2104-R, einer Fibrin-bindenden molekularen MRT-Sonde. EP2104-R besteht aus vier Gd-DOTA (Tetraxetan) Chelaten und einem Bindepeptid, das mit hoher Affinität an ein hoch-konserviertes Neotop – daher auch Spezies-übergreifende Kompatibilität – im (DD)E-Komplex von Fibrin bindet [50, 51]. Bislang lag der Schwerpunkt der (prä-)klinischen Beurteilung hauptsächlich auf der kardiovaskulären Bildgebung [52], wobei auch Leberentzündungen [53] und Lungenfibrose [54] evaluiert wurden. Aufgrund ihrer hervorragenden Biokompatibilität wurde die molekulare Sonde bereits in Phase-II-Studien zur Thrombosebildgebung eingesetzt, ohne signifikante Nebenwirkungen zu verursachen [55].

Die der *Originalarbeit 1* zugrundeliegende Fragestellung war, ob zentralnervöse Fibrin-Ablagerungen, wie sie bei Neuroinflammation auftreten, mittels molekularer MRT-Bildgebung mit EP2104-R in vivo darstellbar sind. Zudem sollte der Stellenwert dieser Fibrin-Plaques als Biomarker für neuroinflammatorische Prozesse evaluiert werden.

Zunächst wurde in einem in vitro-Experiment belegt, dass Fibrin mit hoher Affinität von EP2104-R gebunden wird ($M \pm SD$, 1366 ± 393 ms (Fibrinogen) vs. 562 ± 86 ms (Fibrin), $p = 0.04$), wohingegen keinerlei spezifische Anreicherung im Fall von Fibrinogen ersichtlich war. Anschließend wurde die molekulare Fibrin-Bildgebung in der murinen experimentellen autoimmunen Enzephalomyelitis (EAE), einer etablierten Modellerkrankung für MS, in verschiedenen Krankheitsstadien evaluiert. Die Ergebnisse der molekularen Bildgebung wurden sowohl durch Immunfluoreszenz als auch durch induktiv gekoppelte Plasma-Massenspektrometrie mit Laserablation (LA-ICP-MS) korreliert und validiert. Mit dieser Arbeit wurde erstmalig gezeigt, dass zentralnervöse Fibrin-Ablagerungen mittels molekularer Bildgebung visualisiert und quantifiziert werden können. Aufgrund der spezifischen Bindung konnten Fibringeflechte bis zu 12 Stunden nach Applikation der molekularen Sonde in entzündlichen Läsionen nachgewiesen werden ($M \pm SD$, 1.07 ± 0.10 (Baseline) vs. 0.73 ± 0.09 (EP2104-R), $p = 0.008$). Die Kontrastmittel-induzierte spezifische Signalalteration konnte durch ein nicht-signalgebendes Kontrastmittel-Analogon aufgrund kompetitiver Bindung rückgängig gemacht werden ($M \pm SD$, 0.60 ± 0.14 (EP2104-R) vs. 0.96 ± 0.13 (EP2104-La), $p = 0.006$). Darüber hinaus konnte gezeigt werden, dass Fibrin als bildgebender Biomarker mit der immunentzündlichen Aktivität ($R^2 = 0.85$, $p < 0.001$) und dem Krankheitsstadium ($R^2 = 0.81$, $p < 0.001$) korreliert. Im Vergleich zu klinisch verwendeten Kontrastmitteln weist EP2104-R eine deutlich höhere SNR ($M \pm SD$, 6.6 ± 1 (EP2104-R) vs. 2.7 ± 0.4 (Gadobutrol),

$p = 0.004$) mit dementsprechend größerer Reduktion der longitudinalen Relaxationszeit ($M \pm SD$, 354 ± 89 (EP2104-R) vs. 155 ± 53 (Gadobutrol), $p = 0.006$) auf.

Zusammenfassend zeigten die Ergebnisse von *Originalarbeit 1*, dass durch die molekulare Bildgebung von zentralnervösen Fibrin-Plaques ein neuartiger nicht-invasiver bildgestützter Biomarker für neuroinflammatorische Prozesse bestimmt werden kann. Dieser Biomarker korreliert mit der Krankheitsaktivität und der pathophysiologischen Remodellierung der extrazellulären Matrix. Darüber hinaus weist die molekulare Fibrin-Sonde gegenüber den derzeit verwendeten unspezifischen Kontrastmitteln signifikant günstigere Signalcharakteristika auf, was die Sensitivität bei der klinischen Detektion von fokalen Läsionen verbessern kann. Die molekulare Fibrin-Bildgebung birgt großes Potenzial, die Diagnostik in verschiedenen neurologischen Erkrankungen mit inflammatorischer Komponente in Hinblick auf Früherkennung, Verlaufskontrolle und Risikostratifizierung zu verbessern.

European Journal of Nuclear Medicine and Molecular Imaging (2022) 49:3692–3704
https://doi.org/10.1007/s00259-022-05807-8

ORIGINAL ARTICLE

Fibrin-targeting molecular MRI in inflammatory CNS disorders

Johannes Lohmeier[1] · Rafaela V. Silva[2,3,8] · Anna Tietze[4] · Matthias Taupitz[1] · Takaaki Kaneko[5] · Harald Prüss[6] · Friedemann Paul[7,8] · Carmen Infante-Duarte[2,8] · Bernd Hamm[1] · Peter Caravan[9] · Marcus R. Makowski[1,10]

Received: 26 December 2021 / Accepted: 16 April 2022 / Published online: 4 May 2022

Abstract

Background Fibrin deposition is a fundamental pathophysiological event in the inflammatory component of various CNS disorders, such as multiple sclerosis (MS) and Alzheimer's disease. Beyond its traditional role in coagulation, fibrin elicits immunoinflammatory changes with oxidative stress response and activation of CNS-resident/peripheral immune cells contributing to CNS injury.

Purpose To investigate if CNS fibrin deposition can be determined using molecular MRI, and to assess its capacity as a non-invasive imaging biomarker that corresponds to inflammatory response and barrier impairment.

Materials and methods Specificity and efficacy of a peptide-conjugated Gd-based molecular MRI probe (EP2104-R) to visualise and quantify CNS fibrin deposition were evaluated. Probe efficacy to specifically target CNS fibrin deposition in murine adoptive-transfer experimental autoimmune encephalomyelitis (EAE), a pre-clinical model for MS ($n = 12$), was assessed. Findings were validated using immunohistochemistry and laser ablation inductively coupled plasma mass spectrometry. Deposition of fibrin in neuroinflammatory conditions was investigated and its diagnostic capacity for disease staging and monitoring as well as quantification of immunoinflammatory response was determined. Results were compared using *t*-tests (two groups) or one-way ANOVA with multiple comparisons test. Linear regression was used to model the relationship between variables.

Results For the first time (to our knowledge), CNS fibrin deposition was visualised and quantified in vivo using molecular imaging. Signal enhancement was apparent in EAE lesions even 12-h after administration of EP2104-R due to targeted binding ($M \pm SD$, 1.07 ± 0.10 (baseline) vs. 0.73 ± 0.09 (EP2104-R), $p = .008$), which could be inhibited with an MRI-silent analogue ($M \pm SD$, 0.60 ± 0.14 (EP2104-R) vs. 0.96 ± 0.13 (EP2104-La), $p = .006$). CNS fibrin deposition corresponded to immunoinflammatory activity ($R^2 = 0.85$, $p < .001$) and disability ($R^2 = 0.81$, $p < .001$) in a model for MS, which suggests a clinical role for staging and monitoring. Additionally, EP2104-R showed substantially higher SNR ($M \pm SD$, 6.6 ± 1 (EP2104-R) vs. 2.7 ± 0.4 (gadobutrol), $p = .004$) than clinically used contrast media, which increases sensitivity for lesion detection.

Conclusions Molecular imaging of CNS fibrin deposition provides an imaging biomarker for inflammatory CNS pathology, which corresponds to pathophysiological ECM remodelling and disease activity, and yields high signal-to-noise ratio, which can improve diagnostic neuroimaging across several neurological diseases with variable degrees of barrier impairment.

Keywords Neuroinflammation · Multiple sclerosis · Molecular MRI · EAE · Fibrin

Abbreviations

CNS	Central nervous system
Gd	Gadolinium
La	Lanthanum
EAE	Experimental autoimmune encephalomyelitis

This article is part of the Topical Collection on Preclinical Imaging.

✉ Johannes Lohmeier
johannes.lohmeier@charite.de

Extended author information available on the last page of the article

Introduction

The entire central nervous system (CNS) is in a highly privileged state due to physiological barriers that strictly regulate interaction with circulating blood components. Dysfunction of these barriers is a hallmark of acute CNS inflammation, which results in leakage of plasma components, such as fibrinogen, immunoglobulins or albumin, into the interstitial space. Fibrinogen (340 kDa) is an important effector protein within the coagulation pathway and innate immune response [1]. Synthesised by hepatocytes as an acute phase reactant,

the plasma concentration of fibrinogen varies dependent on the state of inflammation. Upon activation of the coagulation pathway, fibrinogen is converted to the soluble fibrin monomer (see Fig. 1), which self-assembles to an insoluble mesh network that occludes further blood passage. Beyond its traditional role in coagulation, fibrin(ogen) is an active participant in neuroinflammatory processes through ligand-receptor binding mechanisms that activate downstream signalling pathways which mediate neuroinflammation and neurodegeneration [1] and, thereby, contribute to the pathophysiology of several neurological diseases, including Alzheimer's disease [2] and multiple sclerosis (MS) [3, 4]. Disruption of the barrier function is one of the earliest events in MS, resulting in CNS fibrin(ogen) deposition, which was shown to inhibit the

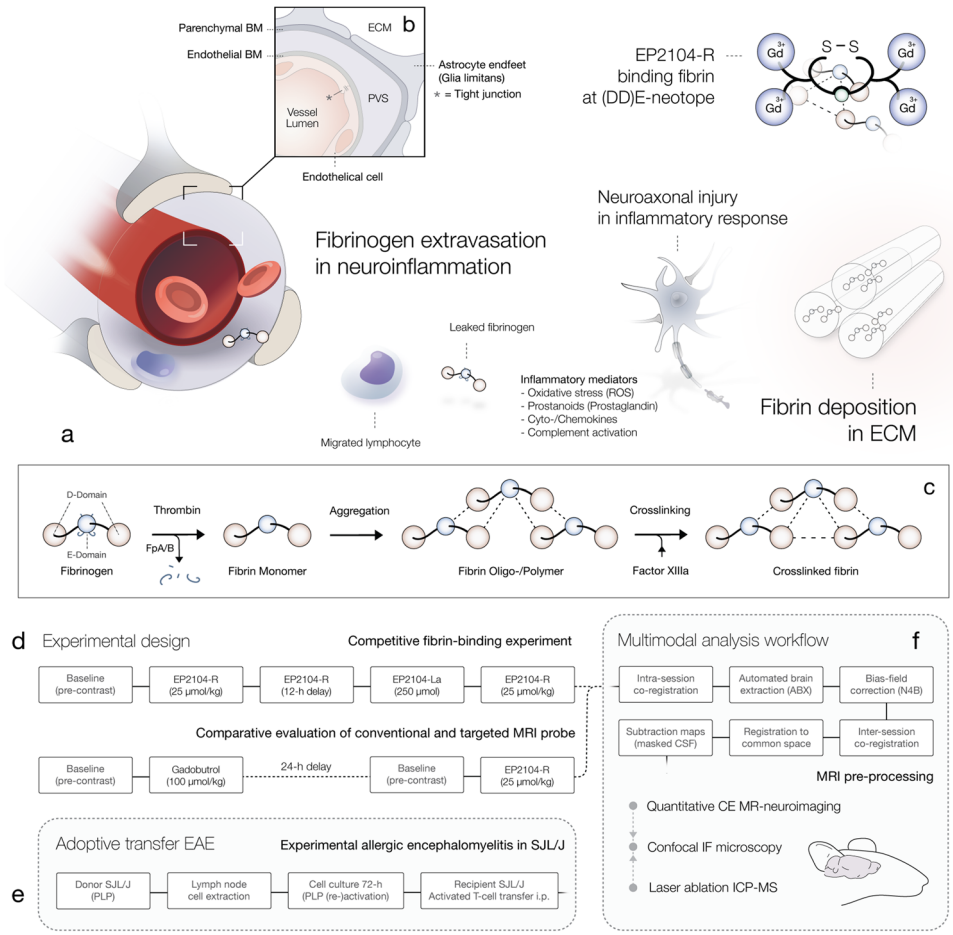

Fig. 1 Fibrin deposition in inflammatory CNS disorders. Dysfunction of the BBB is a hallmark of acute CNS inflammation and one of the earliest events in the pathophysiology of several CNS disorders. Increased barrier permeability is accompanied by extravasation of plasma components and small externally administered compounds into the interstitial space (see **a**) and results in fibrin(ogen) deposition in the perivascular space (PVS) and ECM, which promotes inflammatory response and immune migration into the CNS. Panel **b** demonstrates a cross section of the neurovascular unit, which depicts the ensemble of tight junctions, endothelial cells, basement membranes (BM) and astrocytic endfeet that implements the barrier function. Panel **c** shows the conversion of fibrinogen to fibrin within the coagulation pathway. In the inflammatory component of various CNS diseases, such as MS, aberrant or auto-reactive leucocytes migrate into the CNS. Migrated immune cells promote further CNS migration of peripheral monocytes/macrophages, which accumulate in the PVS and eventually migrate into the interstitial space. Activated peripheral and resident immune cells form clusters around CNS entry points and induce neuroaxonal injury. EP2104-R, a peptide-conjugated Gd-based (Gd^{3+}) positive contrast agent, binds fibrin with high affinity, which is visualised and quantified using molecular MRI. Panel **d** demonstrates experimental designs for the competitive fibrin binding assay and comparative evaluation of EP2104-R and a clinically used (non-targeted) MRI contrast agent. Panel **e** illustrates the induction of murine adoptive-transfer EAE model, a common model for MS. Epitope-primed and (re-)activated T-cells from SJL/J donor mice, immunised with PLP, were transferred to naïve syngeneic recipients, which rapidly develop a characteristic inflammatory demyelinating CNS disorder. Last panel (**f**) illustrates the multimodal analysis workflow for validation of imaging findings from quantitative (contrast-enhanced) MRI with immunofluorescence confocal microscopy (IF-CM) and laser ablation inductively coupled plasma mass spectrometry (LA-ICP MS). BM, basement membrane; ECM, extracellular matrix; PVS, perivascular space; ROS, reactive oxygen species; FpA/B, fibrinopeptide A/B; CSF, cerebrospinal fluid; PLP, proteolipid

regeneration of myelin and promote neuroinflammation, glial scar formation, peripheral macrophage infiltration and microglial response (see [1] for a detailed review). The activation of CNS-resident microglia and peripheral macrophages [5, 6] in addition to the induction of an oxidative stress response [7] was identified as important key mechanism behind these proinflammatory effects.

MS is the most common immune-mediated neuroinflammatory and neurodegenerative disorder of the CNS and a major cause of disability in early adulthood in the Northern Hemisphere [8]. MRI plays a central role in MS patient management; however, clinical imaging is known to suffer from poor specificity for demyelinating lesions as well as low sensitivity for cortical lesions, which is a main cause of long-term disability and cognitive impairment [9]. Due to the weak association between imaging and the degree of disability in patients—which remains a relevant issue to date [10, 11]—there is a need for the development of novel neuroimaging approaches that provide better agreement between clinical and imaging measures, while potentially preparing ground for more predictive and individualised therapeutic frameworks.

Molecular imaging is known to provide biologically relevant information regarding pathophysiological remodelling [12, 13]. Due to increased barrier permeability in acute CNS inflammation, small externally administered compounds, such as targeted contrast media, may pass the blood–brain barrier (BBB) and bind target structures in the extracellular matrix (ECM). EP2104-R is an intermediate molecular-weight MRI probe (< 5 kDa) comprising a short, disulfide bridged cyclic peptide conjugated to 4 Gd-DOTA chelates, which results in 18-fold higher relaxivity (MR signal potency) than Gd-DOTA itself upon fibrin binding [14]. Its cyclic peptide confers high-affinity binding to a highly conserved neotope within fibrin's (DD)E complex [15]. EP2104-R binds to fibrin in several species including human primates (1.7 ± 0.5 µM) and rodents, but does not bind to fibrinogen or serum proteins [14]. Up to the present, (pre-)clinical assessment was primarily focused on cardiovascular imaging [12], but EP2104-R was also found to be useful for the imaging of liver inflammation [16] and lung fibrosis [17]. Based on excellent biocompatibility, the probe was advanced into phase II clinical trials investigating thrombosis imaging [18], where no major adverse effects were reported.

In summary, we hypothesised that fibrin deposition in inflammatory CNS disorders might be determined using molecular MRI (see Fig. 1). We investigated the efficacy and specificity of fibrin-targeting MRI and tested our hypothesis in a murine model for MS, where we showed that fibrin deposition corresponds to underlying tissue damage and immunoinflammatory activity.

Materials and methods

In vitro *fibrin binding assay*

Fibrin targeting was evaluated in vitro using fitted 3D-printed multi-well plates (see Fig. 2, panel a). Wells (40 µl each) with saline solution (NaCl 0.9%), contrast agent (200 µM gadobutrol or 50 µM EP2104-R) as well as probes containing both human fibrinogen (9.75 mg/ml, Enzo Life Sciences, Inc.) and contrast agent, 100 µM non-specific gadobutrol (Gadovist®, Bayer Pharma AG, Berlin, Germany) or 25 µM EP2104-R (Collagen Medical, LLC, Belmont, MA, USA), including optional treatment with pre-activated human thrombin (1:90, Sigma), were evaluated. Upon brief centrifugation (15 min after treatment with thrombin; 84×100 rpm for 5 min) for pellet formation, multi-well plates were examined at room temperature using relaxometry (as described below).

Experimental autoimmune encephalomyelitis (EAE)

All procedures were approved by the local animal welfare authority (LAGeSo, Berlin, Germany; approval number G 0044/19), and all experiments were performed in accordance with approved guidelines and regulations.

In adoptive-transfer EAE, recipient female SJL/J mice ($n = 16$) at the age of 9–11 weeks receive proteolipid protein (PLP) epitope-primed and epitope-reactivated encephalitogenic T-cells from active EAE donor mice ($n = 32$), which previously developed an acute inflammatory demyelinating disease after immunisation with PLP, as illustrated in Fig. 1, panel e. Additional information is available in Appendix E1 (online).

Mice were monitored daily for body weight and clinical signs according to a 5-point scale as follows: 0 = no disease; 1 = complete tail paralysis; 2 = hindlimb paresis; 3 = hindlimb plegia; 4 = paraplegia and forelimb weakness; and 5 = moribund or death. A humane endpoint was set to an EAE score > 3 in accordance with the approved guidelines. Animals were excluded in the case of non-typical disease course or technical problems. A total of 12 animals were included in this study; 2 animals were killed at the humane endpoint; 2 animals were excluded due to contrast agent extravasation or early remission.

Immunofluorescence confocal microscopy (IF-CM)

Frozen brain tissue was dissected into 14-µm-thick Sects. (3 consecutive sections). Slides were (co-)stained with FITC-Fibrin(ogen), AF594-(pan-) Laminin, AF594-PLP and AF488-CD45 antibodies. Additional information is available in Appendix E1 (online).

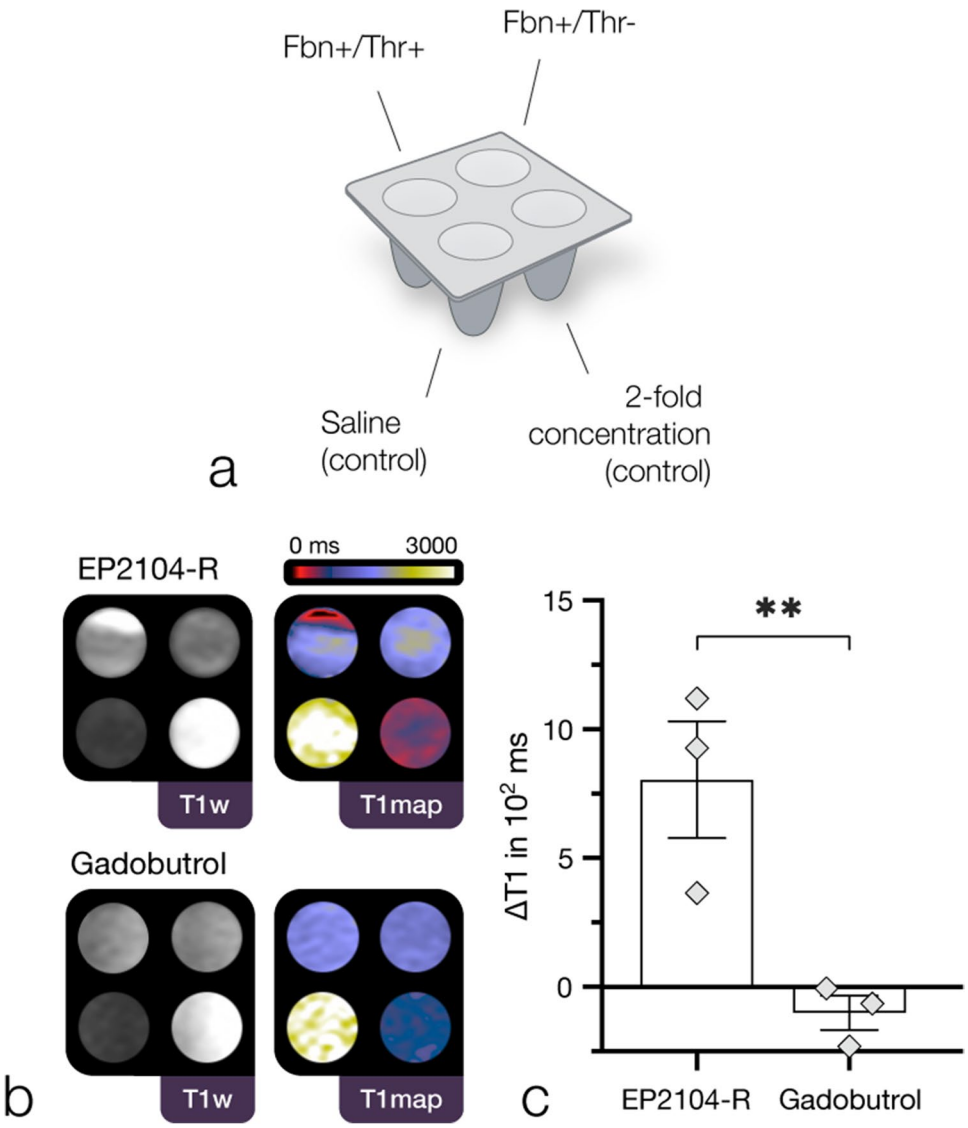

Fig. 2 Fibrin binding (in vitro) assay. First panel (**a**) illustrates the experimental setup using 3D-printed multi-well plates (fitted to the phased array coil). Fbn, fibrinogen; Thr, thrombin. Arrangement as shown in panel **b**: top left, Fbn + /Thr + ; top right, Fbn + /Thr-; bottom left, saline (control); bottom right, twofold higher concentration (control). Panel **b** shows a representative binding experiment with EP2104-R (25 µM) and gadobutrol (100 µM): In contrast to EP2104-R, which presented a substantial local decrease in longitudinal relaxation time for wells with fibrinogen and pre-activated thrombin, suggestive for strong binding to the fibrin pellet, gadobutrol exhibits no particular enhancement pattern. Third panel (**c**) shows substantial difference in ΔT1 (determined from respective Fbn + /Thr + and Fbn + /Thr- samples) between EP2104-R and gadobutrol ($p = 0.009$, $n = 3$, independent samples t-test, E2.2). $M \pm SEM$. In the unbound state, EP2104-R exhibits higher relaxivity due to internal motion of the chelate complex. p-value < .05 was considered statistically significant. $^{**}p$-value < 0.01

Laser ablation inductively coupled plasma mass spectrometry (LA-ICP MS)

Using a NWR 213 laser ablation system (New Wave Research, Fremont, CA, USA) and an Agilent 7900 ICP-MS (Agilent Technologies, Japan), tissue was scanned line by line (spot size 60 µm rectangular, line distance 90 µm, 60 µm/s speed, aerosol transport via argon gas flow). ^{13}C, ^{57}Fe, ^{158}Gd and ^{139}La isotopes were determined in a semi-quantitative manner through calibration using homogenised tissue standards. An in-house software package was used for colour-coded image reconstruction. Measurements were carried out at Forschungszentrum Jülich (ZEA-3, Jülich, Germany).

Magnetic resonance imaging (MRI)

MRI was performed on a clinical MAGNETOM (3 T) Biograph mMR (Siemens Healthcare, Erlangen, Germany) using a 4-channel phased array mouse coil (Rapid Biomedical GmbH, Rimpar, Germany). Prior to in vivo MRI, animals were anaesthetised (upon i.p. administration of medetomidine (500 µg/kg), midazolam (5 mg/kg) and fentanyl (50 µg/kg)). Animals were positioned in supine position. Intravenous bolus administration of non-specific gadobutrol (Gadovist®, Bayer Pharma AG, Berlin, Germany) at a clinical dose (100 µmol/kg) and EP2104-R (Collagen Medical, LLC, Belmont, MA, USA), a fibrin-targeted MRI probe, at Gd-equivalent doses (25 µmol/kg) was performed according to total body weight through tail vein (i.v.) injection.

MRI examinations included a pre-injection T2-weighted 3D_TSE sequence (TR/TE = 800/110 ms, resolution = 0.1 × 0.1 × 0.4 mm, FOV = 55 mm, fat-saturated), a pre- and post-injection 3D_MP2RAGE sequence (TR/TE = 5000/6.53 ms, TI1/TI2 = 846/2850, flip angle 1/2 = 4°/5°, resolution = 0.1 × 0.1 × 0.2 mm, FOV = 55 mm) and a pre- and post-injection T1-weighted 3D_VIBE sequence (TR/TE = 13.75/5.68 ms, flip angles = 4°, 8°, 13°, 21°, 34°, resolution = 0.1 × 0.1 × 0.2 mm, FOV = 59 mm). Native and post-contrast T1 mapping was computed inline using data of the 3D_MP2RAGE sequence [19]. Contrast dynamics for the competitive fibrin binding (in vivo) assay were evaluated using iterated sequences.

While clinical MR imaging in MS is usually recommended with a prolonged delay, preferentially 20-min [20] post-administration, allowing for sufficient Gd accumulation of non-specific Gd-based contrast media, fibrin-targeting molecular MRI was performed with a 12-h delay for the purpose of accurate fibrin determination without the impact of non-specific contrast media extravasation. Competitive fibrin binding experiments were comprised of a first scan session pre-/post-contrast, then a 12-h delay upon administration of EP2104-R, a second session prior and after the administration of a lanthanum (La)-labelled analogue (EP2104-La) at tenfold higher dose, which was followed by a second administration of EP2104-R, as shown in Fig. 1, panel d. For the comparative evaluation between targeted and non-targeted contrast media, animals at stable disease peak received a first scan session pre-/post-contrast with gadobutrol, then a 24-h delay to ensure contrast clearance, followed by a second equivalent scan with EP2104-R. Measurements were then performed at a 20-min delay post-contrast phase, although predominant non-specific MR signal response from contrast media extravasation needs to be assumed at this point in time. In addition, a small group of animals ($n = 3$) at disease onset was scanned with EP2104-R only (due to rapid disease course).

MRI analysis

MRI pre-processing as illustrated in Fig. 1, panel f, included brain extraction using atlasBREX [21], bias-field correction using the N4-method [22] and non-rigid (B-spline) atlas registration using the Advanced Normalization Tools (ANTs) framework [23]. Image analysis was performed using OsiriX MD 11 (Pixmeo, Geneva, Switzerland) in a semi-automated manner (J.L. and M.M., 6 and > 10 years of experience in MR imaging analysis). MRI was correlated with IF-CM and LA-ICP MS using a high-resolution atlas, DSURQE (The Mouse Imaging Centre, Toronto) [24], matched to the respective micro-anatomy. Native measurements of longitudinal relaxation time were determined using atlas labels (GM/WM/CSF sampled from piriform cortex/internal capsule/lateral ventricle) or semi-automated iso-contouring of EAE lesions presenting a hyperintense correlate in T2-weighted imaging. For the competitive fibrin binding experiment, ROIs were determined on subtraction maps using a region growing algorithm with a fixed threshold value. Periventricular signal enhancement was determined using a standardised ROI in atlas space. Most prominent lesion per subject and matching region in the control group were analysed for association between fibrin(ogen) area and difference in longitudinal relaxation times. Cerebrospinal fluid (CSF) compartments were masked on subtraction maps using a fixed threshold. Semi-automated iso-contouring (minimum 60%) derived regions-of-interest (ROIs) were used for the in vitro fibrin binding assay.

Relative longitudinal relaxation time (rT1) was calculated as ratio of mean longitudinal relaxation time in the region-of-interest (ROI) and the unaffected contralateral background (BG):

$$rT1 = \frac{T1_{mean}^{ROI}}{T1_{mean}^{BG}} \quad (1)$$

Signal-to-noise ratio (SNR) for contrast-enhanced T1-weighted imaging was calculated using the following formula (S1, pre-contrast signal; S2, pre-contrast signal; S3, post-contrast signal):

$$SNR_{ROI} = \frac{\sqrt{2}mean(S3_{post} - S2_{pre})}{std(S1_{pre} - S2_{pre})} \quad (2)$$

Statistical analysis

Statistics for each experiment are described in both figure legends and text. Error bars represent the S.E.M. *N*-value indicates number of biological replicates. Independent samples *t*-tests or one-tailed paired *t*-tests were used for comparisons between two groups. One-way ANOVA with the Brown-Forsythe test for equal variances and Holm-Šídák's multiple comparisons test were used for comparing more than two groups. Data distribution was assumed to be normal based on descriptive statistics, the Shapiro-Wilk test and Q-Q plots (available in Appendix E2 (online)). Linear regression was used to model the relationship between variables. p-value < 0.05 was considered statistically significant. Each statistical test is reported with exact p-value, n, F and degrees of freedom. Statistical analysis was performed using Prism v.9 (GraphPad Software, San Diego, CA, USA).

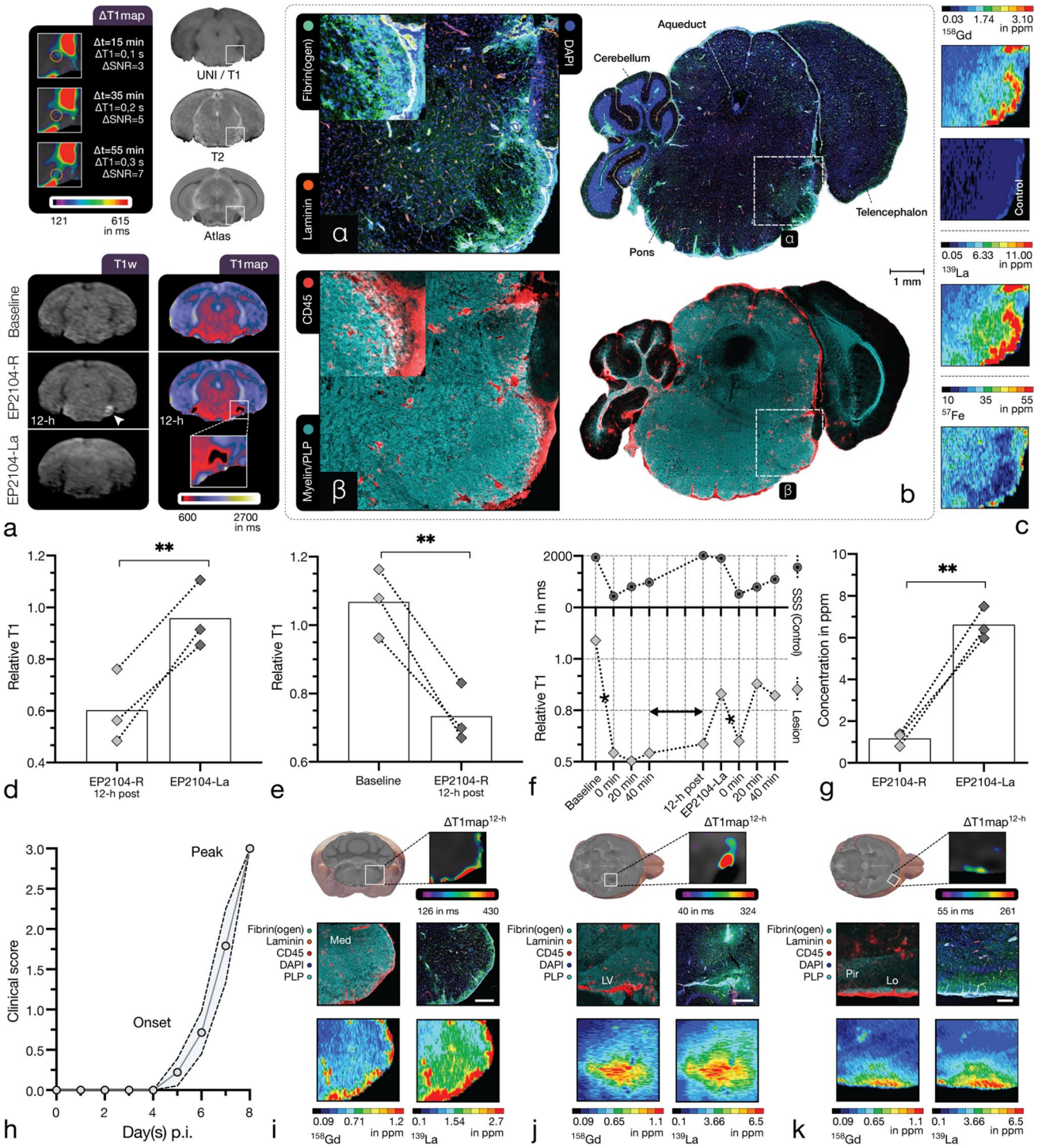

Results

Fibrin binding (in vitro) *assay*

EP2104-R demonstrated high-affinity binding to fibrin in vitro (see Fig. 2, panel b). While there was no particular enhancement pattern for the precursor protein, strong local contrast enhancement was apparent ($M \pm SD$, 1366 ± 393 ms (fibrinogen) vs. 562 ± 86 ms (fibrin), $p = 0.04$, $n = 3$, $t(2) = 3.544$, one-tailed paired t-test, E2.1) when fibrinogen was treated with activated thrombin, resulting in rapid proteolytic conversion to soluble fibrin monomers, which subsequently assemble to fibrin protofibrils and fibres. Correspondingly, there was a substantial difference in longitudinal relaxation time ($M \pm SD$, 804 ± 393 ms (EP2104-R) vs. -101 ± 117 ms (gadobutrol),

◂**Fig. 3** Competitive fibrin binding (in vivo) assay. Competitive binding of EP2104-R to the target protein was evaluated in adoptive-transfer EAE mice at disease peak using a lanthanum-labelled analogue (EP2104-La). Panel **a** shows a representative pontine EAE lesion with prolonged Gd uptake. More than 12-h after the administration of EP2104-R, fibrin-specific contrast enhancement (white arrow) is still apparent, which is displaced with the administration of EP2104-La at tenfold higher dose due to competitive binding. The following panels demonstrate correlated IF-CM (**b**) and LA-ICP MS (**c**). Extensive fibrin(ogen) deposits (**α**) in the brainstem were co-localised with CD45-positive immune cell infiltrates and mild demyelination (**β**). Within EAE lesions, there was a decrease ($p = .008$, $n = 3$, paired one-tailed t-test, E2.3) in relative longitudinal relaxation time between baseline and 12-h post-contrast scans (see **e**). When an excess of EP2104-La, an MRI-inactive analogue of EP2104-R, was administered, an increase ($p = .006$, $n = 3$, paired one-tailed t-test, E2.4) in relative longitudinal relaxation time was apparent (panel **d**), consistent with displacement of EP-2104-R from its fibrin binding site, as shown in panel **f**. Mean relative longitudinal relaxation time of an EAE lesion is shown over time. T1 values within the superior sagittal sinus (SSS) show venous contrast dynamics for comparison. Asterisk indicates administration of EP2104-R. Correspondingly, LA-ICP MS of tissue slides showed a statistically significant difference ($p = .003$, $n = 3$, paired one-tailed t-test, E2.5) between Gd (EP2104-R) and La (EP2104-La) in EAE lesions (see **g**). Panel **h** shows a typical disease course in adoptive-transfer EAE ($n = 9$; pooled from 2 experiments; dotted line, SEM). The following panels (**i**–**k**) show common EAE lesions with corresponding fibrin binding several hours after the administration of EP2104-R. Leptomeningeal inflammation and fibrin binding with extensive myelin damage within the medulla (Med) are shown in panel **i**. Centripetal distribution of fibrin(ogen) and immune cell clustering indicates that inflammation initiates from the meninges (and small perforating venules). Next panel (**j**) shows a prevalent pattern with inflammation and CNS migration through the choroid plexus into periventricular regions (LV, lateral ventricle). Last panel (**k**) illustrates a cortical lesion with subpial and leptomeningeal fibrin deposition with associated immune infiltration and myelin damage affecting the lateral olfactory tract (Lo) and the piriform cortex (Pir). Scale bars, 1 mm (**b**), 500 µm (**i**, **j**), 250 µm (**k**). p-value < 0.05 was considered statistically significant. **p-value < .01

$p = 0.009$, $n = 3$, $t(4) = 3.824$, independent samples t-test, E2.2) between gadobutrol, a clinically used (non-targeted) MRI agent, and EP2104-R at equivalent Gd concentrations (see Fig. 2, panel c).

*Competitive fibrin binding (*in vivo*) assay*

Contrast-enhanced MR-neuroimaging was performed in two sessions with a 12-h delay in adoptive-transfer EAE ($n = 3$) at stable disease peak (see Fig. 1). As shown in Fig. 3, EP2104-R demonstrated targeted binding to fibrin deposits in the extracellular matrix (ECM) with corresponding contrast enhancement and decreased longitudinal relaxation time ($M \pm SD$, 1.07 ± 0.10 (baseline) vs. 0.73 ± 0.09 (EP2104-R), $p = 0.008$, $n = 3$, $t(2) = 7.969$, paired one-tailed t-test, E2.3), until several hours after administration (see Fig. 3, panels e and f). Correlated IF-CM showed fibrin(ogen) deposition in the ECM (see Fig. 3, subpanel α) associated with leucocyte infiltration and demyelination (see Fig. 3, subpanel β). When EP2104-La, an analogue where the paramagnetic Gd^{3+} ions were replaced by diamagnetic La^{3+}, such that EP2014-La binds fibrin, but does not elicit an MR signal response, was administered at tenfold dose, signal change was reversed and an increase in longitudinal relaxation time ($M \pm SD$, 0.60 ± 0.14 (EP2104-R) vs. 0.96 ± 0.13 (EP2104-La), $p = 0.006$, $n = 3$, $t(2) = 8.778$, paired one-tailed t-test, E2.4) was apparent, suggesting that EP2104-R dissociated from its target due to competitive fibrin binding (see Fig. 3, panel d). When EP2104-R was administered at a second time point (shortly after the administration EP2104-La), relaxation measurements over time imply that a relevant proportion of the early signal change is non-specific, suggesting that accurate fibrin quantification requires equilibrium state (see Fig. 3, panel f). As shown in Fig. 3, panels c and g, LA-ICP MS confirmed the presence of La^{3+} and Gd^{3+} in EAE lesions with corresponding difference between both metals ($M \pm SD$, 1.17 ± 0.32 ppm (EP2104-R) vs. 6.63 ± 0.79 ppm (EP2104-La), $p = 0.003$, $n = 3$, $t(2) = 12.85$, paired one-tailed t-test, E2.5). Representative EAE lesions with leptomeningeal, cortical and periventricular fibrin binding are demonstrated in Fig. 3, panels i–k, presenting correlation between MRI, LA-ICP MS and IF-CM.

Fibrin deposition in adoptive-transfer EAE

Fibrin(ogen) deposition progressed with the disease stage (see Fig. 4, panel III) and was associated with progressive leucocyte infiltration and myelin damage. CNS pathology changed from regionally contained at disease onset to more diffuse and extensive inflammation at disease peak with abundant small vessel inflammation and increasing perivascular infiltrates. As shown in Fig. 4, panels I and II, fibrin(ogen) presented a strong association with clinical disability ($R^2 = 0.81$, $p < 0.001$, $n = 11$) and CD45-positive immune cell infiltration ($R^2 = 0.85$, $p < 0.001$, $n = 9$). No fibrin(ogen) deposition or immune cell infiltration was apparent in healthy controls. Leptomeningeal and periventricular inflammation was prominent throughout disease stages. Inflammation in pontine and medullar regions demonstrated centripetal (inward) fibrin(ogen) distribution (see Fig. 3, panels b and i), suggesting that inflammatory activity initiated from the meninges and small perforating vessels. Centrifugal (outward) fibrin(ogen) distribution was typically associated with choroid plexus, perivenular and subarachnoidal pathology (see Fig. 4, panels a–d). Inflammation of the optic chiasm and optic nerve was apparent and showed corresponding fibrin(ogen) deposition, as illustrated in Fig. 4, panel e. Cortical lesions presented association with the pial surface and (sub-)cortical perforating venules (see Fig. 3, panel k).

The subarachnoid space was enlarged at disease peak due to severe immune cell trafficking ($M \pm SD$,

158 ± 0.12 µm (EAE) vs. 49 ± 7 µm (control), $p < 0.001$, $n = 3$, $t(4) = 14.05$, independent sample one-tailed t-test, E2.8), as shown in Fig. 4, panel g, and showed small surrounding clusters of immune cells migrating into brain parenchyma. Laminin-immunostaining depicted basement membranes for further differentiation between lumen, perivascular space and subarachnoidal space. As demonstrated in Fig. 4, panel f, extensive fibrin(ogen) deposition was present in the subarachnoid and perivascular compartment, which was apparent in imaging with EP2104-R, and coincided with strongly dysregulated immune cell trafficking.

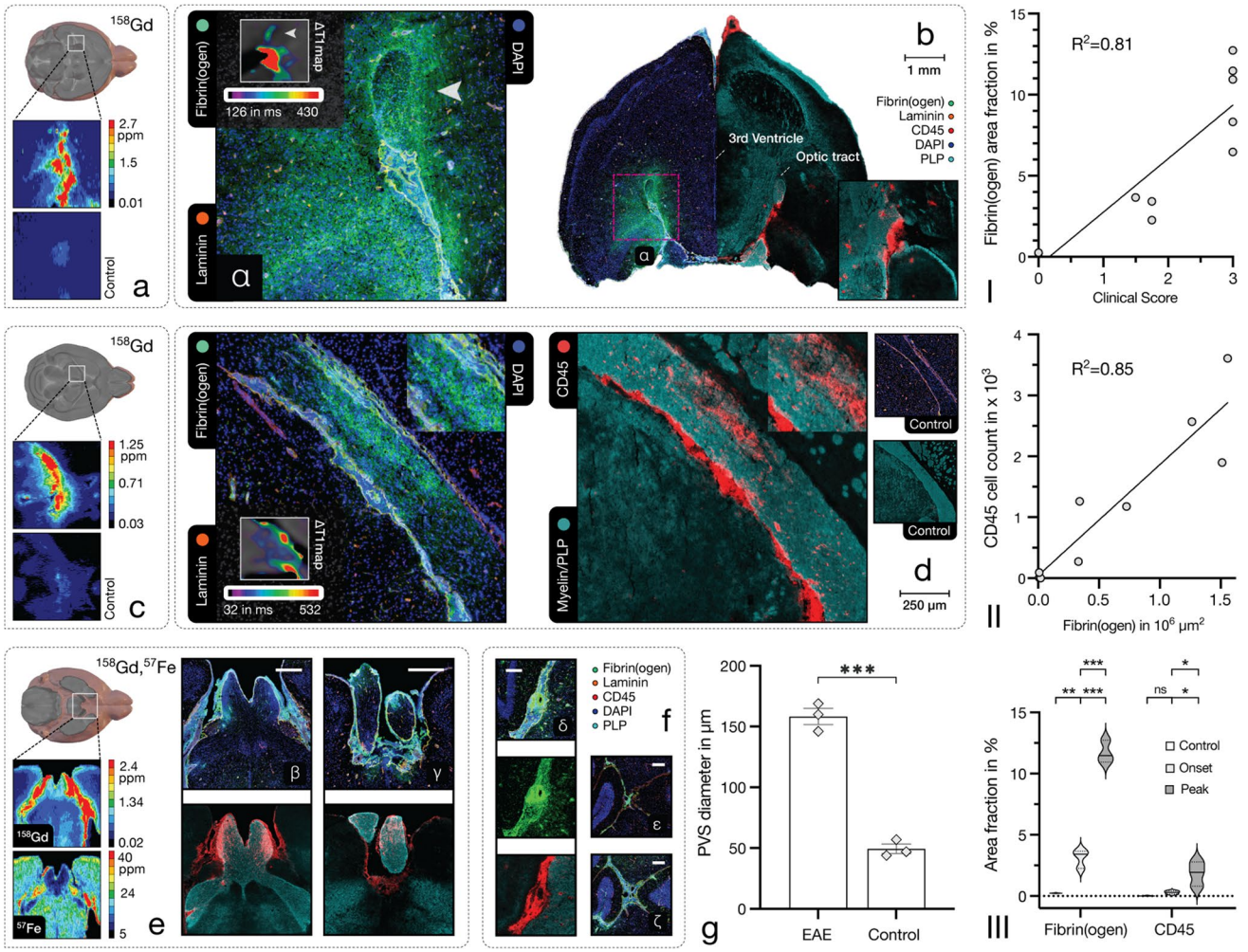

Fig. 4 Fibrin(ogen) deposition and fibrin-targeting molecular MRI. Fibrin(ogen) deposition corresponded to clinical disability and disease score ($R^2 = 0.81$, $p < .001$, $n = 11$) as well as with immune infiltration ($R^2 = 0.85$, $p < .001$, $n = 9$) in EAE, as shown in panel **I** and **II**. Panel **III** shows group differences in fibrin(ogen) and CD45 area fraction between control, disease onset and disease peak (from left to right) samples ($n = 3$, one-way ANOVA with Holm-Šídák's multiple comparisons test; E2.6, fibrin(ogen), E2.7, CD45) illustrated as a violin plot. The following panels (**a**–**e**) demonstrate molecular imaging of CNS fibrin deposition in early disease stages: Panels **a** and **b** present periventricular inflammation with corresponding decrease in longitudinal relaxation time and interstitial Gd detection in tissue samples. Panel **b** shows matching immunohistopathology (same hemisphere of two adjacent slices) with fibrin(ogen) deposits and immune infiltrates with associated demyelination of the optic tract (see white arrow). Prominent CNS migration through the choroid plexus was apparent in an adjacent slide, demonstrated in the inset. Panels **c** and **d** show inflammation affecting the ventral hippocampal commissure and fimbria with respective decrease in longitudinal relaxation time and Gd detection in LA-ICP MS. Centrifugal fibrin(ogen) deposits, immune cell infiltration and pronounced demyelination adjacent to the lateral ventricle, as shown in panel **d**, suggest leucocyte migration through the choroid plexus. Panel **e** shows extensive inflammation of the optic chiasm (**β**) and optic nerve (**γ**) with associated fibrin(ogen) deposition and Gd detection. Panel **f** demonstrates the enlarged subarachnoid space in EAE: Inflammation within the enlarged subarachnoid space (**δ**) is associated with fibrin(ogen) deposition, which is apparent in MRI with EP2104-R. Subpanels (**ε**, **ζ**) compare the enlarged cerebellar subarachnoid space in EAE (**ζ**) to a control (**ε**). Correspondingly, there was a statistically significant enlargement of the subarachnoid space in EAE compared to healthy controls ($p < .001$, $n = 3$, independent sample one-tailed t-test, E2.8), which is shown in panel **g**. $M \pm SEM$. Scale bars, 1 mm (**b**), 250 µm (**d**), 200 µm (**β**–**δ**), 250 µm (**ε**, **ζ**). p-value < 0.05 was considered statistically significant. *p-value < .05, **p-value < .01, ***p-value < .001. ns, non-significant

As shown in Fig. 5, panel a, EP2104-R showed greater reduction of longitudinal relaxation ($M \pm SD$, 354 ± 89 (EP2104-R) vs. 155 ± 53 (gadobutrol), $p = 0.006$, $n = 3$, $t(2) = 9.199$, paired one-tailed t-test, E2.9) as well as higher SNR ($M \pm SD$, 6.6 ± 1 (EP2104-R) vs. 2.7 ± 0.4 (gadobutrol), $p = 0.004$, $n = 3$, $t(2) = 10.73$, paired one-tailed t-test, E2.10) compared to non-specific gadobutrol (at Gd-equivalent dose), when imaged with a 20-min delay post-administration. Difference in longitudinal relaxation time of EP2104-R determined at that time showed an association with corresponding fibrin(ogen) deposition ($R^2 = 0.86$, $p < 0.001$, $n = 9$); however, measurements at this point still reflect a mixed component with non-specific signal.

In native T1 mapping, an increased longitudinal relaxation time ($M \pm SD$, 1.29 ± 0.07 (lesion) vs. 1.0 ± 0.05 (control), $p = 0.005$, $n = 3$, $t(4) = 5.749$, independent sample two-tailed t-test, E2.11) was measured in acute EAE lesions compared to controls (see Fig. 5, panel b). Longitudinal relaxation times for GM/WM/CSF were ($n = 3$, $M \pm SD$) $1311 \pm 34/882 \pm 9/3281 \pm 664$ ms in healthy animals.

Discussion

For the first time (to our knowledge), we demonstrated that CNS fibrin deposition can be determined using molecular MRI, which provides a non-invasive imaging biomarker for inflammatory CNS pathology and barrier impairment. We showed that EP2104-R, a peptide-conjugated Gd-based MRI probe, binds to fibrin deposits with high affinity and specificity. Signal enhancement was apparent in EAE lesions even several hours after administration of EP2104-R due to targeted binding. When EP2104-La, a MRI-silent analogue, was administered at high dose, EP2104-R was displaced from its target due to competitive binding. At the equilibrium state of EP2104-R, fibrin

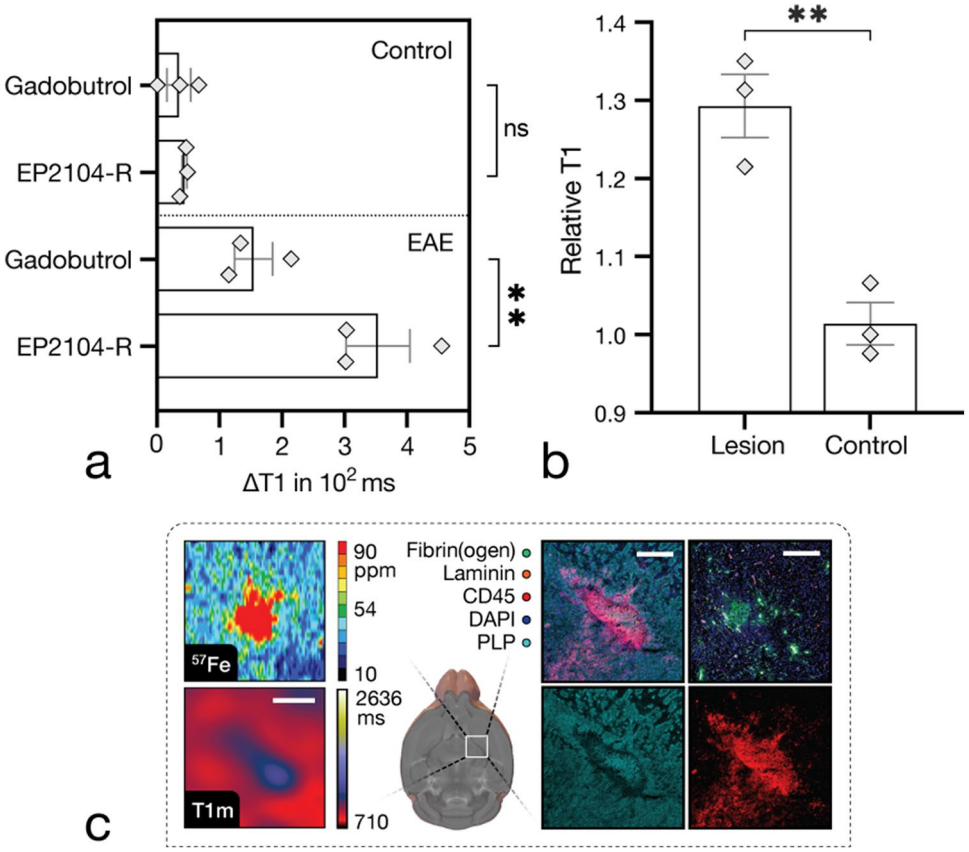

Fig. 5 Comparison between targeted and conventional MRI probes. First panel (**a**) demonstrates a comparison between EP2104-R and gadobutrol (as a clinically used non-targeted MRI contrast agent) in periventricular inflammation. EP2104-R presented greater reduction in longitudinal relaxation time ($p = .006$, $n = 3$, paired one-tailed t-test, E2.9) compared to gadobutrol at Gd ion-matched dose (20-min delay post-administration). $M \pm SEM$. Panel **b** shows increased longitudinal relaxation times ($p = .005$, $n = 3$, independent sample two-tailed t-test, E2.11) in large EAE lesions compared to controls. $M \pm SEM$. Last panel (**c**) demonstrates a representative late active EAE plaque in the internal capsule with increased longitudinal relaxation time. LA-ICP MS revealed an abundance of iron and corresponding immunohistopathology presented a large immune cell conglomerate with extensive myelin damage. Scale bars, 500 µm. p-value < 0.05 was considered statistically significant. **p-value $< .01$. ns, non-significant

deposition may be determined as a quantitative non-invasive imaging biomarker that is strongly associated with immune infiltration, which is directly linked to myelin damage and axonal injury [5, 25]. We demonstrated that fibrin(ogen) deposition progressed with disease stage and corresponded to clinical disability. Fibrin-targeting MRI also revealed extensive deposits in the enlarged perivascular and subarachnoid compartment, which could be visualised and coincided with abnormal cell trafficking.

EP2104-R exhibits high relaxivity as a result of accumulation through specific binding in addition to its internal rotation mechanism [14, 26]. The differences in longitudinal relaxation time and SNR were substantially higher at Gd-equivalent dose than with a non-targeted MRI contrast agent. Lesions with decreased barrier permeability at the time of imaging may be underestimated with clinically used (non-targeted) MRI contrast agents. On the opposite, EP2104-R binds fibrin and gradually accumulates in lesions, increasing MR signal enhancement, which improves the detection of enhancing lesions and, therefore, has the potential to improve the clinical diagnostic capacity, particularly with regard to cortical lesions, which were shown to be main contributors to disability in MS [27], but were reported to be underestimated using clinical MRI [28]. Subpial lesions are characteristic and prevalent cortical pathology in MS [9] and are commonly associated with leptomeningeal inflammation [29]. Our findings suggest that molecular imaging of CNS fibrin deposition might aid the clinical detection of leptomeningeal and cortical inflammation—clinically relevant to MS because of an association with secondary progression, disability and cognitive impairment [30]—due to substantially increased SNR and the possibility of imaging with prolonged delays that exclude the presence of non-specific enhancement in meningeal blood vessels or leakage of contrast media into the surrounding CSF, which may further mask inflammatory foci.

We also observed fibrin(ogen) deposition in the visual pathway, which is an interesting target for the assessment of acute inflammatory events in clinically isolated syndrome (CIS) where optic neuritis is frequently the first clinical manifestation of MS [9, 31]. Further research should evaluate the prognostic value of CNS fibrin deposition for the conversion from CIS to manifest MS.

Moreover, there is potential for dosage reduction—a relevant topic in light of more recent reports of Gd deposition upon serial contrast-enhanced MRI [32]. With regard to reports about increased sensitivity for enhancing lesions with double- and triple-dosing [33, 34], which is not appropriate according to the 2017 revision of the McDonald criteria [28], molecular MRI probes, such as EP2104-R, which provide high relaxivity and specific target binding, appear to be relevant alternative solutions. Furthermore, a Mn-based alternative to EP2104-R was developed [15], which would eliminate the risk of Gd deposition entirely.

While advanced neuroimaging methods [35, 36], such as diffusion tensor imaging (DTI) or magnetisation transfer ratio (MTR), were shown to complement structural MRI, their availability is commonly limited to research environments due to extensive data and hardware requirements with time-consuming measurements and image pre-processing. On the other hand, we demonstrated that molecular MRI is a highly translational approach by using a clinical high-field MRI scanner and the generally available MP2RAGE sequence [19] for fast and robust T1 relaxometry at low transmit-field inhomogeneity. In the current study, acute inflammatory lesions demonstrated an increase in longitudinal relaxation time, suggestive for myelin damage and/or vasogenic edema. When T1 mapping is performed prior to and after the administration of contrast agent, subtraction (ΔT1) maps reflect the change in longitudinal relaxation time primarily induced by the MRI probe, which is a function of local concentration.

Fibrin deposition as a disease biomarker

Fibrin presents a superior cumulative measure for barrier impairment compared to the extravasation measurement of small externally applied agents, such as non-targeted Gd-based contrast agents or fluorescent probes, as fibrin polymers remain in the interstitial space as an insoluble mesh network until proteolytic degradation to fibrin-degradation products (FDP) [1]. However, more importantly, fibrin deposition is a promising biomarker for CNS pathology due to its pathophysiological implications in neurological diseases [1]. There is a growing body of evidence that shows that fibrin deposition plays a role in various inflammatory and neurodegenerative CNS diseases [1], such as MS where extensive fibrin deposits were demonstrated in acute/chronic lesions [37, 38] and persistent dysregulation of the fibrinolytic pathway was reported [39]. Fibrin was also found in the cortex of patients with MS, where its distribution correlated with neuronal loss [40]. CNS fibrin was shown to contribute to the EAE disease course in pre-clinical studies, where disease severity was alleviated using experimental therapeutic agents that block the interaction of fibrin with the CD11b integrin receptor on microglia and macrophages [41] or inhibit the conversion of fibrinogen to fibrin using a thrombin inhibitor [5].

Limitations

Despite certain limitations of the EAE disease model (see [42] for further details), it is still highly relevant to date, due to its significant contributions to the investigation of

inflammatory and demyelinating CNS disorders. Although fibrin-targeting molecular MRI was evaluated and demonstrated in a murine model, CNS fibrin deposition is neither exclusive to EAE nor MS, but presents a critical and fundamental event in the pathophysiology of several CNS disorders [1] with variable degrees of barrier impairment, ranging from autoimmune encephalitis, vasculitis to CNS infections, suggesting that data from this model might be relevant to an even broader spectrum of neurological conditions. Although transitory disruption of the barrier function may occur in several neurological diseases, only a subset of CNS disorders with profound dysregulation of the immune system present a sustained transformation of the neurovascular interface to a proinflammatory milieu, such as in MS (as discussed above) or Alzheimer's disease, where CNS fibrin(ogen) was also shown to play a role in its pathophysiology [1, 43–45]. Hence, CNS fibrin deposition as an imaging biomarker is not specific to a single neurological disease entity, but it yields high sensitivity for the inflammatory component of several CNS pathologies and fibrin-targeting molecular MRI may improve the detection of subtle inflammatory foci, such as in cortical inflammation in MS.

Another limitation is that the administration of contrast media could not be randomised due to prolonged fibrin binding. Although gadobutrol was administered 24-h prior to EP2104-R, an underestimation at clinically and radiologically stable disease peak appears unlikely.

Although molecular imaging using PET can potentially provide biologically relevant information without barrier dysfunction, inherently low spatial resolution makes the detection of most MS or EAE lesions difficult. While increased barrier permeability is a prerequisite for fibrin-targeting molecular MRI, literature suggests that dysfunction of the BBB occurs at an early stage in MS and precedes damage [1].

In conclusion, we demonstrated that CNS fibrin deposition can be determined using molecular MRI and proposed fibrin deposition as an imaging biomarker for CNS pathology, which is sensitive to disease activity, and acts as a surrogate for neuroinflammation and barrier impairment.

Supplementary Information The online version contains supplementary material available at https://doi.org/10.1007/s00259-022-05807-8.

Author contribution J.L. and M.M. conceived the experiments. M.M. and P.C. provided supervision and overall guidance. A.T., M.T., T.K., H.P., F.P. and B.H. assisted in experimental design and interpretation. R.VdS. and C.ID. assisted with the disease model. B.H., C.ID., P.C. and M.M. provided relevant infrastructure. J.L. performed the experiments, analysed the data and wrote the manuscript with input from all authors. All authors have given approval to the final version of the manuscript.

Funding Open Access funding enabled and organized by Projekt DEAL. This research project is funded by the "Deutsche Forschungsgemeinschaft" (DFG, German Research Foundation)—SFB 1340/1 2018. The PET/MRI scanner is co-funded by the "Deutsche Forschungsgemeinschaft" (DFG, German Research Foundation)—INST 335/543–1 FUGG 2015.

Data availability All data generated or analysed during this study are included in this published article (and its supplementary information files).

Declarations

Ethics approval All procedures were approved by the local animal welfare authority (LAGeSo, Berlin, Germany; approval number G 0044/19), and all experiments were performed in accordance with approved guidelines and regulations.

Competing interests P.C. has equity in and is a consultant to Collagen Medical which holds the patent rights to EP-2104-R. The other authors declare no competing interests.

References

1. Petersen MA, Ryu JK, Akassoglou K. Fibrinogen in neurological diseases: mechanisms, imaging and therapeutics. Nat Rev Neurosci. 2018;19:283–301.
2. Strickland S. Blood will out: vascular contributions to Alzheimer's disease. J Clin Invest. 2018;128:556–63.
3. Abbadessa G, Lavorgna L, Treaba CA, Bonavita S, Mainero C. Hemostatic factors in the pathogenesis of neuroinflammation in multiple sclerosis. Mult Scler. 20211352458521103911 1.
4. Ghorbani S, Yong VW. The extracellular matrix as modifier of neuroinflammation and remyelination in multiple sclerosis. Brain. 2021;144:1958–73.
5. Davalos D, Ryu JK, Merlini M, et al. Fibrinogen-induced perivascular microglial clustering is required for the development of axonal damage in neuroinflammation. Nat Commun. 2012;3:1227.
6. Ryu JK, Petersen MA, Murray SG, et al. Blood coagulation protein fibrinogen promotes autoimmunity and demyelination via chemokine release and antigen presentation. Nat Commun. 2015;6:8164.
7. Ryu JK, Rafalski VA, Meyer-Franke A, et al. Fibrin-targeting immunotherapy protects against neuroinflammation and neurodegeneration. Nat Immunol. 2018;19:1212–23.
8. Daiiapc GBD. Global, regional, and national incidence, prevalence, and years lived with disability for 310 diseases and injuries, 1990–2015: a systematic analysis for the Global Burden of Disease Study 2015. Lancet. 2016;388:1545–602.

9. Filippi M, Bar-Or A, Piehl F, et al. Multiple sclerosis. Nat Rev Dis Primers. 2018;4:43.
10. Barkhof F. The clinico-radiological paradox in multiple sclerosis revisited. Curr Opin Neurol. 2002;15:239–45.
11. Mollison D, Sellar R, Bastin M, et al. The clinico-radiological paradox of cognitive function and MRI burden of white matter lesions in people with multiple sclerosis: a systematic review and meta-analysis. PLoS One. 2017;12:e0177727.
12. Salarian M, Ibhagui OY, Yang JJ. Molecular imaging of extracellular matrix proteins with targeted probes using magnetic resonance imaging. Wiley Interdiscip Rev Nanomed Nanobiotechnol. 2020;12:e1622.
13. Gauberti M, Martinez de Lizarrondo S. Molecular MRI of neuroinflammation time to overcome the translational roadblock. Neuroscience. 2021;474:30–6.
14. Overoye-Chan K, Koerner S, Looby RJ, et al. EP-2104R: a fibrin-specific gadolinium-based MRI contrast agent for detection of thrombus. J Am Chem Soc. 2008;130:6025–39.
15. Gale EM, Atanasova IP, Blasi F, Ay I, Caravan P. A manganese alternative to gadolinium for MRI contrast. J Am Chem Soc. 2015;137:15548–57.
16. Atanasova I, Sojoodi M, Leitão HS, et al. Molecular magnetic resonance imaging of fibrin deposition in the liver as an indicator of tissue injury and inflammation. Invest Radiol. 2020;55:209–16.
17. Shea BS, Probst CK, Brazee PL, et al. Uncoupling of the profibrotic and hemostatic effects of thrombin in lung fibrosis. JCI Insight. 2017;2:86608.
18. Vymazal J, Spuentrup E, Cardenas-Molina G, et al. Thrombus imaging with fibrin-specific gadolinium-based MR contrast agent EP-2104R: results of a phase II clinical study of feasibility. Invest Radiol. 2009;44:697–704.
19. Marques JP, Kober T, Krueger G, van der Zwaag W, Van de Moortele PF, Gruetter R. MP2RAGE, a self bias-field corrected sequence for improved segmentation and T1-mapping at high field. Neuroimage. 2010;49:1271–81.
20. Rovira À, Wattjes MP, Tintoré M, et al. Evidence-based guidelines: MAGNIMS consensus guidelines on the use of MRI in multiple sclerosis-clinical implementation in the diagnostic process. Nat Rev Neurol. 2015;11:471–82.
21. Lohmeier J, Kaneko T, Hamm B, Makowski MR, Okano H. atlasBREX: automated template-derived brain extraction in animal MRI. Sci Rep. 2019;9:12219.
22. Tustison NJ, Avants BB, Cook PA, et al. N4ITK: improved N3 bias correction. IEEE Trans Med Imaging. 2010;29:1310–20.
23. Avants BB, Epstein CL, Grossman M, Gee JC. Symmetric diffeomorphic image registration with cross-correlation: evaluating automated labeling of elderly and neurodegenerative brain. Med Image Anal. 2008;12:26–41.
24. Dorr AE, Lerch JP, Spring S, Kabani N, Henkelman RM. High resolution three-dimensional brain atlas using an average magnetic resonance image of 40 adult C57Bl/6J mice. Neuroimage. 2008;42:60–9.
25. Trapp BD, Peterson J, Ransohoff RM, Rudick R, Mörk S, Bö L. Axonal transection in the lesions of multiple sclerosis. N Engl J Med. 1998;338:278–85.
26. Loving GS, Caravan P. Activation and retention: a magnetic resonance probe for the detection of acute thrombosis. Angew Chem Int Ed Engl. 2014;53:1140–3.
27. Filippi M, Preziosa P, Copetti M, et al. Gray matter damage predicts the accumulation of disability 13 years later in MS. Neurology. 2013;81:1759–67.
28. Thompson AJ, Banwell BL, Barkhof F, et al. Diagnosis of multiple sclerosis: 2017 revisions of the McDonald criteria. Lancet Neurol. 2018;17:162–73.
29. Zurawski J, Lassmann H, Bakshi R. Use of magnetic resonance imaging to visualize leptomeningeal inflammation in patients with multiple sclerosis: a review. JAMA Neurol. 2017;74:100–9.
30. Bevan RJ, Evans R, Griffiths L, et al. Meningeal inflammation and cortical demyelination in acute multiple sclerosis. Ann Neurol. 2018;84:829–42.
31. Pawlitzki M, Horbrügger M, Loewe K, et al. MS optic neuritis-induced long-term structural changes within the visual pathway. Neurol Neuroimmunol Neuroinflamm. 2020;7:e665.
32. Pullicino R, Radon M, Biswas S, Bhojak M, Das K. A review of the current evidence on gadolinium deposition in the brain. Clin Neuroradiol. 2018;28:159–69.
33. Rovira A, Auger C, Huerga E, et al. Cumulative dose of macrocyclic gadolinium-based contrast agent improves detection of enhancing lesions in patients with multiple sclerosis. AJNR Am J Neuroradiol. 2017;38:1486–93.
34. van Waesberghe JH, Castelijns JA, Roser W, et al. Single-dose gadolinium with magnetization transfer versus triple-dose gadolinium in the MR detection of multiple sclerosis lesions. AJNR Am J Neuroradiol. 1997;18:1279–85.
35. Moccia M, Ciccarelli O. Molecular and metabolic imaging in multiple sclerosis. Neuroimaging Clin N Am. 2017;27:343–56.
36. Enzinger C, Barkhof F, Ciccarelli O, et al. Nonconventional MRI and microstructural cerebral changes in multiple sclerosis. Nat Rev Neurol. 2015;11:676–86.
37. Vos CM, Geurts JJ, Montagne L, et al. Blood-brain barrier alterations in both focal and diffuse abnormalities on postmortem MRI in multiple sclerosis. Neurobiol Dis. 2005;20:953–60.
38. Kwon EE, Prineas JW. Blood-brain barrier abnormalities in longstanding multiple sclerosis lesions An immunohistochemical study. J Neuropathol Exp Neurol. 1994;53:625–36.
39. Han MH, Hwang SI, Roy DB, et al. Proteomic analysis of active multiple sclerosis lesions reveals therapeutic targets. Nature. 2008;451:1076–81.
40. Yates RL, Esiri MM, Palace J, Jacobs B, Perera R, DeLuca GC. Fibrin(ogen) and neurodegeneration in the progressive multiple sclerosis cortex. Ann Neurol. 2017;82:259–70.
41. Adams RA, Bauer J, Flick MJ, et al. The fibrin-derived gamma377-395 peptide inhibits microglia activation and suppresses relapsing paralysis in central nervous system autoimmune disease. J Exp Med. 2007;204:571–82.
42. Constantinescu CS, Farooqi N, O'Brien K, Gran B. Experimental autoimmune encephalomyelitis (EAE) as a model for multiple sclerosis (MS). Br J Pharmacol. 2011;164:1079–106.
43. Zamolodchikov D, Strickland S. Aβ delays fibrin clot lysis by altering fibrin structure and attenuating plasminogen binding to fibrin. Blood. 2012;119:3342–51.
44. Merlini M, Rafalski VA, Rios Coronado PE, et al. Fibrinogen induces microglia-mediated spine elimination and cognitive impairment in an Alzheimer's disease Model. Neuron. 2019;101:1099-1108.e6.
45. Cajamarca SA, Norris EH, van der Weerd L, Strickland S, Ahn HJ. Cerebral amyloid angiopathy-linked β-amyloid mutations promote cerebral fibrin deposits via increased binding affinity for fibrinogen. Proc Natl Acad Sci U S A. 2020;117:14482–92.

Authors and Affiliations

Johannes Lohmeier[1] · Rafaela V. Silva[2,3,8] · Anna Tietze[4] · Matthias Taupitz[1] · Takaaki Kaneko[5] · Harald Prüss[6] · Friedemann Paul[7,8] · Carmen Infante-Duarte[2,8] · Bernd Hamm[1] · Peter Caravan[9] · Marcus R. Makowski[1,10]

1 Department of Radiology, Charité - Universitätsmedizin Berlin, corporate member of Freie Universität Berlin and Humboldt Universität zu Berlin, Campus Charité Mitte (CCM), Charitéplatz 1, 10117 Berlin, Germany

2 Experimental and Clinical Research Center, a cooperation between the Max Delbrück Center for Molecular Medicine in the Helmholtz Association and Charité Universitätsmedizin Berlin, Berlin, Germany

3 Charité – Universitätsmedizin Berlin, corporate member of Freie Universität Berlin and Humboldt-Universität zu Berlin, Einstein Center for Neurosciences Berlin, Charitéplatz 1, 10117 Berlin, Germany

4 Institute of Neuroradiology, Charité - Universitätsmedizin Berlin, corporate member of Freie Universität Berlin and Humboldt Universität zu Berlin, Campus Charité Mitte (CCM), Charitéplatz 1, 10117 Berlin, Germany

5 Center for the Evolutionary Origins of Human Behavior, Kyoto University, Inuyama, Aichi 484-8506, Japan

6 Department of Neurology and Experimental Neurology, Charité - Universitätsmedizin Berlin, corporate member of Freie Universität Berlin and Humboldt Universität zu Berlin, Campus Charité Mitte (CCM) and German Center for Neurodegenerative Diseases (DZNE) Berlin, Charitéplatz 1, 10117 Berlin, Germany

7 NeuroCure Clinical Research Center and Experimental and Clinical Research Center, Charité - Universitätsmedizin Berlin, corporate member of Freie Universität Berlin and Humboldt Universität zu Berlin, Berlin, Germany

8 Max Delbrueck Center for Molecular Medicine in the Helmholtz Association (MDC), Lindenberger Weg 80, 13125 Berlin, Germany

9 A. A. Martinos Center for Biomedical Imaging, Institute for Innovation in Imaging, Massachusetts General Hospital, Harvard Medical School, 149 Thirteenth Street, Suite 2301, Charlestown, MB 02129, USA

10 Department of Radiology, Klinikum Rechts der Isar, Technische Universität München, Ismaninger Str. 22, 81675 München, Germany

2.2. Entwicklung und Evaluation einer automatisierten Hirn-Segmentierung für präklinische MRT-Studien (Originalarbeit 2)

Lohmeier J, Kaneko T, Hamm B, Makowski MR, Okano H (2019) atlasBREX: Automated template-derived brain extraction in animal MRI.
Scientific Reports
DOI: 10.1038/s41598-019-48489-3

Die Relevanz von Tiermodellen in der Hirnforschung hat durch bedeutende Erkenntnisgewinne in Hinblick auf das ZNS und dessen Erkrankungen zugenommen [56]. Gleichwohl gibt es bisher nur wenige spezialisierte Methoden, die bei präklinischen MRT-Studien eingesetzt werden können. Bei der Nutzung von Schnittbildgebungsverfahren, wie CT oder MRT, in der Hirnforschung ist die Segmentierung des Gehirns ein primärer und zentraler Schritt für die darauffolgende Bildanalyse und -aufbereitung [57]. Hierzu zählen beispielweise Registrierungsverfahren zur räumlichen Normierung, Anwendungen zur Kartierung des Gehirns oder dessen dreidimensionale Darstellung. In der Neurobildgebung des Menschen wurden bereits diverse (teil-)automatisierte Methoden entwickelt [57], deren hoher Grad an Spezialisierung jedoch eine Übertragung auf präklinische Forschungsansätze begrenzt oder sogar unmöglich macht. Obgleich die manuelle Segmentierung als technischer Goldstandard gilt, ist sie arbeitsintensiv und setzt neuroanatomische Kenntnisse voraus. Daher besteht ein wachsender Bedarf an automatisierten, benutzerunabhängigen Lösungen.

Die Zielsetzung von *Originalarbeit 2* war die Entwicklung einer Anwendung zur universellen automatisierten Hirnsegmentierung für präklinische MRT-Studien und dessen Evaluation in diversen Spezies (Makaken, Büscheläffchen, Nagetiere) und MRT-Sequenzen.

Die in *Originalarbeit 2* entwickelte Software-Anwendung, atlasBREX, beruht auf einem teilautomatisierten Algorithmus und einer speziell für das jeweilige Kollektiv angefertigten anatomischen Referenzvorlage. Durch den Einsatz dieser Referenzvorlage sowie einer anfänglichen automatisierten (rudimentären) Segmentierung und der Nutzung von (nicht-)rigiden Deformationsfeldern wird für jedes Individuum eine maßgeschneiderte Segmentierungsmaske berechnet. Mittels einer aus der Kohorte berechneten anatomischen Referenzvorlage [58] erzeugt dieser Ansatz präzise und unvoreingenommene Ergebnisse für

die gesamte Studienkohorte, wohingegen allgemein erhältliche anatomische Referenzvorlagen oft technische Schwierigkeiten aufweisen, bedingt durch Unterschiede in der Anatomie (z.B. bei verschiedenen Entwicklungsstadien oder Gattungen) und/oder MRT-Kontrasten. Weiterhin wurden verschiedene Vorverarbeitungsschritte integriert, wie etwa die Korrektur von Bildverzerrungen und Intensitätsanpassungen. Das Verfahren wurde gegenüber einer Reihe technischer Alternativen ("Marker based watershed scalper", "Brain-Extraction-Tool", "3dSkullStrip", "Primatologist-Toolbox", "Rapid Automatic Tissue Segmentation" and "Robust automatic rodent brain extraction using 3D pulse-coupled neural networks") evaluiert. Als Referenzstandard wurde die manuelle Segmentierung herangezogen. Die Ergebnisse aus *Originalarbeit 2* zeigten, dass atlasBREX im Vergleich zu anderen Methoden, unabhängig von der Spezies und MRT-Protokollen, bessere und zuverlässigere Ergebnisse lieferte. atlasBREX wurde der Öffentlichkeit (zusammen mit Dokumentation, Vorlagen und Beispielmaterial) zur Verfügung gestellt.

In *Originalarbeit 2* wurde eine Anwendung zur automatisierten Hirnsegmentierung entwickelt und veröffentlicht (https://github.com/jlohmeier/atlasBREX). atlasBREX wurde mit einer Reihe von etablierten Techniken verglichen, wobei die manuelle Segmentierung als Goldstandard diente. Hierbei erzielte das neue Verfahren bessere und zuverlässigere Ergebnisse – unabhängig vom verwendeten Untersuchungsprotokoll, der untersuchten Spezies oder Entwicklungsphase. Die Ergebnisse aus *Originalarbeit 2* sind methodisch in *Originalarbeit 1* implementiert worden.

SCIENTIFIC REPORTS
nature research

OPEN

atlasBREX: Automated template-derived brain extraction in animal MRI

Received: 12 February 2019
Accepted: 3 June 2019
Published online: 21 August 2019

Johannes Lohmeier[1], Takaaki Kaneko[2], Bernd Hamm[1], Marcus R. Makowski[1] & Hideyuki Okano[2,3]

We proposed a generic template-derived approach for (semi-) automated brain extraction in animal MRI studies and evaluated our implementation with different animal models (macaque, marmoset, rodent) and MRI protocols (T1, T2). While conventional MR-neuroimaging studies perform brain extraction as an initial step priming subsequent image-registration from subject to template, our proposed approach propagates an anatomical template to (whole-head) individual subjects in reverse order, which is challenging due to the surrounding extracranial tissue, greater differences in contrast pattern and larger areas with field inhomogeneity. As a novel approach, the herein introduced brain extraction algorithm derives whole-brain segmentation using rigid and non-rigid deformation based on unbiased anatomical atlas building with a priori estimates from study-cohort and an initial approximate brain extraction. We evaluated our proposed method in comparison to several other technical approaches including "Marker based watershed scalper", "Brain-Extraction-Tool", "3dSkullStrip", "Primatologist-Toolbox", "Rapid Automatic Tissue Segmentation" and "Robust automatic rodent brain extraction using 3D pulse-coupled neural networks" with manual skull-stripping as reference standard. ABX demonstrated best performance with accurate (≥92%) and consistent results throughout datasets and across species, age and MRI protocols. ABX was made available to the public with documentation, templates and sample material (https://www.github.com/jlohmeier/atlasBREX).

Brain extraction, also referred as skull-stripping or whole-brain segmentation, describes the process of extracting the brain from the surrounding extracranial tissue. In MRI studies, it is common that this procedure is implemented at an early stage, as it plays an important role for further processing, such as spatial normalisation, surface reconstruction and structural analysis[1]. Manual delineation is considered technical standard, but it demands high time investment, experience and neuroanatomical knowledge. Hence, there is need for automated technical alternatives, which are less operator-dependent. Several (semi-) automated (hybrid) approaches were developed for human neuroimaging thus far[1], but present a high degree of specialisation due to a priori estimates. Therefore, established technical approaches for human neuroimaging are often not compatible with animal MRI and the adaption can be demanding due to interspecies differences in brain size, shape and tissue contrast as well as differences in MRI scanners, magnetic field strengths, radiofrequency coils and MRI protocols. A common challenge in skull-stripping animal MR-neuroimaging is the presence of more severe field inhomogeneity, which is attributable to non-uniformity in radiofrequency coils. As illustrated in Fig. 1, both pattern of occurrence (see heterogeneous gradient) as well as the severity of distortion are subject to variation, which affects the performance of processing algorithms that infer information from image intensity. Further challenges arise from low-resolution images (see Fig. 1a,c), such as in functional and diffusion MRI studies.

In recent years, neuroimaging studies with animal models, such as macaque[2], marmoset[3,4] and rodent[5], gained in significance due to their contributions to understanding the central nervous system[6,7]. To date, however, there are only few technical approaches available that can be applied to animal MRI, such as Marker based watershed scalper (MBWSS)[8], Brain-Extraction-Tool (BET)[9], 3dSkullStrip (3DSS) as part of the Analysis of Functional NeuroImages (AFNI) package[10], Primatologist-Toolbox (PRIMA)[11], Rapid Automatic Tissue Segmentation (RATS)[12] and Robust automatic rodent brain extraction using 3D pulse-coupled neural networks (PCNN3D)[13].

[1]Charité Universitätsmedizin Berlin, Radiology, Berlin, Germany. [2]Center for Brain Science Institute, RIKEN, Marmoset Neural Architecture, Wako-shi, Saitama, Japan. [3]Department of Physiology, Keio University School of Medicine, Tokyo, Japan. Correspondence and requests for materials should be addressed to J.L. (email: johannes.lohmeier@charite.de) or H.O. (email: hidokano@a2.keio.jp)

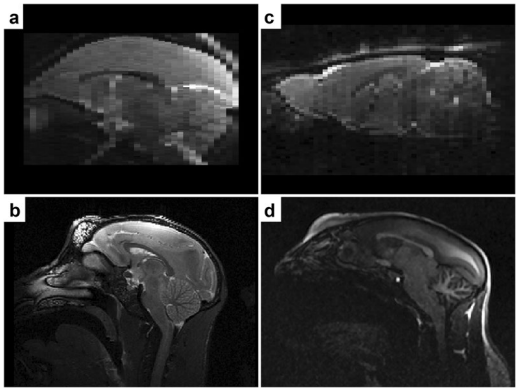

Figure 1. Challenges in skull-stripping animal MR-neuroimaging. Illustration of common difficulties when skull-stripping animal MRI (top-left: marmoset [9.4 T Biospec, Bruker, Germany]; top-right: rat [9.4 T Biospec, Bruker, Germany]; bottom-left: rhesus macaque [3 T Prisma, Siemens, Germany]; bottom-right: marmoset [3 T Prisma, Siemens, Germany]), such as low image resolution (**a**,**c**), strong field inhomogeneity (**a**–**d**) or greater field-of-view (**b**,**d**) with larger areas of non-brain tissue.

However, it is common that results are below standard and require further manual intervention. Hence, there is demand for more robust brain extraction algorithms in animal MRI.

Therefore, we proposed a generic template-derived approach for animal neuroimaging: We present atlas-BREX (ABX), a semi-automated processing pipeline that propagates skull-stripping of an anatomical template built from the study-cohort after rigid and non-rigid deformation to each individual subject (see Fig. 2). First, in a practical and unbiased manner, an anatomical study-specific template is computed from all individual subjects (see Fig. 2, step 1) using an iterative hierarchical group-wise registration framework, Atlas Building by Self-Organized Registration and Bundling (ABSORB)[14]. Next, the study-specific anatomical template is subject to manual (hybrid) skull-stripping (see Fig. 2, step 2). In the following steps, rigid and non-rigid deformation fields are computed from template- to target-space (see Fig. 2, step 5 and 7), which are applied to the template mask in order to compute a subject-specific brain mask (see Fig. 2, step 6 and 8).

While spatial transformation is conventionally performed after image preprocessing (including brain extraction) with the objective to align images within or across individuals, our proposed approach is based on the backpropagation of an anatomical template to the (whole-head) individual subject, which is challenging due to the surrounding extracranial tissue, greater differences in contrast pattern and larger areas with strong field inhomogeneity (see Fig. 1).

Therefore, as a novel approach, the herein introduced brain extraction algorithm derives whole-brain segmentation using rigid and non-rigid deformation based on unbiased anatomical atlas building with a priori estimates from the study-cohort and an initial approximate brain extraction. Thereby, our proposed approach achieves accurate and consistent results for an entire study population using only a single template, which exhibits high anatomical conformance and similarity in contrast. On the contrary, available templates, which were not built from the respective study population, can negatively impact the performance of registration algorithms due to greater divergence in brain morphology and differences in contrast pattern, originating from MRI scanner, radiofrequency coil or imaging protocol. In order to address some of the challenges described above, preprocessing operations, such as voxel-scaling, bias-field correction and intensity normalisation, were additionally implemented into the processing stream.

We evaluated ABX across different MRI protocols (T1, T2) with macaques, marmosets and rodents and compared its performance to several other technical methods.

Method

Datasets and MR-imaging protocols. Rhesus macaque (n = 32, age 0.5–36 months) datasets from the open, longitudinal UNC-Wisconsin Neurodevelopment Rhesus (UNCW-NRh) database[15] were obtained featuring preprocessed (AutoSeg2, N4BiasFieldCorrection and BRAINSfit3 registration to Emory-UNC atlas) T1-/T2-weighted scans (Waisman Lab, University of Wisconsin Madison, 3 T MRI, GE Medical, Milwaukee WI; T1W/GE-BRAVO, TR/TE = 8.684/3.652 ms, FOV = 140 × 140 mm, matrix = 256 × 256, thickness = 0.8 mm, resolution = 0.55 × 0.55 × 0.8 mm; T2W/3D-FSECUBE, TR/TE = 2500/87 ms, FOV = 154 × 154 mm, matrix = 256 × 256, thickness = 0.6 mm, resolution = 0.6 × 0.6 × 0.6 mm) including results from manual hybrid brain extraction using Atlas-Based-Classification and manual intervention, which were used as reference standard.

All procedures were approved by Wako Animal Experiment Committee (Animal Care and Use Committee), RIKEN, and all experiments were performed in accordance with the approved guidelines and regulations. The following datasets were obtained:

Adult marmoset acquired at RIKEN Brain Science Institute (9.4 T MRI, Bruker, Germany; T2W/RARE, TR/TE = 8000/32 ms, FOV = 48 × 38.5 mm, matrix = 320 × 256, thickness = 0.3 mm, slices = 97, resolution = 0.15 × 0.15 × 0.3 mm, RARE-factor = 8; T2*W/Gradient-EPI, TR/TE = 2000/16 ms, FOV = 42 × 22 mm, matrix = 84 × 44, thickness = 1 mm, slices = 35, resolution = 0.5 × 0.5 × 1 mm). At Central Institute for Experimental Animals (CIEA) juvenile (n = 6, age 6–12 months) marmoset (7 T MRI, Bruker, Germany; T1W/

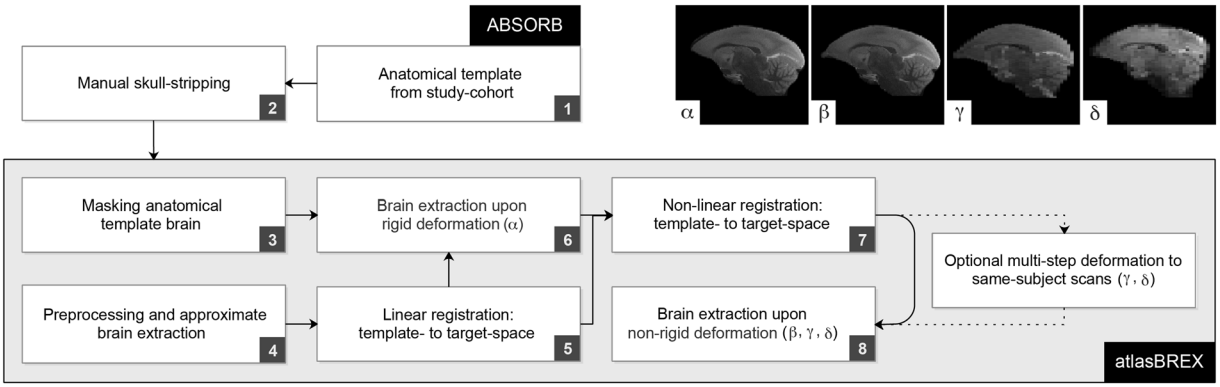

Figure 2. Workflow of atlasBREX for (semi-) automated brain extraction. In a first step (1), an unbiased anatomical template is constructed from the respective study-cohort using ABSORB, which is then subject to manual (hybrid) skull-stripping (2). Upon preprocessing in order to optimize the following image registration and initial approximate brain extraction (3), rigid and non-rigid deformation (5 and 7) fields are computed from template- to target-space, which are applied to the template mask in order to compute a subject-specific brain mask (6 and 8). Optional multi-step deformation to other target volumes, such as structural low-resolution (γ) and functional scans (δ), can be performed. Panels on the top-right demonstrate results from an adult marmoset upon rigid (α) and non-rigid (β) deformation as well as the results from the corresponding structural low-resolution (γ) and functional scans (δ).

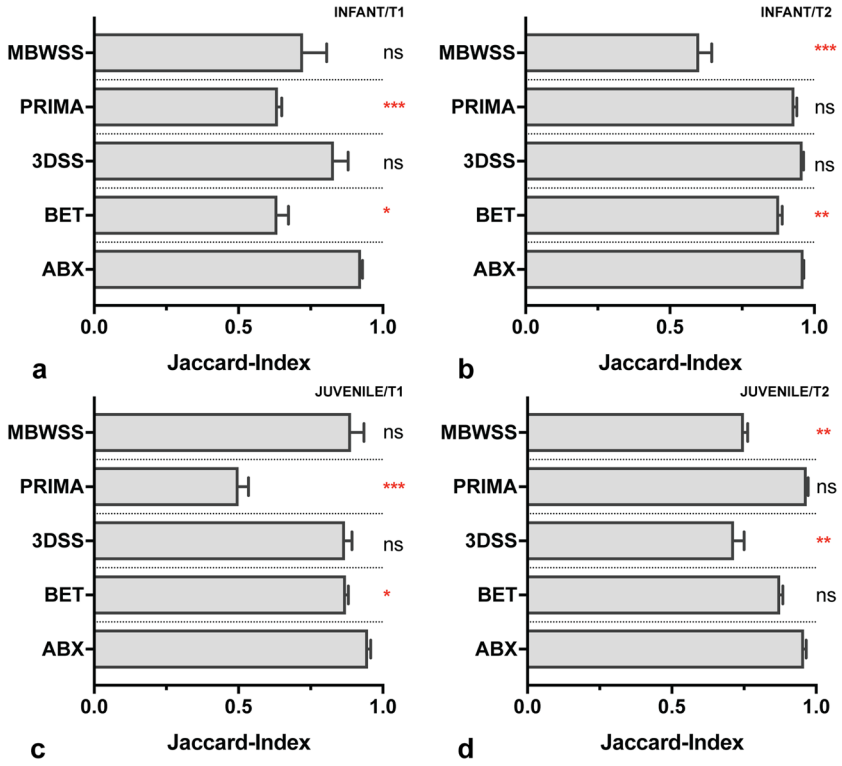

Figure 3. Evaluation with infant and juvenile rhesus macaques. Bar graph diagrams (**a**–**d**) demonstrating results from atlasBREX (ABX), Brain-Extraction-Tool v2 (BET), 3dSkullStrip (3DSS), Primatologist-Toolbox (PRIMA) and Marker based watershed scalper (MBWSS) for each dataset (4 groups, each n = 8). Results from alternate technical methods were compared to ABX using Friedman test followed by Dunn's post-hoc test. (*) p-value < 0.05, (**) p-value < 0.01, (***) p-value < 0.001, (ns) non-significant. Mdn, IQR.

MPRAGE, TR/TE = 14/45 ms, FOV = 50 × 50 mm, matrix = 192 × 192, thickness = 0.27 mm, slice = 120, resolution = 0.26 × 0.26 × 0.27 mm), adult (n = 5) marmoset (3 T MRI, Siemens, Germany; T2W, TR/TE = 3200/562 ms, FOV = 128 × 128 mm, matrix = 256 × 256, thickness = 0.5 mm, slice = 224, resolution = 0.5 × 0.5 × 0.5 mm; one sample excluded for quality reasons) and adult (n = 6) mouse (7 T MRI, Bruker, Germany; T2W/RARE,

	Friedman test	Dunn's test	Mean-rank difference	Adjusted p-value
Infant rhesus macaque T1-weighted, n = 8	F = 16.60 p = 0.002	BET	18.00	p = 0.02 (*)
		3DSS	9.00	p = 0.62
		PRIMA	24.00	p < 0.001 (***)
		MBWSS	14.00	p = 0.11
Infant rhesus macaque T2-weighted, n = 8	F = 30.50 p < 0.001	BET	21.00	p = 0.004 (**)
		3DSS	2.00	p > 0.99
		PRIMA	13.00	p = 0.16
		MBWSS	29.00	p < 0.001 (***)
Juvenile rhesus macaque T1-weighted, n = 8	F = 25.90 p < 0.001	BET	18.00	p = 0.02 (*)
		3DSS	15.00	p = 0.07
		PRIMA	32.00	p < 0.001 (***)
		MBWSS	15.00	p = 0.07
Juvenile rhesus macaque T2-weighted, n = 8	F = 22.10 p < 0.001	BET	10.00	p = 0.46
		3DSS	20.00	p = 0.006 (**)
		PRIMA	−1.00	p > 0.99
		MBWSS	21.00	p = 0.004 (**)
Infant and juvenile rhesus macaque T1-/T2-weighted, n = 32	F = 49.38 p < 0.001	BET	67.00	p < 0.001 (***)
		3DSS	46.00	p = 0.001 (**)
		PRIMA	68.00	p < 0.001 (***)
		MBWSS	79.00	p < 0.001 (***)
Juvenile marmoset T1-weighted, n = 6	F = 17.73 p = 0.001	BET	16.00	p = 0.01 (*)
		3DSS	8.00	p = 0.58
		PRIMA	15.00	p = 0.02 (*)
		MBWSS	21.00	p < 0.001 (***)
Adult marmoset T2-weighted, n = 5	F = 15.52 p = 0.004	BET	15.00	p = 0.01 (*)
		3DSS	9.00	p = 0.29
		PRIMA	8.00	p = 0.44
		MBWSS	18.00	p = 0.001 (**)
Juvenile and adult marmoset T1-/T2-weighted, n = 11	F = 32.00 p < 0.001	BET	31.00	p < 0.001 (***)
		3DSS	17.00	p = 0.09
		PRIMA	23.00	p = 0.008 (**)
		MBWSS	39.00	p < 0.001 (***)
Adult mouse T2-weighted, n = 6	F = 21.73 p < 0.001	BET	19.00	p = 0.002 (**)
		3DSS	10.00	p = 0.27
		PCNN3D	2.00	p > 0.99
		RATS	19.00	p = 0.002 (**)

Table 1. Results from comparative analysis. Comparative analysis between atlasBREX (ABX) and alternate technical methods (each group tested against the results from ABX) was performed using Jaccard-Index and Friedman test with Dunn's post-hoc test. (*) p-value < 0.05, (**) p-value < 0.01, (***) p-value < 0.001.

TR/TE = 6100/48 ms, FOV = 1.92 × 1.92 mm, matrix = 256 × 256, thickness = 0.3 mm, slice = 52, resolution = 0.075 × 0.075 × 0.3 mm, RARE-factor = 8) were obtained. Reference images were skull-stripped using a manual hybrid approach with BrainSuite (v16a1)[16].

Building templates from the study-cohort using ABSORB. A hierarchical group-wise registration framework, Atlas Building by Self-Organized Registration and Bundling (ABSORB)[14], was used for unbiased template building (with histogram-matching and affine-registration; neighbourhood-size: 3; smoothing-kernel: 3,2,1; maximum-levels: 5; registration-to-mean: 3) built from the respective study-cohort (with whole-head images). Datasets were bias-field corrected (N4BiasFieldCorrection, ANTs) and aligned (3dAllineate, AFNI), where the built-in registration algorithm led to insufficient results. Gaussian convolution (3dmerge, AFNI) (smoothing-kernel: 0.3–0.5) was applied to templates after manual (hybrid) skull-stripping with BrainSuite (v16a1).

atlasBREX with unbiased anatomical templates. atlasBREX (ABX) is a semi-automated processing pipeline that propagates skull-stripping of an anatomical template built from the study-cohort upon rigid and non-rigid deformation to each individual subject. It requires functional set-up of FMRIB's Software Library (FSL, v5.0). Several optional features are available making use of Analysis of Functional NeuroImages (AFNI, v17.1.01) and Advanced Normalization Tools (ANTs, v2.1.0)[17].

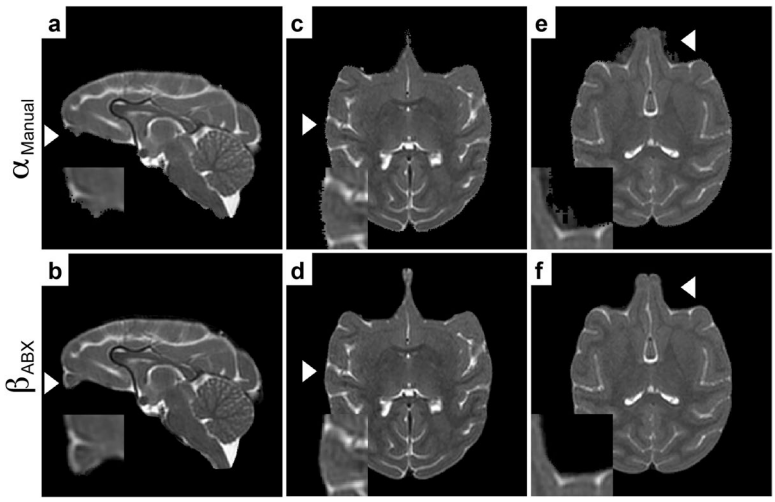

Figure 4. Comparison between atlasBREX (ABX) and manual delineation from UNC-Wisconsin Rhesus Macaque Neurodevelopment Database. Representative cases from juvenile rhesus macaque (n = 8, T2) presenting common disadvantages of manual (hybrid) brain extraction (α), which is operator-dependent and time-consuming, compared to (semi-) automated skull-stripping (β) using ABX. First two panels (**a**,**b**) show common erosion of the olfactory bulb. Jagged edges with marginal erosion of brain tissue are depicted in the following two panels (**c**,**d**). Last panels (**e**,**f**) demonstrate inaccurate delineation. White arrow indicates the magnified region-of-interest.

At first, a template mask is aligned to a subject using linear registration (FLIRT, FSL) between the template brain and an initial approximate brain extraction from Brain-Extraction-Tool v2 (BET, FSL), as shown in Fig. 2. Prior to the provisional brain extraction, voxel dimensions are adjusted to resemble the human brain and (optional) preprocessing can be applied, such as intensity normalisation (3dUnifize, AFNI), recommended for T1-weighted images, and bias-field correction (N4BiasFieldCorrection, ANTs), which compensates for field inhomogeneity. Changes during preprocessing are implemented on intermediates and, therefore, are not present in final results.

In the following steps, a subject-specific brain mask is computed from the non-rigid deformation field based on non-linear registration (FNIRT, FSL), which relies on the affine transformation matrix from the previous linear registration and a (dilated) reference mask based on the result from rigid deformation, which prevents adverse impact of surrounding extracranial tissue at full resolution during registration. Where additional scans from the same subject are available, such as low-resolution structural or functional scans, rigid and non-rigid transformation matrices can be applied upon an additional transformation step.

Prior to automated processing of an entire dataset, a brief interactive user-guided pilot run needs to be performed to determine a suitable intensity threshold (0.3, 0.5 or 0.8) for the initial approximate brain extraction.

Evaluation of atlasBREX. For quantitative evaluation, image datasets from infant (n = 8, 0.5–1 months, T1/T2) and juvenile (n = 8, 24–36 months, T1/T2) rhesus macaques, juvenile marmosets (n = 6, 6–12 months, T1), adult marmosets (n = 5, T2) and adult mice (n = 6, T2) were used. ABX was utilized on each dataset (with a single set of parameters upon a brief pilot run to determine an intensity threshold) with an anatomical template built from the respective study-cohort. In addition to Brain-Extraction-Tool v2 (BET), several dedicated technical methods (3dSkullStrip (3DSS), Primatologist-Toolbox (PRIMA) and Marker based watershed scalper (MBWSS) dedicated to non-human primates; Robust automatic rodent brain extraction using 3-D pulse-coupled neural networks (PCNN3D), Rapid Automatic Tissue Segmentation (RATS) and 3dSkullStrip (3DSS) dedicated to rodents) were applied to each dataset. Brain-Extraction-Tool v2 (BET) was assessed with different fractional intensity thresholds (5 variants, thresholds from 0.1–0.9). 3dSkullStrip (3DSS) was evaluated with dedicated presets ("monkey", "rat" and "marmoset"). Marker based watershed scalper (MBWSS) features an optimized version for macaques, which was evaluated with different parameters (one variant with default parameters with (built-in) bias-field correction; 2 variants with settings recommended by the author: bias-field correction, increased smoothing, mask refinement, increased radius of opening). Primatologist-Toolbox (PRIMA) was assessed using respective options for T1- and T2-weighting and presets for "macaque" and "mouse". For MBWSS and BET, where more than one variant was available, the best result was chosen according to the highest Jaccard-Index. All datasets were analysed on the same multi-core hardware platform (32 × 2.70 Ghz Intel-CPU, 260 GB RAM) running Linux 3.10 Centos 64-bit with FMRIB's Software Library (FSL v5.0.10), Analysis of Functional NeuroImages (AFNI v17.2.09) and Advanced Normalization Tools (ANTs v2.1.0). ABX typically required few hours for computation.

Statistical analysis. After visual inspection, quantitative evaluation was performed with manual (hybrid) skull-stripping as reference standard and Jaccard-Index (1) as similarity metric (metrics reported show Jaccard-Index). Quantitative parameters from the respective groups were analysed for statistically significant

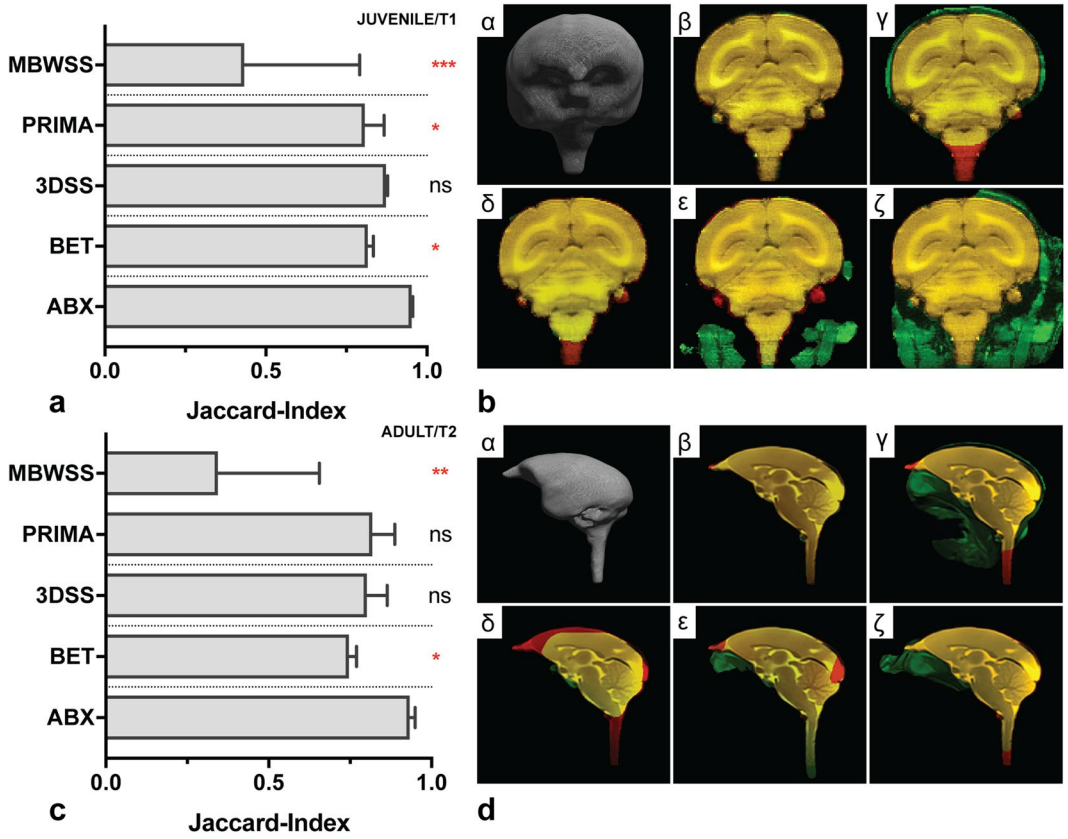

Figure 5. Evaluation with juvenile (n = 6, T1) and adult (n = 5, T2) marmosets. Bar graph diagrams (**a**,**c**) showing results from atlasBREX (ABX), Brain-Extraction-Tool v2 (BET), 3dSkullStrip (3DSS), Primatologist-Toolbox (PRIMA) and Marker based watershed scalper (MBWSS). Results from alternate technical methods were compared to ABX using Friedman test followed by Dunn's post-hoc test. (*) p-value < 0.05, (**) p-value < 0.01, (***) p-value < 0.001, (ns) non-significant. Mdn, IQR. For juvenile (**b**) and adult (**d**) marmoset, results from each method are demonstrated for a representative subject in coronal plane. First image (α) shows a 3D surface model computed from the result of ABX. The following images (β, γ, δ, ε, ζ) demonstrate the same slice using a three-coloured overlay (yellow colour indicates voxel match, while red (brain tissue erosion) or green (residual non-brain tissue) colour show mismatch) between reference and the respective result from ABX (β), BET (γ), 3DSS (δ), PRIMA (ε) and MBWSS (ζ).

difference compared to ABX (each group tested against the results from ABX) using Friedman test followed by Dunn's post-hoc test. Adjusted p-value < 0.05 was considered statistically significant.

$$J(\mathrm{A},\ \mathrm{B}) = \frac{|A \cap B|}{|A \cup B|}$$

Results

Evaluation with infant and juvenile rhesus macaques. We evaluated our approach with infant and juvenile non-human primates, which can be considered challenging due to differences in brain volume and shape with regard to fixed a priori estimates in most brain extraction algorithms. In an overall view, ABX (Mdn[IQR] = 0.95[0.03]) demonstrated best performance regardless of image contrast (T1 vs. T2) and developmental stage (infant vs. juvenile) outperforming BET (Mdn[IQR] = 0.87[0.06], p < 0.001), 3DSS (Mdn[IQR] = 0.86[0.24], p = 0.001), MBWSS (Mdn[IQR] = 0.72[0.18], p < 0.001) and PRIMA (Mdn[IQR] = 0.65[0.36], p < 0.001), as shown in Table 1.

For infant macaque datasets, as shown in Fig. 3a,b, 3DSS (T1, T2) and PRIMA (T2) achieved decent accuracy, however, visual inspection revealed that laborious manual intervention was inevitable for results from 3DSS (T1), while minor adjustments were needed for results from PRIMA (T2). Regarding juvenile macaque datasets (see Fig. 3c,d), PRIMA (T2) showed reliable performance. Although no statistically significant differences were apparent for MBWSS (T1), 3DSS (T1) and BET (T2), visual inspection showed that extensive manual corrections were still required. PRIMA presented better performance with T2-weighted datasets, while MBWSS showed higher accuracy for datasets with T1-weighting. Contrarily, ABX demonstrated robust and consistent brain extraction throughout datasets. Inaccurate delineation from ABX was apparent in a single case (Jaccard-Index = 0.76), which would have required parameter optimisation.

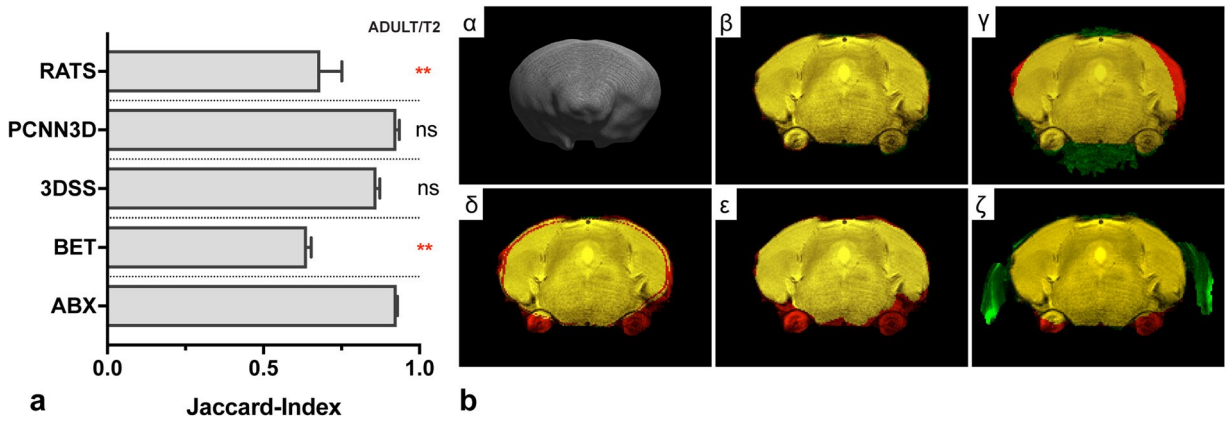

Figure 6. Evaluation with adult (n = 6, T2) mice. First panel (a) presents a bar graph diagram from results of atlasBREX (ABX), Brain-Extraction-Tool v2 (BET), 3dSkullStrip (3DSS), Robust automatic rodent brain extraction using 3-D pulse-coupled neural networks (PCNN3D) and Rapid Automatic Tissue Segmentation (RATS). Results from alternate technical approaches were compared to ABX using Friedman test followed by Dunn's post-hoc test. (**) p-value < 0.01, (ns) non-significant. Mdn, IQR. Second panel (b) demonstrates results from each method for a representative subject in coronal plane. First image (α) shows a 3D surface model computed from the result of ABX. The following images (β, γ, δ, ε, ζ) demonstrate the same coronal slice using a three-coloured overlay (yellow colour indicates voxel match, while red (brain tissue erosion) or green (residual non-brain tissue) colour show mismatch) between reference and the respective result from ABX (β), BET (γ), 3DSS (δ), PCNN3D (ε) and RATS (ζ).

Manual definition of the segmentation boundary is tedious and highly operator-dependent, which makes it prone to human error, e.g. unintentional erosion of brain voxels (see Fig. 4a), remaining non-brain tissue (see Fig. 4e) or insufficient masking with jagged edges (see Fig. 4c). In contrast, as shown in Fig. 4b,d,f, results from ABX presented consistent and accurate brain extraction with a high degree of standardisation through automated processing using a single set of parameters.

Evaluation with juvenile and adult marmosets. We evaluated ABX with datasets from juvenile and adult marmosets obtained with different magnetic field strengths (3 T vs. 7 T) and MRI protocols (T1 vs. T2). In particular, the 3 T (adult) marmoset dataset, acquired on a device originally designed for human imaging, is technically demanding due to a greater field-of-view with larger differences in contrast pattern. ABX (Mdn[IQR] = 0.95[0.02]) presented consistent and highest accuracy across datasets (see Table 1), which was followed by 3DSS (Mdn[IQR] = 0.85[0.08], p = 0.09), PRIMA (Mdn[IQR] = 0.82[0.18], p = 0.008), BET (Mdn[IQR] = 0.77[0.08], p < 0.001) and MBWSS (Mdn[IQR] = 0.34[0.40], p < 0.001).

Although there were no statistically significant differences for 3DSS (for both datasets) and PRIMA (for the adult marmoset dataset), visual inspection showed that (extensive) manual intervention was still required (see Fig. 5b,d). Brain voxel erosion (see red colour), notably affected the rostral/anterior and caudal/posterior brain regions (see Fig. 5,d, panel δ (3DSS) and ε (PRIMA)). Moreover, large areas with non-brain tissue (see green colour) remained, demonstrated in Fig. 5b,d, respectively panel ε (PRIMA). In contrast, ABX presented accurate segmentation of the marmoset brain, illustrated with brain models in Fig. 5b,d, respectively panel α, particularly with regard to the olfactory bulb.

Evaluation with adult mice. Moreover, we evaluated ABX with a rodent dataset, which is challenging to most brain extraction algorithms considering the vastly different brain morphology and difference in contrast between brain and scalp when compared to the primate brain. As shown in Fig. 6, ABX (Mdn[IQR] = 0.93[0.01]) demonstrated accurate results similar to its performance shown with non-human primates. While PCNN3D (Mdn[IQR] = 0.93[0.02], p > 0.99) and 3DSS (Mdn[IQR] = 0.86[0.02], p = 0.27) achieved similar performance (see Fig. 6a), visual inspection suggested (minor) manual corrections in individual cases. Both RATS (Mdn[IQR] = 0.68[0.16], p = 0.002) and BET (Mdn[IQR] = 0.64[0.02], p = 0.002) provided insufficient results, as demonstrated in Fig. 6b, panel γ (BET) and ζ (RATS).

Discussion

We introduced atlasBREX (ABX), a generic automated template-derived approach for brain extraction, and evaluated it with different animal models (macaque, marmoset and rodent) and MRI protocols (T1, T2). ABX demonstrated best performance and presented accurate and consistent results throughout datasets. We showed that (semi-) automated brain extraction using ABX can achieve results similar to manual (hybrid) skull-stripping, which is highly operator-dependent as a function of time-expenditure, neuroanatomical knowledge and experience with subsequent intra-/inter-individual variability. Provided that these premises are not given or present a limiting factor, standardised (semi-) automated skull-stripping using ABX can present a beneficial alternative. While our proposed approach is not entirely operator-independent, the results are substantially less subject to intra-/inter-rater variability compared to manual skull-stripping (as shown in Fig. 4).

We evaluated our proposed method in comparison to several other technical approaches including Marker based watershed scalper (MBWSS), Brain-Extraction-Tool v2 (BET), 3dSkullStrip (3DSS), Primatologist-Toolbox (PRIMA), Rapid Automatic Tissue Segmentation (RATS) and Robust automatic rodent brain extraction using 3D pulse-coupled neural networks (PCNN3D). In certain datasets, some of the alternative technical methods were able to provide accurate results, however, failed in other conditions, which is, inter alia, attributable to variable field inhomogeneity and differences in contrast pattern[1]. Unlike other technical implementations using convoluted inferences derived from intensity, morphology or surface, template-based methods like ABX present a generic approach with greater versatility regarding interspecies differences in brain size, shape and tissue contrast. The current study demonstrated that our proposed approach shows robust performance regardless of difference in the degree of sulcus folding (macaque vs. marmoset), brain size (marmoset vs. rodent), developmental time course (juvenile vs. adult marmosets) and contrast pattern (T1/T2 or 3 T/7 T/9.4 T). Moreover, template-based approaches allow for simple implementation of specific segmentation protocols with in- or exclusion of distinct brain regions, such as the brain stem, optic chiasm or cerebellum.

But these benefits come at the cost of high computational demand (typically a few hours) and the time investment of a single manual operation, which is still considerably less manual effort than manual (hybrid) skull-stripping of an entire dataset. In contrast, computational workload and computation time was for the herein tested alternatives much lower (a few minutes). Although, this downside becomes debatable with regard to the likelihood for laborious manual intervention, the growing availability of advanced computing systems in research environments and faster non-linear registration algorithms using multithreading and GPU computing. With regard to the importance of skull-stripping for further processing and data analysis, it is common that reasonable amount of effort is dedicated towards achieving accurate results. However, where dedicated technical approaches, such as PCNN3D for rodents, achieve accurate and robust results within a fraction of computation time, suchlike methods should be considered. In the near future an emerging number of methods will leverage the potential of artificial intelligence (AI), e.g. using machine learning (ML) algorithms and convolutional neural networks (CNN), however, it remains controversial whether these methods will be able to provide versatile performance across MRI protocols, species and populations.

Study-specific templates provide the advantage of accounting for inter-subject variation and providing favourable contrast pattern, which can improve rigid and non-rigid deformation. A hierarchical group-wise registration framework, Atlas Building by Self-Organized Registration and Bundling (ABSORB)[14], was utilised for unbiased anatomical template building: ABSORB provides accurate templates with sharp structural boundaries using an iterative hierarchical group-wise registration approach, where images are warped towards a set of eligible neighbours and representative images from clusters advance to higher levels. In opposition to other template-based methods, which require either multiple atlases or laborious preparation of probabilistic maps, ABX achieves simple and straightforward skull-stripping with unbiased anatomical atlas building from the study-cohort.

In conclusion, we showed that ABX facilitates robust skull-stripping across T1-/T2-weighted datasets from different species (macaques, marmosets and rodents) at different developmental stages. Due to its generic nature, our proposed approach should be foremost considered for animal MRI studies, where no superior or equivalent dedicated technical method is available. Moreover, it is suitable for neurodevelopmental studies considering the vast morphological changes throughout brain development[18,19], which can be challenging for brain extraction algorithms. Due to implementation as a scriptable (semi-) automated processing pipeline, large-scale, high-throughput application in functional and structural MRI studies is feasible. While ABX makes use of existing neuroimaging frameworks, the provided solution is not implemented in the respective applications and is novel among the technical methods applied. In addition, implementation using popular neuroimaging frameworks may benefit from their ongoing development, such as improvements regarding registration algorithms or parallel computing. Limitations of the current study are (to some extent) small sample size and evaluation restricted to non-human primates and rodents. Future studies should include larger sample size, in particular from open animal neuroimaging databases, which only started gaining in popularity in recent years[15,20].

Data Availability

Authors confirm that all relevant data are included in the article.

References

1. Kalavathi, P. & Prasath, V. B. Methods on skull stripping of MRI head scan images-a review. *J Digit Imaging* **29**, 365–379 (2016).
2. Russ, B. E., Kaneko, T., Saleem, K. S., Berman, R. A. & Leopold, D. A. Distinct fMRI responses to self-induced versus stimulus motion during free viewing in the macaque. *J Neurosci* **36**, 9580–9589 (2016).
3. Kishi, N., Sato, K., Sasaki, E. & Okano, H. Common marmoset as a new model animal for neuroscience research and genome editing technology. *Dev Growth Differ* **56**, 53–62 (2014).
4. Okano, H. & Mitra, P. Brain-mapping projects using the common marmoset. *Neurosci Res* **93**, 3–7 (2015).
5. Komaki, Y. *et al*. Functional brain mapping using specific sensory-circuit stimulation and a theoretical graph network analysis in mice with neuropathic allodynia. *Sci Rep* **6**, 37802, https://doi.org/10.1038/srep37802 (2016).
6. Okano, H. *et al*. Brain/MINDS: A japanese national brain project for marmoset neuroscience. *Neuron* **92**, 582–590 (2016).
7. Lythgoe, M. F., Sibson, N. R. & Harris, N. G. Neuroimaging of animal models of brain disease. *Br Med Bull* **65**, 235–257 (2003).
8. Beare, R. *et al*. Brain extraction using the watershed transform from markers. *Front Neuroinform* **7**, 32, https://doi.org/10.3389/fninf.2013.00032 (2013).
9. Smith, S. M. Fast robust automated brain extraction. *Hum Brain Mapp* **17**, 143–155 (2002).
10. Cox, R. W. AFNI: Software for analysis and visualization of functional magnetic resonance neuroimages. *Comput Biomed Res* **29**, 162–173 (1996).
11. Balbastre, Y. *et al*. Primatologist: A modular segmentation pipeline for macaque brain morphometry. *Neuroimage* **162**, 306–321 (2017).
12. Oguz, I., Zhang, H., Rumple, A. & Sonka, M. RATS: Rapid automatic tissue segmentation in rodent brain MRI. *J Neurosci Methods* **221**, 175–182 (2014).

13. Chou, N., Wu, J., Bai Bingren, J., Qiu, A. & Chuang, K. H. Robust automatic rodent brain extraction using 3-D pulse-coupled neural networks (PCNN). *IEEE Trans Image Process* **20**, 2554–2564 (2011).
14. Jia, H., Wu, G., Wang, Q. & Shen, D. ABSORB: Atlas building by self-organized registration and bundling. *Neuroimage* **51**, 1057–1070 (2010).
15. Young, J. T. *et al*. The UNC-Wisconsin rhesus macaque neurodevelopment database: A structural MRI and DTI database of early postnatal development. *Front Neurosci* **11**, 29, https://doi.org/10.3389/fnins.2017.00029 (2017).
16. Shattuck, D. W. & Leahy, R. M. BrainSuite: An automated cortical surface identification tool. *Med Image Anal* **6**, 129–142 (2002).
17. Avants, B. B., Epstein, C. L., Grossman, M. & Gee, J. C. Symmetric diffeomorphic image registration with cross-correlation: Evaluating automated labeling of elderly and neurodegenerative brain. *Med Image Anal* **12**, 26–41 (2008).
18. Sanchez, C. E., Richards, J. E. & Almli, C. R. Age-specific MRI templates for pediatric neuroimaging. *Dev Neuropsychol* **37**, 379–399 (2012).
19. Lenroot, R. K. & Giedd, J. N. Brain development in children and adolescents: Insights from anatomical magnetic resonance imaging. *Neurosci Biobehav Rev* **30**, 718–729 (2006).
20. Sakai, T. *et al*. The japan monkey centre primates brain imaging repository for comparative neuroscience: An archive of digital records including records for endangered species. *Primates* **59**, 553–570 (2018).

Acknowledgements

We would like to thank Drs Yuji Komako and Fumiko Seki (Central Institute for Experimental Animals), Dr. Takuya Hayashi (RIKEN Center for Life Science Technologies) for their respective datasets. Moreover, sincere gratitude goes to the German Academic Scholar Foundation (Studienstiftung des deutschen Volkes) and Japan Agency for Medical Research and Development (A-MED). This research project was supported by Brain/MINDS from A-MED (JP19dm0207001).

Author Contributions

J.L.: Study design, data collection, data analysis, interpretation of data, writing of manuscript drafts, revising and approving final content of manuscript. T.K.: Study design, data collection, data analysis, revising and approving final content of manuscript. B.H.: Study design, revising and approving final content of manuscript. M.M.: Study design, revising and approving final content of manuscript. H.O.: Study design, supervision, revising and approving final content of manuscript. All authors critically revised the manuscript.

Additional Information

Competing Interests: The authors declare no competing interests.

Publisher's note: Springer Nature remains neutral with regard to jurisdictional claims in published maps and institutional affiliations.

2.3. Nicht-invasive IDH-Genotypisierung durch Bestimmung der metabolischen Heterogenität mittels ^{18}F-FET PET (Originalarbeit 3)

> **Lohmeier J**, Radbruch H, Brenner W, Hamm B, Tietze A, Makowski MR (2023). Predictive IDH-genotyping based on the evaluation of spatial metabolic heterogeneity by compartmental uptake characteristics in preoperative glioma using ^{18}F-FET PET. The Journal of Nuclear Medicine.
> DOI: 10.2967/jnumed.123.265642

Bei Erwachsenen sind Gliome die am häufigsten vorkommenden primären malignen Neoplasien des ZNS. Molekulare Marker spielen eine zunehmend wichtigere Rolle bei der Klassifizierung, der individuellen Prognose und multimodalen Therapie von Tumoren des ZNS [34]. Ein wichtiger molekularer Marker sind Mutationen in den Isocitrat-Dehydrogenase (IDH)-Genen, die ein Schlüsselenzym im Krebszyklus codieren und damit zentrale Regulatoren des Glukose- und Aminosäurestoffwechsels darstellen [59]. Drei verschiedene IDH-Isoformen werden exprimiert, wobei in Gliomen die IDH1 am häufigsten mutiert vorliegt. Durch eine „Gain-of-Function"-Mutation wird die physiologische Umwandlung von Isocitrat zu Alpha-Ketoglutarat (α-KG) gehemmt; stattdessen wird ein neomorphes Enzym gebildet, das einen Onkometaboliten, D-2-Hydroxyglutarat (D-2-HG), bildet, was mit einer Veränderung der zellulären Differenzierung, Proliferation und Genexpression einhergeht [60, 61].
Insbesondere in Hinblick auf die zuletzt 2021 aktualisierte WHO Klassifikation der Tumoren des ZNS [62] sind IDH-Mutationen weiter in den Fokus gerückt und zu einem zentralen Merkmal in der Diagnose und Behandlung von Patienten mit Gliomen geworden. So geht eine supramaximale Resektion von IDH-mutierten Gliomen mit einem verbesserten Gesamtüberleben [63–65] einher. Darüber hinaus zeigen IDH-mutierte Gliome eine gesteigerte Vulnerabilität gegenüber reaktiven Sauerstoffspezies und Radiochemotherapeutika, was mit einer günstigeren Prognose assoziiert ist [66]. Allerdings ist der IDH-Genotyp typischerweise präoperativ nicht bekannt und eine (stereotaktische oder offene) Biopsie birgt die Gefahr zusätzlicher Komplikationen. Bis zum heutigen Zeitpunkt gibt es nur wenige zuverlässige Methoden für die nicht-invasive IDH-Genotypisierung [66].

Der *Originalarbeit 3* lag die Hypothese zugrunde, dass genetische Veränderungen mit

unterschiedlichen metabolischen Phänotypen einhergehen. Die Studie zielte darauf ab, die metabolische Umprogrammierung von Gliomen durch parametrisches ^{18}F-FET PET zu untersuchen und dessen diagnostisches Potenzial für die IDH-Genotypisierung zu bewerten.
Um die metabolische Heterogenität des Aminosäure-Stoffwechsels zu charakterisieren, wurde zunächst ein neuer bildgestützter Biomarker entwickelt. Dieser (semi-)quantitative Biomarker wurde anschließend in einer Patientenkohorte (27 Männer, 25 Frauen; Durchschnittsalter 51 ± 16 Jahre, M ± SD) mit Gliomen vor neurochirurgischer Operation mittels statischer ^{18}F-FET PET evaluiert. Die Evaluation des neu entwickelten bildgestützten Biomarkers (engl. „volumetric CU-ratio“) bestimmte den IDH-Genotyp mit hoher diagnostischer Genauigkeit (AUC=0.88, $p < 0.001$) mit einer Sensitivität von 86% und Spezifität von 90% – und deutet damit auf eine Assoziation zwischen räumlich-metabolischer Heterogenität und dem mitochondrialen Citratzyklus sowie genomischen Merkmalen hin. Zudem war eine molekulare Klassifizierung von LOH1p/19q (AUC = 0.75; $p = 0.019$), MGMT-Promotor-Methylierung (AUC = 0.70; $p = 0.011$) und ATRX-Verlust (AUC = 0.73; $p = 0.004$) anhand metabolischer Muster möglich. Ähnlich wie in früheren PET-Bildgebungsstudien konnte der IDH-Genotyp anhand der durchschnittlichen ^{18}F-FET Aufnahme mit nur bescheidener diagnostischer Genauigkeit (AUC = 0.68; $p = 0.016$) differenziert werden und war dem neuen Biomarker deutlich unterlegen. Die Quantifizierung des metabolischen Tumorvolumens (MTV and MTV_{60}) war zur IDH-Klassifizierung gänzlich ungeeignet ($p > 0.05$). Im Vergleich zur Kontrastmittel-anreichernden Läsion zeigte das metabolisch-definierte Tumorvolumen (MTV_{60}) eine signifikant größere Ausdehnung ($p = 0.046$).

Zusammenfassend konnte in *Originalarbeit 3* erstmalig aufgezeigt werden, dass parametrisches ^{18}F-FET PET und die Evaluation der metabolischen Heterogenität mittels eines neu entwickelten nicht-invasiven metabolischen Biomarkers eine bildgestützte Klassifizierung des IDH-Genotyps mit hoher diagnostischer Sicherheit ermöglicht. Die bisher vorgeschlagenen Methoden zur IDH-Genotypisierung sind oftmals komplex oder wenig zuverlässig und haben daher keinen Weg in die klinische Routine finden können. Die in dieser Studie erstmalig dargestellte Methode ermöglicht hingegen eine robuste Klassifizierung des IDH-Genotyps mittels statischer ^{18}F-FET PET ohne die Notwendigkeit komplexer Analysemethoden.

Journal of Nuclear Medicine, published on August 31, 2023 as doi:10.2967/jnumed.123.265642

Predictive IDH Genotyping Based on the Evaluation of Spatial Metabolic Heterogeneity by Compartmental Uptake Characteristics in Preoperative Glioma Using ^{18}F-FET PET

Johannes Lohmeier[1], Helena Radbruch[2], Winfried Brenner[3], Bernd Hamm[1], Anna Tietze*[4], and Marcus R. Makowski*[5]

[1]*Department of Radiology, Charité–Universitätsmedizin Berlin, Berlin, Germany;* [2]*Department of Neuropathology, Charité–Universitätsmedizin Berlin, Berlin, Germany;* [3]*Department of Nuclear Medicine, Charité–Universitätsmedizin Berlin, Berlin, Germany;* [4]*Institute of Neuroradiology, Charité–Universitätsmedizin Berlin, Berlin, Germany; and* [5]*Department of Radiology, Technical University Munich, Munich, Germany*

Molecular markers are of increasing importance for classifying, treating, and determining the prognosis for central nervous system tumors. Isocitrate dehydrogenase (IDH) is a critical regulator of glucose and amino acid metabolism. Our objective was to investigate metabolic reprogramming of glioma using compartmental uptake (CU) characteristics in *O*-(2-^{18}F-fluoroethyl)-L-tyrosine (FET) PET and to evaluate its diagnostic potential for IDH genotyping. **Methods:** Between 2017 and 2022, patients with confirmed glioma were preoperatively investigated using static ^{18}F-FET PET. Metabolic tumor volume (MTV), MTV for 60%–100% uptake (MTV_{60}), and T2-weighted and contrast-enhancing lesion volumes were automatically segmented using U-Net neural architecture and isocontouring. Volume intersections were determined using the Dice coefficient. Uptake characteristics were determined for metabolically defined compartments (central [80%–100%] and peripheral [60%–75%] areas of ^{18}F-FET uptake). CU ratio was defined as the fraction between the peripheral and central compartments. Mean target-to-background ratio was calculated. Comparisons were performed using parametric and nonparametric tests. Receiver-operating-characteristic curves, regression, and correlation were used for statistical analysis. **Results:** In total, 52 participants (male, 27, female, 25; mean age ± SD, 51 ± 16 y) were evaluated. MTV_{60} was greater and distinct from contrast-enhancing lesion volume ($P = 0.046$). IDH-mutated tumors presented a greater volumetric CU ratio and SUV CU ratio than IDH wild-type tumors ($P < 0.05$). Volumetric CU ratio determined IDH genotype with excellent diagnostic performance (area under the curve [AUC], 0.88; $P < 0.001$) at more than 5.49 (sensitivity, 86%, specificity, 90%), because IDH-mutated tumors presented a greater peripheral metabolic compartment than IDH wild-type tumors ($P = 0.045$). MTV_{60} and MTV were not suitable for IDH classification ($P > 0.05$). SUV CU ratio (AUC, 0.72; $P = 0.005$) and target-to-background ratio (AUC, 0.68; $P = 0.016$) achieved modest diagnostic performance—inferior to the volumetric CU ratio. Furthermore, the classification of loss of heterozygosity of chromosomes 1p and 19q (AUC, 0.75; $P = 0.019$), MGMT promoter methylation (AUC, 0.70; $P = 0.011$), and ATRX loss (AUC, 0.73; $P = 0.004$) by amino acid PET was evaluated. **Conclusion:** We proposed parametric ^{18}F-FET PET as a noninvasive metabolic biomarker for the evaluation of CU characteristics, which differentiated IDH genotype with excellent diagnostic performance, establishing a critical association between spatial metabolic heterogeneity, mitochondrial tricarboxylic acid cycle, and genomic features with critical implications for clinical management and the diagnostic workup of patients with central nervous system cancer.

Key Words: ^{18}F-FET PET/MRI; amino acid metabolism; IDH genotyping; biomarker; spatial metabolic heterogeneity

J Nucl Med 2023; 00:1–7
DOI: 10.2967/jnumed.123.265642

Gliomas are the most common primary malignant neoplasms of the central nervous system (CNS) in adults and comprise a large spectrum of molecular subtypes with intricate pathophysiology. Molecular stratification is essential for diagnosis, treatment planning, and individual prognosis. In recent years, the World Health Organization (WHO) classification of tumors of the CNS has undergone several updates (*1*) introducing several important changes, such as the incorporation of molecular and genetic information. One important molecular marker that has gained significant attention is the mutation status of the isocitrate dehydrogenase (IDH) gene (*2–4*). IDH gene mutations play a central role in glioma pathophysiology, occurring early in the glioma genesis and characterizing a group of tumors that is molecularly distinct from primary glioblastoma. Because IDH mutations are associated with a more favorable prognosis (*5*), the IDH genotype has become a central feature in the diagnosis and management of patients with CNS cancer. In recent years, considerable progress in understanding the molecular mechanisms and pathophysiology underlying IDH mutations has been made. IDH genes encode a key enzyme in the tricarboxylic acid cycle, which is a central cellular pathway for energy production. When IDH genes are altered, a profound disruption in the tricarboxylic acid cycle with dysregulation of the amino acid metabolism is induced—a hallmark of CNS cancer—which is leveraged for bioenergetic processes and protein synthesis. By a gain-of-function mutation, the physiologic conversion of isocitrate to α-ketoglutarate, an important intermediate metabolite in the Krebs cycle, is inhibited, whereas the production of D-2-hydroxyglutarate is propagated. High levels of the oncometabolite D-2-hydroxyglutarate mediate global DNA and histone hypermethylation, impairment of DNA break repair mechanisms, and a decrease in hypoxia-inducible factors through competitive inhibition

Received Feb. 27, 2023; revision accepted Jun. 13, 2023.
For correspondence, contact Johannes Lohmeier (johannes.lohmeier@charite.de).
*Contributed equally to this work.
Published online Aug. 31, 2023.

of tumor suppressors in the α-ketoglutarate–dependent dioxygenase family that contribute to glioma pathogenesis and progression through alteration of cellular differentiation, proliferation, and gene expression (*2,3*).

In the surgical management of patients with preoperative IDH-mutated glioma, supramaximal resection was shown to improve overall survival (*5–8*). However, the IDH genotype is typically unknown before surgery, and a preceding (stereotactic or open) biopsy involves the hazards of perioperative complications. To date, there are few reliable means for noninvasive and predictive genotyping of IDH mutation status in clinical practice (*5*).

On the basis of the hypothesis that specific genetic alterations are linked with distinct metabolic phenotypes, we introduced the compartmental uptake (CU) ratio as a noninvasive metabolic imaging biomarker characterizing the spatially heterogeneous glioma metabolism by differentiating the metabolic tumor core from its periphery. Predictive genotyping of IDH mutation status was then investigated using *O*-(2-^{18}F-fluoroethyl)-L-tyrosine (FET) PET, as an established marker for amino acid metabolism, in a patient cohort with preoperative glioma.

MATERIALS AND METHODS

Study Design and Patients

This retrospective clinical cohort study was conducted according to the principles of the Helsinki Declaration. Approval from the institutional ethics board was obtained (EA2/019/23). Informed consent was obtained from all participants. From 200 consecutive suspected-glioma patients evaluated using a simultaneous ^{18}F-FET PET/MRI approach between 2017 and 2022, 52 participants with hybrid imaging before resection (Fig. 1) were included according to the eligibility criteria.

Neuropathologic Analysis

The molecular status of IDH mutation (IDH-mutated or wild-type), 1p/19q codeletion (loss of heterozygosity of chromosomes 1p and 19q [LOH1p/19q]–positive, codeleted; LOH1p/19q-negative, nondeleted), MGMT promoter methylation (MGMT-positive, methylated; MGMT-negative, unmethylated), and ATRX loss (ATRX-positive, deficient; ATRX-negative, retention) were determined from formalin-fixed paraffin-embedded tissue specimens during routine diagnostic workup procedures using fluorescence in situ hybridization analysis, pyrosequencing, EPIC DNA methylation arrays (Illumina), or immunostainings according to the requirements of the WHO classification of tumors of the CNS (*1*). When pyrosequencing of MGMT promoter methylation was used, a cutoff of 10% was defined to classify MGMT methylated versus unmethylated cases, a cutoff that is commonly applied and has been validated for routine clinical diagnostics (*9*). Gliomas were classified using the 2021 WHO classification (*1*) according to the molecular data available at that time point.

PET/MRI Acquisition

Simultaneous PET/MRI was performed on a Magnetom Biograph mMR scanner (Siemens Healthcare) with an averaged axial spatial resolution of 6 mm in full width at half maximum, which was determined in a 3-dimensional Hoffman brain phantom measurement (ordered-subsets expectation maximization, 3 iterations and 21 subsets, postfiltering by a 3-dimensional gaussian kernel of 3 mm in full width at half maximum, as in patient data) following the method by Joshi et al. (*10*). PET and clinical high-field (3-T) MRI were performed in list mode for up to 60 min after intravenous administration of ^{18}F-FET (mean ± SD, 163 ± 23 MBq; 180-MBq standard dose and individually calculated dose for body weight < 60 kg). Fasting for at least 4 h before PET acquisition was recommended. A gadolinium-based contrast agent (Gadovist; Bayer Pharma AG) was administered according to the patient's total body weight (0.1 mmol/kg). The MRI acquisition protocol included a transversal T1-weighted ultrashort echo time sequence for attenuation and scatter correction, a T2-weighted sequence (repetition time/echo time, 5,320/88 ms; matrix size, 230 × 230 × 230; voxel size, 0.4 × 0.4 × 3.0 mm), and a postcontrast T1-weighted magnetization-prepared rapid gradient echo sequence (repetition time/echo time/inversion time, 2,400/2.26/900 ms; flip angle, 8°; matrix size, 256 × 256 × 256; voxel size, 1.0 × 1.0 × 1.0 mm; thickness, 1 mm; slices, 192). Vendor-based attenuation correction (software versions MR B20P and MR E11P) using ultrashort echo time was performed. The PET acquisition was reconstructed into transaxial slices using an iterative ordered-subset expectation maximization algorithm (ordered-subsets expectation maximization, 3 iterations and 21 subsets; matrix size, 344 × 344 × 127; voxel size, 1.0 × 1.0 × 2.3 mm; gaussian filter, 3 mm). Emission data were corrected for decay, randoms, dead time, scatter, and attenuation.

PET and MRI Analysis

Quantitative analysis was performed using OsiriX MD 12 (Pixmeo SARL). Contrast-enhancing and T2-weighted lesion volumes were determined in an automated manner using an attention-based U-Net architecture with postcontrast T1-weighted magnetization-prepared rapid gradient echo and T2-weighted/fluid-attenuated inversion recovery images as input (*11*). When applicable, regions of interest (ROIs) of T2-weighted and contrast-enhancing lesion volumes were slightly adapted. ^{18}F-FET uptake was measured in an automated manner using isocontouring based on attenuation-corrected ^{18}F-FET tracer uptake, yielding an uptake-based total (60%–100%, MTV_{60}), peripheral (60%–75%, ROI_{60}), and central (80%–100%, ROI_{80}) metabolic compartment (thresholds were iteratively determined in a pilot experiment, differentiating uptake pattern into a central and peripheral compartment based on visual assessment). Segmentations were marginally adapted to exclude large intracranial blood vessels (when applicable). For definition of metabolic tumor volume, both a percentage method (60%–100%, MTV_{60}) and an absolute threshold method (1.8 times the mean uptake of the healthy contralateral background, MTV) were used. CU ratio was defined as the fraction between ROI_{60} and ROI_{80}, yielding a volumetric CU ratio for the uptake-based volume or SUV CU ratio for the mean SUV. Mean target-to-background ratio was determined from SUV_{mean} on the basis of a 3-dimensional VOI (ROI_{80}) from an ^{18}F-FET–active lesion compared with the mean unaffected contralateral background to account for nonspecific and regional uptake behavior. In multifocal tumor manifestations, the most prominent ^{18}F-FET–active lesion was chosen as the target lesion. Mean background tracer uptake was computed from a contralateral 2-dimensional ROI of similar size in unaffected brain tissue on a representative slice with the highest mean uptake within the tumor volume. Three-dimensional ROIs from magnetization-prepared rapid gradient echo and ^{18}F-FET PET were then transformed to a structural T2-weighted image using rigid deformation (ANTs, version 2.3.4).

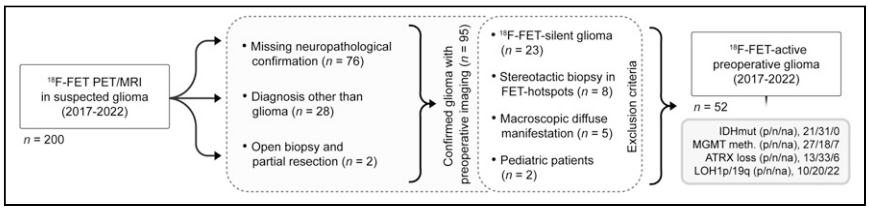

FIGURE 1. Study selection flowchart. ATRX = α-thalassemia/mental retardation syndrome, X-linked; MGMT = O^6-methylguanine DNA methyltransferase. p/n/na = positive/negative/not applicable.

Statistics

Statistical analysis was performed using Prism version 9 (GraphPad Software) and MedCalc version 20.104 (MedCalc Software Ltd.). Mann–Whitney *U* (2-tailed) tests (with Holm-Šídák multiple-comparison testing) were used for comparisons between 2 groups. Wilcoxon signed-rank (1-tailed) testing was used for matched pairs. Kruskal–Wallis testing (with Dunn multiple-comparison testing) was used for comparisons among 3 groups. Receiver-operating-characteristic analysis was performed using the DeLong method reporting area under the curve (AUC), 95% CIs, and *P* value. Sensitivity and specificity were reported for the best cutoff point independent of the prevalence determined using the Youden index. Logistic regression was used to model binary outcome (predictive accuracy based on a *P* value cutoff of 0.5). Measurements were correlated and evaluated using the nonparametric Spearman correlation coefficient (2-tailed). Intersections between volumes were computed on the basis of the Dice coefficient (Eq. 1) and the Jaccard index. In all tests, a *P* value of less than 0.05 was considered statistically significant.

$$2\times\frac{|X\cap Y|}{|X|+|Y|} \quad \text{Eq. 1}$$

RESULTS

Patient Population

Overall, the patient cohort comprised 52 participants (male, 27, female, 25; age, mean ± SD, 51 ± 16 y) with preoperative ^{18}F-FET–active glioma (high-grade glioma, 45; low-grade glioma, 5; not applicable, 2) and available neuropathologic classification (Fig. 1; Table 1). Molecular data of IDH mutation (IDH-mutated, 40%, IDH wild-type, 60%), MGMT promoter methylation (MGMT-positive, 52%; MGMT-negative, 35%; unknown, 13%), LOH1p/19q (LOH1p/19q-positive, 19.2%; LOH1p/19q-negative, 38.5%; unknown, 42.3%), and ATRX loss (ATRX-positive, 25%; ATRX-negative, 63%; unknown,12%) were determined. CNS WHO grade 4 tumors were predominantly IDH wild-type (93%), whereas most WHO CNS grade 2–3 tumors were IDH-mutated (86%). IDH-mutated gliomas included both astrocytoma (48%) and oligodendroglioma (52%). The study cohort comprised a case of diffuse pediatric-type high-grade glioma in an adult patient. A detailed overview of the

TABLE 1
Characteristics of Patient Cohort

Characteristic	Data
Participants	52
Age (mean ± SD in y)	51 ± 16
Sex	
Male	27
Female	25
IDH mutation status	
Positive	21
Negative	31
Not applicable	0
MGMT promoter methylation status	
Positive	27
Negative	18
Not applicable	7
ATRX loss	
Positive	13
Negative	33
Not applicable	6
LOH1p/19q	
Positive	10
Negative	20
Not applicable	22

Data are number, except for age.

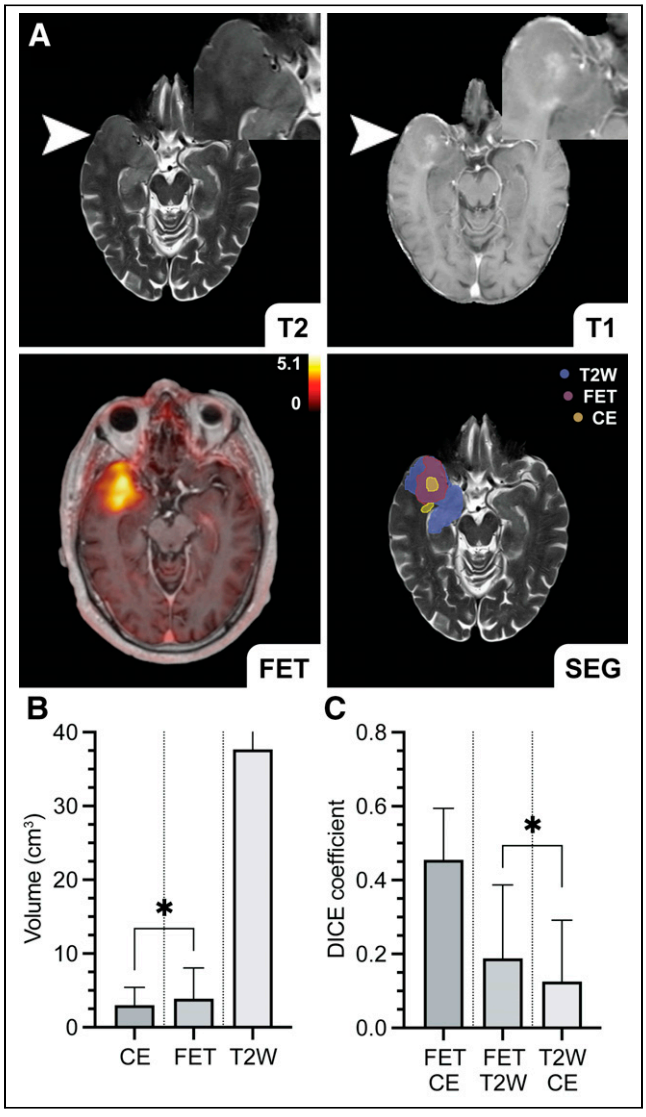

FIGURE 2. Volumetric analysis in multimodal ^{18}F-FET PET/contrast-enhanced MRI. (A) Automated segmentation based on ^{18}F-FET PET, contrast-enhancing, and T2-weighted lesion volume in multimodal dataset of patient with glioblastoma IDH wild-type (CNS WHO grade 4, MGMT-negative, ATRX-negative; arrowheads) is illustrated. (B and C) In intrasubject comparison, MTV_{60} was greater than contrast-enhancing lesion volume ($P = 0.046$, $n = 30$). Furthermore, intersection or overlap between T2-weighted lesion volume and MTV_{60} was greater than its overlap with contrast-enhanced MRI ($P = 0.038$, $n = 30$). Dice coefficients presented low to moderate degree of overlap or similarity between respective volumes, although MTV_{60} and contrast-enhancing lesion volume showed highest concordance (C). Data are median ± IQR. *$P < 0.05$. SEG = segmentation.

molecular stratification is available in Supplemental Table 1 (supplemental materials are available at http://jnm.snmjournals.org).

Comparison of Volumetric Attributes in Preoperative Glioma

MTV_{60} from ^{18}F-FET PET was greater than contrast-enhancing lesion volume (median, 3.87 cm^3 [interquartile range (IQR), 5.47] vs. 3.00 cm^3 [IQR, 4.66], $P = 0.046$, $n = 30$, Kendall W statistic, −165) in intrasubject comparison (Fig. 2). Correspondingly, the intersection of T2-weighted lesion volume with MTV_{60} was greater than its overlap with contrast-enhancing lesion volume (median, 0.189 [IQR, 0.327] vs. 0.125 [IQR, 0.262], $P = 0.038$, $n = 30$, Kendall W statistic, −173) as determined by the Dice coefficient. T2-weighted lesion volume showed the greatest dimensions and variability because of perilesional edema and diffuse infiltration. Volume intersections between MTV_{60}, contrast-enhancing lesion volume, and T2-weighted lesion volume presented a low to moderate degree of overlap or similarity (Fig. 2C), although MTV_{60} and contrast-enhancing lesion volume (Dice coefficient; median, 0.455 [IQR, 0.372]) presented the greatest concordance and were weakly correlated (Spearman rank correlation coefficient, 0.38; $P = 0.038$).

Association Between Molecular Status and CU Characteristics

IDH-mutated tumors presented a greater volumetric CU ratio (median, 7.84 [IQR, 5.20, $n = 21$] vs. 3.92 [IQR, 2.32, $n = 31$], $P < 0.001$, $U = 76$) and SUV CU ratio (median, 0.781 [IQR, 0.024, $n = 21$] vs. 0.768 [IQR, 0.022, $n = 31$], $P = 0.032$, $U = 185$) than IDH wild-type, as demonstrated in Table 2. For further evaluation of the volumetric CU ratio, the clinical cohort was randomly split into an independent model-building-and-assessment dataset based on neuropathologic IDH classification. Excellent diagnostic performance for the differentiation between IDH genotype (Fig. 3E) was apparent in the model-building dataset (AUC ± SE, 0.86 ± 0.09; $P < 0.001$; 95% CI, 0.66–0.96; IDH wild-type, 16; IDH-mutated, 10), which determined an optimal threshold of 5.43 (sensitivity, 80%; specificity, 88%; accuracy, 81%) based on the Youden index. This was then confirmed in the independent evaluation dataset (AUC ± SE, 0.89 ± 0.06; $P < 0.001$; 95% CI, 0.70–0.98; IDH wild-type, 15; IDH-mutated, 11) applying the previously determined threshold of 5.43 for IDH-mutated (sensitivity, 91%; specificity, 87%; accuracy, 88%) with similar results for the entire cohort (AUC ± SE, 0.88 ± 0.05; $P < 0.001$; 95% CI, 0.76–0.96). As shown in Figures 3A–3D, IDH-mutated tumors presented a greater peripheral metabolic compartment (corresponding to ROI_{60}) than IDH wild-type (median, 5.33 [IQR, 7.47, $n = 21$] vs. 2.78 [IQR, 4.94, $n = 31$], $P = 0.045$, $U = 218$), whereas no difference for the central metabolic compartment was apparent ($P > 0.05$). MTV_{60} and MTV were not suitable for IDH classification ($P > 0.05$). A low correlation between volumetric CU ratio was observed for MTV_{60} (Spearman rank correlation coefficient, 0.356; $P = 0.01$) but not for MTV ($P > 0.05$). With a more conservative thresholding method, MTV_{60} underestimated the total tumor volume compared with the clinically established MTV (median, 4.95 cm^3 [IQR, 7.46] vs. 7.75 cm^3 [IQR, 10.77]; $P = 0.018$; $n = 52$; Kendall W statistic, 460). SUV CU ratio (AUC ± SE, 0.72 ± 0.08; $P = 0.005$; accuracy, 67%) and target-to-background ratio (AUC ± SE, 0.68 ± 0.07; $P = 0.016$; accuracy, 63%) achieved modest diagnostic power, although the performance of target-to-background ratio was inferior to that of volumetric CU ratio (difference in AUC ± SE, 0.203 ± 0.080; $P = 0.01$).

Comparisons between IDH-mutated oligodendroglioma ($n = 11$), IDH-mutated astrocytoma ($n = 8$), and IDH wild-type glioblastoma ($n = 25$) with regard to target-to-background ratio ($P > 0.05$; Kruskal–Wallis test, 4.125), SUV CU ratio ($P = 0.028$; Kruskal–Wallis test, 7.163; adjusted $P > 0.05$), and volumetric CU ratio ($P < 0.001$; Kruskal–Wallis test, 18.55) demonstrated that IDH wild-type glioblastoma presented lower volumetric CU ratios than IDH-mutated oligodendroglioma (median, 3.88 [IQR, 1.97] vs. 8.75 [IQR, 7.21]; $P < 0.001$; mean rank difference, 17.40) with a classification threshold (AUC ± SE, 0.88 ± 0.07; $P < 0.001$; 95% CI, 0.73–0.96; sensitivity, 82%; specificity 88%; accuracy, 81%) at 5.26 (based on the Youden index) and IDH-mutated astrocytoma (median, 3.88 [IQR, 1.97] vs. 7.89 [IQR, 2.17]; $P = 0.007$; mean rank difference, 16.01) with the same classification threshold (AUC ± SE, 0.89 ± 0.09; $P < 0.001$; 95% CI, 0.73–0.97; sensitivity, 88%; specificity 88%; accuracy, 82%) at 5.26 (based on the Youden index). No differences between IDH-mutated astrocytoma and oligodendroglioma were apparent ($P > 0.05$). Supplemental Table 2 provides further details.

Molecular classification of LOH1p/19q (AUC ± SE, 0.75 ± 0.11; $P = 0.019$; accuracy, 67%), MGMT promoter methylation (AUC ± SE, 0.70 ± 0.08; $P = 0.011$; accuracy, 64%), and ATRX loss (AUC ± SE, 0.73 ± 0.08; $P = 0.004$; accuracy, 74%) were additionally evaluated using volumetric CU ratio (Fig. 3F).

DISCUSSION

We introduced a noninvasive metabolic imaging biomarker for the assessment of metabolic reprogramming in gliomas and

TABLE 2
Diagnostic Measures from ^{18}F-FET PET for IDH Classification

	Mann–Whitney *U* test			ROC					
Metric	Adjusted *P*	Mean rank difference	*U*	*P*	AUC ± SE	95% CI	Threshold	Sensitivity (%)	Specificity (%)
Volumetric CU ratio	<0.001	−19.93	76	<0.001	0.88 ± 0.05	0.76–0.96	>5.49	86	90
MTV_{60}	>0.05	−6.430	245	>0.05	0.62 ± 0.08	0.48–0.75	—		
MTV	>0.05	−1.717	304	>0.05	0.53 ± 0.09	0.39–0.67	—		
SUV CU ratio	0.032	−11.22	185	0.005	0.72 ± 0.08	0.57–0.83	>0.77	76	71
Target-to-background ratio	>0.05	9.386	208	0.016	0.68 ± 0.07	0.54–0.80	≤2.73	76	58

ROC = receiver operating characteristic.

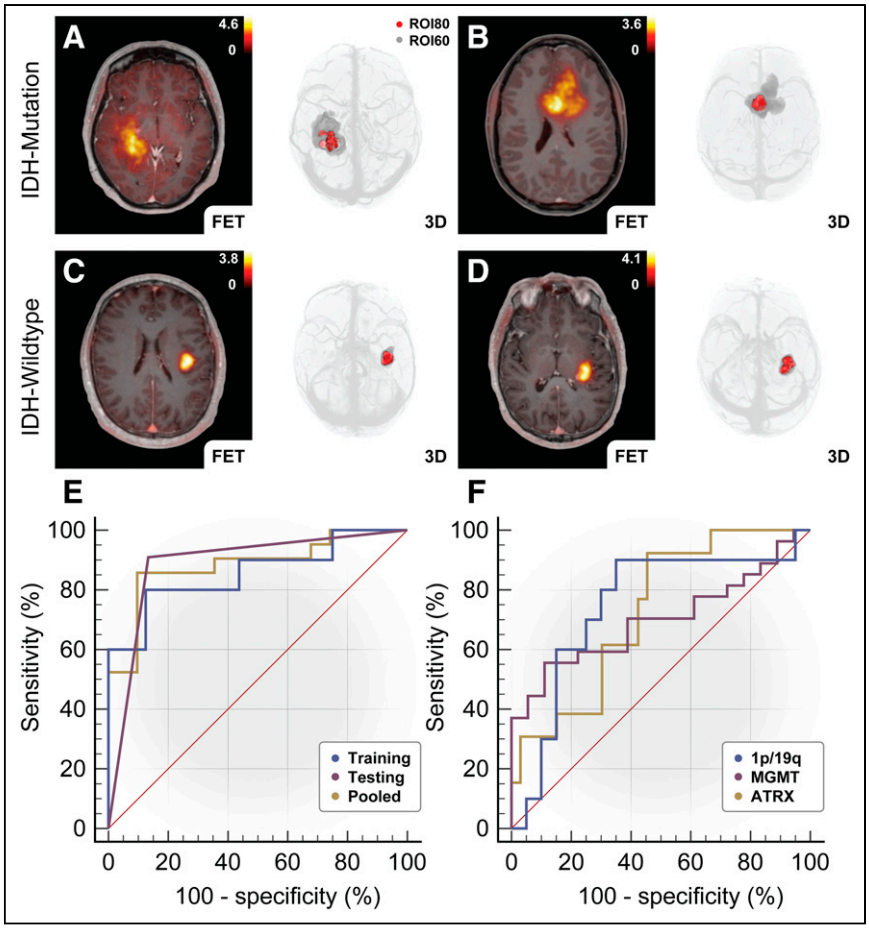

FIGURE 3. Evaluation of volumetric CU ratio for differentiation between IDH mutation status. (A and B) Representative cases of IDH-mutated high-grade astrocytoma (CNS WHO grade 3) (A) and IDH-mutated low-grade oligodendroglioma 1p/19q codeleted (CNS WHO grade 2) (B) are illustrated with ^{18}F-FET PET/magnetization-prepared rapid gradient echo fusion image and 3-dimensional rendering, respectively, demonstrating increased volumetric CU ratio (ROI_{60}/ROI_{80}). (C and D) In contrast, IDH wild-type presented low volumetric CU ratio as shown in glioblastoma IDH wild-type (CNS WHO grade 4). (E and F) Genotyping of IDH mutation status using CU ratio based on receiver-operating-characteristic analysis: volumetric CU ratio demonstrated robust diagnostic performance for differentiation between IDH-mutated and IDH wild-type tumors in independent model-building (training) dataset (AUC, 0.86 ± 0.09; $P < 0.001$; 95% CI, 0.66–0.96; IDH wild-type, 16; IDH-mutated, 10) with threshold > 5.43 (sensitivity, 80%, specificity, 88%) and evaluation (testing) dataset (AUC, 0.89 ± 0.06; $P < 0.001$; 95% CI, 0.70–0.98; IDH wild-type, 15; IDH-mutated, 11) as well as in entire study cohort (AUC, 0.88 ± 0.05; $P < 0.001$; 95% CI, 0.76–0.96) (E); in addition, differentiation between LOH1p/19q status, MGMT promoter methylation status, and ATRX loss was evaluated, presenting moderate diagnostic performance ($P < 0.05$) (F).

demonstrated its diagnostic potential for the predictive genotyping of IDH mutation status by characterizing the spatially heterogeneous amino acid metabolism in a patient cohort with preoperative glioma. First, we showed that the MTV_{60} in ^{18}F-FET PET is distinct from contrast-enhanced MRI, which is the clinical standard for the initial diagnosis, biopsy targeting, and surveillance of brain tumors. Furthermore, MTV_{60} presented greater dimensions than contrast-enhanced MRI, which is known to underestimate tumor margins because of diffuse infiltration beyond areas of blood–brain barrier impairment (*12,13*). Exploiting the cancer amino acid metabolism, we proposed the volumetric CU ratio as a biologic determinant for the assessment of CU characteristics, which determined IDH mutation status in this cohort of treatment-naïve glioma patients with excellent diagnostic accuracy, suggesting a central role for noninvasive genotyping before surgical intervention.

Gene expression in glioma is known to be spatially distinct, for example, presenting differential upregulation of tyrosine aminotransferase—where increased expression in the tumor core as opposed to the periphery was reported—and a corresponding activation of the tyrosine metabolism (*14*). Because of this differential expression and metabolism, the IDH genotype, which is a critical regulator of both glucose and amino acid metabolism (*15*), was determined in an indirect bottom-up approach in the current study. Interestingly, LOH1p/19q, MGMT promoter methylation, and ATRX loss were differentiated by spatial metabolic patterns—although diagnostic performance was moderate—suggesting indirect associations. Similar to results from previous metabolic imaging studies (*16–18*), the averaged ^{18}F-FET uptake differentiated IDH genotype with modest diagnostic performance—inferior to the volumetric CU ratio. MTV_{60} and MTV were not suitable for differentiation between IDH genotypes, but a weak correlation between MTV_{60} and volumetric CU ratio was observed. CU characteristics may also be determined as a ratio of total (summed) uptake (instead of volume) or may be accessible from histogram analysis. Although IDH-mutated astrocytoma and oligodendroglioma are considered distinct tumor entities, both could be independently differentiated from IDH wild-type glioblastoma at the same threshold, further suggesting that the volumetric CU ratio reflects metabolic reprogramming dependent on the IDH genotype. We could not observe increased uptake in IDH-mutated oligodendroglioma compared with IDH-mutated astrocytoma, as suggested in previous studies (*17,19*)—likely because of the relatively low number of these tumors in the cohort. When metabolic compartments were compared between IDH-mutated and IDH wild-type glioma, only the peripheral compartment was increased in IDH-mutated tumors, which corresponded to a visually apparent heterogeneous uptake observed in some tumors.

IDH Genotyping Using Advanced Imaging

Determination of the IDH mutation status from conventional MRI is difficult, although IDH-mutated, LOH1p/19q-negative low-grade gliomas were reported to present T2-weighted or fluid-attenuated inversion recovery mismatch (*20*), which has low sensitivity (42%) but high specificity (nearly 100%) for this distinct entity. It must, however, be noted that dysembryoplastic neuroepithelial tumors were also reported to exhibit this imaging characteristic (*21*). Previous research efforts focused predominantly on measurement of D-2-hydroxyglutarate using MR spectroscopy (*22–26*), but its clinical implementation has been limited by low spatial resolution (voxel size > 1 cm^3) and signal-to-noise ratio,

as well as the propensity to artifacts, particularly in the posttreatment setting. Moreover, D-2-hydroxyglutarate MR spectroscopy requires off-line postprocessing, currently impeding more widespread implementation. Of note is that single-voxel MR spectroscopy depends on the accuracy of the voxel placement in often heterogeneous tumors. Diffusion MRI was shown to correspond to the IDH genotype in CNS WHO 2 and 3 gliomas (*27*); however, modest diagnostic power for the differentiation of IDH mutation status was apparent using both single- and multiple-shell imaging. A study by Lohmann et al. (*28*) using ^{18}F-FET PET radiomics suggested that the combined biparametric analysis of conventional uptake parameters with additional textural features can achieve a similar diagnostic accuracy (as reported here); nonetheless, textural feature analysis is a complex and time-demanding approach, which suffers from well-known issues of restricted generalizability, overfitting, or other methodologic flaws (*29*). Experimental advanced imaging techniques, such as chemical exchange saturation transfer (*30*) or hyperpolarized ^{13}C-MRI (*31*), were also demonstrated to show correspondence to the IDH genotype, but clinical implementation is currently challenging. In contrast, the current study's approach demonstrated robust IDH classification based on static ^{18}F-FET PET without the need for complex analysis.

Clinical Relevance of Biomarker-Driven IDH Classification

The IDH genotype is a clinically important marker for molecular targeting, surgical planning, and individual prognosis (*5*). With the paradigm shift to molecular markers in clinical management of CNS cancer, there is a great clinically unmet need for noninvasive biomarker-driven classification. In clinical settings where limited tissue specimens are obtained, such as in stereotactic minimally invasive MRI-guided laser ablation or laser interstitial thermal therapy (*32*), an additional clinical benefit is expected. Molecular stratification before surgical intervention provides opportunities for more effective individualized neoadjuvant therapeutic strategies, an important topic in multimodal cytoreductive therapy because IDH-mutated gliomas are associated with better outcomes from radiochemotherapy (*2,3*). Furthermore, an imaging biomarker–driven classification aids the identification of patients with an increased risk of recurrence, allowing for earlier and more aggressive treatment regimens.

Limitations

General conclusions should be drawn with caution because of the retrospective nature of this study. Further research with larger multicenter cohorts (with different scanners and reconstruction settings) and a prospective study design is required. The CU ratio using isocontouring may be sensitive to spatial image resolution and PET scanner variability. Subsequent investigations should evaluate the impact of different spatial resolutions and PET scanners, incorporating harmonization techniques (e.g., scanner-specific calibration phantoms or image postprocessing methods) and sensitivity analyses, thereby improving generalizability and clinical applicability.

Findings from the current study are restricted to ^{18}F-FET–active tumors (76% of confirmed preoperative glioma with available imaging in the current study). In PET photopenic CNS cancer, advanced imaging techniques, such as MR spectroscopy, chemical exchange saturation transfer, or diffusion MRI, would certainly provide supplementary information, which should also be investigated in multimodal and multiparametric research for IDH genotyping—with potential to obviate a preceding biopsy. Furthermore, diffuse and multifocal tumor manifestations may result in divergent metabolic and molecular signatures. The current cohort comprised a mixed patient population, which is reflective of the situation in clinical practice. A study population with the same histologic subtype could provide greater comparability at the cost of restricted generalizability; nonetheless, our results suggest that the CU ratio reflects metabolic reprogramming independent of tumor entity. Of particular note is that former IDH-mutated glioblastomas are classified as astrocytoma CNS WHO grade 4 and that oligodendrogliomas are genetically defined by IDH mutation and LOH1p/19q according to the 2021 WHO classification (*1*). Although the determined isocontouring thresholds achieve plausible segmentation into central and peripheral metabolic compartments, an immunohistochemical correlation and further optimization of thresholds based on tissue specimens merit further research. Future studies should investigate response assessment of IDH-targeted therapy, as well as CU characteristics in other IDH mutation–associated tumors, including acute myeloid leukemia, cholangiocarcinoma, or chondrosarcoma. Multilateral interactions between cancer metabolism, oncogenic pathways, and the tumor microenvironment, particularly interactions between cancer, immune, and neuronal cells, are further areas for future studies.

CONCLUSION

The IDH genotype has a significant impact on the diagnosis and treatment of glioma. We proposed parametric ^{18}F-FET PET as a noninvasive metabolic biomarker for the classification of IDH genotype—with critical implications for clinical management and the diagnostic workup of patients with CNS cancer.

DISCLOSURE

This research project was funded by the "Deutsche Forschungsgemeinschaft" (DFG, German Research Foundation) (SFB1340/1 2018, SFB1315, and SFB295RETUNE). The PET/MRI scanner was cofunded by the "Deutsche Forschungsgemeinschaft" (INST 335/543-1 FUGG 2015). No other potential conflict of interest relevant to this article was reported.

KEY POINTS

QUESTION: Is the IDH genotype—a critical regulator of glucose and amino acid metabolism—associated with a distinct metabolic phenotype in amino acid PET?

PERTINENT FINDINGS: Fifty-two patients with preoperative glioma were retrospectively investigated using static ^{18}F-FET PET. Metabolic tumor volume was distinct and presented greater dimensions than contrast enhancement, which is known to underestimate tumor margins. Evaluation of compartmental ^{18}F-FET uptake characteristics determined IDH genotype with excellent diagnostic performance, establishing a critical association between spatial metabolic heterogeneity, mitochondrial tricarboxylic acid cycle, and genomic features. Molecular classification of LOH1p/19q, MGMT promoter methylation, and ATRX loss by spatial metabolic patterns was possible, suggesting indirect associations with tyrosine metabolism.

IMPLICATIONS FOR PATIENT CARE: We proposed parametric ^{18}F-FET PET as a noninvasive metabolic biomarker for the classification of IDH genotype before surgical intervention, with implications for clinical management and the diagnostic workup of patients with glioma.

REFERENCES

1. Louis DN, Perry A, Wesseling P, et al. The 2021 WHO Classification of Tumors of the Central Nervous System: a summary. *Neuro Oncol.* 2021;23:1231–1251.
2. Gagné L, Boulay K, Topisirovic I, Huot MÉ, Mallette FA. Oncogenic activities of IDH1/2 mutations: from epigenetics to cellular signaling. *Trends Cell Biol.* 2017; 27:738–752.
3. Waitkus MS, Diplas BH, Yan H. Isocitrate dehydrogenase mutations in gliomas. *Neuro Oncol.* 2016;18:16–26.
4. Pirozzi CJ, Yan H. The implications of IDH mutations for cancer development and therapy. *Nat Rev Clin Oncol.* 2021;18:645–661.
5. Miller JJ, Gonzalez Castro LN, McBrayer S et al. Isocitrate dehydrogenase (IDH) mutant gliomas: a Society for Neuro-Oncology (SNO) consensus review on diagnosis, management, and future directions. *Neuro Oncol.* 2023;25:4–25.
6. Motomura K, Chalise L, Ohka F, et al. Impact of the extent of resection on the survival of patients with grade II and III gliomas using awake brain mapping. *J Neurooncol.* 2021;153:361–372.
7. Rossi M, Gay L, Ambrogi F, et al. Association of supratotal resection with progression-free survival, malignant transformation, and overall survival in lower-grade gliomas. *Neuro Oncol.* 2021;23:812–826.
8. Beiko J, Suki D, Hess KR, et al. IDH1 mutant malignant astrocytomas are more amenable to surgical resection and have a survival benefit associated with maximal surgical resection. *Neuro Oncol.* 2014;16:81–91.
9. Xie H, Tubbs R, Yang B. Detection of MGMT promoter methylation in glioblastoma using pyrosequencing. *Int J Clin Exp Pathol.* 2015;8:1790–1796.
10. Joshi A, Koeppe RA, Fessler JA. Reducing between scanner differences in multi-center PET studies. *Neuroimage.* 2009;46:154–159.
11. Bouget D, Pedersen A, Hosainey SAM, Solheim O, Reinertsen I. Meningioma segmentation in T1-weighted MRI leveraging global context and attention mechanisms. *Front Radiol.* 2021;1:711514.
12. Song S, Cheng Y, Ma J, et al. Simultaneous FET-PET and contrast-enhanced MRI based on hybrid PET/MR improves delineation of tumor spatial biodistribution in gliomas: a biopsy validation study. *Eur J Nucl Med Mol Imaging.* 2020;47: 1458–1467.
13. Lohmann P, Stavrinou P, Lipke K, et al. FET PET reveals considerable spatial differences in tumour burden compared to conventional MRI in newly diagnosed glioblastoma. *Eur J Nucl Med Mol Imaging.* 2019;46:591–602.
14. Yamashita D, Bernstock JD, Elsayed G, et al. Targeting glioma-initiating cells via the tyrosine metabolic pathway. *J Neurosurg.* 2020;134:721–732.
15. Bi J, Chowdhry S, Wu S, Zhang W, Masui K, Mischel PS. Altered cellular metabolism in gliomas: an emerging landscape of actionable co-dependency targets. *Nat Rev Cancer.* 2020;20:57–70.
16. Kudulaiti N, Zhang H, Qiu T, et al. The relationship between IDH1 mutation status and metabolic imaging in nonenhancing supratentorial diffuse gliomas: a ^{11}C-MET PET study. *Mol Imaging.* 2019;18:1536012119894087.
17. Verger A, Stoffels G, Bauer EK, et al. Static and dynamic ^{18}F-FET PET for the characterization of gliomas defined by IDH and 1p/19q status. *Eur J Nucl Med Mol Imaging.* 2018;45:443–451.
18. Lopci E, Riva M, Olivari L, et al. Prognostic value of molecular and imaging biomarkers in patients with supratentorial glioma. *Eur J Nucl Med Mol Imaging.* 2017; 44:1155–1164.
19. Kim D, Chun JH, Kim SH, et al. Re-evaluation of the diagnostic performance of ^{11}C-methionine PET/CT according to the 2016 WHO classification of cerebral gliomas. *Eur J Nucl Med Mol Imaging.* 2019;46:1678–1684.
20. Park SI, Suh CH, Guenette JP, Huang RY, Kim HS. The T2-FLAIR mismatch sign as a predictor of IDH-mutant, 1p/19q-noncodeleted lower-grade gliomas: a systematic review and diagnostic meta-analysis. *Eur Radiol.* 2021;31:5289–5299.
21. Onishi S, Amatya VJ, Kolakshyapati M, et al. T2-FLAIR mismatch sign in dysembryoplasticneuroepithelial tumor. *Eur J Radiol.* 2020;126:108924.
22. Choi C, Ganji SK, DeBerardinis RJ, et al. 2-hydroxyglutarate detection by magnetic resonance spectroscopy in IDH-mutated patients with gliomas. *Nat Med.* 2012;18:624–629.
23. Andronesi OC, Arrillaga-Romany IC, Ly KI, et al. Pharmacodynamics of mutant-IDH1 inhibitors in glioma patients probed by in vivo 3D MRS imaging of 2-hydroxyglutarate. *Nat Commun.* 2018;9:1474.
24. Choi C, Raisanen JM, Ganji SK, et al. Prospective longitudinal analysis of 2-hydroxyglutarate magnetic resonance spectroscopy identifies broad clinical utility for the management of patients with IDH-mutant glioma. *J Clin Oncol.* 2016; 34:4030–4039.
25. Bumes E, Wirtz FP, Fellner C, et al. Non-invasive prediction of IDH mutation in patients with glioma WHO II/III/IV based on F-18-FET PET-guided in vivo ^{1}H-magnetic resonance spectroscopy and machine learning. *Cancers (Basel).* 2020;12:3406.
26. Tietze A, Choi C, Mickey B, et al. Noninvasive assessment of isocitrate dehydrogenase mutation status in cerebral gliomas by magnetic resonance spectroscopy in a clinical setting. *J Neurosurg.* 2018;128:391–398.
27. Figini M, Riva M, Graham M, et al. Prediction of isocitrate dehydrogenase genotype in brain gliomas with MRI: single-shell versus multishell diffusion models. *Radiology.* 2018;289:788–796.
28. Lohmann P, Lerche C, Bauer EK, et al. Predicting IDH genotype in gliomas using FET PET radiomics. *Sci Rep.* 2018;8:13328.
29. Gidwani M, Chang K, Patel JB et al. Inconsistent partitioning and unproductive feature associations yield idealized radiomic models. *Radiology.* 2023;307:e220715.
30. Paech D, Windschuh J, Oberhollenzer J, et al. Assessing the predictability of IDH mutation and MGMT methylation status in glioma patients using relaxation-compensated multipool CEST MRI at 7.0 T. *Neuro Oncol.* 2018;20:1661–1671.
31. Chaumeil MM, Larson PE, Woods SM, et al. Hyperpolarized [1-^{13}C] glutamate: a metabolic imaging biomarker of IDH1 mutational status in glioma. *Cancer Res.* 2014;74:4247–4257.
32. Schupper AJ, Chanenchuk T, Racanelli A, Price G, Hadjipanayis CG. Laser hyperthermia: past, present, and future. *Neuro Oncol.* 2022;24(suppl 6):S42–S51.

2.4. Detektion von Gliomrezidiven durch die mikrostrukturelle Charakterisierung metabolischer Kompartimente mittels multimodaler und integrativer ^{18}F-FET PET und „Diffusion Kurtosis Imaging“ (DKI) (Originalarbeit 4)

Lohmeier J, Radbruch H, Brenner W et al. (2023) Detection of recurrent high-grade glioma using microstructure characteristics of distinct metabolic compartments in a multimodal and integrative ^{18}F-FET PET/fast-DKI approach.
European Radiology.
DOI: 10.1007/s00330-023-10141-0

Obwohl es bedeutende Fortschritte in der Behandlung von Gliomen gibt, ist die Prognose bei höhergradigen Gliomen weiterhin ungünstig, was hauptsächlich auf die hohe Wahrscheinlichkeit für das Auftreten eines Rezidivs zurückzuführen ist. Die frühzeitige Erkennung von Gliomrezidiven besitzt eine hohe klinische Relevanz für die Prognose. Die klinische Abgrenzung zwischen einem Rezidiv und posttherapeutischen Veränderungen stellt jedoch eine Herausforderung dar. Aufgrund des Risikos perioperativer Komplikationen wird die Durchführung von neurochirurgischen Biopsien nach Möglichkeit vermieden. Obwohl die kontrastmittelverstärkte MRT als Bildgebungsstandard gilt, weist sie erhebliche Einschränkungen hinsichtlich der Identifizierung von Rezidiven auf und unterschätzt oftmals die Tumorausdehnung [38]. In Ergänzung zur konventionellen MRT hat sich die Diffusionsbildgebung in diesem Zusammenhang als hilfreich erwiesen. Während in der klinischen Umgebung hauptsächlich einfache Diffusionsmodelle zum Einsatz kommen, sind fortschrittlichere Methoden, wie das „Diffusion Kurtosis Imaging“ (DKI), erst durch neue, schnelle Untersuchungsprotokolle für den klinischen Einsatz praktikabel geworden. Diese ermöglichen eine detailliertere Charakterisierung der Gewebemikrostruktur [67–69]. Zudem hat sich die PET-Bildgebung mit radiomarkierten synthetischen Aminosäuren, insbesondere ^{18}F-FET, als vielversprechendes Instrument in der neuroonkologischen Bildgebung etabliert [35, 70, 71]. Mit der hybriden PET/MRT-Bildgebung ergeben sich neue Möglichkeiten für den synergistischen Einsatz von PET und MRT, wobei metabolische und mikrostrukturelle Daten nun integriert werden können, um eine nicht-invasive Früherkennung von Rezidiven und die Abgrenzung zu Behandlungseffekten zu ermöglichen.

Zielsetzung der *Originalarbeit 4* war die Kombination und Integration der multimodalen ^{18}F-FET PET/MRT mit einem beschleunigten DKI-Protokoll zur mikrostrukturellen Charakterisierung metabolischer Kompartimente bei der klinischen Fragestellung nach Tumorprogress (oder Behandlungseffekten) bei multimodal therapierten Gliomen. Die diagnostische Güte dieses integrativen Verfahrens wurde retrospektiv in einer Patientenkohorte evaluiert. Zudem wurden mikrostrukturelle Korrelate des IDH-Genotyps im posttherapeutischen Kontext untersucht.

Im Rahmen einer retrospektiven Studie wurden insgesamt 59 PatientInnen (29 Männer, 30 Frauen; Durchschnittsalter, 48 ± 12 Jahre, M ± SD) untersucht, die zuvor eine multimodale Therapie bei diagnostizierten Gliomen erhalten hatten. Gemäß Einschlusskriterien wurden 39 PatientInnen mit neuropathologisch gesichertem Rezidiv sowie 20 PatientInnen mit Behandlungseffekten gemäß neuropathologischem Bericht oder RANO-Kriterien in die Studie aufgenommen. Zwischen dem letzten therapeutischen Eingriff und der PET/MRT-Untersuchung vergingen im Median 30 Monate.
Bei der Evaluation der statischen ^{18}F-FET PET zeigten höhergradige Gliomrezidive eine signifikant höhere ^{18}F-FET Aufnahme im Vergleich zu Behandlungseffekten ($p < 0.001$), was mit einer hohen diagnostischen Güte (AUC = 0.86, $p < 0.001$) einherging. Diffusionsmetriken aus der metabolischen Peripherie zeigten größere Unterschiede zwischen den beiden Gruppen, was sich letztlich auch in günstigeren diagnostischen Kenngrößen widerspiegelte. Bei Gliomrezidiven wurde sowohl eine höhere mittlere Diffusivität (MD) als auch ein geringerer relativer „mean kurtosis tensor“ (rMKT) sowie verminderte fraktionale Anisotropie (FA) im Vergleich zu posttherapeutischen Veränderungen beobachtet. Dieser Unterschied zwischen den metabolischen Kompartimenten war für die FA besonders ausgeprägt, die sowohl eine negative Korrelation zur ^{18}F-FET PET ($rs = -0.46$, $p < 0.001$) als auch eine hierzu vergleichbare diagnostischen Leistung (AUC = 0.86, $p < .001$) zeigte. Die Kombination der mikrostrukturellen Diffusionsmetriken und ^{18}F-FET PET in einem biparametrischen Ansatz erbrachte die beste diagnostische Leistung (AUC ± SE, 0.93 ± 0.04, $p < 0.001$) sowie einen Mehrwert gegenüber der alleinigen ^{18}F-FET PET (Unterschied in AUC ± SE, 0.069 ± 0.034, $p = 0.04$). Der IDH-Genotyp konnte mittels mikrostruktureller Diffusionsmetriken unterschieden werden.

Diese Ergebnisse der *Originalarbeit 4* zeigten, dass eine multimodale und integrative Bildgebung bei der schwierigen und komplexen Fragestellung nach einer Differenzierung

zwischen Tumorprogress und Behandlungseffekt einen diagnostischen Mehrwert bietet. Es wurde eine Methodik entwickelt, die sowohl die metabolische Aktivität als auch die Gewebestruktur berücksichtigt und dabei die Erkennung von Rezidiven durch genauere Charakterisierung von Tumoren verbessert. Diese Ergebnisse legen nahe, dass eine integrative Analyse von multimodalen Datensätzen neue Maßstäbe für die onkologische Diagnostik von Gliomen und anderen Tumoren setzen wird.

European Radiology
https://doi.org/10.1007/s00330-023-10141-0

European Radiology
ESR EUROPEAN SOCIETY OF RADIOLOGY

NUCLEAR MEDICINE

Detection of recurrent high-grade glioma using microstructure characteristics of distinct metabolic compartments in a multimodal and integrative 18F-FET PET/fast-DKI approach

Johannes Lohmeier[1] · Helena Radbruch[2] · Winfried Brenner[3] · Bernd Hamm[1] · Brian Hansen[4] · Anna Tietze[5] · Marcus R. Makowski[6]

Received: 29 January 2023 / Revised: 25 June 2023 / Accepted: 6 July 2023

Abstract

Objectives Differentiation between high-grade glioma (HGG) and post-treatment-related effects (PTRE) is challenging, but advanced imaging techniques were shown to provide benefit. We aim to investigate microstructure characteristics of metabolic compartments identified from amino acid PET and to evaluate the diagnostic potential of this multimodal and integrative O-(2-^{18}F-fluoroethyl)-L-tyrosine-(FET)-PET and fast diffusion kurtosis imaging (DKI) approach for the detection of recurrence and IDH genotyping.

Methods Fifty-nine participants with neuropathologically confirmed recurrent HGG ($n = 39$) or PTRE ($n = 20$) were investigated using static ^{18}F-FET PET and a fast-DKI variant. PET and advanced diffusion metrics of metabolically defined (80–100% and 60–75% areas of ^{18}F-FET uptake) compartments were assessed. Comparative analysis was performed using Mann–Whitney *U* tests with Holm-Šídák multiple-comparison test and Wilcoxon signed-rank test. Receiver operating characteristic (ROC) curves, regression, and Spearman's correlation analysis were used for statistical evaluations.

Results Compared to PTRE, recurrent HGG presented increased ^{18}F-FET uptake and diffusivity (MD60), but lower (relative) mean kurtosis tensor (rMKT60) and fractional anisotropy (FA60) (respectively $p < .05$). Diffusion metrics determined from the metabolic periphery showed improved diagnostic performance — most pronounced for FA60 (AUC = 0.86, $p < .001$), which presented similar benefit to ^{18}F-FET PET (AUC = 0.86, $p < .001$) and was negatively correlated with amino acid uptake ($rs = -0.46$, $p < .001$). When PET and DKI metrics were evaluated in a multimodal biparametric approach, TBRmax + FA60 showed highest diagnostic accuracy (AUC = 0.93, $p < .001$), which improved the detection of relapse compared to PET alone (difference in AUC = 0.069, $p = .04$). FA60 and MD60 distinguished the IDH genotype in the post-treatment setting.

Conclusion Detection of glioma recurrence benefits from a multimodal and integrative PET/DKI approach, which presented significant diagnostic advantage to the assessment based on PET alone.

Clinical relevance statement A multimodal and integrative ^{18}F-FET PET/fast-DKI approach for the non-invasive microstructural characterization of metabolic compartments provided improved diagnostic capability for differentiation between recurrent glioma and post-treatment-related changes, suggesting a role for the diagnostic workup of patients in post-treatment settings.

The last two senior authors, A.T and M.M., contributed equally to this research article (by providing supervision, essential expertise in advanced imaging and neuroradiology as well as necessary infrastructure).

✉ Johannes Lohmeier
johannes.lohmeier@charite.de

1 Department of Radiology, Charité - Universitätsmedizin Berlin, corporate member of Freie Universität Berlin and Humboldt Universität Zu Berlin, Charitéplatz 1, 10117 Berlin, Germany

2 Department of Neuropathology, Charité - Universitätsmedizin Berlin, corporate member of Freie Universität Berlin and Humboldt Universität Zu Berlin, Charitéplatz 1, 10117 Berlin, Germany

3 Department of Nuclear Medicine, Charité - Universitätsmedizin Berlin, corporate member of Freie Universität Berlin and Humboldt Universität Zu Berlin, Augustenburger Platz 1, 13353 Berlin, Germany

4 Department of Clinical Medicine, Center of Functionally Integrative Neuroscience (CFIN), Aarhus University, Universitetsbyen 3, 8000 Aarhus C, Denmark

5 Institute of Neuroradiology, Charité - Universitätsmedizin Berlin, corporate member of Freie Universität Berlin and Humboldt Universität Zu Berlin, Charitéplatz 1, 10117 Berlin, Germany

6 Department of Radiology, Technical University Munich, Ismaninger Str. 22, 81675 München, Germany

Published online: 06 September 2023

Key Points

- *Multimodal PET/MRI with integrative analysis of ^{18}F-FET PET and fast-DKI presents clinical benefit for the assessment of CNS cancer, particularly for the detection of recurrent high-grade glioma.*
- *Microstructure markers of the metabolic periphery yielded biologically pertinent estimates characterising the tumour microenvironment, and, thereby, presented improved diagnostic accuracy with similar accuracy to amino acid PET.*
- *Combined ^{18}F-FET PET/fast-DKI achieved the best diagnostic performance for detection of high-grade glioma relapse with significant benefit to the assessment based on PET alone.*

Keywords Glioma · Metabolism · Positron-emission tomography · Multimodal imaging · Diffusion magnetic resonance imaging

Abbreviations

ATRX	Alpha-thalassemia/mental retardation syndrome X-linked
DKI	Diffusion kurtosis imaging
FA	Fractional anisotropy
FET	O-(2-^{18}F-fluoroethyl)-L-tyrosine
HGG/LGG	High-/low-grade glioma
IDH	Isocitrate dehydrogenase
LOH1p/19q	Loss of heterozygosity on chromosomes 1p and 19q
MD	Mean diffusivity
MGMT	O6-methylguanine-DNA methyltransferase
MKT	Mean kurtosis tensor
PTRE	Post-treatment-related effects

Introduction

Cerebral gliomas are the most common primary brain tumours in adults. Despite comprehensive therapeutic regimens and significant advances in treatment strategies in recent years [1], the survival prospects for patients with high-grade glioma (HGG) remain poor due to a high risk for recurring disease. The glioma microenvironment, characterized by its complex molecular pathophysiology, dynamic plasticity and multifaceted cellular interactions [2–5], plays a central role in several aspects of cancer progression, including diffuse infiltration, drug resistance and immune escape [6].

Early recognition of relapsing glioma is difficult, but crucial for patient survival, as prompt medical intervention may change the otherwise dismal prognosis. Given the potential for perioperative complications, neurosurgical biopsies are considered a last resort for the diagnosis of recurrence. Moreover, the accuracy of diagnosis is highly dependent on accurate targeting in often heterogeneous lesions, where benign treatment-associated changes may be co-existent. Contrast-enhanced magnetic resonance imaging (CE-MRI) is the clinical standard for the initial diagnosis and surveillance of brain tumours, but clinical imaging provides poor sensitivity for the detection of recurrence, as post-treatment-related effects (PTRE) — e.g. radiation effects, necrosis, neuroinflammation or postsurgical changes — are often indistinguishable [7]. Definition of tumour boundaries based on CE-MRI is furthermore known to underestimate tumour margins, due to a well-known mismatch between contrast-enhancing regions and diffuse infiltration [8]. Particularly in the post-treatment setting, where concurrent therapy-associated changes may be apparent, CE-MRI becomes less reliable [7]. Unlike gadolinium-based contrast media, metabolic imaging using O-(2-^{18}F-fluoroethyl)-L-tyrosine (FET), an established amino acid tracer with a clinical role in the diagnosis, tumour grading, treatment planning, and follow-up imaging of primary brain tumours [9–12], is independent of blood–brain barrier (BBB) impairment, enabling a more accurate determination of the tumour extent [7, 13–15].

Besides conventional CE-MRI, diffusion MRI (dMRI) emerged as an important clinical application in cancer imaging, which determines the diffusion properties of protons within tissue, and, thereby, provides an indirect probe of the cellular-level tissue architecture. By taking a more complex diffusion profile into account — beyond the scope of traditional diffusion-weighted (DWI) and diffusion tensor (DTI) imaging — a greater microstructural sensitivity towards alterations of tissue composition is achieved using diffusion kurtosis imaging (DKI) [16]. However, further clinical evaluation and translation of DKI have been impeded by time-consuming acquisitions and computationally demanding kurtosis tensor analysis. To alleviate these demands, a fast-DKI method was recently proposed [17]. In this novel DKI variant, estimates from (non-)Gaussian diffusion are rapidly obtained from 19 diffusion-weighted images at a fraction of the measurement time, which renders this technique suitable for routine diagnostic imaging, particularly when prolonged measurements cannot be endured (with motion artefacts or early termination of the examination as consequence) or in clinical hybrid PET/MRI examinations where tracer decay excludes extensive acquisition protocols.

Although several advanced MRI techniques have been investigated to characterize structural, metabolic, or vascular features of brain tumours, the diagnostic performance of PET and MRI alone remain restricted. With the increasing clinical

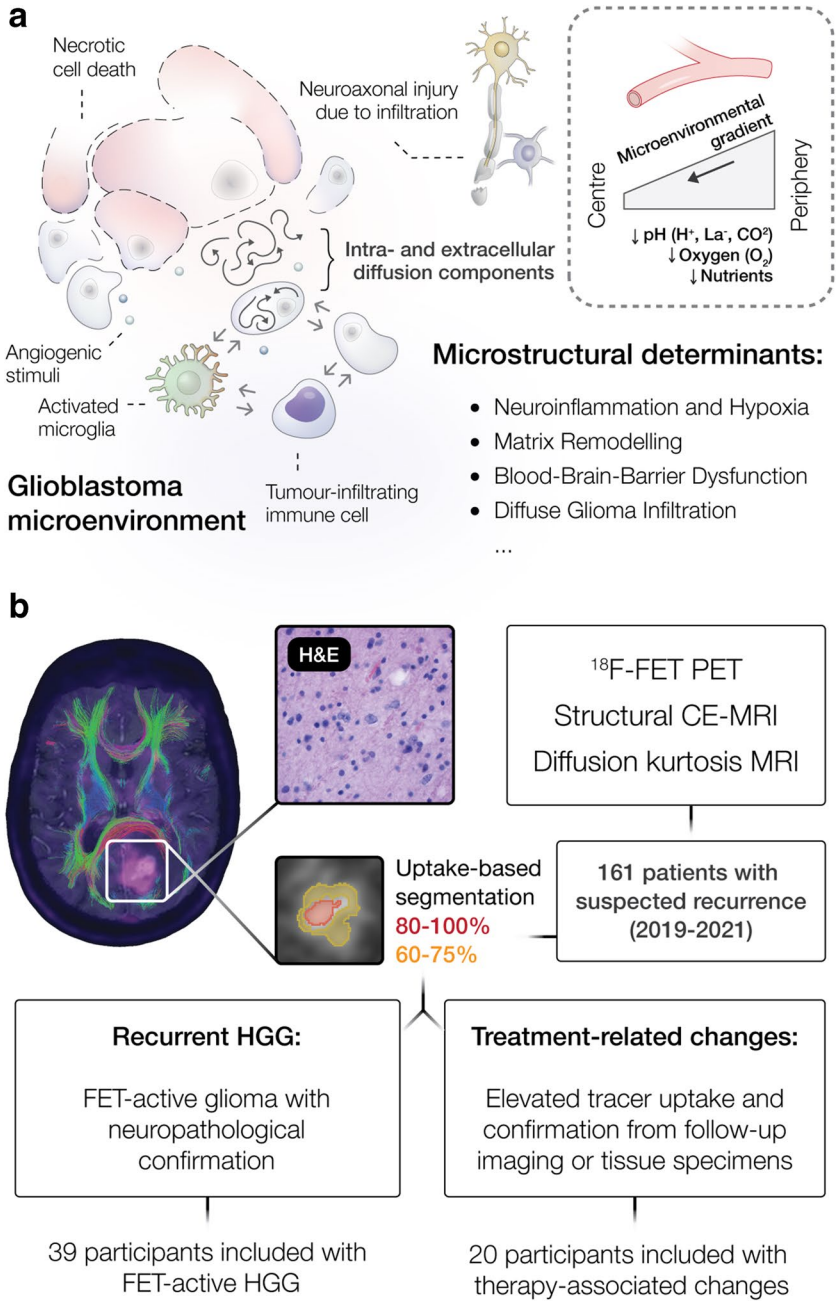

Fig. 1 Microstructural disarray in the glioblastoma microenvironment. Advanced diffusion techniques can determine microstructural tissue properties (**a**) in relapsing cancer. Due to a dysregulated cancer metabolism, the glioblastoma microenvironment is transformed into a hypoxic, acidic and nutrient-depleted milieu. While central regions of highly aggressive tumours typically present necrotic features, the periphery shows higher proliferation rates due to increased vascularity in response to angiogenic stimuli and, therefore, improved nutrient/oxygen supply and metabolic waste disposal. Blood–brain barrier (BBB) impairment is accompanied by vasogenic edema, deposition of plasma proteins or the occurrence of haemorrhage at microvascular disruption. Tumour infiltrating leucocytes aggregate in the tumour parenchyma and periphery, where a distinct immune microenvironment of CNS-resident and peripheral immune cells is established, that can inhibit or promote cancer development and growth. Multimodal data from hybrid PET/MRI (see **b**) combining CE-MRI, ^{18}F-FET PET and DKI — acquired in a single session in clinically practicable acquisition time — is demonstrated in recurrent glioma, which presents a mismatch between contrast enhancement and ^{18}F-FET-active tumour. As amino acid PET is known to provide more accurate information on the tumour extent compared to CE-MRI, we determined microstructural diffusion markers in metabolic compartments defined by ^{18}F-FET uptake in a combined and integrative PET/DKI approach. Haematoxylin and eosin (H&E) staining from the same patient confirms recurrence (magnification 400-fold). Patients with suspected cancer relapse that received concurrent PET/MRI between 2019 and 2021 were retrospectively investigated. BBB, blood–brain barrier; HGG, high-grade glioma

availability of hybrid PET/MRI systems and recommendations for the synergistic use of amino acid PET and MRI [18], there is urgent need for the development of neuroimaging techniques that integrate metabolic and microstructural data into biological determinants, characterising the heterogenous tumour environment (see Fig. 1, panel a), and, thereby, guide precision diagnostics and the non-invasive detection of cancer. Therefore, we established a methodology for combined and integrative multimodal PET/MRI analysis, targeting the microstructural characterization of the metabolically active tumour environment. Using metabolic imaging for the definition of ^{18}F-FET-active tumour margins (see Fig. 1, panel b), we investigated microstructural diffusion markers of distinct metabolic compartments and evaluated the diagnostic potential of this integrative PET/DKI approach for the detection of glioma relapse and IDH genotyping in a patient cohort previously treated for glioma.

Patients and methods

Study design and patients

In this retrospective clinical cohort study, consecutive patients with previously treated glioma, referred for PET/MRI due to suspected recurrence between 2019 and 2021, were investigated using concurrent multimodal O-(2-^{18}F-fluoroethyl)-L-tyrosine (FET) PET, CE-MRI and fast-DKI. Participants with newly diagnosed ^{18}F-FET-active lesions were included according to the eligibility criteria, as shown in Fig. 1, panel b. Neuropathological confirmation or follow-up in line with the Response Assessment in Neuro-Oncology (RANO) criteria [19] was used as reference. This study was conducted in accordance with the ethical standards of the institutional and national research committee and with the 1964 Helsinki Declaration and its later amendments. Approval from the institutional ethics board was obtained (EA2/019/23). Informed consent was obtained from all patients included in the study.

Neuropathological analysis

Glioma recurrence was classified according to the latest revision of the World Health Organization (WHO) classification of tumours of the CNS [20] (according to the molecular data available at that time point). Molecular characteristics of IDH mutation (IDH-MT/WT, IDH-mutant/wildtype), 1p/19q co-deletion (LOH1p/19q+, co-deleted, LOH1p/19q-, non-deleted), O6-methylguanine-DNA-methyltransferase promoter methylation (MGMT+, methylated, MGMT-, unmethylated) and alpha-thalassemia/mental retardation syndrome X-linked loss (ATRX+, deficient, ATRX-, retention) were determined from formalin-fixed paraffin-embedded tissue specimens during routine diagnostic procedures based on fluorescence in situ hybridisation, pyrosequencing, EPIC DNA methylation arrays or immunostaining. MGMT promoter methylation status was determined by pyrosequencing with an established cutoff value of $\geq 10\%$, differentiating methylated vs. unmethylated cases [21] or EPIC DNA methylation array. Molecular status was determined ex domo in one instance. An overview of the molecular stratification is available in Table 1 and in Appendix E1 (online), Table 1.

Imaging and pre-processing

Simultaneous PET/MR imaging was performed on a MAGNETOM Biograph mMR (Siemens Healthcare) [22]. Static PET and clinical high-field (3 T) MRI were acquired in list mode for up to 60 min after intravenous (i.v.) administration of ^{18}F-FET (M ± SD, 163 ± 23 MBq; standard-dose 180 MBq and individually calculated dose for body weight < 60 kg). Gadolinium-based contrast agent (Gadovist®, Bayer Pharma AG) was administered according to the patient's total body weight (0.1 mmol/kg). Fasting for at least 4 h before PET acquisition was recommended [23].

The MRI acquisition protocol included a transversal T1-weighted ultrashort echo time (UTE) for attenuation and scatter correction, a T2-weighted (TR/

Table 1 Summarised characteristics of the study cohort. *NA*, not applicable/available; *WHO*, World Health Organization; *IDH*, isocitrate dehydrogenase; *MGMT*, O6-methylguanine-DNA-methyltransferase; *ATRX*, alpha-thalassemia/mental retardation syndrome X-linked; *LOH1p/19q*, loss of heterozygosity (LOH) of 1p/19q

	Entire cohort	Recurrent glioma	Post-treatment-related changes
Participants (*n*)	59	39	20
Age (M ± SD in a)	48 ± 12	48 ± 12	48 ± 11
Gender (male/female)	29/30	19/20	10/10
WHO tumour classification (II°/III°/IV°)	7/24/28	0/16/23	7/8/5
LOH1p/19q (negative/positive/NA)	24/16/19	20/7/12	4/9/7
IDH mutation status (negative/positive/NA)	24/35/0	19/20/0	5/15/0
MGMT promoter methylation status (negative/positive/NA)	15/34/10	13/19/7	2/15/3
ATRX loss (negative/positive/NA)	38/17/4	25/11/3	13/6/1

TE = 5320/88 ms; matrix size = 230 × 230 × 230; voxel size = 0.4 × 0.4 × 3.0 mm^3), a post-contrast T1-weighted magnetization-prepared rapid gradient echo (TR/TE/TI = 2400/2.26/900 ms; flip angle = 8°; matrix size = 256 × 256 × 256; voxel size = 1.0 × 1.0 × 1.0 mm^3; thickness = 1 mm; slices = 192) and a rapid (approx. 3 min) DKI (TR/TE = 9200/111 ms; matrix size = 342 × 342 × 342; voxel size = 3.6 × 3.6 × 2.5 mm^3; thickness = 2.5 mm; slices = 50; diffusion scheme = bipolar; *b*-values = 0 s/mm^2, 1000 s/mm^2, 2500 s/mm^2; echo spacing = 0.68 ms; EPI factor = 96; bandwidth = 1578 Hz/Px) sequence with distinct diffusion encoding directions and a custom gradient table [17].

PET acquisition was reconstructed into transaxial slices using an iterative ordered subset expectation maximisation algorithm (OSEM, 3 iterations and 21 subsets; matrix size = 344 × 344 × 127; voxel size = 1.0 × 1.0 × 2.3 mm^3; gaussian filter = 3 mm). Emission data was corrected for decay, randoms, dead time, scatter and attenuation. Summed images over a time frame of 20 min p.i. were used for evaluation of PET.

Pre-processing of medical images included a denoising algorithm [24], Gibbs artefacts correction [25], eddy-currents correction and adjustment for patient motion using FMRIB's Software Library (FSL, v6.0.3) [26] and MRtrix (v3) [24, 26, 27] as well as bias-field correction using the N4 method [28]. Following these steps, medical images were visually inspected to ensure sufficient data quality prior to DKI calculation. Using the calculation methods for the 1–9-9 scheme introduced by Hansen et al [17], a robust mean kurtosis estimate (MKT), mean diffusivity (MD) and fractional anisotropy (FA) were computed using a generally available software in Matlab 2020a (Mathworks).

PET and MRI analysis

Quantitative analysis was performed using OsiriX MD 12 (Pixmeo SARL) using matched multimodal datasets. Where applicable, the most prominent lesion with greatest lesion size, ^{18}F-FET tracer uptake and contrast enhancement, closest to the resection cavity or primary tumour location was chosen as target lesion. Segmentation was performed using automated 3D iso-contouring based on ^{18}F-FET tracer uptake (J.L. and M.M., 6 and > 10 years of experience in MR imaging analysis), yielding a metabolically defined centre (80–100%, ROI80) and peripheral (60–75%, ROI60) 3D region-of-interest. In order to account for non-specific and regional uptake behaviour, mean and maximum target-to-background (TBRmean, TBRmax) ratios were determined from the standardized uptake value (SUV) measured in ROI80 and the mean background uptake in the unaffected contralateral hemisphere, which was determined using a 2D ROI with similar size (in the slice with highest mean uptake within the 3D ROI).

Where applicable, PET-derived ROIs were marginally adapted to avoid fluid compartments (e.g. resection cavities and macrocystic components) or large blood vessels in order to reflect solid tumour components. 3D ROIs were then transformed to DKI space using non-rigid deformation (ANTs, v2.3.4) [29]. Due to the distinct regional differences in non-Gaussian diffusion, MKT was normalised as a ratio between the mean diffusion signal from the lesion and the corresponding diffusion signal in the unaffected contralateral hemisphere. Quantitative analysis was performed for each scalar map (MD, MKT, FA) using both ROIs (ROI60, ROI80), yielding metrics for each metabolic compartment (MD60/MD80; rMKT60/rMKT80; FA60/FA80).

Statistics

Statistical analysis was performed using Prism v.9 (GraphPad Software) and MedCalc v20.104 (MedCalc Software Ltd). The Mann–Whitney *U* (two-tailed) tests (with Holm-Šídák's multiple-comparison test) were used for comparisons between two groups. The Wilcoxon signed-rank (two-tailed) test was used for matched pairs. Receiver operating characteristic (ROC) analysis was performed using the DeLong method reporting area under the curve (AUC), 95% confidence intervals (CI) and *p*-value. Sensitivity and specificity were reported for the best cutoff point independent from prevalence determined using Youden's index [30]. Logistic regression was used to model binary outcome. Measurements were correlated and evaluated using the Spearman correlation coefficient. *p*-value < 0.05 was considered statistically significant. M = Mean. SD = Standard deviation. SE = Standard error. Mdn = Median. IQR = Interquartile range.

Results

Patient cohort

In summary, 59 patients (29 men, 30 women; age, M ± SD, 48 a ± 12) were retrospectively identified. Recurrent HGGs (*n* = 39) were histopathologically validated upon neurosurgical intervention comprising 16 WHO grade 3 and 23 WHO grade 4 tumours. PTRE (*n* = 20) was confirmed by follow-up imaging with a median post-treatment surveillance of 21.50 months [IQR, 9.75 mo] or neuropathological reports (10%). Median time interval between last intervention scheme and PET/MRI examination was 30 months [IQR, 49 mo]. An overview of the molecular stratification is available in Table 1. Additional information is available in Appendix E1 (online), Table 1.

Table 2 Diagnostic measures from ^{18}F-FET PET and DKI. Among diffusion metrics, FA60 showed highest diagnostic power with similar diagnostic benefit to ^{18}F-FET PET. No difference in (SUV and MKT) background signal was apparent between both groups ($p > .05$). p-value < .05 was considered statistically significant. *ROC*, receiver operating characteristic; *AUC*, area under the curve; *DTI*, diffusion tensor imaging; *DKI*, diffusion kurtosis imaging

		Mann–Whitney *U* test	ROC analysis	
	Metric	Adjusted *p*-value, mean rank difference, MWU	*p*-value, AUC ± SE, 95% CI	Threshold, sensitivity/specificity
^{18}F-FET PET Target-to-background ratio	$TBRmean_{80}$ (TBRmean)	$p < .001$, 21.26, $U = 109$	$p < .001$, AUC = 0.86 ± 0.05, 95% CI = 0.75–0.94	> 1.73, 82%/85%
	$TBRmax_{80}$ (TBRmax)	$p < .001$, 21.10, $U = 111$	$p < .001$, AUC = 0.86 ± 0.05, 95% CI = 0.74–0.94	> 2.42, 69%/95%
Diffusivity	$MDmean_{80}$ (MD80)	$p = .034$, 11.19, $U = 242$	$p = .014$, AUC = 0.69 ± 0.08, 95% CI = 0.56–0.80	> 1.05, 97%/40%
	$MDmean_{60}$ (MD60)	$p < .001$, 17.25, $U = 162$	$p < .001$, AUC = 0.79 ± 0.07, 95% CI = 0.67–0.89	> 1.24, 77%/75%
Kurtosis	$rMKTmean_{80}$ (rMKT80)	$p = .008$, − 13.92, $U = 206$	$p < .001$, AUC = 0.74 ± 0.07, 95% CI = 0.60–0.84	≤ 0.78, 72%/90%
	$rMKTmean_{60}$ (rMKT60)	$p < .001$, − 17.93, $U = 153$	$p < .001$, AUC = 0.80 ± 0.07, 95% CI = 0.68–0.90	≤ 0.79, 77%/90%
Fract. anisotropy	FAmean80 (FA80)	$p = .003$, − 14.60, $U = 197$	$p < .001$, AUC = 0.75 ± 0.07, 95% CI = 0.62–0.85	≤ 0.21 74%/70%
	FAmean60 (FA60)	$p < .001$, − 21.48, $U = 106$	$p < .001$, AUC = 0.86 ± 0.05, 95% CI = 0.75–0.94	≤ 0.23, 74%/90%
Biparametric ^{18}F-FET PET/DKI	$TBRmax_{80}$ + $MDmean_{60}$	-	$p < .001$, AUC = 0.91 ± 0.04, 95% CI = 0.80–0.97	85%/85%
	$TBRmax_{80}$ + $rMKTmean_{60}$	-	$p < .001$, AUC = 0.92 ± 0.04, 95% CI = 0.82–0.98	90%/85%
	$TBRmax_{80}$ + $FAmean_{60}$	-	$p < .001$, AUC = 0.93 ± 0.04, 95% CI = 0.83–0.98	87%/90%

Evaluation of static ^{18}F-FET PET and DKI

Recurrent HGG demonstrated higher mean (TBRmean, Mdn, 2.41 [IQR, 1.15, $n = 39$] vs. 1.46 [IQR, 0.32, $n = 20$], $p < 0.001$, $U = 109$) and maximum (TBRmax, Mdn, 2.86 [IQR = 1.60, $n = 39$] vs. 1.72 [IQR, 0.46, $n = 20$], $p < 0.001$, $U = 111$) ^{18}F-FET tracer uptake compared to treatment effects, which presented reliable diagnostic performance (AUC ± SE, 0.86 ± 0.05, $p < 0.001$) for the differentiation between relapse and therapy-associated changes, as shown in Table 2 and Fig. 2, panel d. A difference in lesion volume between metabolic compartments was apparent (Mdn, 0.59 cm^3 [IQR, 0.68] (ROI80) vs. 2.38 cm^3 [IQR, 3.72] (ROI60), $p < 0.001$, $n = 59$, W = 1770), while there was no substantial difference ($p > 0.05$) between recurrent HGG and PTRE.

Quantitative diffusion metrics sampled from the metabolic periphery (see ROI60) presented greater distinction between diagnostic groups (see Table 2 and Fig. 2). Most notably, in the peripheral metabolic region, relapsing glioma presented higher MD (Mdn, 1.40 [IQR, 0.23, $n = 39$] vs. 1.12 [IQR, 0.29, $n = 20$], $p < 0.001$, $U = 162$), lower rMKT (Mdn, 0.736 [IQR, 0.100, $n = 39$] vs. 0.844 [IQR, 0.060, $n = 20$], $p < 0.001$, $U = 153$) and decreased FA (Mdn, 0.198 [IQR, 0.081, $n = 39$] vs. 0.292 [IQR, 0.087, $n = 20$], $p < 0.001$, $U = 106$) than PTRE, as exemplified in Figs. 3 and 4. On the opposite, neuropathologically described (radio-)necrosis (see Fig. 3, panel f and Fig. 4, panel a) demonstrated an inverse signal behaviour with an increase in rMKT and decreased MD. Interestingly, the study comprised a case of a highly proliferative glioblastoma distant to the primary

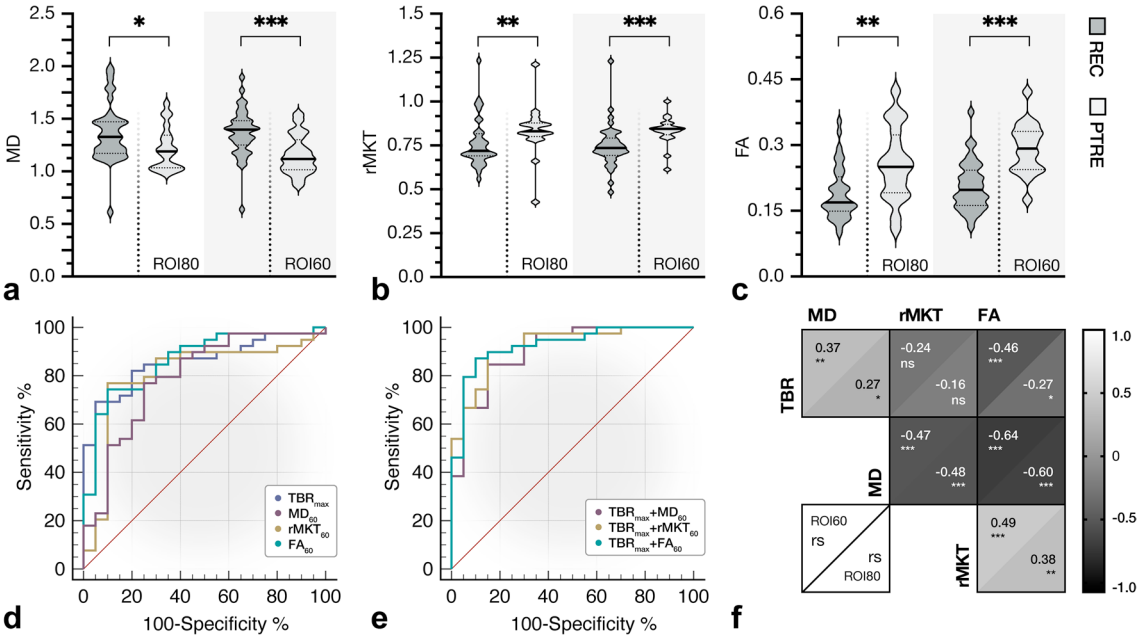

Fig. 2 Statistical analysis of ^{18}F-FET PET and DKI. Comparative statistics of diffusion metrics are shown in panels **a**–**c**. Compared to treatment-related changes, recurrence presented higher MD, lower rMKT and a decrease in FA. Receiver operating characteristic (ROC) analysis (**d** and **e**) demonstrated that TBRmax (AUC ± SE, 0.86 ± 0.05, $p < .001$) and FA60 (AUC ± SE, 0.86 ± 0.05, $p < .001$) showed the best performance in univariate analysis, while biparametric assessment of TBRmax + FA60 presented highest diagnostic performance (AUC ± SE, 0.93 ± 0.04, $p < .001$) with additional diagnostic benefit (difference in AUC ± SE, 0.069 ± 0.034, $p = .04$). **f** Correlative evaluation of ^{18}F-FET PET and DKI showed notable correlation of amino acid uptake with FA60 ($rs = -0.46$, $p < .001$) and MD60 ($rs = 0.37$, $p = .004$) within the peripheral metabolic compartment. Peripheral metabolic compartments presented slightly increased Spearman's correlation coefficients. p-value < .05 was considered statistically significant. (*) p-value < .05, (**) p-value < .01, (***) p-value < .001, (ns) non-significant

resection site, which presented diffusion restriction and an increase in rMKT, as shown in Fig. 3, panel e. No differences between PTRE with previously treated HGG and LGG (respectively $p > 0.05$) were observed.

Metabolic compartments showed disparate diagnostic performances, which was most pronounced for FA and MD (see Table 2). Among diffusion metrics, FA60 presented highest diagnostic power (AUC ± SE, 0.86 ± 0.05, $p < 0.001$), essentially yielding similar benefit to PET, while rMKT60 (AUC ± SE, 0.80 ± 0.07, $p < 0.001$) and MD60 (AUC ± SE, 0.79 ± 0.07, $p < 0.001$) presented moderate discriminative capability, as illustrated in Fig. 2, panel d. When DKI-derived metrics and ^{18}F-FET PET were evaluated in a multimodal biparametric approach (see Fig. 2, panel e), highest AUC was apparent for the clinically established TBRmax combined with FA60 (AUC ± SE, 0.93 ± 0.04, $p < 0.001$), which improved the diagnostic performance compared to PET alone (difference in AUC ± SE, 0.069 ± 0.034, $p = 0.04$).

Correlation of metabolic and diffusion metrics

The Spearman correlation coefficients showed a trend towards slightly increased correlation for metrics from the metabolic periphery. Notably, ^{18}F-FET uptake in the peripheral metabolic compartment was correlated with FA60 ($rs = -0.46$, $p < 0.001$) and MD60 ($rs = 0.37$, $p = 0.004$), as shown in Fig. 2, panel f. As expected, a moderate to strong association was apparent between (non-)Gaussian diffusion metrics.

IDH genotype and diffusion properties

IDH mutation was discriminated from wildtype both in the entire cohort (AUC ± SE, 0.78 ± 0.06, $p < 0.001$) and in a subgroup analysis of recurrent HGG (AUC ± SE, 0.74 ± 0.08, $p = 0.005$) at MD60 ≤ 1.29. In participants with PTRE, IDH mutation was distinguished likewise at lower MD60 (AUC ± SE, 0.83 ± 0.10, $p = 0.002$) and at higher FA60 (AUC ± SE, 0.84 ± 0.12, $p = 0.003$), suggesting less severe tissue damage in the post-treatment situation.

Discussion

We demonstrated that the detection of recurrent glioma benefits from a multimodal and integrative PET/DKI approach using diffusion microstructure markers of

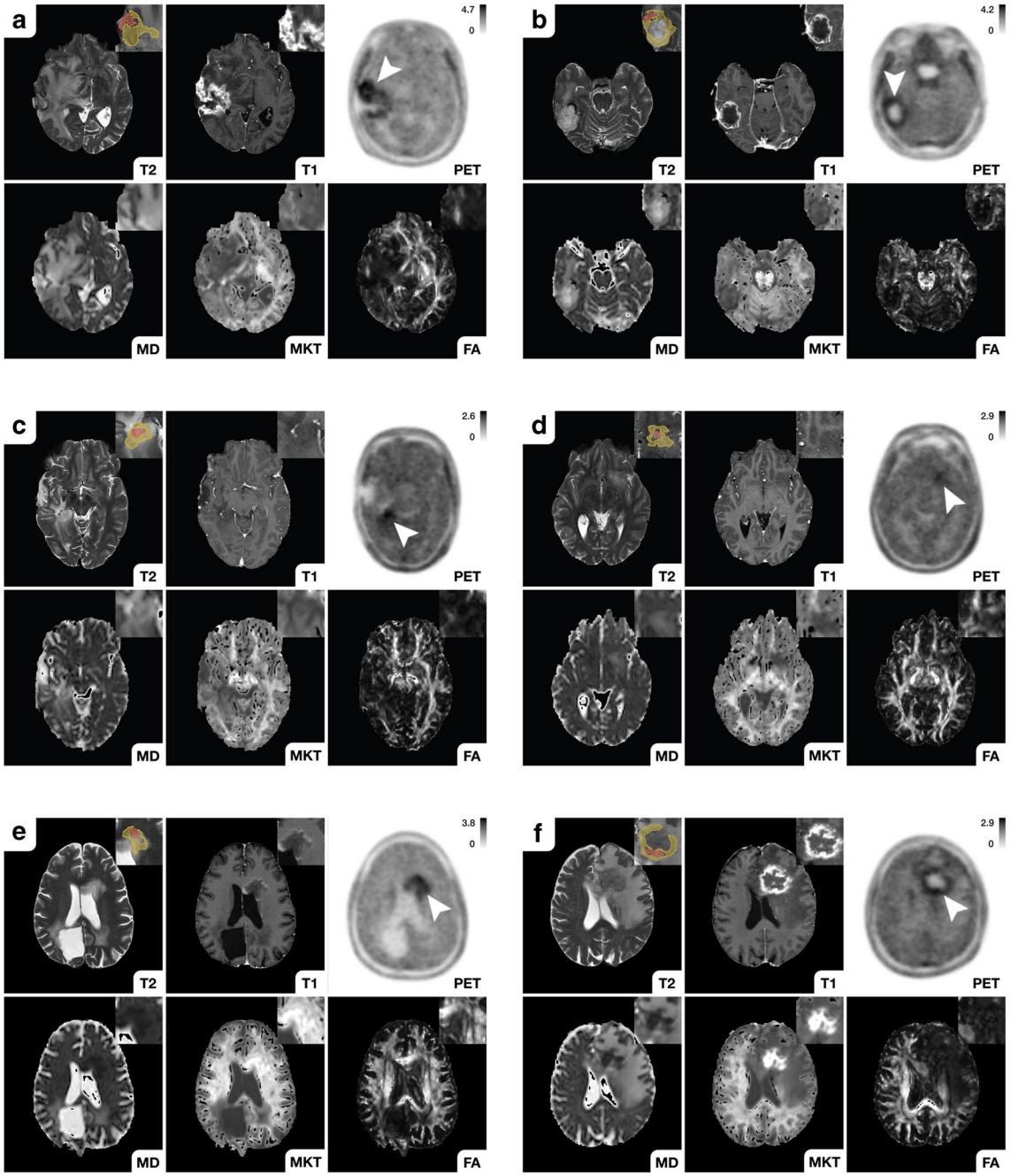

distinct compartments identified from metabolic imaging. We showed that glioma relapse elicits characteristic changes in diffusion properties that can be used to distinguish recurrence from treatment effects in previously treated glioma. Diffusion metrics determined from the metabolic periphery yielded biologically pertinent estimates characterising the tumour microenvironment, and, thereby, presented improved diagnostic performance for the differentiation between recurrent glioma and therapy-associated changes — most notably for FA, which showed similar diagnostic benefit to ^{18}F-FET PET. When ^{18}F-FET PET and DKI metrics were evaluated in a multimodal biparametric approach, this could be used to achieve improved diagnostic accuracy and an additional diagnostic benefit to the assessment based on PET alone.

(Non-)Gaussian diffusion metrics from DKI are highly sensitive to the tissue microstructure [31]. Low FA was apparent in recurrent HGG, suggesting compromised fibre integrity, such as in diffuse infiltration. When FA — as an index of the directional variation of diffusivity — is decreased, diffusion is almost equal in all directions, whereas an increase indicates that distinct directions show

◂**Fig. 3** Diffusion characteristics of recurrent glioma. Recurrent HGG typically presented an increase in MD as well as a decrease in rMKT and FA in both metabolic tumour compartments (see **a**–**d**). ^{18}F-FET-active lesions are indicated by the white arrow (first row, last column). Magnified insets are shown at the top right. Both metabolic compartments (ROI60, yellow; ROI80, red) are illustrated (the first row, first column). Panel **a** shows an extensive glioblastoma recurrence (CNS WHO grade 4, IDH-WT, MGMT+, ATRX-) with high ^{18}F-FET uptake (TBRmax, 3.5) and considerable gadolinium-based contrast enhancement. Histopathology revealed an astroglial tumour with mixed radiogenic, reactive and regressive changes. **b** Recurrent glioblastoma (CNS WHO grade 4, MGMT+, IDH-WT, ATRX-) surrounding the resection cavity. A surrounding rim (see peripheral metabolic compartment) with elevated tracer uptake (TBRmax, 3) and contrast enhancement, which was later shown to correspond to vital tumour cells mixed with radiogenic features and signs of diffuse haemorrhage. Diffusion metrics in this area presented high MD, decreased rMKT and low FA. **c** Localized ^{18}F-FET uptake (TBRmax, 2.5) corresponding to elevated MD and decreased rMKT that was confirmed to be a recurrent astrocytoma (CNS WHO grade 3, IDH-MT, MGMT-, ATRX+, LOH1p/19q-). In panel **d**, a small non-enhancing lesion with increased ^{18}F-FET uptake (TBRmax, 2.1) is demonstrated in a patient with multifocal recurrence. Lesion size and ^{18}F-FET uptake might be underestimated in PET due to partial volume effects. Diffusion metrics showed increased MD, low rMKT and FA, suggesting recurrence. Panels **e** and **f** exemplify less common clinical presentations of recurrent glioma with low MD and increased rMKT. A recurrent astrocytoma (CNS WHO grade 4, IDH-MT, MGMT+, ATRX+, LOH1p/19q-) distant to the primary resection site (see **e**) is illustrated with high ^{18}F-FET uptake (TBRmax, 4), low MD and elevated rMKT. Histopathology showed a glial tumour with high proliferation rate in the absence of necrotic features. High cellular (mutant) P-53 accumulation was reported, which is known to have an impact on the expression of various cancer-related genes, suggesting hindered diffusion also as a result of dysregulated protein synthesis. **f** Recurrent oligodendroglioma (CNS WHO grade 3, LOH1p/19q+, IDH-MT, ATRX-) close to the resection site (not shown in the axial slice) with extensive necrosis and a contrast-enhancing edge with elevated ^{18}F-FET tracer uptake (TBRmax, 2.8). The first biopsy revealed radionecrosis, but a second biopsy 6 months later confirmed recurrence with vital tumour cells, reactive/regressive CNS tissue and necrosis. Although a large fraction of the spherical mass presented elevated rMKT and low MD, diffusion metrics sampled from the metabolically active regions showed inverse signal behaviour with high MD and low rMKT, already suggesting cancer relapse at imaging prior to the first biopsy

faster diffusion (e.g. along intact fibre tracts). Due to a highly dysregulated amino acid metabolism in HGG [32] and a destructive infiltrative growth pattern with extensive neuroaxonal injury [33], FA60 demonstrated reliable diagnostic performance and a moderate negative correlation with ^{18}F-FET tracer uptake. Consistently, a previous study reported that decreased peritumoural FA in pre-surgical glioblastoma predicted later recurrence due to an underestimation of tumour extent based on structural CE-MRI [34]. Our findings suggest that the assessment of perifocal FA for the differentiation between relapse and treatment-related changes might be a viable option for follow-up imaging, particularly in circumstances where PET is unavailable, considering that DTI protocols are widely accessible and clinically used for DTI fibre tracking-based neuronavigation. Pre-operative and radiation planning may further benefit from the integration of diffusion microstructure markers, as there is potential to detect diffuse infiltration beyond the margins of contrast enhancement.

Recurrent HGG showed decreased rMKT, consistent with less diffusion compartmentalization as in microstructural damage and cellular loss. Our findings indicate a role for the identification of (radio-)necrosis, as we observed elevated rMKT in neuropathologically confirmed necrosis corresponding to microstructural complexity. Moreover, there was a case of a recurrent glioblastoma with high proliferation rate distant to the primary resection site — presumably less affected from previous treatment efforts — which demonstrated an atypical signal behaviour with increased rMKT, suggesting high cellularity with a more restrictive and compartmentalized diffusion environment.

We found increased MD in recurrence, which could indicate the presence of vasogenic oedema, altered vascularity or inflammatory changes. A restricted diffusion component, assumed to be caused by high cellularity in HGG, might be obfuscated by these concurrent pathophysiological effects in previously treated glioma. Considering that DKI is known to provide more accurate estimates of Gaussian diffusion metrics [35], the observed high variability of MD suggests that a directionally averaged diffusivity might be less robust for the diagnostic differentiation between recurrent HGG and PTRE.

With the recent revision of the World Health Organization (WHO) classification of tumours for the central nervous system [36], there has been considerable interest in molecular markers, which now play a central role for the integrated classification of CNS cancers. IDH mutation status, as an important clinical marker for molecular targeting and prognosis [37], was reflected in microstructural diffusion properties. Higher FA60 and lower MD60 distinguished IDH mutation in patients with previously treated gliomas, suggesting less radical microstructural tissue damage in the post-treatment situation, which could be a result of distinct therapeutic consequences or a less aggressive phenotype of IDH-mutated glioma.

While multiple studies have proposed to combine PET and advanced MRI to improve diagnostic accuracy for the diagnosis of true tumour progression [38–40], each modality is usually assessed in a separate manner and quantitative endpoints are ultimately combined. Here, we showed that there is a benefit in a combined and integrated methodology where microstructure markers were determined in metabolically active tumour compartments guided by ^{18}F-FET PET using 3D ROIs from automated iso-contouring — whereas most studies employ a sampling strategy based on manually drawn 2D ROIs within a contrast-enhancing lesion. In a recent retrospective study comprising 40 patients, Wu et al

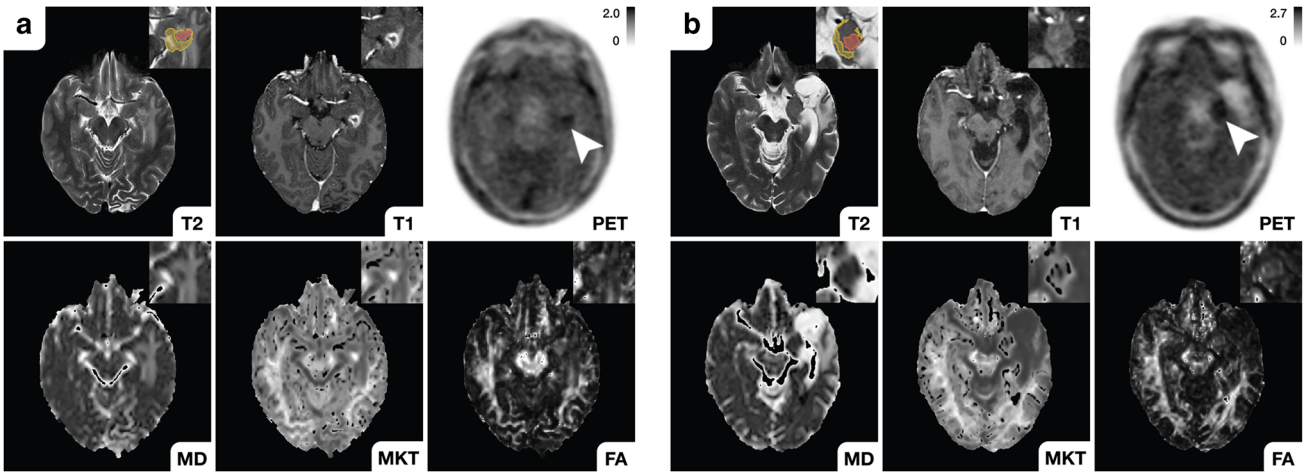

Fig. 4 Imaging of treatment-related changes. Clinical presentations of histopathologically confirmed PTRE are illustrated. ^{18}F-FET-active lesions are indicated by the white arrow (first row, last column). Magnified insets are shown at the top right. Both metabolic compartments (ROI60, yellow; ROI80, red) are illustrated (the first row, first column). First panel (**a**) shows a patient with a previously treated anaplastic pleomorphic xanthoastrocytoma (CNS WHO grade 3, LOH1p/19q-, IDH-WT, MGMT-, ATRX-), who presented with a new focal contrast-enhancing lesion with low ^{18}F-FET uptake (TBRmax, 1.7). Following primary resection, the patient received a combined therapy according to the Stupp's regimen. Upon first relapse, a second-line therapy was started with BRAF/MEK inhibitors and radiotherapy. The new lesion was histopathologically confirmed to be radionecrosis with moderate reactive tissue changes. Diffusion metrics showed increased rMKT and low MD, suggesting microstructural complexity. A patient with a progressive hippocampal lesion (see **b**) with low ^{18}F-FET tracer uptake (TBRmax, 1.6) is demonstrated, who was previously treated for an oligodendroglioma (CNS WHO grade 3, LOH1p/19q+, IDH-MT, ATRX-) with resection and concomitant radiochemotherapy (CCNU/PCV). Histopathology showed reactive CNS changes without malignancy or active inflammation. Diffusion characteristics were similar to the unaffected contralateral hemisphere indicating low microstructural disarray

[41] suggested in contrast to our findings that DKI metrics are superior to DTI metrics in differentiating HGG recurrence from pseudoprogression. However, small circular ROIs were manually drawn in contrast-enhancing lesions and perilesional oedema, which could be prone to sampling error or might result in measurements that are less representative and/or objective. Dang et al [42] retrospectively evaluated ^{11}C-MET PET and DKI in 86 glioblastoma patients with suspected recurrence after radiotherapy. ROIs were manually drawn in a single slice of a contrast-enhancing lesion, restricting the biological pertinence and generalisability of quantitative measurements in these heterogenous lesions. Consequently, mean rMD (AUC = 0.57) and rMK (AUC = 0.65) demonstrated limited diagnostic capability, although the kurtosis texture metrics (AUC = 0.76–0.79) facilitated slightly better differentiation between recurrence and radioinjury. Unfortunately, FA was not determined in this study. Furthermore, the study is limited by the absence of an appropriate multiple-comparison correction despite comparative analysis of a plethora of histogram features (translating into an increased risk for type 1 error and inflated statistical associations) and a short follow-up period (median 10.6 months). Nevertheless, there is a minor difference in sample size compared to the current study and metrics were evaluated in independent groups. Despite relevant differences with regard to the methodology and study population (acute vs. late post-treatment radiographic changes), the combined analysis of DKI and ^{11}C-MET PET presented an improved diagnostic accuracy (AUC = 0.95), further suggesting that multiparametric analysis might provide benefit to patients with glioma.

In opposition to conventional DKI, Q space imaging [43] or diffusion spectrum imaging [44], which respectively depend on lengthy and extensive imaging protocols, the fast-DKI variant proposed by Hansen et al [17] substantially shortens acquisition time and reduces data requirements, which enables the concurrent use in clinical hybrid PET/MRI protocols. While diffusion-weighted imaging (DWI) is still widely used for follow-up imaging and DTI is usually performed for preoperative imaging, the fast-DKI variant provides higher sensitivity towards alterations of the tissue microstructure with benefits for tumour grading [45] or the detection of relapsing cancer (this study) at the same or even shorter measurement time of clinically used diffusion protocols.

Limitations There were certain limitations due to retrospective data analysis. Because inconclusive CE-MRI usually results in referral for hybrid PET/MRI, a selection bias is possible. Recurrent HGG were retrospectively evaluated — therefore, data from this study may not apply to the detection of recurrent low-grade gliomas (LGG). Although the PTRE cohort comprised a small subset of

cases currently classified as LGG according to the 2021 WHO classification — previously categorised as HGG according to the 2016 WHO classification — we presume a low probability of false negative classifications, given the extended follow-up period. Furthermore, no differences between PTRE with previously treated HGG and LGG were apparent. Sample size is restricted; however, neuropathological validation of imaging was mostly available (70%) and patients were examined using same PET/MRI device assuring comparability and high spatiotemporal conformance. Nonetheless, further validation in independent cohorts with prospective study design is needed.

Direct comparison to the existing literature is difficult due to methodological differences (as discussed above). However, data from this study highlights the importance of sampling strategy, suggesting a benefit of the synergistic assessment of PET and MRI.

Because the current study's focus is the characterization of tumour microstructure using dMRI, other advanced MRI techniques, such as magnetic resonance spectroscopy (MRS) or perfusion weighted imaging (PWI), which allow insights into biochemical or perfusion alterations in CNS cancer, were not evaluated. Further studies should evaluate fractional kurtosis anisotropy [46], which was not calculated due to higher signal-to-noise (SNR) requirements [47]. MKT from the fast-DKI variant is known to be accurate and robust, but may present marginal differences to mean kurtosis (MK) computed using the traditional DKI framework [17]. Although DKI provides high sensitivity towards alterations of the tissue microstructure, diffusion metrics are not specific to the cancer pathology and need to be carefully interpreted in multimorbid patients.

Conclusion

Multimodal PET/MR imaging with combined and integrative analysis of ^{18}F-FET PET and DKI presents clinical benefit for the assessment of CNS cancer, particularly with regard to the detection of glioma relapse. Microstructure markers of the metabolic periphery yielded more biologically pertinent estimates, characterising the tumour microenvironment, and, thereby, presented improved diagnostic accuracy for the detection of relapsing glioma with similar accuracy to amino acid PET, while multimodal biparametric analysis presented an additional benefit to the assessment based on PET alone.

Supplementary information The online version contains supplementary material available at https://doi.org/10.1007/s00330-023-10141-0.

Funding Open Access funding enabled and organized by Projekt DEAL. This research project is funded by the "Deutsche Forschungsgemeinschaft" (DFG, German Research Foundation)—SFB 1340/1 2018, SFB1315 and SFB295RETUNE. The PET/MRI scanner is co-funded by the "Deutsche Forschungsgemeinschaft" (DFG, German Research Foundation)—INST 335/543–1 FUGG 2015.

Declarations

Guarantor The scientific guarantor of this publication is Prof. Marcus R. Makowski.

Conflict of interest The authors of this manuscript declare no relationships with any companies, whose products or services may be related to the subject matter of the article.

Statistics and biometry No complex statistical methods were necessary for this paper.

Informed consent Written informed consent was obtained from all subjects (patients) in this study.

Ethical approval Institutional Review Board approval was obtained.

Study subjects or cohorts overlap There is no subject overlap with previously published works.

Methodology
- retrospective
- diagnostic or prognostic study
- performed at one institution

References

1. van Solinge TS, Nieland L, Chiocca EA, Broekman MLD (2022) Advances in local therapy for glioblastoma - taking the fight to the tumour. Nat Rev Neurol 18:221–236. https://doi.org/10.1038/s41582-022-00621-0
2. Jung E, Osswald M, Ratliff M et al (2021) Tumor cell plasticity, heterogeneity, and resistance in crucial microenvironmental niches in glioma. Nat Commun 12:1014. https://doi.org/10.1038/s41467-021-21117-3
3. Gieryng A, Pszczolkowska D, Walentynowicz KA, Rajan WD, Kaminska B (2017) Immune microenvironment of gliomas. Lab Invest 97:498–518. https://doi.org/10.1038/labinvest.2017.19
4. Bonavia R, Inda MM, Cavenee WK, Furnari FB (2011) Heterogeneity maintenance in glioblastoma: a social network. Cancer Res 71:4055–4060. https://doi.org/10.1158/0008-5472.CAN-11-0153
5. Kristensen BW, Priesterbach-Ackley LP, Petersen JK, Wesseling P (2019) Molecular pathology of tumors of the central nervous system. Ann Oncol 30:1265–1278. https://doi.org/10.1093/annonc/mdz164

6. Osuka S, Van Meir EG (2017) Overcoming therapeutic resistance in glioblastoma: the way forward. J Clin Invest 127:415–426. https://doi.org/10.1172/JCI89587
7. Langen KJ, Galldiks N, Hattingen E, Shah NJ (2017) Advances in neuro-oncology imaging. Nat Rev Neurol 13:279–289. https://doi.org/10.1038/nrneurol.2017.44
8. Price SJ, Gillard JH (2011) Imaging biomarkers of brain tumour margin and tumour invasion. Br J Radiol 84(Spec No 2):S159-67. https://doi.org/10.1259/bjr/26838774
9. Galldiks N, Law I, Pope WB, Arbizu J, Langen KJ (2017) The use of amino acid PET and conventional MRI for monitoring of brain tumor therapy. Neuroimage Clin 13:386–394. https://doi.org/10.1016/j.nicl.2016.12.020
10. Kim MM, Parolia A, Dunphy MP, Venneti S (2016) Non-invasive metabolic imaging of brain tumours in the era of precision medicine. Nat Rev Clin Oncol 13:725–739. https://doi.org/10.1038/nrclinonc.2016.108
11. Brendle C, Maier C, Bender B et al (2022) Impact of ^{18}F-FET PET/MRI on clinical management of brain tumor patients. J Nucl Med 63:522–527. https://doi.org/10.2967/jnumed.121.262051
12. Maurer GD, Brucker DP, Stoffels G et al (2020) ^{18}F-FET PET Imaging in differentiating glioma progression from treatment-related changes: a single-center experience. J Nucl Med 61:505–511. https://doi.org/10.2967/jnumed.119.234757
13. Song S, Cheng Y, Ma J et al (2020) Simultaneous FET-PET and contrast-enhanced MRI based on hybrid PET/MR improves delineation of tumor spatial biodistribution in gliomas: a biopsy validation study. Eur J Nucl Med Mol Imaging 47:1458–1467. https://doi.org/10.1007/s00259-019-04656-2
14. Lohmann P, Stavrinou P, Lipke K et al (2019) FET PET reveals considerable spatial differences in tumour burden compared to conventional MRI in newly diagnosed glioblastoma. Eur J Nucl Med Mol Imaging 46:591–602. https://doi.org/10.1007/s00259-018-4188-8
15. Floeth FW, Sabel M, Ewelt C et al (2011) Comparison of (18) F-FET PET and 5-ALA fluorescence in cerebral gliomas. Eur J Nucl Med Mol Imaging 38:731–741. https://doi.org/10.1007/s00259-010-1690-z
16. Jensen JH, Helpern JA, Ramani A, Lu H, Kaczynski K (2005) Diffusional kurtosis imaging: the quantification of non-gaussian water diffusion by means of magnetic resonance imaging. Magn Reson Med 53:1432–1440. https://doi.org/10.1002/mrm.20508
17. Hansen B, Lund TE, Sangill R, Stubbe E, Finsterbusch J, Jespersen SN (2016) Experimental considerations for fast kurtosis imaging. Magn Reson Med 76:1455–1468. https://doi.org/10.1002/mrm.26055
18. Albert NL, Weller M, Suchorska B et al (2016) Response Assessment in Neuro-Oncology working group and European Association for Neuro-Oncology recommendations for the clinical use of PET imaging in gliomas. Neuro Oncol 18:1199–1208. https://doi.org/10.1093/neuonc/now058
19 Chukwueke UN, Wen PY (2019) Use of the Response Assessment in Neuro-Oncology (RANO) criteria in clinical trials and clinical practice. CNS Oncol 8:CNS28. https://doi.org/10.2217/cns-2018-0007
20. Louis DN, Perry A, Wesseling P et al (2021) The 2021 WHO Classification of Tumors of the Central Nervous System: a summary. Neuro Oncol 23:1231–1251. https://doi.org/10.1093/neuonc/noab106
21. Xie H, Tubbs R, Yang B (2015) Detection of MGMT promoter methylation in glioblastoma using pyrosequencing. Int J Clin Exp Pathol 8:1790–1796
22. Delso G, Furst S, Jakoby B et al (2011) Performance measurements of the Siemens mMR integrated whole-body PET/MR scanner. J Nucl Med 52:1914–1922. https://doi.org/10.2967/jnumed.111.092726
23. Law I, Albert NL, Arbizu J et al (2019) Joint EANM/EANO/RANO practice guidelines/SNMMI procedure standards for imaging of gliomas using PET with radiolabelled amino acids and [^{18}F]FDG: version 1.0. Eur J Nucl Med Mol Imaging 46:540–557. https://doi.org/10.1007/s00259-018-4207-9
24. Veraart J, Novikov DS, Christiaens D, Ades-Aron B, Sijbers J, Fieremans E (2016) Denoising of diffusion MRI using random matrix theory. Neuroimage 142:394–406. https://doi.org/10.1016/j.neuroimage.2016.08.016
25. Kellner E, Dhital B, Kiselev VG, Reisert M (2016) Gibbs-ringing artifact removal based on local subvoxel-shifts. Magn Reson Med 76:1574–1581. https://doi.org/10.1002/mrm.26054
26. Andersson JLR, Sotiropoulos SN (2016) An integrated approach to correction for off-resonance effects and subject movement in diffusion MR imaging. Neuroimage 125:1063–1078. https://doi.org/10.1016/j.neuroimage.2015.10.019
27. Tournier J-D, Smith R, Raffelt D et al (2019) MRtrix3: a fast, flexible and open software framework for medical image processing and visualisation. Neuroimage 202:116137. https://doi.org/10.1016/j.neuroimage.2019.116137
28. Tustison NJ, Avants BB, Cook PA et al (2010) N4ITK: improved N3 bias correction. IEEE Trans Med Imaging 29:1310–1320. https://doi.org/10.1109/TMI.2010.2046908
29. Avants BB, Epstein CL, Grossman M, Gee JC (2008) Symmetric diffeomorphic image registration with cross-correlation: evaluating automated labeling of elderly and neurodegenerative brain. Med Image Anal 12:26–41. https://doi.org/10.1016/j.media.2007.06.004
30. Youden WJ (1950) Index for rating diagnostic tests. Cancer 3:32–35. https://doi.org/10.1002/1097-0142(1950)3:1%3c32::aid-cncr2820030106%3e3.0.co;2-3
31. Alexander DC, Dyrby TB, Nilsson M, Zhang H (2019) Imaging brain microstructure with diffusion MRI: practicality and applications. NMR Biomed 32:e3841. https://doi.org/10.1002/nbm.3841
32. Bi J, Chowdhry S, Wu S, Zhang W, Masui K, Mischel PS (2020) Altered cellular metabolism in gliomas - an emerging landscape of actionable co-dependency targets. Nat Rev Cancer 20:57–70. https://doi.org/10.1038/s41568-019-0226-5
33. Claes A, Idema AJ, Wesseling P (2007) Diffuse glioma growth: a guerilla war. Acta Neuropathol 114:443–458. https://doi.org/10.1007/s00401-007-0293-7
34. Bette S, Huber T, Gempt J et al (2017) Local fractional anisotropy is reduced in areas with tumor recurrence in glioblastoma. Radiology 283:499–507. https://doi.org/10.1148/radiol.2016152832
35. Veraart J, Poot DH, Van Hecke W et al (2011) More accurate estimation of diffusion tensor parameters using diffusion kurtosis imaging. Magn Reson Med 65:138–145. https://doi.org/10.1002/mrm.22603
36. Louis DN, Perry A, Reifenberger G et al (2016) The 2016 World Health Organization Classification of Tumors of the Central Nervous System: a summary. Acta Neuropathol 131:803–820. https://doi.org/10.1007/s00401-016-1545-1
37. Pirozzi CJ, Yan H (2021) The implications of IDH mutations for cancer development and therapy. Nat Rev Clin Oncol 18:645–661. https://doi.org/10.1038/s41571-021-00521-0
38. Pyka T, Hiob D, Preibisch C et al (2018) Diagnosis of glioma recurrence using multiparametric dynamic 18F-fluoroethyl-tyrosine PET-MRI. Eur J Radiol 103:32–37. https://doi.org/10.1016/j.ejrad.2018.04.003
39. Steidl E, Langen KJ, Hmeidan SA et al (2021) Sequential implementation of DSC-MR perfusion and dynamic [^{18}F]FET PET allows efficient differentiation of glioma progression from treatment-related changes. Eur J Nucl Med Mol Imaging 48:1956–1965. https://doi.org/10.1007/s00259-020-05114-0

40. Werner JM, Stoffels G, Lichtenstein T et al (2019) Differentiation of treatment-related changes from tumour progression: a direct comparison between dynamic FET PET and ADC values obtained from DWI MRI. Eur J Nucl Med Mol Imaging 46:1889–1901. https://doi.org/10.1007/s00259-019-04384-7
41. Wu XF, Liang X, Wang XC et al (2021) Differentiating high-grade glioma recurrence from pseudoprogression: comparing diffusion kurtosis imaging and diffusion tensor imaging. Eur J Radiol 135:109445. https://doi.org/10.1016/j.ejrad.2020.109445
42. Dang H, Zhang J, Wang R et al (2022) Glioblastoma recurrence versus radiotherapy injury: combined model of diffusion kurtosis imaging and 11C-MET using PET/MRI may increase accuracy of differentiation. Clin Nucl Med 47:e428–e436. https://doi.org/10.1097/RLU.0000000000004167
43. Assaf Y, Mayk A, Cohen Y (2000) Displacement imaging of spinal cord using q-space diffusion-weighted MRI. Magn Reson Med 44:713–722. https://doi.org/10.1002/1522-2594(200011)44:5%3c713::aid-mrm9%3e3.0.co;2-6
44. Wedeen VJ, Hagmann P, Tseng WY, Reese TG, Weisskoff RM (2005) Mapping complex tissue architecture with diffusion spectrum magnetic resonance imaging. Magn Reson Med 54:1377–1386. https://doi.org/10.1002/mrm.20642
45. Bai Y, Lin Y, Tian J et al (2016) Grading of gliomas by using monoexponential, biexponential, and stretched exponential diffusion-weighted MR imaging and diffusion kurtosis MR imaging. Radiology 278:496–504. https://doi.org/10.1148/radiol.2015142173
46. Hansen B (2019) An introduction to kurtosis fractional anisotropy. AJNR Am J Neuroradiol 40:1638–1641. https://doi.org/10.3174/ajnr.A6235
47. Hansen B, Jespersen SN (2016) Kurtosis fractional anisotropy, its contrast and estimation by proxy. Sci Rep 6:23999. https://doi.org/10.1038/srep23999

2.5. Quantitative biparametrische Beurteilung von hybrider ^{18}F-FET PET/MRT zur Differenzierung von Gliomrezidiven und Behandlungseffekten (Originalarbeit 5)

> **Lohmeier J**, Bohner G, Siebert E, Brenner W, Hamm B, Makowski MR (2019) Quantitative biparametric analysis of hybrid 18 F-FET PET/MR-neuroimaging for differentiation between treatment response and recurrent glioma. Scientific Reports
> DOI: 10.1038/s41598-019-50182-4

Die *Originalarbeit 5* widmete sich ebenfalls der Unterscheidung zwischen wahrem Tumorprogress von Behandlungseffekten, (wie (Radio-)Nekrosen und/oder Inflammation) bei zuvor multimodal behandelten Gliomen mittels simultaner ^{18}F-FET PET/MRT. Anstatt einer visuellen und getrennten Bewertung von PET und MRT, wie es in der klinischen Routine oftmals gehandhabt wird, wurde in dieser Arbeit eine biparametrische Beurteilung anhand der ^{18}F-FET PET und eines klinisch etablierten, einfachen Diffusionsmodells (engl. „Diffusion-weighted imaging“, DWI) evaluiert.

In der vorliegenden retrospektiven Studie wurden anhand eines in der klinischen Routine etablierten ^{18}F-FET PET/MRT-Untersuchungsprotokolls insgesamt 42 PatientInnen (24 Männer, 18 Frauen; Durchschnittsalter, 47 ± 13 Jahre, M ± SD) hinsichtlich eines Rezidiv beurteilt. Unter den betrachteten Fällen waren 32 bestätigte Krankheitsrückfälle und 10 Fälle mit belegten Behandlungseffekten. Hierzu wurde ein automatisiertes und (semi-)quantitatives 3D-Analyseverfahren basierend auf der ^{18}F-FET Aufnahme implementiert. Dabei wurde unter konservativer Schwellenwertsetzung (80%) die ^{18}F-FET Aufnahme als "Standardized uptake value" (SUV) und "Target-to-Background Ratio" (TBR) gemessen und der "Apparent diffusion coefficient" (ADC-Wert) aus der Diffusionsbildgebung in metabolischen "Hotspots" ermittelt. Rezidive zeigten höhere mittlere ADC-Werte ($p = 0.003$) und maximale TBR-Werte ($p = 0.02$) als therapieinduzierte Veränderungen. Sowohl der mittlere ADC-Wert ($AUC = 0.82$, $p < 0.001$) als auch der maximale TBR-Wert ($AUC = 0.81$, $p < 0.001$) erlaubten eine zuverlässige diagnostische Differenzierung zwischen beiden Entitäten. Die höchste diagnostische Güte ($AUC \pm SE = 0.90 \pm 0.05$, $p < 0.001$) wurde jedoch durch die biparametrische Kombination beider Biomarker erreicht.

Aus *Originalarbeit 5* lässt sich ableiten, dass eine parametrische und multimodale Beurteilung von PET and MRT – unter Verwendung eines klinisch fest etablierten und weitverbreiteten DWI-Protokolls und ^{18}F-FET PET – einen klinischen Mehrwert bei der Unterscheidung zwischen Gliomrezidiven und Behandlungseffekten aufweist. *Originalarbeit 5* kann somit als wissenschaftliche Vorarbeit für *Originalarbeit 4* betrachtet werden.

SCIENTIFIC REPORTS
nature research

Corrected: Author Correction

OPEN

Quantitative biparametric analysis of hybrid ^{18}F-FET PET/MR-neuroimaging for differentiation between treatment response and recurrent glioma

Received: 8 January 2019
Accepted: 4 September 2019
Published online: 10 October 2019

Johannes Lohmeier[1], Georg Bohner[2], Eberhard Siebert[2], Winfried Brenner[3], Bernd Hamm[1] & Marcus R. Makowski[1]

We investigated the diagnostic potential of simultaneous ^{18}F-FET PET/MR-imaging for differentiation between recurrent glioma and post-treatment related effects (PTRE) using quantitative volumetric (3D-VOI) lesion analysis. In this retrospective study, a total of 42 patients including 32 patients with histologically proven glioma relapse and 10 patients with PTRE (histopathologic follow-up, n = 4, serial imaging follow-up, n = 6) were evaluated regarding recurrence. PET/MR-imaging was semi-automatically analysed based on FET tracer uptake using conservative SUV thresholding (isocontour 80%) with emphasis on the metabolically most active regions. Mean (relative) apparent diffusion coefficient (ADCmean, rADCmean), standardised-uptake-value (SUV) including target-to-background (TBR) ratio were determined. Glioma relapse presented higher ADCmean (MD ± SE, 284 ± 91, p = 0.003) and TBRmax (MD ± SE, 1.10 ± 0.45, p = 0.02) values than treatment-related changes. Both ADCmean (AUC ± SE = 0.82 ± 0.07, p-value < 0.001) and TBRmax (AUC ± SE = 0.81 ± 0.08, p-value < 0.001) achieved reliable diagnostic performance in differentiating glioma recurrence from PTRE. Bivariate analysis based on a combination of ADCmean and TBRmax demonstrated highest diagnostic accuracy (AUC ± SE = 0.90 ± 0.05, p-value < 0.001), improving clinical (false negative and false positive) classification. In conclusion, biparametric analysis using DWI and FET PET, both providing distinct information regarding the underlying pathophysiology, presented best diagnostic accuracy and clinical benefit in differentiating recurrent glioma from treatment-related changes.

Glioma recurrence after multimodal treatment with surgery and/or radio-/chemotherapy is still common. Early detection of relapse and immediate therapy play an important role in clinical follow-up. Neurosurgical biopsy is considered the current diagnostic standard, but it involves the hazards of invasive surgical intervention, such as neurological deficits, post-operative infection or intracranial haematoma. Thus, there is great interest in the development and application of non-invasive diagnostic approaches, potentially reducing the risk of severe side effects for patients as well as health care costs. Differentiation between recurrent glioma and post-treatment related effects (PTRE), such as pseudoprogression and radionecrosis, can be challenging as both share clinical symptoms and morphological imaging characteristics[1,2]. Therefore, as a clinical guideline, the Response Assessment in Neuro-Oncology (RANO) Working Group published criteria for response evaluation[3,4], taking more advanced imaging approaches into consideration, such as perfusion magnetic resonance imaging (pMRI), magnetic resonance spectroscopy (MRS), single-photon emission computed tomography (SPECT) or positron emission tomography (PET). Commonly, however, many of these alternative methods are not established in clinical routine due to their limited clinical availability and considerable complexity. In particular, the ^{18}F-labelled

[1]Charité Universitätsmedizin Berlin, Department of Radiology, Campus Charité Mitte (CCM), Charitéplatz 1, 10117, Berlin, Germany. [2]Charité Universitätsmedizin Berlin, Department of Neuroradiology, Campus Charité Mitte (CCM), Charitéplatz 1, 10117, Berlin, Germany. [3]Charité Universitätsmedizin Berlin, Department of Nuclear Medicine, Campus Virchow-Klinikum (CVK), Augustenburger Platz 1, 13353, Berlin, Germany. Correspondence and requests for materials should be addressed to J.L. (email: johannes.lohmeier@charite.de)

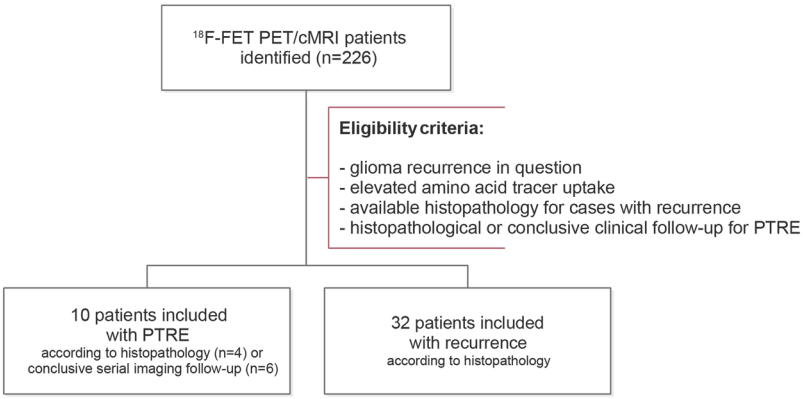

Figure 1. Flow diagram illustrating the study selection process. Between 2017 and 2018, we identified 226 patients, who received hybrid ^{18}F-FET PET/cMRI. According to the eligibility criteria, a total of 42 patients with glioma recurrence in question were included into our retrospective study.

non-natural amino acid ^{18}F-fluoroethyl-L-tyrosine (FET) emerged as a promising PET tracer candidate, targeting the tumour metabolism without relevant background signal, favourable half-life and efficient routine tracer production[5–7]. In contrast to long-established tracers in the field of neurooncology, such as ^{18}F-fludeoxyglucose (FDG) and ^{11}C-L-methionine (MET), FET was reported to exhibit relatively low uptake in inflammation[8,9]. In the last few years, several studies provided evidence that FET is a useful tracer for diagnosis of primary brain tumours, treatment planning and tumour grading[7].

In clinical routine, PET tracer uptake evaluation is either performed using qualitative visual assessment, which is subjective and dependent on clinical experience, or using semi-quantitative approaches based on standardised-uptake-value (SUV). Upon tumour segmentation using a 2D region-of-interest (2D-ROI), which is more common, or a 3D volume-of-interest (3D-VOI), which determines tracer uptake in a more robust manner[10], quantitative image-derived parameters can be computed from the respective delineation.

Prior to the adoption of hybrid PET/MR-imaging, sequential image acquisition with alignment during post-processing was standard practice. However, with the recent development of hybrid PET/MRI, simultaneous multimodal imaging was introduced, which combines the informative value of functional and structural MR-imaging as well as metabolic PET-imaging with the benefit of high spatial and temporal conformance and improved technical correction methods[11].

In the current study, we investigated whether differentiation between recurrent glioma and treatment-related changes could be improved by simultaneous PET/MR-imaging, including diffusion weighted imaging (DWI) and FET PET, using quantitative volumetric (3D-VOI) lesion analysis with emphasis on the metabolically most active regions.

Patients and Methods

Patient collective. Approval from the institutional ethics board (Charité University Hospital Berlin, Germany, EA1/175/18) was obtained. The study was performed in accordance with the principles of the Helsinki Declaration. In this retrospective study, a total of 42 consecutive patients (PTRE/recurrence, 10/32, female/male, 18/24, age (M ± SD), 47 ± 13 a, high-/low-grade glioma (HGG/LGG), 40/2, O6-methylguanine DNA methyltransferase (MGMT+/−) mutation, 22/14 (6 unknown), isocitrate dehydrogenase 1 (IDH1+/−) mutation, 21/18 (3 unknown), loss of heterozygosity on chromosomes 1p and 19q (LOH1p/19q+/−), 10/17 (15 unknown)) with hybrid FET PET/MR-imaging (Charité University Hospital Berlin, Germany, 2017–2018) were included, as shown in Fig. 1. According to the eligibility criteria, all patients with recurrent glioma presented available histopathology, while patients with PTRE either had follow-up with histopathology (n = 4) or conclusive serial imaging (n = 6, ≥ 4 MRI follow-up examinations) in accordance to the Response Assessment in Neuro-Oncology (RANO) criteria and the conclusion of an interdisciplinary board of clinical experts. Conventional clinical evaluation was derived from the final conclusion of the written imaging report. All patients gave written informed consent regarding the use of their data.

PET-MR Imaging protocols. Simultaneous FET PET/MRI acquisition was performed on MAGNETOM Biograph mMR (Siemens Healthcare, Erlangen, Germany; 3 T PET/MRI hybrid, 45 mT/m maximum gradient amplitude, 200 T/m/s maximum gradient slew rate, LSO crystal, 4.3 mm average spatial resolution at FWHM at 1 cm, 15.0 kcps/MBq sensitivity at center, 13.8 kcps/MBq sensitivity at radial offset of 10 cm[12]). After intravenous FET tracer injection (M ± SD, 163 ± 23 MBq; 180 MBq standard-dose for adults with body-weight ≥ 60 kg, individual dose is calculated according to a weight scale for body-weight < 60 kg) simultaneous FET PET/MRI acquisition was performed in list-mode for up to 60 minutes. Gadolinium (Gd) contrast administration was applied according to the patient's total body-weight.

PET/MRI examinations included, inter alia, a transversal T1-weighted ultrashort echo time (UTE) sequence for attenuation and scatter correction (TR/TE1/TE2 = 4.64/0.07/2.46 ms; flip-angle = 10°; matrix-size = 192 × 192 × 192; voxel-size = 1.6 × 1.6 × 1.6 mm), PET acquisition, DWI/ep2d-DIFF 3-scan trace (TR/TE = 10000/101 ms; matrix-size = 230 × 230 × 230; voxel-size = 1.2 × 1.2 × 3.0 mm; thickness = 3 mm; slices = 48;

apparent diffusion coefficient (ADC) map; diffusion-scheme = bipolar; diffusion-weighting = 2; b-values = 0 s/mm², 1000 s/mm²; echo-spacing = 1.08 ms; EPI-factor = 192; bandwidth = 1002 Hz/Px) and post-contrast T1/FL2D-TRA (TR/TE = 250/2.66 ms; flip-angle = 70°; matrix-size = 230 × 230 × 230; voxel-size = 0.7 × 0.7 × 5.0 mm; thickness = 5 mm; slices = 30). PET was sorted into a sinogram, which was reconstructed into transaxial slices using an iterative ordered-subset expectation maximisation algorithm (OSEM) with 3 iterations and 21 subsets (matrix-size = 344 × 344 × 127; voxel-size = 1.0 × 1.0 × 2.3 mm; zoom = 2; gaussian-filter = 3 mm). Emission data were corrected for decay, randoms, dead time, scatter and attenuation.

Volumetric image analysis. Image analysis was performed using OsiriX MD 10. Attenuation corrected PET was matched to the respective apparent diffusion coefficient (ADC) map. Using conservative SUV thresholding (isocontour 80%, IC80; threshold determined in a pilot experiment) with emphasis on the metabolically most active regions, a volume-of-interest (3D-VOI) was semi-automatically delineated based on attenuation-corrected PET. Mean background signal was computed from a contralateral 2D-ROI with similar size (unaffected brain tissue including grey and white matter) on a representative slice (slice with highest mean uptake within the 3D-VOI), as an adaptation of recommendations from the German guideline[13]. Where more than one lesion was apparent, the most prominent lesion (greatest lesion size, contrast-enhancement and PET tracer uptake, closest to the resection cavity or primary tumour location) was analysed.

Apparent diffusion coefficients (all reported values in 10^{-6} mm²/s) were determined using the same 3D-VOI based on high tracer uptake upon marginal adaptation to avoid overlap with resection cavity or cerebrospinal fluid space. Relative apparent diffusion coefficient (rADC) and target-to-background (TBR) ratio were calculated from standardised-uptake-value (SUVmean, SUVmax) or apparent diffusion coefficient (ADCmean) and the unaffected contralateral background signal (ratio of lesion signal and contralateral mean background signal).

Statistical analysis. Receiver Operating Characteristic (ROC) curves were computed with respective Area Under the Curve (AUC), p-value, sensitivity and specificity. Youden's index was determined to find the best cut-off point (independent from prevalence). ROC curves from univariate and bivariate analysis were compared for differences using a non-parametric approach. Biparametric analysis was performed in a step-wise approach (each parameter was evaluated separately, one parameter above threshold was classified as recurrence) using a binary model. Comparative analysis between recurrence (REC) and post-treatment-related (PTRE) groups were performed using independent samples t-tests (reported values show mean and standard error). p-value < 0.05 was considered statistically significant.

Results

Evaluation of DWI- and FET PET-derived imaging parameters. Recurrent glioma presented higher ADCmean (1313 (REC) vs. 1029 (PTRE), MD ± SE, 284 ± 91, p = 0.003), rADCmean (1.72 (REC) vs. 1.37 (PTRE), MD ± SE, 0.349 ± 0.125, p = 0.008), TBR80mean (2.75 (REC) vs. 1.80 (PTRE), MD ± SE, 0.95 ± 0.38, p = 0.02) and TBRmax (3.18 (REC) vs. 2.09 (PTRE), MD ± SE, 1.10 ± 0.45, p = 0.02) values than post-treatment related effects, as shown in Fig. 2.

Due to conservative SUV thresholding with emphasis on regions with highest metabolic activity, mean and maximum SUV demonstrated high positive correlation for both recurrent glioma (R = 0.999, 95%-CI = 0.997–0.999, p < 0.001) and post-treatment related effects (R = 0.999, 95%-CI = 0.999–1.000, p < 0.001) groups.

No statistically significant association was apparent for SUV (0.94 (REC) vs. 1.11 (PTRE), MD ± SE, −0.174 ± 0.107) or ADC (768 (REC) vs. 755 (PTRE), MD ± SE, 13 ± 29) contralateral background signals (see Fig. 2).

Diagnostic performance of DWI, FET PET and biparametric analysis. Mean apparent diffusion coefficient (AUC ± SE, 0.82 ± 0.07, p-value < 0.001, 95%-CI = 0.666–0.918) presented good diagnostic performance with an optimal cut-off at ADCmean > 1254 (62% sensitivity, 100% specificity), as shown in Fig. 3b and Table 1.

Maximum target-to-background ratio (AUC ± SE = 0.81 ± 0.08, p-value < 0.001, 95%-CI = 0.660–0.915) showed similar diagnostic performance (see Fig. 3a and Table 1) with 81% sensitivity and 60% specificity at the clinically established threshold TBRmax > 2.

ADCmean presented additional diagnostic value, when TBRmax was close to the clinically established threshold (TBRmax > 2), effectively improving clinical detection and decision-making, as demonstrated in Fig. 4. Few cases showed recurrent glioma, as suggested by increased TBRmax > 2, with considerably lower mean apparent diffusion coefficient (ADCmean < 900), suggesting diffusion restriction due to high tumour cellularity (see Fig. 5).

When both DWI- and FET-derived parameters were combined in biparametric approach, the highest accuracy (AUC ± SE = 0.90 ± 05, p-value < 0.001, 95%-CI = 0.768–0.971) was achieved (see Fig. 3c). Compared to conventional clinical assessment, as shown in Table 1, biparametric analysis with ADCmean > 1254 and TBRmax > 2 presented increased sensitivity (97% vs. 91%) and specificity (60% vs. 44%), improving clinical false negative (−6%) and false positive (−16%) classification. However, no statistically significant differences regarding diagnostic power were observed between bivariate analysis and univariate analysis with either TBRmax (difference in AUC ± SE = 0.09 ± 0.05, 95%-CI = −0.00702–0.185, p = 0.07) or ADCmean (difference in AUC ± SE = 0.08 ± 0.05; 95%-CI = −0.0197–0.188, p = 0.11).

Benefit of biparametric analysis compared to conventional clinical assessment is demonstrated in Fig. 6, indicating that either surgery could have been prevented or earlier detection could have been achieved. First row (see Fig. 6, panel α) demonstrates a patient with a treated WHO III° oligodendroglioma (MGMT+, IDH1+, LOH1p/19q+), originally classified as relapse. In concordance with histopathology, TBRmax (TBRmax = 1.82)

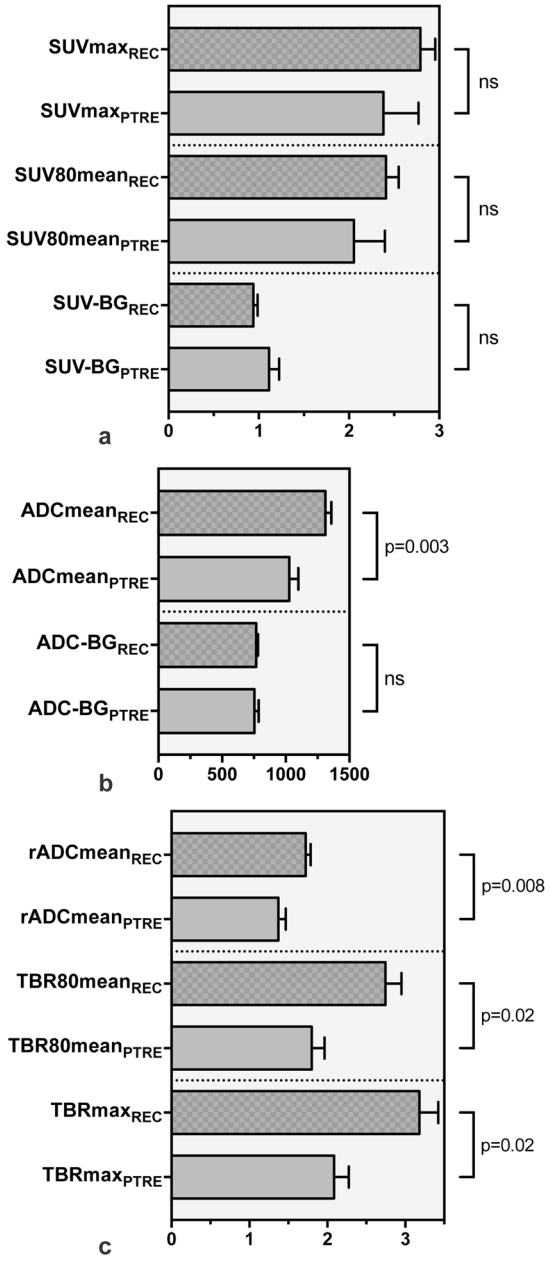

Figure 2. Bar graph diagrams comparing quantitative imaging parameters from FET PET and DWI between recurrent glioma (REC) and treatment-related effects (PTRE) groups. First panel (a) shows FET PET parameters (SUVmax, SUV80mean and SUV-BG). Second panel (b) demonstrates DWI parameters (ADCmean, ADC-BG) showing a statistically significant difference between recurrence and treatment-related changes with regard to ADCmean ($p = 0.003$). No significant differences between background values were apparent. Last panel shows relative imaging parameters for both modalities (rADCmean, TBRmax and TBR80mean). Statistically significant differences for rADCmean ($p = 0.008$), TBR80mean ($p = 0.02$) and TBRmax ($p = 0.02$) were found. Independent samples t-test, p-value < 0.05 was considered statistically significant. $M \pm SE$.

and ADCmean (ADCmean = 1133) indicated treatment-related changes. Second row (see Fig. 6, panel β) presents a patient with a WHO III° astrocytoma (MGMT+, IDH1+, LOH1p/19q−) with an ambiguous report concluding that no high-grade recurrence was detected. An MRI follow-up examination (after 4 months) gave rise to the suspicion of relapse, which was later histologically proven (5 months after hybrid PET/MRI). While TBRmax was close to the threshold (TBRmax = 1.99), ADCmean (ADCmean = 1757) suggested recurrent glioma. Third row (see Fig. 6, panel γ) shows recurrence of a WHO III° oligodendroglioma (MGMT−, IDH1−), originally categorised as treatment-related effect. Both TBRmax (TBRmax = 2.57) and ADCmean (ADCmean = 1815) suggested recurrence. A follow-up examination (after 3 months) suggested tumour progression (with midline shift), which was later histologically proven in surgery (4 months after hybrid PET/MRI). Fourth row (see Fig. 6, panel δ) presents a patient with WHO III° oligodendroglioma (MGMT−, IDH1+, LOH1p/19q+), which was classified

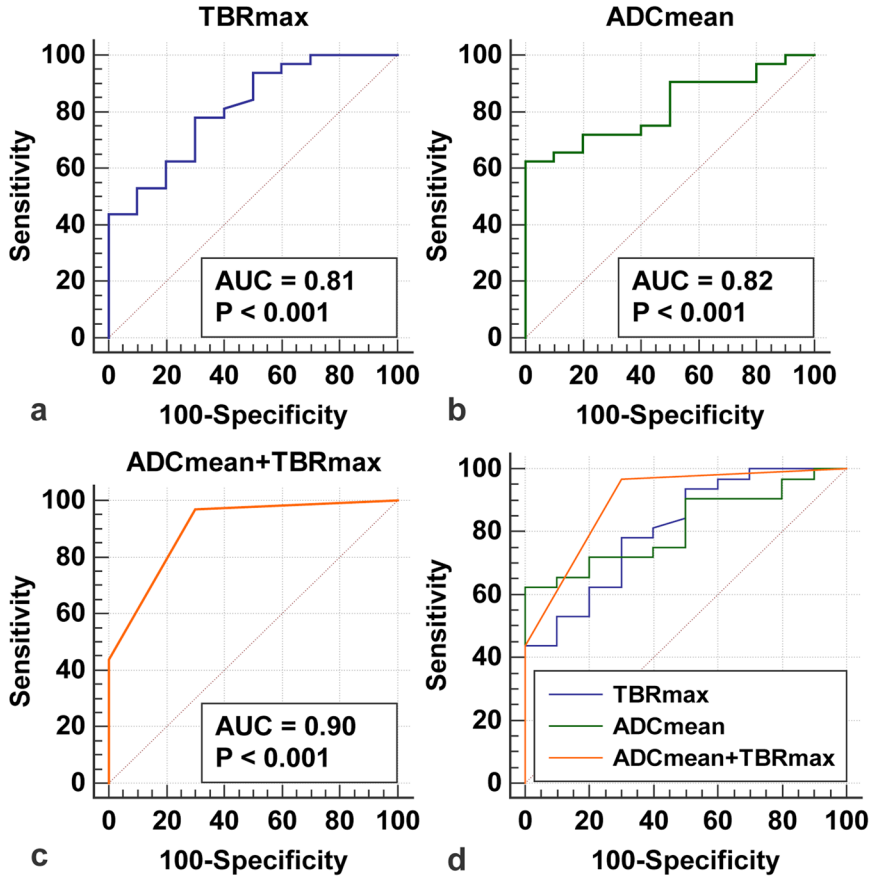

Figure 3. Receiver Operating Characteristic (ROC) analysis. ROC curves for TBRmax (**a**), ADCmean (**b**) and biparametric analysis of DWI- and FET PET-derived parameters (c, ADCmean and TBRmax) were illustrated. Biparametric analysis (**c**) presented highest AUC (Area Under the Curve). Last panel (d) shows a comparison between ROC curves. p-value < 0.05 was considered statistically significant.

	Sensitivity/ Specificity	Positive/negative predictive value	AUC
ADCmean + TBRmax	**97%/60%**	**71%/95%**	**0.90**
ADCmean > 1254	62%/100%	100%/72%	0.82
TBRmax > 2	81%/60%	67%/76%	0.81
Clinical rating	91%/44%	62%/83%	—

Table 1. Diagnostic measures of clinical assessment and quantitative PET/MRI analysis. Biparametric analysis using DWI- and FET PET-derived parameters presents improved diagnostic measures compared to clinical assessment.

as post-treatment related effect. While TBRmax was below the clinically established threshold (TBRmax = 1.73), ADCmean (ADCmean = 1362) indicated recurrence. Follow-up MRI examinations (after 3.5 and 6 months) suggested relapse with progressive contrast enhancement, which eventually led to surgery (7 months after hybrid PET/MRI) confirming recurrent glioma.

Discussion

In the current study, we demonstrated that the mean apparent diffusion coefficient (ADCmean) in the metabolically most active regions was higher in patients with recurrent glioma than in patients with post-treatment related effects. Both DWI and FET PET facilitated reliable differentiation between glioma recurrence and post-treatment related effects. Furthermore, we showed that mean apparent diffusion coefficient (ADCmean) was valuable, where maximum target-to-background (TBRmax) ratio remained inconclusive. Thus, highest accuracy (90%) was achieved when both DWI- and ^{18}F-FET-derived parameters were combined in a biparametric approach, which was superior to evaluating maximum target-to-background (TBRmax) ratio or mean apparent diffusion coefficient (ADCmean) alone. When compared to conventional clinical assessment, both false negative (−6%) and false positive (−16%) classification rates were improved by biparametric analysis, which results in earlier detection of recurrence or avoidance of surgery.

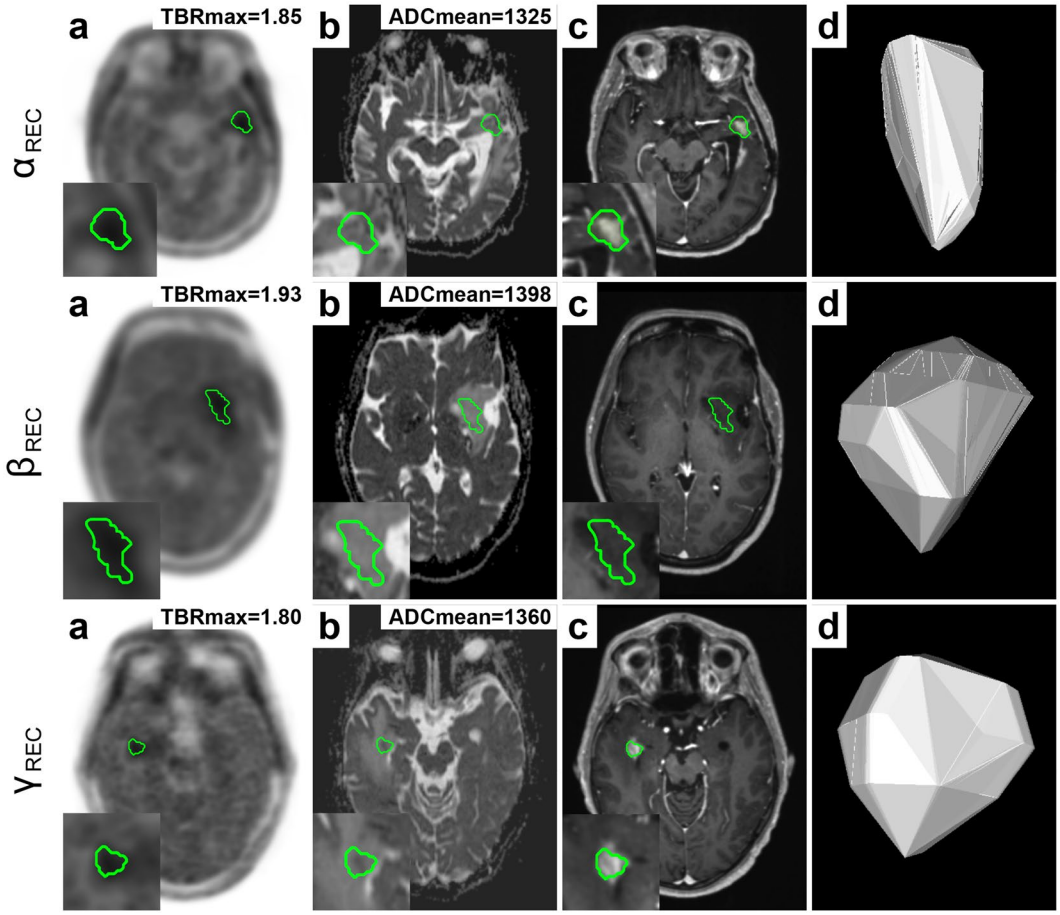

Figure 4. Additional value of diffusion weighted imaging (DWI) for differentiation between recurrent glioma (REC) and treatment-related effects (PTRE). Semi-automated delineation (IC80) of lesion VOI based on PET (**a**) was transferred to the respective ADC map (**b**). The following panels show post-contrast T1W (**c**) and a 3D lesion model (**d**) for illustration. Each row (α, β, γ) shows a patient with recurrent glioma. While TBRmax was at the border of the clinically established threshold (TBRmax > 2), ADCmean values were above threshold (ADCmean > 1254) suggesting recurrence.

While reports regarding the application of quantitative DWI-derived parameters for the differentiation between recurrence and treatment-related effects in glioma patients are inconsistent[2,7], our results showed that glioma relapse presents higher mean apparent diffusion coefficient (ADCmean) compared to treatment-related effects, presumably due to tumour necrosis in the centre of solid tumours. While this finding is in accordance with some earlier reports[14,15], a larger share of previous studies reported that treatment-related effects show higher apparent diffusion coefficient (ADC) values than recurrent glioma[2].

In these studies, the presumed mechanism for lower ADC values in glioma relapse is higher cellularity due to rapid cell proliferation, resulting in relatively impaired diffusivity. This observation is in accordance with individual cases in our study, showing recurrent glioma with lower ADC values (ADCmean < 900), likely reflecting high tumour cellularity in regions with high tracer uptake, which is in contrast to the larger share of patients in this study, presenting increased ADC in recurrent glioma. In a study by Berro *et al.*[16], no link was found between increased ^{18}F-fluoro-L-thymidine (FLT) uptake as a marker for cellular proliferation and decreased ADC in preoperative glioblastoma multiforme (GBM).

The current study expands knowledge on tumour metabolism and concurrent diffusivity, showing that the metabolically most active tumour sites, where glucose and amino acid uptake are known to be deregulated[17], present increased ADC values. We assume that the underlying mechanism for increased diffusivity in regions with high metabolic activity is tumour necrosis in close proximity to areas with high growth rates, where tumour cells eventually become hypoxic and glucose-depleted due to insufficient oxygen and nutrient supply, resulting in tumour cell death[17]. A similar finding was reported by Gadda *et al.*[14], which determined increased ADC values for high-grade glioma (HGG) in areas with lactate and lipid compounds as markers for necrosis and hypoxia using magnetic resonance spectroscopy (MRS) and conventional MRI. Discrepancies observed between studies are likely attributable to methodological and technical differences (e.g. manual lesion segmentation, delineation based on contrast-enhancement, perilesional measurements, or less representative 2D-ROIs) in contrast to the current study's rationale of measuring ADC values exclusively in regions with highest tracer uptake.

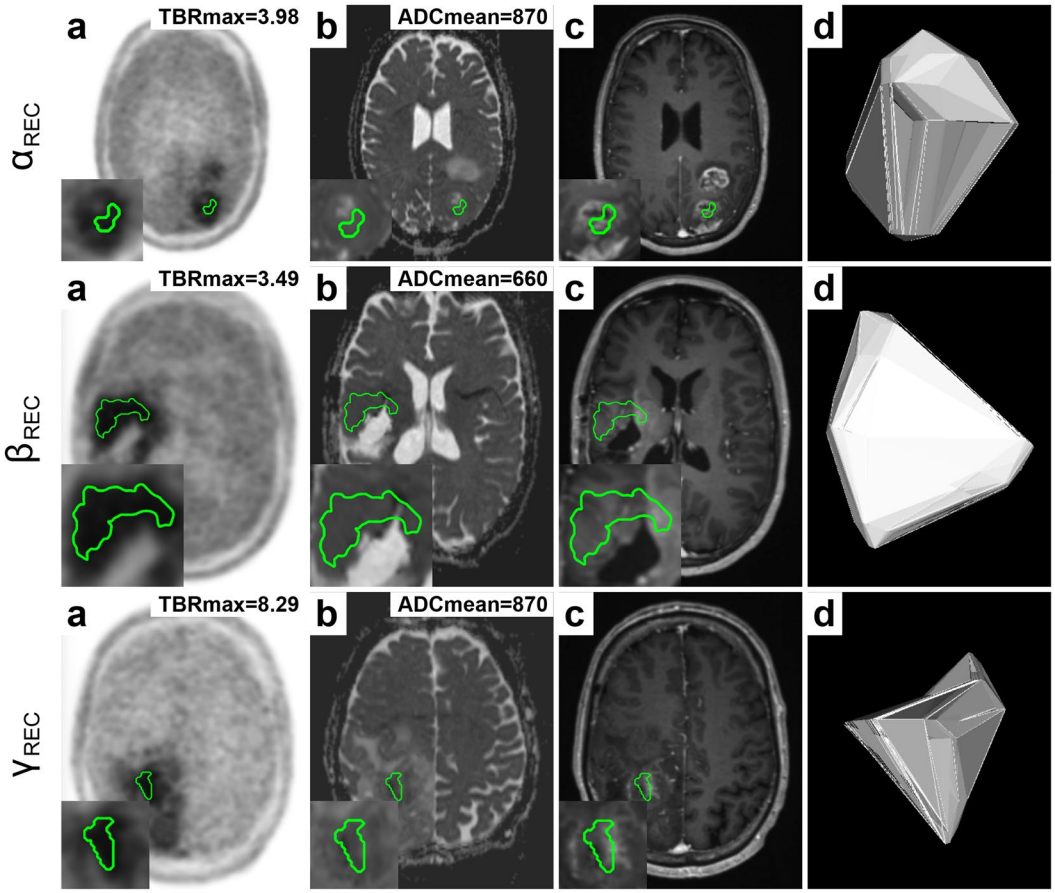

Figure 5. Glioma recurrence with restricted diffusion. Semi-automated delineation (IC80) of lesion VOI based on PET (**a**) was transferred to the respective ADC map (**b**). The following panels show post-contrast T1W (**c**) and a 3D lesion model (**d**) for illustration. Each row (α, β, γ) shows a patient with recurrence. While TBRmax is above the clinically established threshold (TBRmax > 2) suggesting recurrence, ADCmean shows lower readings (ADCmean < 900) indicating diffusion restriction due to high tumour cellularity.

While mean apparent diffusion coefficient (ADCmean) was elevated in most patients with recurrent glioma, few individual cases showed high diffusion restriction, therefore, suggesting that recurrence should also be considered at lower levels (ADCmean < 900) in regions with particularly high metabolic activity (TBRmax > 2). Moreover, our findings suggest that there is no direct benefit in computing the relative apparent diffusion coefficient (rADCmean) in contrast to the clinically established target-to-background (TBR) ratio for FET PET, which provided additional informative value.

An earlier study from Jena *et al.*[18] indicated that multiparametric imaging using a combination of FET PET, dynamic susceptibility contrast (DSC) and magnetic resonance spectroscopy (MRS) may achieve a maximum AUC of 0.94 based on logistic regression (n = 26, PTRE/recurrence, 7/19, histopathological/imaging follow-up, 9/17). However, lesions were manually delineated based on contrast enhancement and/or FET tracer uptake and no practical implementation of multiparametric assessment was provided.

To date, several methodological approaches for the discrimination between glioma relapse and treatment-related changes were proposed, such as the evaluation of structural criteria[2], qualitative assessment of T1-/T2-mismatch[19], defined as the contrast-enhanced lesion on a T1W image without matching lesion in a T2W image, or quantitative evaluation of the lesion quotient (LQ)[20], which is the ratio of lesion size in a T2W image and its corresponding size on a T1W image. However, in previous studies, some of these qualitative and semi-quantitative methods were shown to yield inconsistent results[21,22].

In recent years, it was shown that FET PET is a valuable imaging method for the diagnosis and staging of primary brain tumours and pre-therapeutic planning[7]. The current study demonstrated that simultaneous biparametric FET PET/MR-imaging is a useful diagnostic approach for the differentiation between recurrent glioma and treatment-related changes, which benefits from the integration and combination of structural, metabolic, and functional imaging as well as the high spatial and temporal conformance.

Limitations of the current study are a heterogeneous patient collective, restricted sample size, retrospective study design as well as semi-automated lesion segmentation. A comparison of the current study's results to the existing literature is limited due to the differences in methodology, as discussed above. Moreover, it should be taken into account that our findings might not apply to low malignant and slow-growing brain tumours, considering the predominance of high-grade glioma in this study. In contrast to manual delineation, which is

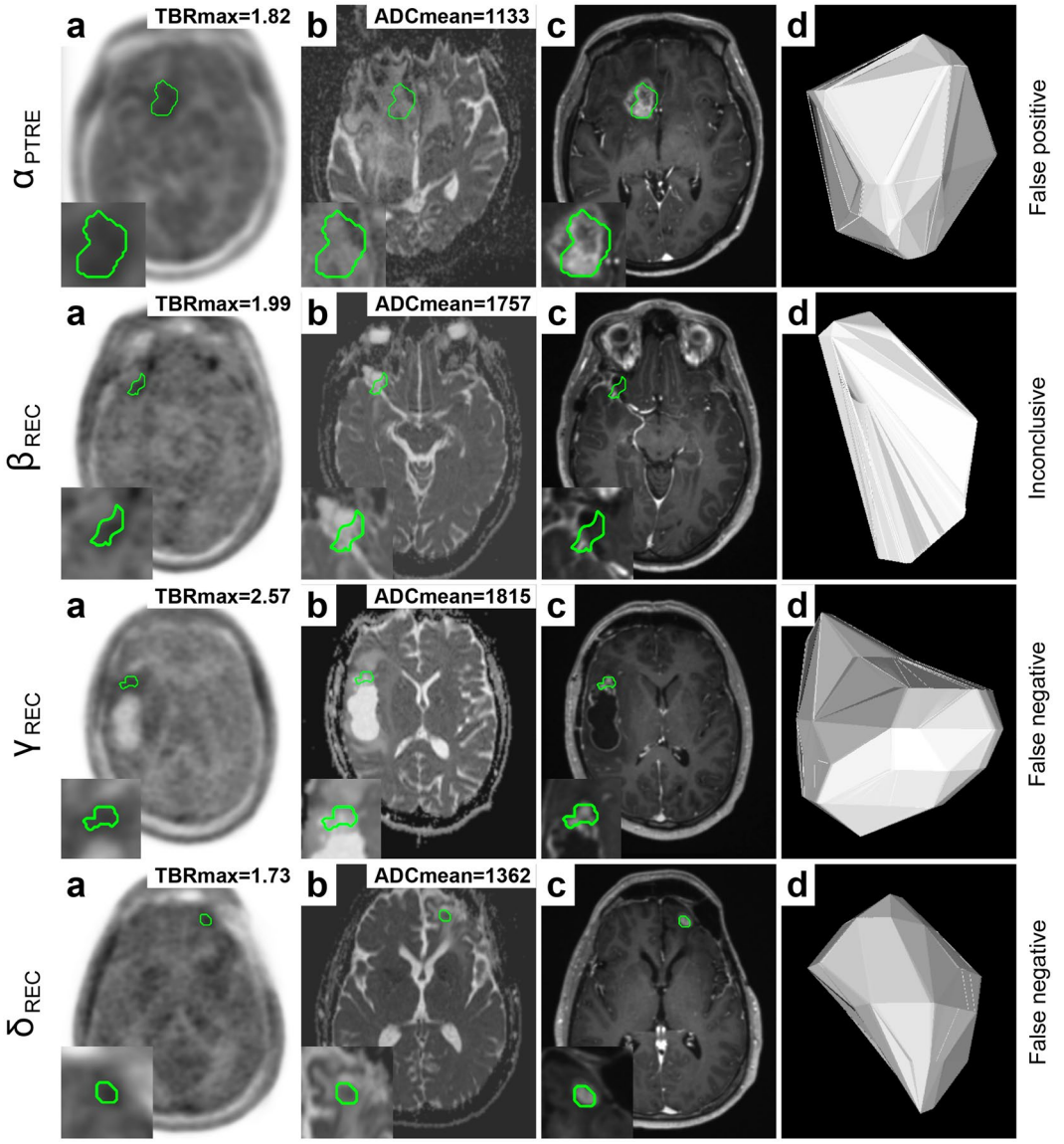

Figure 6. Benefit of biparametric analysis of DWI- and FET PET-derived parameters compared to conventional clinical evaluation. Semi-automated delineation (IC80) of lesion VOI based on PET (**a**) was transferred to the respective ADC map (**b**). The following panels show post-contrast T1W (**c**) and a 3D lesion model (**d**) for illustration. Labels on the most right show conventional clinical assessment. First row (α) shows a patient with PTRE, which was originally classified as glioma recurrence, which led to surgical intervention. Second row (β) shows a case with an inconclusive clinical evaluation, which was later shown to be glioma relapse. The following rows (γ, δ) present patients with relapse according to histopathology, originally classified as treatment-related changes. Clinical assessment would have benefitted from biparametric analysis using TBRmax (TBRmax > 2) and ADCmean (ADCmean > 1254), reducing clinical false positive and negative classification.

subject to intra- and inter-rater variation, semi-automated segmentation using isocontours, where thresholds commonly vary between 40–90%[23,24], presents a more objective and robust approach, despite not being (entirely) operator-independent. With regard to the mean apparent diffusion coefficient (ADCmean), where the threshold for differentiation was determined from the current patient collective, optimistic performance estimates are possible. Therefore, future studies should investigate and validate simultaneous bi- and multiparametric PET/MR-imaging in prospective multicentric trials. Further research should explore the potential of fully automated feature extraction and radiomics for identification of novel imaging biomarkers as well as radiogenomics for the exploration of correlations between imaging phenotypes and genomics.

In conclusion, biparametric analysis using DWI and FET PET in hybrid PET/MR-imaging, both providing distinct information regarding the underlying physiology, presented best diagnostic accuracy and clinical benefit in differentiating recurrent glioma from treatment-related effects.

Data Availability

Authors confirm that all relevant data are included in the article.

References

1. Parvez, K., Parvez, A. & Zadeh, G. The diagnosis and treatment of pseudoprogression, radiation necrosis and brain tumor recurrence. *Int J Mol Sci* **15**, 11832–11846 (2014).
2. Verma, N., Cowperthwaite, M. C., Burnett, M. G. & Markey, M. K. Differentiating tumor recurrence from treatment necrosis: a review of neuro-oncologic imaging strategies. *Neuro Oncol* **15**, 515–534 (2013).
3. Law, I. *et al*. Joint EANM/EANO/RANO practice guidelines/SNMMI procedure standards for imaging of gliomas using PET with radiolabelled amino acids and [(18)F]FDG: version 1.0. *Eur J Nucl Med Mol Imaging* **46**, 540–557 (2019).
4. Chukwueke, U. N. & Wen, P. Y. Use of the Response Assessment in Neuro-Oncology (RANO) criteria in clinical trials and clinical practice. *CNS Oncol* **8**, CNS28 (2019).
5. Hamacher, K. & Coenen, H. H. Efficient routine production of the 18F-labelled amino acid O-2-18F fluoroethyl-L-tyrosine. *Appl Radiat Isot* **57**, 853–856 (2002).
6. Heiss, P. *et al*. Investigation of transport mechanism and uptake kinetics of O-(2-[18F]fluoroethyl)-L-tyrosine *in vitro* and *in vivo*. *J Nucl Med* **40**, 1367–1373 (1999).
7. Muoio, B., Giovanella, L. & Treglia, G. Recent Developments of 18F-FET PET in Neuro-oncology. *Curr Med Chem* **25**, 3061–3073 (2018).
8. Hutterer, M. *et al*. [18F]-fluoro-ethyl-L-tyrosine PET: a valuable diagnostic tool in neuro-oncology, but not all that glitters is glioma. *Neuro Oncol* **15**, 341–351 (2013).
9. Kaim, A. H. *et al*. (18)F-FDG and (18)F-FET uptake in experimental soft tissue infection. *Eur J Nucl Med Mol Imaging* **29**, 648–654 (2002).
10. Soret, M., Bacharach, S. L. & Buvat, I. Partial-volume effect in PET tumor imaging. *J Nucl Med* **48**, 932–945 (2007).
11. Rosenkrantz, A. B. *et al*. Current Status of Hybrid PET/MRI in Oncologic Imaging. *AJR Am J Roentgenol* **206**, 162–172 (2016).
12. Delso, G. *et al*. Performance measurements of the Siemens mMR integrated whole-body PET/MR scanner. *J Nucl Med* **52**, 1914–1922 (2011).
13. Langen, K. J. *et al*. [German guidelines for brain tumour imaging by PET and SPECT using labelled amino acids]. *Nuklearmedizin* **50**, 167–173 (2011).
14. Gadda, D. *et al*. Relationship between Apparent Diffusion Coefficients and MR Spectroscopy Findings in High-Grade Gliomas. *J Neuroimaging* **27**, 128–134 (2017).
15. Sundgren, P. C. *et al*. Differentiation of recurrent brain tumor versus radiation injury using diffusion tensor imaging in patients with new contrast-enhancing lesions. *Magn Reson Imaging* **24**, 1131–1142 (2006).
16. Berro, D. H. *et al*. Comparison between MRI-derived ADC maps and ^{18}FLT-PET in pre-operative glioblastoma. *J Neuroradiol* (2019) (in press).
17. Lee, S. Y. *et al*. Regulation of Tumor Progression by Programmed Necrosis. *Oxid Med Cell Longev* **2018**, 3537471 (2018).
18. Jena, A. *et al*. Glioma Recurrence Versus Radiation Necrosis: Single-Session Multiparametric Approach Using Simultaneous O-(2-18F-Fluoroethyl)-L-Tyrosine PET/MRI. *Clin Nucl Med* **41**, e228–236 (2016).
19. Kano, H. *et al*. Differentiating radiation effect from tumor progression after stereotactic radiosurgery: T1/T2 matching. *Clin Neurosurg* **57**, 160–165 (2010).
20. Dequesada, I. M., Quisling, R. G., Yachnis, A. & Friedman, W. A. Can standard magnetic resonance imaging reliably distinguish recurrent tumor from radiation necrosis after radiosurgery for brain metastases? A radiographic-pathological study. *Neurosurgery* **63**, 898–904 (2008).
21. Stockham, A. L. *et al*. Conventional MRI does not reliably distinguish radiation necrosis from tumor recurrence after stereotactic radiosurgery. *J Neurooncol* **109**, 149–158 (2012).
22. Leeman, J. E. *et al*. Extent of perilesional edema differentiates radionecrosis from tumor recurrence following stereotactic radiosurgery for brain metastases. *Neuro Oncol* **15**, 1732–1738 (2013).
23. Popperl, G. *et al*. Value of O-(2-[18F]fluoroethyl)- L-tyrosine PET for the diagnosis of recurrent glioma. *Eur J Nucl Med Mol Imaging* **31**, 1464–1470 (2004).
24. Debus, C. *et al*. Impact of (18)F-FET PET on Target Volume Definition and Tumor Progression of Recurrent High Grade Glioma Treated with Carbon-Ion Radiotherapy. *Sci Rep* **8**, 7201 (2018).

Acknowledgements

We acknowledge support from the German Research Foundation (DFG) and the Open Access Publication Funds of Charité – Universitätsmedizin Berlin. This research project is partly funded by the "Deutsche Forschungsgemeinschaft" (DFG, German Research Foundation) - SFB 1340/1 2018. The PET/MRI scanner is co-funded by the "Deutsche Forschungsgemeinschaft" (DFG, German Research Foundation) - INST 335/543-1 FUGG 2015.

Author Contributions

J.L.: Conception and study design, data analysis, interpretation of data, writing of manuscript drafts, revising and approving final content of manuscript. G.B.: Study design, approving final content of manuscript. E.S., W.B. and B.H. Study design, critical revision, approving final content of manuscript. M.M.: Study design, supervision, critical revision, approving final content of manuscript. All authors critically revised the manuscript.

Additional Information

Competing Interests: The authors declare no competing interests.

Publisher's note Springer Nature remains neutral with regard to jurisdictional claims in published maps and institutional affiliations.

3. Diskussion

3.1. Neuromolekulare MRT-Bildgebung von Fibrin-Plaques

In *Originalarbeit 1* konnte erstmalig der Nachweis erbracht werden, dass proinflammatorische Fibrin-Plaques im ZNS mittels molekularer Bildgebung visualisiert werden können. Diese Fibrin-Ablagerungen können als nicht-invasiver Biomarker für immunentzündliche Prozesse und eine BHS-Störung quantifiziert werden. In einem in vitro-Experiment ließ sich belegen, dass die molekulare Sonde, EP2104-R, mit hoher Affinität und Spezifität an Fibrin (nicht jedoch Fibrinogen) bindet. Selbst bis zu 12 Stunden nach der Applikation von EP2104-R war eine spezifische Anreicherung der molekularen Sonde in einem etablierten Tiermodell für MS erkennbar. Durch den Einsatz eines nicht-signalgebenden Analogons konnte diese Kontrastverstärkung infolge konkurrierender Bindung aufgehoben werden. Im Rahmen der immunhistochemischen Aufarbeitung zeigte sich, dass diese Fibrin-Plaques einen deutlichen Zusammenhang mit einer Infiltration von Immunzellen aufwiesen und mit einer fokalen Demyelinisierung einhergingen. Ferner wurde gezeigt, dass das Ausmaß der Ablagerungen mit dem Krankheitsfortschritt zunimmt und mit dem Grad der physischen Beeinträchtigung assoziiert ist.

Eine Fehlfunktion der neurovaskulären Einheit ist ein zentraler und gemeinsamer Pathomechanismus verschiedener ZNS-Krankheiten [43]. Dies führt dazu, dass Plasmabestandteile – insbesondere Fibrinogen – die physiologische Barriere passieren. Oftmals ist dies mit einer Aktivierung des Komplementsystems verbunden und resultiert in der Bildung eines interstitiellen und perivaskulären Fibringeflechts. Vermittelt über (CD11b-CD18-) Integrin-Rezeptoren löst Fibrin dort eine immuninflammatorische Reaktion aus, einschließlich einer oxidativen Stressreaktion und Aktivierung von ortsständigen und peripheren Immunzellen, die signifikant zu neurodegenerativen und -entzündlichen Prozessen beitragen [43, 44, 72]. In einer kürzlich veröffentlichten Studie konnte gezeigt werden, dass dieser rezeptorvermittelte Signalweg eine Fibrin-abhängige neurotoxische Umprogrammierung von Mikroglia auslösen kann, die mit einer spezifischen Genhochregulation (unabhängig von Albumin oder C3) einhergeht, und dadurch neurodegenerative Prozesse begünstigt [44]. Durch den Einsatz therapeutischer Wirkstoffe (monoklonaler Antikörper und einem inhibitorischem Peptid), die die Interaktion von Fibrin

mit dem CD11b-Integrin-Rezeptor auf Mikroglia und Makrophagen blockieren [73, 74], konnte die Krankheitslast im EAE-Modell und 5XFAD (Alzheimer)-Modell reduziert werden. Da Fibrin-Plaques in akuten, chronischen und kortikalen Läsionen bei MS [43, 75–78] und Morbus Alzheimer [45, 79–84] aufgrund einer dysregulierten Koagulationskaskade oftmals fortbestehen, stellt die Fibrin-induzierte Dysregulation der angeborenen Immunität eine relevante Ursache für chronische Neuroinflammation und -degeneration dar. Eine Reihe von ZNS-Erkrankungen, wie MS und die Alzheimer-Krankheit, haben wiederkehrende (intermittierende) Störungen der BHS gemein, die durch die Entstehung von Fibrin-Plaques und einer nachfolgenden angeborenen Immunantwort gekennzeichnet sind. Dieser Mechanismus hat vermutlich auch immunpathologische Auswirkungen in Bezug auf hämorrhagische Schlaganfälle, traumatische Hirnverletzungen oder auch Neuro-COVID, wo endotheliale Schäden und parenchymatöse Fibrin-Ablagerungen in der Literatur beschrieben sind [85].
Gleichzeitig besteht in der medizinischen Versorgung und Forschung ein ungedeckter Bedarf an neuen Biomarkern, die entzündliche Prozesse abbilden und damit eine frühzeitige Diagnose oder Risikostratifizierung ermöglichen. In Zusammenschau mit der Literatur und den Ergebnissen aus *Originalarbeit 1* wurde letztlich ein neues Anwendungsgebiet für die molekulare Fibrin-Bildgebung erschlossen.

Gemäß *Originalarbeit 1* waren bei Gd-äquivalenter Dosis die Reduktion der longitudinalen Relaxationszeit und die SNR im direkten Vergleich höher als bei der Verwendung von Gadobutrol, einem unspezifischen und in der Klinik etablierten MRT-Kontrastmittel. Diese Eigenschaften sind sowohl auf eine spezifische Bindung als auch auf einen internen Rotationsmechanismus zurückzuführen [51, 86]. Aufgrund dieser vorteilhaften Eigenschaften eignet sich die molekulare Bildgebung, um beispielsweise floride Läsionen mit einem geringeren Grad an Schrankenstörung oder geringer Läsionsgröße darzustellen, die mit konventioneller MRT-Bildgebung maskiert bleiben würden. So wurde in verschiedenen Studien eine erhöhte Sensitivität für floride Läsionen nach Doppel- und/oder Dreifachdosierung von unspezifischen Gd-basierten Kontrastmitteln beschrieben [87, 88]. Vor dem Hintergrund neuerer Studien, die Gd-Ablagerungen bei wiederholten Kontrastmittel-Untersuchungen beschreiben [89], erscheinen exzessive Dosierungen von Kontrastmitteln derzeit fragwürdig. Durch die spezifische Anreicherung in Läsionen mit Fibringeflechten sowie günstigen Signalcharakteristika besteht daher erhebliches Potenzial, die klinische Detektionsrate von Läsionen zu verbessern. Dies gilt insbesondere für kortikale Läsionen mit

leptomeningealer Entzündung, die als relevante Ursache für kognitive und physische Einschränkungen bei MS identifiziert wurden [49, 90, 91], jedoch mit konventioneller MRT-Bildgebung i.d.R. deutlich unterschätzt werden. Unsere Ergebnisse legen nahe, dass die molekulare Bildgebung von zentralnervösen Fibrin-Plaques die klinische Beurteilung von leptomeningealer und kortikaler Entzündung verbessern kann – sofern noch ein gewisser Grad der Schrankenstörung vorliegt. Zudem besteht die Möglichkeit einer erheblichen Dosisreduktion. Darüber hinaus wurde eine Mn-basierte Variante von EP2104-R [50] sowie ein PET-Radiotracer [92] entwickelt, die das Risiko einer Ablagerung von Gd vollständig beseitigen würden.
In *Originalarbeit 1* wurde demonstriert, dass die Durchführung der molekularen MRT mit klinisch etablierten Hochfeld-MRT-Scannern und allgemein verfügbaren T1-gewichteten 3D-Sequenzen möglich ist. Unter Nutzung der MP2RAGE-Sequenz [93] war eine schnelle und robuste T1-Relaxometrie mit hoher räumlicher Auflösung möglich. Durch den Einsatz der T1-Relaxometrie vor und nach Kontrastmittelgabe, konnten quantitative Subtraktionskarten berechnet werden, die eine Änderung der longitudinalen Relaxationszeit (in Abhängigkeit der lokalen Konzentration der MRT-Sonde) widerspiegeln.

Die Ergebnisse aus *Originalarbeit 2* haben einen wichtigen Beitrag zur methodischen Implementierung von *Originalarbeit 1* geleistet. Die Notwendigkeit einer exakten Übereinstimmung der Datenpunkte bei einer dynamischen Kontrastmittel-Untersuchung, insbesondere wenn diese zu unterschiedlichen Zeitpunkten (i.e. 12 Stunden) akquiriert wurden, ist unabdingbar für eine robuste quantitative Datenauswertung. Eine vorangehende Segmentierung ermöglicht eine genauere Registrierung der Bilddaten und ist daher relevant, um eine hohe Übereinstimmung der Datenpunkte zu gewährleisten. Ohne diesen Schritt der Datennachverarbeitung können Varianzen (z.B. durch Bewegungen während der Untersuchung oder Unterschiede in der Lagerung zwischen den Untersuchungen) in den Bilddaten entstehen, und so die Reproduzierbarkeit und Reliabilität einer quantitativen Datenauswertung beeinträchtigen. In diesem Sinne hat die automatisierte Gehirnsegmentierung, einen maßgeblichen Beitrag zur methodischen Umsetzung von *Originalarbeit 1* geleistet.

Limitationen. Auch wenn Ergebnisse aus dem Tiermodell in der Regel nicht direkt auf den Menschen übertragen werden können, ist dem entgegenzusetzen, dass die beschriebene Fibrin-induzierte Pathologie nicht auf die murine EAE beschränkt ist, sondern einen

fundamentalen Pathomechanismus verschiedener ZNS-Erkrankungen mit neuroinflammatorischer Komponente darstellt. Eine Einschränkung besteht darin, dass die Verabreichung von Kontrastmitteln aufgrund der lang andauernden Bindung von Fibrin nicht randomisiert werden konnte. Daher wurde Gadobutrol stets 24 Stunden vor EP2104-R verabreicht, um eine vollständige Ausscheidung zu gewährleisten. Trotz des raschen Krankheitsverlaufs in dieser Modellerkrankung, erscheint eine Unterschätzung bei klinisch (i.e. gemäß EAE-Score) und radiologisch stabilem Krankheitsgipfel unwahrscheinlich. Bei der molekularen Bildgebung von Neuroinflammation könnte die Notwendigkeit einer Schrankenstörung in der Fibrin-Bildgebung zunächst als ein Nachteil wahrgenommen werden. Während lipophile niedermolekulare Substanzen (z.B. TSPO) die BHS leichter passieren, da die Membranen der BHS-bildenden Zellen aus Lipiden bestehen, bedürfen Kontrastmittel meist einer Dysfunktion dieser Barriere, um in das Interstitium gelangen zu können, oder eines (nicht-)invasiven Passage-Mechanismus (z.B. Nutzung von Transport-/Trägersystemen). Diese Bedingung ist eine relative Einschränkung bei neuroinflammatorischen Prozessen in Anbetracht episodischer bzw. intermittierender Schrankenstörung in diversen Erkrankungen. Aufgrund der grundsätzlich niedrigen räumlichen Auflösung der PET kann die Visualisierung von überwiegend kleinen inflammatorischen Läsionen hingegen eine beachtenswerte Limitation darstellen.

3.2. Quantitative PET/MRT-Bildgebung in der molekularen Neuroonkologie

Nicht-invasive IDH-Genotypisierung. Die Umprogrammierung des Tumorstoffwechsels durch Onkogene ist ein zentrales Konzept der Tumorbiologie und eine wichtige Überlebensstrategie von entarteten Zellen [94]. In Hirntumoren lässt sich häufig ein entgleister Stoffwechsel beobachten, darunter auch eine erhöhte Aufnahme von Aminosäuren, wie Tyrosin, Methionin, Glutamat und Aspartat. Durch die rasanten Entwicklungen der letzten Jahre bei der Decodierung der molekularen Grundlagen von Hirntumoren sowie einem Paradigmenwechsel zu molekularen Markern in der neuroonkologischen Diagnostik und Behandlung, existiert ein klinischer Bedarf nach nicht-invasiven Methoden zur Bestimmung von molekularen Veränderungen auf Basis von Biomarkern und deren Integration in die klinische Praxis [35]. Unter Nutzung der dysregulierten Stoffwechselprozesse ergibt sich die Möglichkeit, molekulare Marker indirekt mit metabolischen Bildgebungsverfahren zu verknüpfen. Mit dieser Grundüberlegung wurde in *Originalarbeit 3* ein nicht-invasiver Bildgebungsmarker entwickelt, der die metabolische Umprogrammierung von Gliomen charakterisiert, um Aussagen über deren molekularen Status treffen zu können. Dieser Biomarker wurde retrospektiv in einer Patientenkohorte mit behandlungsnaiven Gliomen mittels ^{18}F-FET PET/MRT evaluiert. Durch die Bestimmung der metabolischen Heterogenität konnte der IDH-Mutationsstatus in Gliomen mit hervorragender diagnostischer Genauigkeit bestimmt werden. Diese Ergebnisse von *Originalarbeit 3* belegen, dass auf Grundlage des veränderten Aminosäure-Stoffwechsels [95] in einem Bottom-up-Ansatz vom metabolischen Phänotyp auf den IDH-Genotyp geschlossen werden kann. Ein möglicher Erklärungsansatz hierfür ist die räumlich heterogene Genexpression in Gliomen – so zeigte beispielweise eine Arbeit von Yamashita et al. (2022) [96] eine differentielle Hochregulation der Tyrosinaminotransferase im Tumorkern im Kontrast zu dessen Peripherie. Interessanterweise wurden andere molekulare Marker, wie LOH1p/19q, MGMT-Promotor Methylierung und ATRX-Verlust, mit mäßiger diagnostischer Leistung differenziert, was vermutlich durch indirekte Assoziationen zu erklären ist. Obwohl IDH-mutierte Astrozytome und Oligodendrogliome sehr unterschiedliche Tumorentitäten darstellen, konnten beide unabhängig voneinander vom IDH-Wildtyp-Glioblastom beim gleichen Schwellenwert differenziert werden, was weiter darauf hindeutet, dass der Biomarker die metabolische Umprogrammierung in Abhängigkeit vom IDH-Genotyp widerspiegelt. Die diagnostische Güte des neuen Biomarkers war der relativen ^{18}F-FET Aufnahme (i.e. mittlerer TBR-Wert)

bei der Differenzierung des IDH-Genotyps deutlich überlegen. Das metabolische Tumorvolumen war zur Differenzierung des IDH-Genotyps ungeeignet.

Frühere Forschungsansätze konzentrierten sich überwiegend auf die direkte Messung von D-2-Hydroxyglutarat mittels MR-Spektroskopie [36, 97]. Um eine Unterscheidung des D-2-Hydroxyglutarat-Resonanzgipfels von den überlappenden Metaboliten-Resonanzpeaks, insbesondere Glutamin, Glutamat und N-Acetylaspartat (NAA), zu ermöglichen, bedarf es optimierter Protokolle und Techniken [98, 99]. Obwohl die Resultate der Spektroskopie mit einer gepoolten Sensitivität und Spezifität von 95% und 91% laut einer Metaanalyse von Suh et al. (2018) [100] vielversprechend erscheinen, hat eine klinische Translation aufgrund verschiedener Faktoren nicht stattgefunden, wie der Notwendigkeit einer komplexen Daten-Nachverarbeitung, eine hohe Anfälligkeit für Artefakte und Empfindlichkeit gegenüber Nekrosen [101], sowie weiteren methodenbedingten Nachteilen (z.B. relativ lange Messzeiten in Abhängigkeit von der Voxelgröße und SNR). Im Gegensatz zu aufwändigen und experimentellen Bildgebungstechniken, wie CEST [102], hyperpolarisierter ^{13}C-MRT [103] und Radiomics [104], deren klinische Implementierung herausfordernd ist, ermöglicht das in *Originalarbeit 3* etablierte Verfahren, eine robuste IDH-Klassifizierung basierend auf statischer ^{18}F-FET PET ohne die Notwendigkeit komplexer Analyseverfahren. Auch wenn bei IDH-mutierten, LOH1p/19q-negativen niedridgradigen Gliomen das sogenannte „T2/FLAIR-Mismatch“-Zeichen [105] beschrieben ist, wodurch sie mit hoher Spezifität (nahezu 100% Spezifität bei 42% Sensitivität) differenziert werden können, bleibt die Bewertung molekularer Veränderungen auf Basis der konventionellen MRT unzureichend. In *Originalarbeit 4* konnte gezeigt werden, dass der IDH-Genotyp auch in der posttherapeutischen Situation mittels Diffusionsmetriken differenziert werden kann. Dieses Ergebnis kann eine Folge des unterschiedlichen Behandlungskonzepts bei IDH-mutierten Gliomen sein und/oder für eine geringere (posttherapeutische) Architekturstörung bei (i.d.R. weniger aggressiven) IDH-mutierten Tumoren sprechen. Analog hierzu wurde in der Literatur auch in der präoperativen Situation ein Zusammenhang von Diffusionsmarkern und dem IDH-Genotyp beschrieben [106]. In dieser Hinsicht können erweiterte Diffusionsmodelle (z.B. als Kombination von DKI mit „Intravoxel incoherent motion (IVIM) imaging“) einen weiteren Mehrwert bei der nicht-invasiven IDH-Genotypisierung liefern.

Der IDH-Genotyp ist ein bedeutender Marker für molekulare Behandlungsstrategien, für die chirurgische Planung sowie individuelle Prognosen [66]. Bei der Erstdiagnose ist die

neuropathologische Diagnostik, einschließlich der genomischen Sequenzierung, die Methode der Wahl zur Bestimmung des IDH-Genotyps. Eine präoperative molekulare Stratifizierung kann mit Vorteilen einhergehen: Im Wissen über den IDH-Genotyp bietet sich die Möglichkeit, bei IDH-mutierten Gliomen gezielt eine supramaximale Resektion durchzuführen, die gemäß Literatur mit einem verbesserten Gesamtüberleben einhergeht [63–65]. In klinischen Szenarien, in denen nur begrenzt Gewebeproben asserviert werden können, wie bei MRT-gesteuerter Laserablation oder Laser-interstitieller Thermotherapie [107], kann eine bildgestützte molekulare Klassifizierung eine relevante Alternative darstellen. In Hinblick auf nicht-resektable Hirntumoren, wie bei Manifestationen in eloquenten Hirnarealen (z.B. Motorkortex oder Sehrinde), kann eine nicht-invasive präoperative Stratifizierung außerdem dabei unterstützten, alternative Behandlungsstrategien zu evaluieren. Zudem ermöglicht eine präoperative molekulare Stratifizierung neue personalisierte neoadjuvante (molekulare oder zytotoxische) Therapiestrategien – besonders da IDH-mutierte Tumoren eine erhöhte Vulnerabilität gegenüber reaktiven Sauerstoffspezies und Radiochemotherapeutika aufweisen [66]. Auch im Rahmen von derzeit evaluierten molekularen IDH-Targetingstrategien, wie Ivosidenib (Handelsname: Tibsovo®), ein oraler IDH1-Inhibitor, Endasidenib (Handelsname: Idhifa®), ein IDH2-Inhibitor, oder Vorasidenib, einem Inhibitor von IDH1- und IDH2-Mutationen, können diese Ergebnisse von Relevanz sein. Ferner befinden sich neuartige Impfstoffe in Untersuchung, die das IDH1-Neoepitop angreifen [108]. Während die neuropathologische Diagnostik nur Aussagen über die jeweiligen eingesandten Gewebeschnitte ermöglicht, können bildgestützte Biomarker auch für eine longitudinale Bildgebung und zur Kontrolle von Therapieansprechen nach molekularem IDH-Targeting eingesetzt werden.

Detektion von Rezidiv-Gliomen. Nach operativen Eingriffen und dem Einsatz von zytotoxischen, strahlentherapeutischen und antiangiogenen Therapien kommt es zu zahlreichen Veränderungen im Tumorgewebe und dessen Mikroumgebung. Früh und spät auftretende posttherapeutische Veränderungen sind eine klinische Herausforderung bei der nicht-invasiven Erkennung von Gliomrezidiven. Es handelt sich dabei um therapieinduzierte Veränderungen, wie Nekrose und Entzündung, die in konventionellen MRTs ein Rezidiv vortäuschen können. Metabolische Veränderungen im Tumorgewebe können genutzt werden, um ein Rezidiv von Behandlungseffekten zu unterscheiden. So konnten in *Originalarbeit 4 und 5* gezeigt werden, dass die metabolische PET-Bildgebung mit radiomarkierten Aminosäuren hilfreich sein kann, posttherapeutische Veränderungen von einer echten Krankheitsprogression zu differenzieren. Diese Ergebnisse konnten in einer Metaanalyse bestätigt werden [109], in der eine gepoolte Sensitivität und Spezifität von 88% und 78% berechnet wurde. Jedoch können Behandlungsveränderungen im Tumorbett nach operativen Eingriffen, Immuntherapie, Strahlen- und/oder Chemotherapie zu einer reaktiv erhöhten Aminosäure-Aufnahme führen, die eine zuverlässige Unterscheidung von einem Tumorrezidiv einschränken. Während falsch positive Diagnosen oft zu unnötigen zusätzlichen chirurgischen Eingriffen und den damit verbundenen perioperativen Risiken führen, bedeuten falsch negative Befunde eine unbehandelte Tumorprogression. Mit dem Aufkommen der hybriden PET/MRT bietet die Beurteilung mehrerer Biomarker aus beiden Modalitäten die Möglichkeit, besser zwischen diesen Entitäten unterscheiden zu können und damit die diagnostische Genauigkeit zu steigern. Da die Differenzierung zwischen Gliomrezidiven und benignen posttherapeutischen Veränderungen weiterhin eine Herausforderung darstellt, besteht ein dringender klinischer Bedarf an bildgestützten Techniken, die metabolische und mikrostrukturelle Daten in biologische Determinanten integrieren und eine nicht-invasive Früherkennung von Rezidiven sowie eine Abgrenzung zu Behandlungseffekten zulassen.

In *Originalarbeit 3 und 4* wurde dieses diagnostischen Dilemma behandelt, um eine zuverlässigere Unterscheidung durch die kombinierte und integrative Analyse von PET und Diffusionsbildgebung zu erreichen. Durch die Fortschritte in bildgebenden Verfahren ist es heute möglich, Informationen über biophysikalische Gewebeeigenschaften auf der Makroskala (cm/mm) zu erheben und mittels bioinformatischer Modelle entsprechende Rückschlüsse auf die Mesoskala bis Mikroskala zu ziehen. Unter diesem Gesichtspunkt kann die Diffusionsbildgebung, die Bewegungseigenschaften von Wasserprotonen im Gewebe erfasst, einen indirekten Einblick in die Gewebearchitektur bieten. Während im klinischen Kontext meist einfache Diffusions-gewichtete Sequenzen mit zwei b-Werten (zwischen 0 und

1000 s/mm^2) verwendet werden, sind in der neurowissenschaftlichen und -onkologischen Forschung fortschrittlichere Diffusionsmodelle etabliert. Unter Berücksichtigung eines komplexeren Diffusionsprofils, ermöglicht das DKI eine noch höhere mikrostrukturelle Sensitivität gegenüber Veränderungen der Gewebearchitektur als konventionelle Diffusionsmodelle [67]. Allerdings haben zeitaufwändige Untersuchungsprotokolle sowie rechenintensive Datenverarbeitungen und -auswertungen die weitere klinische Evaluation der DKI ausgebremst. Daher haben Hansen et al. (2016) [69] eine neue Variante der DKI entwickelt und validiert, die die nicht Gauß-verteilte Diffusion aus nur 19 diffusionsgewichteten Bilddaten in einem Bruchteil der sonst üblichen Messzeit berechnen kann. Durch diese technische Innovation ist die "fast-DKI" nun auch für den Einsatz in der routinemäßigen diagnostischen Bildgebung geeignet, insbesondere wenn lang andauernde Messungen nicht durchführbar sind. Dies betrifft auch die hybride PET/MRT-Bildgebung, bei der ein Zerfall von Radionukliden langwierige Messungen ausschließt. Schnelle Untersuchungsprotokolle, wie die in *Originalarbeit 4* eingesetzte beschleunigte DKI, bieten bei vergleichbarer Untersuchungszeit zur DWI (ca. 3 min) sowohl eine höhere Sensitivität als auch einen informationellen Mehrwert.

In *Originalarbeit 4* wurde eine Methodik für eine kombinierte und integrative multimodale Analyse von ^{18}F-FET PET/fast-DKI entwickelt, die eine mikrostrukturelle Charakterisierung der metabolisch aktiven Tumorumgebung ermöglicht. Es konnte gezeigt werden, dass die Anwendung von PET und DKI, bei der Erkennung von Gliomrezidiven von Nutzen sein kann. Durch die Untersuchung mikrostruktureller Diffusionsmarker, die sich im Zusammenhang mit einem Rezidiv oder reaktiver (inflammatorischer) Gewebeanpassungen verändern, konnte die diagnostische Unterscheidung zwischen echter Tumorprogression und therapiebedingten Veränderungen verbessert werden. Unter den Diffusionsmetriken erwies sich die FA als besonders aussagekräftig und erzielte bei uniparametrischer Betrachtung eine ähnliche diagnostische Leistung wie die ^{18}F-FET PET. Ein geringer FA-Wert, wie bei Rezidiven beobachtet, weist auf eine Beeinträchtigung der Faserintegrität hin, während ein hoher Wert auf eine gerichtete Diffusion schließen lässt. In einer Meta-Analyse von Miloushev et al. (2015) [110] wurde beschrieben, dass höhergradige Gliome in der Peripherie eine reduzierte FA aufweisen – eine Beobachtung, die mit vermehrt infiltrativem Wachstum und Faserdestruktion vereinbar wäre. Im Einklang hierzu wurde in einer Studie von Bette et al. (2017) [111] berichtet, dass eine verminderte peritumorale FA bei präoperativen Glioblastomen einen späteren Rückfall prognostiziert, was auf eine Unterschätzung der Tumorausdehnung anhand der strukturellen MRT zurückgeführt wurde. Zusammen mit

unseren Ergebnisse legt dies nahe, dass eine Beurteilung der perifokalen FA zur Unterscheidung zwischen höhergradigem Gliomrezidiv und therapiebedingten Veränderungen nützlich sein könnte, insbesondere wenn PET-Untersuchungen mit radiomarkierten Aminosäuren nicht verfügbar sind. Die multiparametrische Integration von Diffusionsmetriken könnte weiterhin einen Mehrwert für die OP- und Bestrahlungsplanung bieten, indem sie die Erkennung diffuser Infiltration über die Grenzen der Kontrastverstärkung hinaus ermöglicht. FA-Werte aus der Peripherie zeigten zudem eine moderate negative Korrelation mit der ^{18}F-FET Aufnahme. Diese Beobachtung lässt sich gut durch das bei höhergradigen Gliomen bekannte infiltrative Wachstum mit neuroaxonaler Destruktion [112] und einem dysregulierten Aminosäurestoffwechsels [95] erklären. Es wurde ebenfalls gezeigt, dass die Bestimmung des relativen MKT-Werts weitere Einblicke in die mikrostrukturelle Komplexität bietet und im Fall eines Rezidivs für Architektur- und Zellverlust (z.B. bei Infiltration) spricht.

Zudem wurde eine Steigerung des MD-Werts bei Rezidiven festgestellt. Ähnlich wie in *Originalarbeit 5*, wo der ADC-Wert bei Rezidiven ebenfalls erhöht war, kann dies auf verschiedene pathophysiologische Effekte hindeuten, wie auf das Vorhandensein von vasogenem Ödem, einer veränderten Gefäßstruktur oder entzündlichen Veränderungen. Eine restringierte Diffusionskomponente, die mutmaßlich durch hohe Zellularität im höhergradigen Gliomrezidiv verursacht wird (mit erwartungsgemäß niedrigem ADC-Wert, da erhöhte Zelldichte den extrazellulären Raum reduziert und damit auch die Diffusion von Wasser durch das Interstitium), könnte durch diese parallel auftretenden pathophysiologischen Effekte in zuvor behandelten Gliomen verschleiert werden. In Zusammenschau legen die Ergebnisse aus *Originalarbeit 4* jedoch nahe, dass eine gemittelte Diffusivität für die diagnostische Differenzierung zwischen Tumorrückfall und posttherapeutischen Effekten weniger robust sein könnte. Insbesondere die DWI kann durch Einflüsse der Durchblutung im Kapillarnetzwerk beeinflusst werden, was zu einer Überschätzung des ADC-Wertes in stark vaskularisierten Tumoren führen kann [113]. Die in der Literatur beschriebenen ADC-Werte in onkologischen Studien sind zudem häufig variabel und teilweise widersprüchlich. Neben technischen und methodologischen Gründen (z.B. unterschiedliche Bildnachbearbeitung und ADC-Berechnungsmethoden oder manuelle Segmentierung) ist diese Variabilität auch auf die zugrunde liegende Tumorheterogenität zurückzuführen [114–116]. Letzteres gilt insbesondere für höhergradige Hirntumoren, die zwar oftmals eine hohe Zellularität zeigen, jedoch auch häufiger mit Nekrose und/oder vasogenem Ödem vergesellschaftet sind, was den ADC-Wert beeinflussen kann.

Mittels konventioneller MRT-Sequenzen lässt sich nur eingeschränkt zwischen Ödem und infiltrierendem Tumor bei Gliomen unterscheiden. Dies stellt eine Herausforderung für die genaue Bestimmung der Ausdehnung von Gliomen dar. Ähnlich wie in *Originalarbeit 3* konnten andere PET-Studien mit Hilfe von radiomarkierten Aminosäuren zeigen, dass eine Definition des Tumorvolumens anhand der Kontrastmittelaufnahme in der konventionellen MRT das Tumorausmaß signifikant unterschätzt [117, 118]. Denn im Gegensatz zu Gd-basierten Kontrastmitteln ermöglicht die metabolische Bildgebung eine Beurteilung der Tumorausdehnung, die nicht von der Beeinträchtigung der BHS abhängt [38]. Hier kann insbesondere die multiparametrische Integration mehrerer Modalitäten zu einer Verbesserung bei der Definition der Tumorausdehnung und einer Differenzierung zwischen Arealen mit Tumorinfiltration und vasogenem Ödem beitragen – klinisch ist dies für die Planung von operativen Eingriffen sowie die Abgrenzung von Zielbereichen für die Strahlentherapie relevant.

Limitationen. Allgemeine Schlussfolgerungen sollten aufgrund der retrospektiven Natur und den relativ geringen Fallzahlen in den *Originalarbeiten 3,4 und 5* unter Vorbehalt gezogen werden. Des Weiteren sind multizentrische Studien mit prospektivem Studiendesign zur unabhängigen Validierung angezeigt. In Hinblick auf *Originalarbeit 3* sollten nachfolgende Untersuchungen auch die Auswirkungen unterschiedlicher räumlicher Auflösungen und PET-Scanner evaluieren. Die Ergebnisse der *Originalarbeiten 3,4 und 5* beschränken sich jeweils auf ^{18}F-FET-aktive und damit zumeist höhergradige Gliome. Bei ^{18}F-FET-photopenischen Hirntumoren könnten fortgeschrittene Bildgebungsmethoden, wie die 2-Hydroxyglutarat-MRS, zusätzliche molekulare Daten bereitstellen, die in der multimodalen und multiparametrischen Beurteilung zur IDH-Genotypisierung berücksichtigt werden sollten. Die Patientenkohorten der retrospektiven Studien umfassen jeweils gemischte Patientenpopulationen, die die Situation in der klinischen Praxis widerspiegeln – wobei Analysen mit den gleichen histologischen Subtypen ggf. eine bessere Vergleichbarkeit gewährleisten würden. Obgleich die *Originalarbeiten 4 und 5* hauptsächlich auf Diffusionsbildgebung ausgerichtet sind, sollten andere Methoden zur Charakterisierung der Tumorbiologie in ähnlicher Art und Weise multimodal integriert und evaluiert werden. In den *Originalarbeiten 4 und 5* ist eine Auswahlverzerrung (engl. „sampling bias“) durch die Überweisung von primär unklaren Fällen zur weiteren Abklärung mittels PET/MRT möglich.

3.3. Weiterführende Forschungsgebiete und Ausblick

Da mit den Ergebnissen von *Originalarbeit 1* ein neues Anwendungsgebiet für die molekulare Fibrin-Bildgebung erschlossen wurde, leitet sich ein weitreichender Forschungsbedarf in Hinblick auf diverse ZNS-Erkrankungen ab, wie z.B. Morbus Alzheimer, Enzephalitiden, Schlaganfälle oder intrakranielle Blutungen. Speziell im Rahmen der MS sollte Fibrin als Biomarker für Therapieansprechen (beispielsweise als Endpunkt für klinische Studien) oder als Prognosekriterium untersucht werden. Ein weiteres relevantes Forschungsgebiet für die Fibrin-induzierte Pathologie ist die sogenannte „schwelende Entzündung“ bei MS (engl. "smouldering MS“). Als Sammelbezeichnung beschreibt dies entzündliche Prozesse im ZNS, die nicht unmittelbar mit klinischen Schüben oder einem Progress gemäß Bildgebung assoziiert sind. Dieser Fortschritt, unabhängig von Schubaktivität, stellt einen wesentlichen Faktor für die schleichend progressive Pathologie bei MS-Patienten dar.
Die Erforschung und Entwicklung neuer molekularer Sonden eröffnet weitere Möglichkeiten zur Charakterisierung von Pathologien sowie biochemischer Prozesse. Hierzu gehören biochemisch reaktive Sonden, wie beispielsweise $Fe^{3+/2+}$-PyC3A, ein Redox-aktiver Eisen-Komplex, der für die molekulare Bildgebung von akuter Inflammation mit Freisetzung von reaktiven Sauerstoffspezies eingesetzt werden kann und eine selektive Kontrastverbesserung ermöglicht [119]. Die Verknüpfung von diagnostischen Bildgebungsverfahren mit zielgerichteten Therapieansätzen, beispielsweise mittels multifunktionaler Nanopartikel (deren biokompatible Beschichtung zur selektiven Abgabe von Wirkstoffen verwendet werden kann) [120], birgt ein enormes Potenzial für die individualisierte Medizin.

In Hinblick auf *Originalarbeit 3* sollten zukünftige Studien den hier etablierten Biomarker auch in anderen IDH-mutierten Malignomen (z.B. dem Cholangiokarzinom oder Chondrosarkom) untersuchen, wo molekulares IDH-Targeting in Zukunft vermutlich auch eine Rolle spielen könnte. Neue IDH1-zielgerichtete PET-Tracer werden hierbei vermutlich ebenfalls einen diagnostischen Mehrwert bieten [121–123].
Die multimodale Integration verschiedener bildgebender Verfahren, ähnlich wie in den *Originalarbeiten 4 und 5* veranschaulicht, ermöglicht eine komplexere, mehrdimensionale Erfassung molekularer und mikrostruktureller Prozesse. Diese Herangehensweise kann auch in anderen Erkrankungen die diagnostische Sensitivität und Spezifität steigern.

Weitere vielversprechende Forschungsgebiete sind die Integration von künstlicher Intelligenz (KI) in verschiedene Aspekte der neuromolekularen Bildgebung. Zentrale Forschungsbereiche sind die Anwendung von KI in der Bildrekonstruktion und der Entwicklung molekularer Sonden. Bereits zum aktuellen Zeitpunkt gibt es entsprechend zertifizierte und klinisch eingesetzte Produkte, die die Effizienz der Bildrekonstruktion und Bildqualität unter dem Mehrwert einer Messzeitverkürzung (durch unvollständige Objektabtastung) und/oder Dosisreduktion steigern können. Des Weiteren können KI-gestützt neue Bildkontraste und Artefakt-reduzierte Bilddaten generiert werden.

Obwohl die Anwendung von KI in der Arzneimittelentwicklung noch in den Kinderschuhen steckt, sind bereits jetzt automatisierte Analysen großer Datenmengen möglich [124], um z.B. Eigenschaften von Molekülen vorherzusagen oder Zielstrukturen zu identifizieren. Ein Beispiel für eine solche Technik ist das "molekulare Docking" [125], bei dem simuliert wird, wie Moleküle interagieren und binden. Dies kann dazu beitragen, die Bindungsaffinität und Selektivität potenzieller molekularer Sonden vorherzusagen. Ein weiterer Ansatz ist die Verwendung von großen Sprachmodellen (engl. „large language models“), die in der Lage sind, Proteinsequenzen mit vorhersagbarer Funktion über Protein-Familien hinweg zu generieren [126]. Außerdem können KI-Algorithmen zur automatisierten Analyse von Bildgebungsdaten verwendet werden, wie beispielsweise zur Detektion von komplexen Mustern oder der Entwicklung von Prognosemodellen. Ferner besteht ein erhebliches Potenzial in der Entwicklung von Harmonisierungsstrategien auf KI-Basis, die es ermöglichen, quantitative Bilddaten im Kontext unterschiedlicher Untersuchungsprotokolle und Gerätehersteller vergleichbar zu machen, was einen relevanten Beitrag zur Validierung von Bildgebungsbiomarkern leisten würde.

4. Zusammenfassung

Die molekulare Bildgebung ist ein wichtiger Bestandteil der Präzisionsmedizin. Diese Habilitationsschrift ist der neuromolekularen Bildgebung gewidmet und beschreibt verschiedene Aspekte der klinischen Translation von bildgestützten molekularen Biomarkern, die eine nicht-invasive Charakterisierung von neuroonkologischen und -inflammatorischen Pathomechanismen ermöglichen. Für die Entwicklung und Validierung von Biomarkern wurden in den vorliegenden Arbeiten weitreichende Untersuchungen sowohl in vitro, in vivo im Tiermodell als auch durch klinische Studien durchgeführt.

In *Originalarbeit 1* wurde erstmalig gezeigt, dass proinflammatorische Fibrin-Plaques im ZNS mittels molekularer MRT-Bildgebung erfasst werden können und als nicht-invasiver Biomarker für immunentzündliche Veränderungen und BHS-Störung messbar sind. Fibrinablagerungen im Gehirn waren mit einer Remodellierung der extrazellulären Matrix, der Krankheitsaktivität und dem Grad der physischen Beeinträchtigung in einem Tiermodell für MS assoziiert. Damit implizieren die Ergebnisse eine wichtige Rolle für das klinische Management bei der Überwachung von Krankheitsaktivität. Darüber hinaus ermöglicht die molekulare Fibrin-Bildgebung aufgrund einer hohen SNR sowie einer spezifischen Bindung an eine krankheitsassoziierte Zielstruktur eine Detektion subtiler Läsionen (z.B. klinisch relevanter kortikaler Läsionen), die mit konventioneller MRT und nicht-spezifischen Kontrastmitteln maskiert bleiben. Die Ergebnisse aus *Originalarbeit 2* haben bedeutsam zur methodischen Implementierung von *Originalarbeit 1* beigetragen, da eine genaue Übereinstimmung mittels Registrierung der dynamischen KM-Untersuchung lediglich nach Anwendung der automatisierten Hirnsegmentierung möglich war. Zusammenfassend wurde mit diesen Ergebnissen ein neues Anwendungsgebiet für die molekulare Fibrin-Bildgebung im Kontext der Neurobildgebung erschlossen.

In *Originalarbeit 3* wurde die metabolische Umprogrammierung von Gliomen mittels parametrischem ^{18}F-FET PET evaluiert und dessen diagnostisches Potenzial zur nicht-invasiven Bestimmung des IDH-Genotyps bewertet. Hierfür wurde zunächst ein neuer Biomarker entwickelt, der die metabolische Heterogenität des Aminosäure-Stoffwechsels charakterisiert. Dieser (semi-)quantitative bildgestützte Biomarker wurde dann retrospektiv in einer Patientenkohorte (27 Männer, 25 Frauen) mit Gliomen vor neurochirurgischer Operation

mittels statischer ^{18}F-FET PET evaluiert. Über eine Quantifizierung der metabolischen Heterogenität konnte der IDH-Genotyp mit hoher diagnostischer Genauigkeit bestimmt werden. Dies deutet auf eine Assoziation zwischen dem metabolischen Phänotyp und genomischen Merkmalen hin. Im Unterschied zu anderen komplexen und experimentellen Bildgebungstechniken, deren klinische Integration häufig schwierig ist, erlaubt das hier entwickelte Verfahren eine solide IDH-Klassifizierung basierend auf statischer ^{18}F-FET PET ohne der Notwendigkeit für aufwändige Analysemethoden. Da der IDH-Genotyp ein zentraler Marker für die Behandlung und die individuelle Prognose ist, können die Ergebnisse der *Originalarbeit 3* von hoher Relevanz für das klinische Vorgehen und die diagnostische Aufarbeitung von PatientInnen mit primären Hirntumoren sein.

Die *Originalarbeiten 4 und 5* widmen sich dem diagnostischen Dilemma der Unterscheidung von posttherapeutischen Veränderungen zu Gliomrezidiven. Diese therapieinduzierten Veränderungen sind mittels konventioneller MRTs kaum vom wahren Tumorprogress zu differenzieren. Obgleich sich die metabolische ^{18}F-FET PET-Bildgebung in beiden Arbeiten hierfür als hilfreich erwies, war dessen diagnostische Güte eingeschränkt, da Behandlungseffekte auch zu einer reaktiv gesteigerten Aminosäure-Aufnahme führen können, was letztlich eine sichere Abgrenzung zur tatsächlichen Krankheitsprogression erschwert. Daher wurde die Diffusionsbildgebung in einem multimodalen Ansatz hinzugezogen, um metabolisch-aktive Kompartimente weiter zu charakterisieren. In der klinischen Anwendung kommen vornehmlich einfache Diffusionsmodelle zum Einsatz – wie auch in *Originalarbeit 5* evaluiert. So wurde in *Originalarbeit 5* dargelegt, dass eine biparametrische Untersuchung mittels DWI und PET eine höhere diagnostische Güte und klinischen Nutzen bei der Unterscheidung zwischen Gliomrezidiv und behandlungsbedingten Veränderungen aufweist. Komplexere Techniken, wie die DKI, haben erst mit der Entwicklung neuer, beschleunigter Untersuchungsprotokolle an Bedeutung gewonnen und erlauben eine umfassendere Charakterisierung der Gewebemikrostruktur. Mit der Rationale einer synergistischen und komplementären Anwendung der hybriden PET und MRT, wurde in *Originalarbeit 4* eine Methodik für eine kombinierte und integrative Analyse von ^{18}F-FET PET zusammen mit einer fast-DKI Variante entwickelt, die eine detaillierte mikrostrukturelle Charakterisierung der metabolisch aktiven (Tumor-)Umgebung ermöglicht. Unsere Ergebnisse verdeutlichen, dass die gemeinsame Anwendung von PET und Diffusionsbildgebung einen erheblichen diagnostischen Mehrwert im Vergleich zur alleinigen Nutzung der PET aufweist. Durch die Analyse von Diffusionsmarkern, die aus dem metabolischen Randgebiet ermittelt wurden,

war eine besonders aussagekräftige Charakterisierung der Tumormikroumgebung möglich. Unter den Diffusionsmetriken ist besonders die fraktionale Anisotropie (FA) hervorzuheben, die eine vergleichbare diagnostische Güte zur ^{18}F-FET PET aufwies. So zeigten Gliomrezidive besonders niedrige FA-Werte, was auf eine kompromittierte Faserintegrität (z.B. bei diffuser Infiltration) hinweist, die zudem mit der ^{18}F-FET Aufnahme negativ korreliert waren. Hierbei ist hervorzuheben, dass die in *Originalarbeit 4* erarbeitete Methodik als eine ^{18}F-FET PET-gesteuerte „virtuelle Biopsie“ zu verstehen ist, in der eine mikrostrukturelle Charakterisierung von automatisiert (3D-)segmentierten metabolisch-aktiven (Tumor-)Kompartimenten erfolgt. Dies unterscheidet sich wesentlich von bisherigen Studien, in denen Läsionen typischerweise auf der Basis von Kontrastmittel-Anreicherung in einer einzigen Schicht manuell segmentiert werden. Angesichts der Heterogenität von Tumoren und der bereits diskutierten Diskrepanzen zwischen Regionen mit Kontrastverstärkung und Arealen mit diffuser Infiltration erscheint dies jedoch als unzureichend. Zusammenfassend zeigen die *Originalarbeiten 4 und 5*, dass eine kombinierte und integrative Analyse der PET/MRT-Bildgebung im Sinne einer PET-gesteuerten „virtuellen Biopsie“ zur mikrostrukturellen Gewebecharakterisierung des metabolisch-aktiven Tumors, einschließlich einer parametrischen modalitätsübergreifenden Auswertung, einen signifikanten klinischen Nutzen und Mehrwert bringen können. Diese Ergebnisse gelten insbesondere für therapierte Gliome, dürften aber ebenso für eine Reihe anderer Tumorentitäten von erheblicher Bedeutung sein.

Die größten Herausforderungen der (neuro-)molekularen Bildgebung sind gegenwärtig die Validierung von Biomarkern, u.a. im Rahmen von multizentrischen Studien, sowie die Standardisierung mittels Konsensus-Empfehlungen und Leitlinien für Mess- und Bewertungsprozesse. Insbesondere als Querschnittsfach profitiert die neuromolekulare Bildgebung von einem verstärkt interdisziplinären Ansatz, in dem sich Experten aus den bildgebenden Fachgebieten, der Molekularbiologie, der Chemie, der Bioinformatik sowie weiteren assoziierten Querschnittsfächern zusammenschließen und austauschen. Anstelle einer sequenziellen Entwicklungsstrategie sollten Innovationen in der Bildgebungstechnologie simultan zu klinischen Neuerungen in einem translationalen und interaktiven Kontext evaluiert und beurteilt werden. In Anbetracht der rasanten technologischen Entwicklungen, einschließlich KI-Anwendungen, digitaler Detektorsysteme und Ultrahochfeld-MRTs, ist davon auszugehen, dass die molekulare Bildgebung beträchtliche Fortschritte verzeichnen wird und noch detailliertere Einblicke in biologische Strukturen und Prozesse möglich sein

werden. Diese Entwicklungen könnten den Weg für eine breitere klinische Anwendung ebnen.

"Medicine is not only a science; it is also an art. It does not consist of compounding pills and plasters; it deals with the very processes of life, which must be understood before they may be guided." – Paracelsus

Die Weiterentwicklungen in der molekularen Medizin bringen eine zunehmende Komplexität mit sich. Gerade in Hinblick auf rasant wachsende medizinische Datenbestände, sollte es imperativ sein, dass das Individuum stets im Mittelpunkt der ärztlichen Tätigkeit steht. Die personalisierte Medizin stellt eine entscheidende Kehrtwende von der traditionellen Universalmedizin dar. Sie erfordert nicht nur eine interdisziplinäre Zusammenarbeit und umfassende medizinische Kenntnisse, einschließlich der vielschichtigen Wechselwirkungen zwischen genetischen, molekularbiologischen, umwelt- und lebensstilbedingten Faktoren, sondern auch die Fähigkeit, dieses Wissen auf individueller Ebene zu interpretieren und anzuwenden. Um eine effektive und individualisierte Diagnostik, Behandlung und Prävention zu ermöglichen, ist es unerlässlich, einen ganzheitlichen Blick auf die Bedürfnisse und Umstände des Menschen zu werfen, der über die bloße Pathologie hinausgeht. In diesem Sinne sollte sich die moderne Medizin daher als die Kunst des Heilens auf dem Fundament der modernen Wissenschaft verstehen.

5. Literatur

1. Wehrl HF, Sauter AW, Divine MR, Pichler BJ (2015) Combined PET/MR: a technology becomes mature. J Nucl Med 56:165–168. doi: 10.2967/jnumed.114.150318
2. Veit-Haibach P, Ahlström H, Boellaard R et al. (2023) International EANM-SNMMI-ISMRM consensus recommendation for PET/MRI in oncology. Eur J Nucl Med Mol Imaging. doi: 10.1007/s00259-023-06406-x
3. Brady AP, Bello JA, Derchi LE et al. (2021) Radiology in the Era of Value-based Healthcare: A Multi-Society Expert Statement from the ACR, CAR, ESR, IS3R, RANZCR, and RSNA. Radiology 298:486–491. doi: 10.1148/radiol.2020209027
4. European Society of Radiology ESR (2022) The role of radiologist in the changing world of healthcare: a White Paper of the European Society of Radiology (ESR). Insights Imaging 13:100. doi: 10.1186/s13244-022-01241-4
5. James ML, Gambhir SS (2012) A molecular imaging primer: modalities, imaging agents, and applications. Physiol Rev 92:897–965. doi: 10.1152/physrev.00049.2010
6. Rowe SP, Pomper MG (2022) Molecular imaging in oncology: Current impact and future directions. CA Cancer J Clin 72:333–352. doi: 10.3322/caac.21713
7. Sellmyer MA, Lee IK, Mankoff DA (2021) Building the Bridge: Molecular Imaging Biomarkers for 21st Century Cancer Therapies. J Nucl Med 62:1672–1676. doi: 10.2967/jnumed.121.262484
8. Wu T, Liu C, Thamizhchelvan AM et al. (2023) Label-Free Chemically and Molecularly Selective Magnetic Resonance Imaging. Chemical & Biomedical Imaging 1:121–139. doi: 10.1021/cbmi.3c00019
9. Biomarkers DWG (2001) Biomarkers and surrogate endpoints: preferred definitions and conceptual framework. Clin Pharmacol Ther 69:89–95. doi: 10.1067/mcp.2001.113989
10. Dorfman GS, Sullivan DC, Schnall MD, Matrisian LM, Translational RWG (2008) The Translational Research Working Group developmental pathway for image-based assessment modalities. Clin Cancer Res 14:5678–5684. doi: 10.1158/1078-0432.CCR-08-1264
11. Buckler AJ, Bresolin L, Dunnick NR et al. (2011) Quantitative imaging test approval and biomarker qualification: interrelated but distinct activities. Radiology 259:875–884. doi: 10.1148/radiol.10100800

12. O'Connor JP, Aboagye EO, Adams JE et al. (2017) Imaging biomarker roadmap for cancer studies. Nat Rev Clin Oncol 14:169–186. doi: 10.1038/nrclinonc.2016.162
13. Drucker E, Krapfenbauer K (2013) Pitfalls and limitations in translation from biomarker discovery to clinical utility in predictive and personalised medicine. EPMA J 4:7. doi: 10.1186/1878-5085-4-7
14. Chitnis T, Weiner HL (2017) CNS inflammation and neurodegeneration. J Clin Invest 127:3577–3587. doi: 10.1172/JCI90609
15. Filippi M, Brück W, Chard D et al. (2019) Association between pathological and MRI findings in multiple sclerosis. Lancet Neurol 18:198–210. doi: 10.1016/S1474-4422(18)30451-4
16. Thomas AM, Barkhof F, Bulte JWM (2022) Opportunities for Molecular Imaging in Multiple Sclerosis Management: Linking Probe to Treatment. Radiology 303:486–497. doi: 10.1148/radiol.211252
17. Nutma E, Stephenson JA, Gorter RP et al. (2019) A quantitative neuropathological assessment of translocator protein expression in multiple sclerosis. Brain 142:3440–3455. doi: 10.1093/brain/awz287
18. Bodini B, Tonietto M, Airas L, Stankoff B (2021) Positron emission tomography in multiple sclerosis - straight to the target. Nat Rev Neurol 17:663–675. doi: 10.1038/s41582-021-00537-1
19. Gui Y, Marks JD, Das S, Hyman BT, Serrano-Pozo A (2020) Characterization of the 18 kDa translocator protein (TSPO) expression in post-mortem normal and Alzheimer's disease brains. Brain Pathol 30:151–164. doi: 10.1111/bpa.12763
20. Kelloff GJ, Hoffman JM, Johnson B et al. (2005) Progress and promise of FDG-PET imaging for cancer patient management and oncologic drug development. Clin Cancer Res 11:2785–2808. doi: 10.1158/1078-0432.CCR-04-2626
21. Blinkenberg M, Rune K, Jensen CV et al. (2000) Cortical cerebral metabolism correlates with MRI lesion load and cognitive dysfunction in MS. Neurology 54:558–564. doi: 10.1212/wnl.54.3.558
22. Chen JW, Breckwoldt MO, Aikawa E, Chiang G, Weissleder R (2008) Myeloperoxidase-targeted imaging of active inflammatory lesions in murine experimental autoimmune encephalomyelitis. Brain 131:1123–1133. doi: 10.1093/brain/awn004

23. Forghani R, Wojtkiewicz GR, Zhang Y et al. (2012) Demyelinating diseases: myeloperoxidase as an imaging biomarker and therapeutic target. Radiology 263:451–460. doi: 10.1148/radiol.12111593
24. Sipkins DA, Gijbels K, Tropper FD, Bednarski M, Li KC, Steinman L (2000) ICAM-1 expression in autoimmune encephalitis visualized using magnetic resonance imaging. J Neuroimmunol 104:1–9. doi: 10.1016/s0165-5728(99)00248-9
25. Serres S, Mardiguian S, Campbell SJ et al. (2011) VCAM-1-targeted magnetic resonance imaging reveals subclinical disease in a mouse model of multiple sclerosis. FASEB J 25:4415–4422. doi: 10.1096/fj.11-183772
26. Global BODCC, Fitzmaurice C, Allen C et al. (2017) Global, Regional, and National Cancer Incidence, Mortality, Years of Life Lost, Years Lived With Disability, and Disability-Adjusted Life-years for 32 Cancer Groups, 1990 to 2015: A Systematic Analysis for the Global Burden of Disease Study. JAMA Oncol 3:524–548. doi: 10.1001/jamaoncol.2016.5688
27. Miller KD, Ostrom QT, Kruchko C et al. (2021) Brain and other central nervous system tumor statistics, 2021. CA Cancer J Clin 71:381–406. doi: 10.3322/caac.21693
28. Wang WH, Sung CY, Wang SC, Shao YJ (2023) Risks of leukemia, intracranial tumours and lymphomas in childhood and early adulthood after pediatric radiation exposure from computed tomography. CMAJ 195:E575–E583. doi: 10.1503/cmaj.221303
29. Braganza MZ, Kitahara CM, Berrington de González A, Inskip PD, Johnson KJ, Rajaraman P (2012) Ionizing radiation and the risk of brain and central nervous system tumors: a systematic review. Neuro Oncol 14:1316–1324. doi: 10.1093/neuonc/nos208
30. Farrell CJ, Plotkin SR (2007) Genetic causes of brain tumors: neurofibromatosis, tuberous sclerosis, von Hippel-Lindau, and other syndromes. Neurol Clin 25:925–46, viii. doi: 10.1016/j.ncl.2007.07.008
31. Ostrom QT, Cioffi G, Gittleman H et al. (2019) CBTRUS Statistical Report: Primary Brain and Other Central Nervous System Tumors Diagnosed in the United States in 2012-2016. Neuro Oncol 21:v1–v100. doi: 10.1093/neuonc/noz150
32. Wen PY, Weller M, Lee EQ et al. (2020) Glioblastoma in adults: a Society for Neuro-Oncology (SNO) and European Society of Neuro-Oncology (EANO) consensus review on current management and future directions. Neuro Oncol 22:1073–1113. doi: 10.1093/neuonc/noaa106

33. Tan AC, Ashley DM, López GY, Malinzak M, Friedman HS, Khasraw M (2020) Management of glioblastoma: State of the art and future directions. CA Cancer J Clin 70:299–312. doi: 10.3322/caac.21613
34. Siegal T (2015) Clinical impact of molecular biomarkers in gliomas. J Clin Neurosci 22:437–444. doi: 10.1016/j.jocn.2014.10.004
35. Kim MM, Parolia A, Dunphy MP, Venneti S (2016) Non-invasive metabolic imaging of brain tumours in the era of precision medicine. Nat Rev Clin Oncol 13:725–739. doi: 10.1038/nrclinonc.2016.108
36. Choi C, Ganji SK, DeBerardinis RJ et al. (2012) 2-hydroxyglutarate detection by magnetic resonance spectroscopy in IDH-mutated patients with gliomas. Nat Med 18:624–629. doi: 10.1038/nm.2682
37. Werner JM, Lohmann P, Fink GR, Langen KJ, Galldiks N (2020) Current Landscape and Emerging Fields of PET Imaging in Patients with Brain Tumors. Molecules 25:1471. doi: 10.3390/molecules25061471
38. Langen KJ, Galldiks N, Hattingen E, Shah NJ (2017) Advances in neuro-oncology imaging. Nat Rev Neurol 13:279–289. doi: 10.1038/nrneurol.2017.44
39. Juhász C, Dwivedi S, Kamson DO, Michelhaugh SK, Mittal S (2014) Comparison of amino acid positron emission tomographic radiotracers for molecular imaging of primary and metastatic brain tumors. Mol Imaging 13(6). doi: 10.2310/7290.2014.00015
40. Hutterer M, Nowosielski M, Putzer D et al. (2013) [18F]-fluoro-ethyl-L-tyrosine PET: a valuable diagnostic tool in neuro-oncology, but not all that glitters is glioma. Neuro Oncol 15:341–351. doi: 10.1093/neuonc/nos300
41. Kaim AH, Weber B, Kurrer MO et al. (2002) (18)F-FDG and (18)F-FET uptake in experimental soft tissue infection. Eur J Nucl Med Mol Imaging 29:648–654. doi: 10.1007/s00259-002-0780-y
42. Muoio B, Giovanella L, Treglia G (2018) Recent Developments of 18F-FET PET in Neuro-oncology. Curr Med Chem 25:3061–3073. doi: 10.2174/0929867325666171123202644
43. Petersen MA, Ryu JK, Akassoglou K (2018) Fibrinogen in neurological diseases: mechanisms, imaging and therapeutics. Nat Rev Neurosci 19:283–301. doi: 10.1038/nrn.2018.13
44. Mendiola AS, Yan Z, Dixit K et al. (2023) Defining blood-induced microglia functions in neurodegeneration through multiomic profiling. Nature Immunology 10.1038/s41590-023-01522-0

45. Strickland S (2018) Blood will out: vascular contributions to Alzheimer's disease. J Clin Invest 128:556–563. doi: 10.1172/JCI97509
46. Abbadessa G, Lavorgna L, Treaba CA, Bonavita S, Mainero C (2021) Hemostatic factors in the pathogenesis of neuroinflammation in multiple sclerosis. Mult Scler 13524585211039111. doi: 10.1177/13524585211039111
47. Mollison D, Sellar R, Bastin M et al. (2017) The clinico-radiological paradox of cognitive function and MRI burden of white matter lesions in people with multiple sclerosis: A systematic review and meta-analysis. PLoS One 12:e0177727. doi: 10.1371/journal.pone.0177727
48. Barkhof F (2002) The clinico-radiological paradox in multiple sclerosis revisited. Curr Opin Neurol 15:239–245. doi: 10.1097/00019052-200206000-00003
49. Filippi M, Bar-Or A, Piehl F et al. (2018) Multiple sclerosis. Nat Rev Dis Primers 4:43. doi: 10.1038/s41572-018-0041-4
50. Gale EM, Atanasova IP, Blasi F, Ay I, Caravan P (2015) A Manganese Alternative to Gadolinium for MRI Contrast. J Am Chem Soc 137:15548–15557. doi: 10.1021/jacs.5b10748
51. Overoye-Chan K, Koerner S, Looby RJ et al. (2008) EP-2104R: a fibrin-specific gadolinium-Based MRI contrast agent for detection of thrombus. J Am Chem Soc 130:6025–6039. doi: 10.1021/ja800834y
52. Salarian M, Ibhagui OY, Yang JJ (2020) Molecular imaging of extracellular matrix proteins with targeted probes using magnetic resonance imaging. Wiley Interdiscip Rev Nanomed Nanobiotechnol 12:e1622. doi: 10.1002/wnan.1622
53. Atanasova I, Sojoodi M, Leitão HS et al. (2020) Molecular Magnetic Resonance Imaging of Fibrin Deposition in the Liver as an Indicator of Tissue Injury and Inflammation. Invest Radiol 55:209–216. doi: 10.1097/RLI.0000000000000631
54. Shea BS, Probst CK, Brazee PL et al. (2017) Uncoupling of the profibrotic and hemostatic effects of thrombin in lung fibrosis. JCI Insight 2:86608. doi: 10.1172/jci.insight.86608
55. Vymazal J, Spuentrup E, Cardenas-Molina G et al. (2009) Thrombus imaging with fibrin-specific gadolinium-based MR contrast agent EP-2104R: results of a phase II clinical study of feasibility. Invest Radiol 44:697–704. doi: 10.1097/RLI.0b013e3181b092a7
56. Lythgoe MF, Sibson NR, Harris NG (2003) Neuroimaging of animal models of brain disease. Br Med Bull 65:235–257.

57. Kalavathi P, Prasath VB (2016) Methods on Skull Stripping of MRI Head Scan Images-a Review. J Digit Imaging 29:365–379. doi: 10.1007/s10278-015-9847-8
58. Jia H, Wu G, Wang Q, Shen D (2010) ABSORB: Atlas Building by Self-organized Registration and Bundling. Neuroimage 51:1057–1070. doi: 10.1016/j.neuroimage.2010.03.010
59. Pirozzi CJ, Yan H (2021) The implications of IDH mutations for cancer development and therapy. Nat Rev Clin Oncol 18:645–661. doi: 10.1038/s41571-021-00521-0
60. M Gagné L, Boulay K, Topisirovic I, Huot MÉ, Mallette FA (2017) Oncogenic Activities of IDH1/2 Mutations: From Epigenetics to Cellular Signaling. Trends Cell Biol 27:738–752. doi: 10.1016/j.tcb.2017.06.002
61. Waitkus MS, Diplas BH, Yan H (2016) Isocitrate dehydrogenase mutations in gliomas. Neuro Oncol 18:16–26. doi: 10.1093/neuonc/nov136
62. Louis DN, Perry A, Wesseling P et al. (2021) The 2021 WHO Classification of Tumors of the Central Nervous System: a summary. Neuro Oncol 23:1231–1251. doi: 10.1093/neuonc/noab106
63. Beiko J, Suki D, Hess KR et al. (2014) IDH1 mutant malignant astrocytomas are more amenable to surgical resection and have a survival benefit associated with maximal surgical resection. Neuro Oncol 16:81–91. doi: 10.1093/neuonc/not159
64. Rossi M, Gay L, Ambrogi F et al. (2021) Association of supratotal resection with progression-free survival, malignant transformation, and overall survival in lower-grade gliomas. Neuro Oncol 23:812–826. doi: 10.1093/neuonc/noaa225
65. Motomura K, Chalise L, Ohka F et al. (2021) Impact of the extent of resection on the survival of patients with grade II and III gliomas using awake brain mapping. J Neurooncol 153:361–372. doi: 10.1007/s11060-021-03776-w
66. Miller JJ, Gonzalez Castro LN, McBrayer S et al. (2022) Isocitrate dehydrogenase (IDH) mutant gliomas: A Society for Neuro-Oncology (SNO) consensus review on diagnosis, management, and future directions. Neuro Oncol noac207. doi: 10.1093/neuonc/noac207
67. Jensen JH, Helpern JA, Ramani A, Lu H, Kaczynski K (2005) Diffusional kurtosis imaging: the quantification of non-gaussian water diffusion by means of magnetic resonance imaging. Magn Reson Med 53:1432–1440. doi: 10.1002/mrm.20508
68. Hansen B, Lund TE, Sangill R, Jespersen SN (2013) Experimentally and computationally fast method for estimation of a mean kurtosis. Magn Reson Med 69:1754–1760. doi: 10.1002/mrm.24743

69. Hansen B, Lund TE, Sangill R, Stubbe E, Finsterbusch J, Jespersen SN (2016) Experimental considerations for fast kurtosis imaging. Magn Reson Med 76:1455–1468. doi: 10.1002/mrm.26055
70. Brendle C, Maier C, Bender B et al. (2022) Impact of ^{18}F-FET PET/MRI on Clinical Management of Brain Tumor Patients. J Nucl Med 63:522–527. doi: 10.2967/jnumed.121.262051
71. Galldiks N, Law I, Pope WB, Arbizu J, Langen KJ (2017) The use of amino acid PET and conventional MRI for monitoring of brain tumor therapy. Neuroimage Clin 13:386–394. doi: 10.1016/j.nicl.2016.12.020
72. Pansieri J, Hadley G, Lockhart A, Pisa M, DeLuca GC (2023) Regional Contribution of Vascular Dysfunction in White Matter Dementia: Clinical and Neuropathological Insights. Frontiers in Neurology 14:1109. doi: 10.3389/fneur.2023.1199491
73. Adams RA, Bauer J, Flick MJ et al. (2007) The fibrin-derived gamma377-395 peptide inhibits microglia activation and suppresses relapsing paralysis in central nervous system autoimmune disease. J Exp Med 204:571–582. doi: 10.1084/jem.20061931
74. Ryu JK, Rafalski VA, Meyer-Franke A et al. (2018) Fibrin-targeting immunotherapy protects against neuroinflammation and neurodegeneration. Nat Immunol 19:1212–1223. doi: 10.1038/s41590-018-0232-x
75. Kwon EE, Prineas JW (1994) Blood-brain barrier abnormalities in longstanding multiple sclerosis lesions. An immunohistochemical study. J Neuropathol Exp Neurol 53:625–636. doi: 10.1097/00005072-199411000-00010
76. Vos CM, Geurts JJ, Montagne L et al. (2005) Blood-brain barrier alterations in both focal and diffuse abnormalities on postmortem MRI in multiple sclerosis. Neurobiol Dis 20:953–960. doi: 10.1016/j.nbd.2005.06.012
77. Kirk J, Plumb J, Mirakhur M, McQuaid S (2003) Tight junctional abnormality in multiple sclerosis white matter affects all calibres of vessel and is associated with blood-brain barrier leakage and active demyelination. J Pathol 201:319–327. doi: 10.1002/path.1434
78. Yates RL, Esiri MM, Palace J, Jacobs B, Perera R, DeLuca GC (2017) Fibrin(ogen) and neurodegeneration in the progressive multiple sclerosis cortex. Ann Neurol 82:259–270. doi: 10.1002/ana.24997

79. Cajamarca SA, Norris EH, van der Weerd L, Strickland S, Ahn HJ (2020) Cerebral amyloid angiopathy-linked β-amyloid mutations promote cerebral fibrin deposits via increased binding affinity for fibrinogen. Proc Natl Acad Sci U S A 117:14482–14492. doi: 10.1073/pnas.1921327117
80. Bowman GL, Kaye JA, Moore M, Waichunas D, Carlson NE, Quinn JF (2007) Blood-brain barrier impairment in Alzheimer disease: stability and functional significance. Neurology 68:1809–1814. doi: 10.1212/01.wnl.0000262031.18018.1a
81. Ujiie M, Dickstein DL, Carlow DA, Jefferies WA (2003) Blood-brain barrier permeability precedes senile plaque formation in an Alzheimer disease model. Microcirculation 10:463–470. doi: 10.1038/sj.mn.7800212
82. Cortes-Canteli M, Zamolodchikov D, Ahn HJ, Strickland S, Norris EH (2012) Fibrinogen and altered hemostasis in Alzheimer's disease. J Alzheimers Dis 32:599–608. doi: 10.3233/JAD-2012-120820
83. Cortes-Canteli M, Mattei L, Richards AT, Norris EH, Strickland S (2015) Fibrin deposited in the Alzheimer's disease brain promotes neuronal degeneration. Neurobiol Aging 36:608–617. doi: 10.1016/j.neurobiolaging.2014.10.030
84. Paul J, Strickland S, Melchor JP (2007) Fibrin deposition accelerates neurovascular damage and neuroinflammation in mouse models of Alzheimer's disease. J Exp Med 204:1999–2008. doi: 10.1084/jem.20070304
85. Natale NR, Lukens JR, Petri WA (2022) The nervous system during COVID-19: Caught in the crossfire. Immunol Rev. doi: 10.1111/imr.13114
86. Loving GS, Caravan P (2014) Activation and retention: a magnetic resonance probe for the detection of acute thrombosis. Angew Chem Int Ed Engl 53:1140–1143. doi: 10.1002/anie.201308607
87. Rovira A, Auger C, Huerga E et al. (2017) Cumulative Dose of Macrocyclic Gadolinium-Based Contrast Agent Improves Detection of Enhancing Lesions in Patients with Multiple Sclerosis. AJNR Am J Neuroradiol 38:1486–1493. doi: 10.3174/ajnr.A5253
88. van Waesberghe JH, Castelijns JA, Roser W et al. (1997) Single-dose gadolinium with magnetization transfer versus triple-dose gadolinium in the MR detection of multiple sclerosis lesions. AJNR Am J Neuroradiol 18:1279–1285.
89. Pullicino R, Radon M, Biswas S, Bhojak M, Das K (2018) A Review of the Current Evidence on Gadolinium Deposition in the Brain. Clin Neuroradiol 28:159–169. doi: 10.1007/s00062-018-0678-0

90. Filippi M, Preziosa P, Copetti M et al. (2013) Gray matter damage predicts the accumulation of disability 13 years later in MS. Neurology 81:1759–1767. doi: 10.1212/01.wnl.0000435551.90824.d0
91. Zurawski J, Lassmann H, Bakshi R (2017) Use of Magnetic Resonance Imaging to Visualize Leptomeningeal Inflammation in Patients With Multiple Sclerosis: A Review. JAMA Neurol 74:100–109. doi: 10.1001/jamaneurol.2016.4237
92. Oliveira BL, Blasi F, Rietz TA, Rotile NJ, Day H, Caravan P (2015) Multimodal Molecular Imaging Reveals High Target Uptake and Specificity of 111In- and 68Ga-Labeled Fibrin-Binding Probes for Thrombus Detection in Rats. J Nucl Med 56:1587–1592. doi: 10.2967/jnumed.115.160754
93. Marques JP, Kober T, Krueger G, van der Zwaag W, Van de Moortele PF, Gruetter R (2010) MP2RAGE, a self bias-field corrected sequence for improved segmentation and T1-mapping at high field. Neuroimage 49:1271–1281. doi: 10.1016/j.neuroimage.2009.10.002
94. Ward PS, Thompson CB (2012) Metabolic reprogramming: a cancer hallmark even warburg did not anticipate. Cancer Cell 21:297–308. doi: 10.1016/j.ccr.2012.02.014
95. Bi J, Chowdhry S, Wu S, Zhang W, Masui K, Mischel PS (2020) Altered cellular metabolism in gliomas - an emerging landscape of actionable co-dependency targets. Nat Rev Cancer 20:57–70. doi: 10.1038/s41568-019-0226-5
96. Yamashita D, Bernstock JD, Elsayed G et al. (2020) Targeting glioma-initiating cells via the tyrosine metabolic pathway. J Neurosurg 134:721–732. doi: 10.3171/2019.11.JNS192028
97. Andronesi OC, Kim GS, Gerstner E et al. (2012) Detection of 2-hydroxyglutarate in IDH-mutated glioma patients by in vivo spectral-editing and 2D correlation magnetic resonance spectroscopy. Sci Transl Med 4:116ra4. doi: 10.1126/scitranslmed.3002693
98. Turcan S, Rohle D, Goenka A et al. (2012) IDH1 mutation is sufficient to establish the glioma hypermethylator phenotype. Nature 483:479–483. doi: 10.1038/nature10866
99. Andronesi OC, Kim GS, Gerstner E et al. (2012) Detection of 2-hydroxyglutarate in IDH-mutated glioma patients by in vivo spectral-editing and 2D correlation magnetic resonance spectroscopy. Sci Transl Med 4:116ra4. doi: 10.1126/scitranslmed.3002693
100. Suh CH, Kim HS, Jung SC, Choi CG, Kim SJ (2018) 2-Hydroxyglutarate MR spectroscopy for prediction of isocitrate dehydrogenase mutant glioma: a systemic review and meta-analysis using individual patient data. Neuro Oncol 20:1573–1583. doi: 10.1093/neuonc/noy113

101. Suh CH, Kim HS, Paik W et al. (2019) False-Positive Measurement at 2-Hydroxyglutarate MR Spectroscopy in Isocitrate Dehydrogenase Wild-Type Glioblastoma: A Multifactorial Analysis. Radiology 291:752–762. doi: 10.1148/radiol.2019182200
102. Paech D, Windschuh J, Oberhollenzer J et al. (2018) Assessing the predictability of IDH mutation and MGMT methylation status in glioma patients using relaxation-compensated multipool CEST MRI at 7.0 T. Neuro Oncol 20:1661–1671. doi: 10.1093/neuonc/noy073
103. Chaumeil MM, Larson PE, Woods SM et al. (2014) Hyperpolarized [1-13C] glutamate: a metabolic imaging biomarker of IDH1 mutational status in glioma. Cancer Res 74:4247–4257. doi: 10.1158/0008-5472.CAN-14-0680
104. Lohmann P, Lerche C, Bauer EK et al. (2018) Predicting IDH genotype in gliomas using FET PET radiomics. Sci Rep 8:13328. doi: 10.1038/s41598-018-31806-7
105. Park SI, Suh CH, Guenette JP, Huang RY, Kim HS (2021) The T2-FLAIR mismatch sign as a predictor of IDH-mutant, 1p/19q-noncodeleted lower-grade gliomas: a systematic review and diagnostic meta-analysis. Eur Radiol 31:5289–5299. doi: 10.1007/s00330-020-07467-4
106. Figini M, Riva M, Graham M et al. (2018) Prediction of Isocitrate Dehydrogenase Genotype in Brain Gliomas with MRI: Single-Shell versus Multishell Diffusion Models. Radiology 289:788–796. doi: 10.1148/radiol.2018180054
107. Schupper AJ, Chanenchuk T, Racanelli A, Price G, Hadjipanayis CG (2022) Laser hyperthermia: Past, present, and future. Neuro Oncol 24:S42–S51. doi: 10.1093/neuonc/noac208
108. Platten M, Bunse L, Wick A et al. (2021) A vaccine targeting mutant IDH1 in newly diagnosed glioma. Nature 592:463–468. doi: 10.1038/s41586-021-03363-z
109. Cui M, Zorrilla-Veloz RI, Hu J, Guan B, Ma X (2021) Diagnostic Accuracy of PET for Differentiating True Glioma Progression From Post Treatment-Related Changes: A Systematic Review and Meta-Analysis. Front Neurol 12:671867. doi: 10.3389/fneur.2021.671867
110. Miloushev VZ, Chow DS, Filippi CG (2015) Meta-analysis of diffusion metrics for the prediction of tumor grade in gliomas. AJNR Am J Neuroradiol 36:302–308. doi: 10.3174/ajnr.A4097

111. Bette S, Huber T, Gempt J et al. (2017) Local Fractional Anisotropy Is Reduced in Areas with Tumor Recurrence in Glioblastoma. Radiology 283:499–507. doi: 10.1148/radiol.2016152832
112. Claes A, Idema AJ, Wesseling P (2007) Diffuse glioma growth: a guerilla war. Acta Neuropathol 114:443–458. doi: 10.1007/s00401-007-0293-7
113. Hirschler L, Sollmann N, Schmitz-Abecassis B et al. (2023) Advanced MR Techniques for Preoperative Glioma Characterization: Part 1. J Magn Reson Imaging 57:1655–1675. doi: 10.1002/jmri.28662
114. Schmeel FC (2019) Variability in quantitative diffusion-weighted MR imaging (DWI) across different scanners and imaging sites: is there a potential consensus that can help reducing the limits of expected bias. Eur Radiol 29:2243–2245. doi: 10.1007/s00330-018-5866-4
115. Vermoolen MA, Kwee TC, Nievelstein RA (2012) Apparent diffusion coefficient measurements in the differentiation between benign and malignant lesions: a systematic review. Insights Imaging 3:395–409. doi: 10.1007/s13244-012-0175-y
116. Bisgaard ALH, Keesman R, van Lier ALHMW et al. (2023) Recommendations for improved reproducibility of ADC derivation on behalf of the Elekta MRI-linac consortium image analysis working group. Radiother Oncol 186:109803. doi: 10.1016/j.radonc.2023.109803
117. Song S, Cheng Y, Ma J et al. (2020) Simultaneous FET-PET and contrast-enhanced MRI based on hybrid PET/MR improves delineation of tumor spatial biodistribution in gliomas: a biopsy validation study. Eur J Nucl Med Mol Imaging 47:1458–1467. doi: 10.1007/s00259-019-04656-2
118. Lohmann P, Stavrinou P, Lipke K et al. (2019) FET PET reveals considerable spatial differences in tumour burden compared to conventional MRI in newly diagnosed glioblastoma. Eur J Nucl Med Mol Imaging 46:591–602. doi: 10.1007/s00259-018-4188-8
119. Wang H, Jordan VC, Ramsay IA et al. (2019) Molecular Magnetic Resonance Imaging Using a Redox-Active Iron Complex. J Am Chem Soc 141:5916–5925. doi: 10.1021/jacs.9b00603
120. Bao G, Mitragotri S, Tong S (2013) Multifunctional nanoparticles for drug delivery and molecular imaging. Annu Rev Biomed Eng 15:253–282. doi: 10.1146/annurev-bioeng-071812-152409

121. Chitneni SK, Reitman ZJ, Gooden DM, Yan H, Zalutsky MR (2016) Radiolabeled inhibitors as probes for imaging mutant IDH1 expression in gliomas: Synthesis and preliminary evaluation of labeled butyl-phenyl sulfonamide analogs. Eur J Med Chem 119:218–230. doi: 10.1016/j.ejmech.2016.04.066
122. Chitneni SK, Yan H, Zalutsky MR (2018) Synthesis and Evaluation of a ^{18}F-Labeled Triazinediamine Analogue for Imaging Mutant IDH1 Expression in Gliomas by PET. ACS Med Chem Lett 9:606–611. doi: 10.1021/acsmedchemlett.7b00478
123. Chitneni SK, Reitman ZJ, Spicehandler R, Gooden DM, Yan H, Zalutsky MR (2018) Synthesis and evaluation of radiolabeled AGI-5198 analogues as candidate radiotracers for imaging mutant IDH1 expression in tumors. Bioorg Med Chem Lett 28:694–699. doi: 10.1016/j.bmcl.2018.01.015
124. Gentile F, Yaacoub JC, Gleave J et al. (2022) Artificial intelligence-enabled virtual screening of ultra-large chemical libraries with deep docking. Nat Protoc 17:672–697. doi: 10.1038/s41596-021-00659-2
125. Crampon K, Giorkallos A, Deldossi M, Baud S, Steffenel LA (2022) Machine-learning methods for ligand-protein molecular docking. Drug Discov Today 27:151–164. doi: 10.1016/j.drudis.2021.09.007
126. Madani A, Krause B, Greene ER et al. (2023) Large language models generate functional protein sequences across diverse families. Nat Biotechnol 41:1099–1106. doi: 10.1038/s41587-022-01618-2

Liste der eingebrachten Originalarbeiten

Originalarbeit 1:

Fibrin-targeting molecular MRI in inflammatory CNS disorders.

Johannes Lohmeier, Rafaela V. Silva, Anna Tietze, Matthias Taupitz, Takaaki Kaneko, Harald Prüss, Friedemann Paul, Carmen Infante-Duarte, Bernd Hamm, Peter Caravan & Marcus R. Makowski

EUROPEAN JOURNAL OF NUCLEAR MEDICINE AND MOLECULAR IMAGING

Year: 2022, DOI: 10.1007/s00259-022-05807-8

Originalarbeit 2:

atlasBREX: Automated template-derived brain extraction in animal MRI.

Johannes Lohmeier, Takaaki Kaneko, Bernd Hamm, Marcus R. Makowski, Hideyuki Okano

SCIENTIFIC REPORTS

Year: 2019, DOI: 10.1038/s41598-019-48489-3

Originalarbeit 3:

Predictive IDH Genotyping Based on the Evaluation of Spatial Metabolic Heterogeneity by Compartmental Uptake Characteristics in Preoperative Glioma Using ^{18}F-FET PET.

Johannes Lohmeier, Helena Radbruch, Winfried Brenner, Bernd Hamm, Anna Tietze, Marcus R. Makowski

THE JOURNAL OF NUCLEAR MEDICINE

Year: 2023, DOI: 10.2967/jnumed.123.265642

Originalarbeit 4:

Detection of recurrent high-grade glioma using microstructure characteristics of distinct metabolic compartments in a multimodal and integrative ^{18}F-FET PET/fast-DKI approach.

Johannes Lohmeier, Helena Radbruch, Winfried Brenner, Bernd Hamm, Brian Hansen, Anna Tietze, Marcus R. Makowski

EUROPEAN RADIOLOGY

Year: 2023, DOI: 10.1007/s00330-023-10141-0

Originalarbeit 5:

Quantitative biparametric analysis of hybrid ^{18}F-FET PET/MR-neuroimaging for differentiation between treatment response and recurrent glioma.

Johannes Lohmeier, Georg Bohner, Eberhard Siebert, Winfried Brenner, Bernd Hamm, Marcus R. Makowski

SCIENTIFIC REPORTS

Year: 2019, DOI: 10.1038/s41598-019-50182-4

Danksagung

Meine Anerkennung und Dankbarkeit gilt insbesondere Herrn Prof. Dr. med. B. Hamm als Leiter des CharitéCentrum 6 für Diagnostische und Interventionelle Radiologie und Nuklearmedizin der Charité – Universitätsmedizin Berlin, der mich kontinuierlich in meiner klinisch und wissenschaftlichen Laufbahn begleitet und unterstützt hat.

Mein aufrichtiger Dank gilt zudem Herrn Prof. Dr. med. M. Makowski als langjährigem Mentor für die frühzeitige Förderung meiner wissenschaftlichen Selbstständigkeit und die zahlreichen gemeinsamen Projekte.

Herrn Prof. Dr. med. F. Paul und Frau PD Dr. med. A. Tietze möchte ich außerdem für ihren Rat und Expertise in klinischen und wissenschaftlichen Belangen danken.

Zuletzt möchte ich meiner Familie und meiner Lebenspartnerin für Ihre stetige Unterstützung meinen tiefsten Dank aussprechen!

Erklärung

§ 4 Abs. 3 (k) der HabOMed der Charité

Hiermit erkläre ich, dass

- weder früher noch gleichzeitig ein Habilitationsverfahren durchgeführt oder angemeldet wurde,

- die vorgelegte Habilitationsschrift ohne fremde Hilfe verfasst, die beschriebenen Ergebnisse selbst gewonnen sowie die verwendeten Hilfsmittel, die Zusammenarbeit mit anderen Wissenschaftlern/Wissenschaftlerinnen und mit technischen Hilfskräften sowie die verwendetet Literatur vollständig in der Habilitationsschrift angegeben wurden,

- mir die geltende Habilitationsordnung bekannt ist.

Ich erkläre ferner, dass mir die Satzung der Charité – Universitätsmedizin Berlin zur Sicherung Guter Wissenschaftlicher Praxis bekannt ist und ich mich zur Einhaltung dieser Satzung verpflichte.

Berlin, den 01.11.2023 Dr. med. Johannes Lohmeier